

MAX PLANCK INSTITUTE
FOR DYNAMICS AND
SELF-ORGANIZATION



GERRIT GREEN

**Effective Description of
Superstructures in Turbulent
Convection**

DISSERTATION



Effective Description of Superstructures in Turbulent Convection

Dissertation

for the award of the degree
"Doctor rerum naturalium"
of the Georg-August-Universität Göttingen

within the doctoral program

Physics of Biological and Complex Systems (PBCS)
of the Göttingen Graduate Center for Neurosciences, Biophysics,
and Molecular Biosciences (GGNB)
of the Georg-August University School of Science (GAUSS)

submitted by

Gerrit Green

from Preetz, Germany
Göttingen, 2020

Thesis committee:

Dr. Michael Wilczek

Max Planck Research Group Turbulence, Complex Flows and Active Matter
Max Planck Institute for Dynamics and Self-Organization

Prof. Dr. Jens Niemeyer

Astrophysical Cosmology, Institute for Astrophysics
University of Göttingen

Prof. Dr. Andreas Tilgner

Geophysical Fluid Dynamics, Institute of Geophysics
University of Göttingen

Members of the examination board:

Referee: Dr. Michael Wilczek

MPRG Turbulence, Complex Flows and Active Matter
Max Planck Institute for Dynamics and Self-Organization

2nd Referee: Prof. Dr. Andreas Tilgner

Geophysical Fluid Dynamics, Institute of Geophysics
University of Göttingen

Further members of the examination board:

Prof. Dr. Jens Niemeyer

Astrophysical Cosmology, Institute for Astrophysics
University of Göttingen

PD Dr. Olga Shishkina

Theory of Turbulent Convection, Laboratory for Fluid Dynamics, Pattern Formation
and Biocomplexity
Max Planck Institute for Dynamics and Self-Organization

Prof. Dr. Steffen Schumann

Theoretical Particle Physics - Particle Phenomenology, Institute for Theoretical Physics
University of Göttingen

Dr. David Zwicker

Max Planck Research Group Theory of Biological Fluids
Max Planck Institute for Dynamics and Self-Organization

Date of oral examination: 17 November 2020

Abstract

This thesis is dedicated to the study of turbulent superstructures in Rayleigh-Bénard convection. Turbulent superstructures are horizontally extended large-scale flow patterns that emerge despite the presence of strong fluctuations. They persist for long time scales, evolve slowly compared to the fluctuations, and their extent increases with increasing driving. This phenomenon is observed in large-aspect-ratio experiments and simulations and is very important for various geo- and astrophysical flows. There are many open questions regarding their origin and dynamics, and we study some aspects thereof. How do small-scale fluctuations and superstructures interact? How is the emergence and stability of the large-scale flow influenced by the fluctuations? Can the effect of the fluctuations be described effectively?

In the first part, we present a numerical study of superstructures to shed light on the energetic interaction between superstructures and small-scale fluctuations. For this, we make use of a filtering approach to derive scale-resolved energy and temperature variance budgets. In those, transfer terms occur that characterize the transfer rates of energy and temperature variance between scales. At the scale of the superstructure, we find that the energy transfer rate between scales acts on average as an energy sink. Therefore, the small scales are effectively a dissipation channel for the large scales. However, if considered horizontally averaged, a more complex behaviour is revealed. Close to the wall, an inverse energy transfer rate is present at moderate Rayleigh numbers. With increasing Rayleigh number the profiles become more complex and the inverse transfer layer finally vanishes. In contrast, the transfer rate is always direct, i.e. from large to small scales in the bulk. Locally, the direction of the energy transfer is closely linked to the dynamics of the plumes. At locations of plume detaching we observe a direct energy transfer and at plume impinging an inverse transfer. Similar observations are made for the transfer rate of temperature variance. On average, the transfer is from large to small scales. In contrast, also the horizontally averaged transfer rate is almost exclusively a sink and, in addition, strongly restricted to the regions close to the wall. These results may guide future investigations of reduced three-dimensional models of superstructures.

In the second part, we study the influence of small-scale fluctuations on generic large-scale flow patterns in a phenomenological model. We base our model on the Swift-Hohenberg equation, which is a well-known reduced model for Rayleigh-Bénard convection at onset of convection. We supplement the Swift-Hohenberg equation, which leads to stationary large-scale patterns, with a random advection term to include turbulent fluctuations. Here, we use a Gaussian random velocity field, which is white in time. In combination, large-scale patterns superposed by small-scale fluctuations emerge. We show that the presence of the fluctuations shifts the onset of pattern formation to larger control parameters and increases the characteristic wavelength of the pattern. The latter effect is also observed in Rayleigh-Bénard convection, in which the length scale of the superstructures increases with increasing Rayleigh number. Therefore, our phenomenological model can qualitatively explain this observation.

It may serve as the basis to derive more realistic models of superstructures, which, e.g., also capture the temporal evolution.

The last part is committed to the development of a reduced model for turbulent superstructures in Rayleigh-Bénard convection. Due to the large range of involved scales ranging from turbulent fluctuations to superstructures, the numerical and theoretical analysis of the full governing equations is very demanding. Thus, a reduced model offers the possibility of more feasible studies and, hence, more insights into the fundamental mechanisms. We propose to average the governing equations over height to reduce the dimensionality and to spatially coarse-grain to remove the fluctuations. The resulting equations contain unclosed terms that originate from the nonlinearity and the solid top and bottom wall. We propose and validate closure models based on direct numerical simulations for these terms. We show in this *a priori* study that rather simple closure models can reproduce the unclosed terms very well. In comparison to the previous phenomenological model, this has the advantage that it makes contact with the full governing equations and, therefore, quantitative comparisons are possible. But, in this first study of this kind, the horizontal velocity field is still introduced *ad hoc* as a mean flow. The proposed model provides an ideal starting point for future investigations.

In summary, in this thesis we gain insights into the energetic interaction between superstructures and turbulent fluctuations, qualitatively explain the shift of the wavelength in Rayleigh-Bénard convection, and take the first steps towards a reduced model of superstructures.

Contents

Abstract	ii
Contents	iv
1 Introduction	2
1.1 Thesis outline	5
2 Rayleigh-Bénard convection	6
2.1 Introduction	6
2.2 Governing equations	7
2.3 Pattern formation	9
2.4 Reduced model equations	20
2.5 Turbulent superstructures	29
I Manuscript I	33
3 Resolved energy budget of superstructures in Rayleigh-Bénard convection	34
3.1 Introduction	35
3.2 Theoretical and numerical background	37
3.3 Results	43
3.4 Summary	52
3.A Connection between volume-averaged resolved energy budget and original budget	55
3.B Volume-averaged resolved temperature variance budget	56
3.C Height-dependent spectra	57
3.D Horizontally averaged Π_l for varying filter scale	57
II Manuscript II	61
4 Large-Scale Pattern Formation in the Presence of Small-Scale Random Advection	62
4.1 Main text	63
4.2 Supplemental Material	70
4.3 Additional supplementary information	76

III Effective description of turbulent superstructures	81
5 Height-averaged Oberbeck-Boussinesq equations	82
5.1 Introduction	82
5.2 Derivation of averaged equation	84
5.3 Development of closure models	87
5.4 Reduced model of turbulent superstructures	99
5.5 Quantitative model evaluation	99
5.6 Linear stability analysis	104
5.7 Conclusions	106
5.A Representation of two-dimensional isotropic functions	108
5.B Numerically determined prefactors	112
5.C Temporal change	112
5.D Application to higher Rayleigh number	116
IV Conclusions	121
6 Summary & discussion	122
V Appendix	127
A Superstructures in two-dimensional convection	128
A.1 Numerical setup	131
Backmatter	133
Bibliography	134

Introduction

Large-scale flow patterns in the presence of small-scale fluctuations are a common observation in natural flows. They occur in many geo- and astrophysical settings [1, 2]. An outstanding example is solar granulation, i.e. cellular convection currents on the surface of the sun [2, 3]. For a recent remarkable visualization showing convection cells with the size of the US state of Texas, see Johnston [4]. Among the most harmful examples are tropical cyclones and tornadoes [5–9]. In figure 1.1 a satellite image of the cyclone *Idai* on March 2019 is shown. Less harmful, though



Figure 1.1: Satellite view on the tropical cyclone *Idai*. Image: NASA Worldview [10].

also prominent examples, are quasi-two-dimensional cloud streets [1, 11–13], which we consider in a little more detail in the following. In the atmosphere, quasi-two-dimensional structures are quite common [12] but may have very different origins. They can result from, e.g., shear-driven surface-layer turbulence, gravity waves, or buoyancy-driven turbulence [12]. A basic mechanism from which cloud streets form is when heated air rises through the atmosphere hitting a warmer upper air layer above a flat topography, e.g. the ocean [14–18]. This layer acts as a lid, causing the columns of heated air (thermals) to roll over and descend. In this

process, parallel cylinders of rotating air form convection rolls typically aligned almost parallel to the wind. Here, (cumulus) clouds form in the area of uprising fluid and the sky is clear in the descending area, see figure 1.2a. They can have a very large extent from 20 km up to 500 km, and the spacing between the bands is 2 km to 8 km [18]. Figure 1.2b shows an example of such cloud streets. Even though the basic principles for the formation of these large-scale flow patterns are known, there are many open questions regarding the dynamics of the large-scale patterns, their horizontal extent, as well as their coexistence and interaction with small-scale turbulent fluctuations. Studying this in real situations, e.g. the atmosphere,

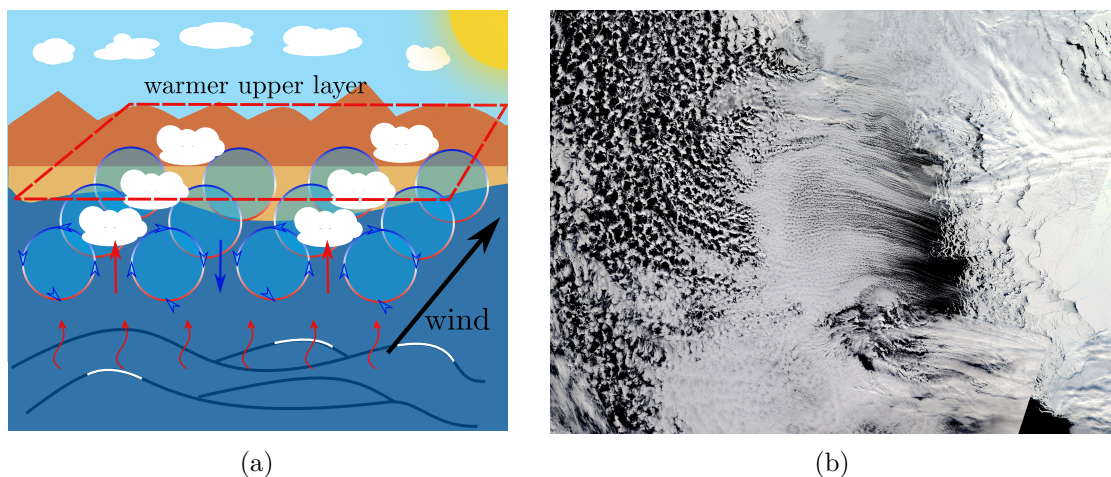


Figure 1.2: (a) Sketch of a generation mechanism for cloud streets. In the presence of convection rolls clouds can form in the area of uprising moist fluid. They are regularly formed over the sea surface. (b) Cloud streets near Antarctica over the open water of the Amundsen Sea on September 2018. Image: NASA’s Earth Observatory [14]

is currently impracticable due to the involved range of scales and the complex nature of the system connecting different areas of physics such as microphysics, thermodynamics, and fluid physics [18–20]. However, large-scale flow patterns in turbulent flows are also present in a variety of idealized model systems such as wall-bounded and convection-driven flows [21–35]. These patterns are often referred to as (turbulent) superstructures. Explicit examples are so-called Taylor rolls (or vortices) in Taylor-Couette turbulence [24, 25] and large-scale convection rolls in turbulent Rayleigh-Bénard convection (RBC). These are two canonical fluid systems that have many similarities, i.e. basically the same stability criteria, relations between the non-dimensional parameters, and transport processes characterized by boundary layers and turbulent bulks [36–38]. Also, in the idealized setting of a turbulent Kolmogorov flow large-scale patterns have been reported and systematically studied [39–42], e.g. with respect to the dependence on the domain size [41]. Large-scale motions also exist in turbulent channel and pipe as well as boundary layer flows [29, 43–45]. Typically, large domains are needed for these observations, and the dynamics of all of the previously mentioned flows can be described by the Navier-Stokes equations [46, 47]. It is, therefore, suspected that there are universal principles in the generation of large-scale flows.

Regular flow patterns are well understood and studied close to onset when the flow state evolves from a homogeneous base state into a spatially (and temporally) varying pattern, as well as in the weakly nonlinear regime [48–50]. The coherent large-scale flow in the turbu-

lent regime represents a regular pattern if considered on its own, i.e. if the fluctuations are removed. The field of pattern formation connects various research areas and phenomena such as classical fluid dynamics, astrophysics, active matter, chemistry, or biology which can all be considered as nonequilibrium systems [48, 49]. Prominent examples are the textures on animals (e.g. tigers, zebras, or giraffes), ripples in sandy deserts or at the beach, snowflakes, but also the organization of galaxies or stripe patterns on gas giants [48, 49], see figure 1.3. However,



Figure 1.3: Examples of pattern formation in nature. (a) Ripples in the sand dunes [51], (b) giraffe skin texture [52], taken from www.publicdomainpictures.net.

the theoretical methods used close to onset cannot be applied directly to understand patterns far away from onset. One possible approach to better understand patterns in turbulent flows is to find simplified models of the large-scale flow only. Such models might, therefore, help to gain insights into general mechanisms and advance the understanding of turbulent large-scale flows.

In this thesis, I will focus on convection-driven flows and study turbulent patterns in Rayleigh-Bénard convection, which is an idealized basic convection system. In this simple system, a fluid layer is heated from below and cooled from above in a homogeneous gravitational field [53–56]. Although the setup is remarkably simple, the observed phenomena are manifold [53–60]. For very small driving the fluid is at rest and heat is transported by conduction. If the driving is increased above a critical threshold, convection patterns appear in the form of steady convection rolls or hexagons, structures observed in, e.g., the atmosphere [1, 13] or on the sun [2, 4]. The patterns become increasingly unsteady and complex with increasing driving. At large driving, small-scale thermal plumes emerge and the flow becomes turbulent. Here, one classically expects a chaotic and irregular fluid motion. However, in large-aspect-ratio systems, a horizontally extended coherent large-scale flow pattern superposed by small-scale fluctuations is present. These flows persist on very long time scales and on horizontal scales much larger than the height of the fluid layer [22, 30, 31, 35]. These patterns are named turbulent superstructures in RBC. Turbulent superstructures have first been revealed numerically in RBC in the seminal work by Hartlep et al. [22] and studied in detail thereafter [27, 30–32, 35, 61–65]. Their horizontal extent increases with increasing driving [22, 30, 31, 35, 64] and they are composed of clustered plumes [62], which form effective large-scale convection rolls. The large-scale patterns are reminiscent of patterns observed right above the onset of convection such as spiral defect chaos [27, 30]. This opens several questions. How do small-scale fluctuations and turbulent superstructures interact? Why is the characteristic length-scale increasing, when at the same time increasingly smaller fluctuations emerge? Is the dynamics of the large-scale

pattern captured by reduced models developed for spiral defect chaos?

1.1 Thesis outline

In order to tackle the previously raised questions, the [first part](#) of this work is dedicated to understanding the energetic interaction between the large-scale superstructures and the small-scale fluctuations in RBC in more detail. The [second part](#) focuses on the emerging wavelength of generic large-scale flow patterns in the presence of small-scale fluctuations. Finally, with the insights from the previous parts, we develop a reduced model of turbulent superstructures in an *a priori* study in the [third part](#). The latter is very important because studying the full system is theoretically as well as computationally very demanding due to the large range of scales that need to be considered. Therefore, a reduced model will allow for a more detailed understanding of the dynamics and the origin of the large-scale flow patterns.

I will start in chapter [2](#) with a basic introduction to RBC. I review fundamental principles from pattern formation such as linear stability analysis, reduced-order models, as well as envelope equations, and additionally describe spiral defect chaos. This also includes an introduction to the Swift-Hohenberg equation [[48](#), [49](#), [66](#)], a prominent model for pattern formation and a reduced description of RBC. This first part ends with an introduction to turbulent superstructures in RBC. In chapter [3](#) the manuscript Green et al. [[67](#)] is reproduced. Here, I present direct numerical simulations (DNS) of RBC in large-aspect-ratio systems studying the energetic interaction of turbulent fluctuations and superstructures in the resolved energy and thermal variance budget. The article Ibbeken et al. [[68](#)] is presented in chapter [4](#). This study deals with the influence of small-scale fluctuations on generic large-scale patterns in a generalized Swift-Hohenberg equation. Here, we especially focus on the emerging wavelengths. The subsequent chapter [5](#) is dedicated to the development of a reduced model for turbulent superstructures. In this part, I extract the large-scale flow pattern by averaging over height and coarse-graining to reduce the dimensionality and remove the fluctuations. In combination, this is a novel approach to reduce the governing equations of RBC, which, however, results in unclosed terms. Based on the previous results and literature knowledge, closure models for these terms are developed and validated with DNS. In the remaining chapter [6](#), the results and open questions are summarized and discussed.

Rayleigh-Bénard convection

2.1 Introduction

Many natural flows are driven by thermal gradients. This includes fluid motion in the interior of stars and planets as well as the atmosphere and the ocean [1, 2, 19, 53, 69, 70].

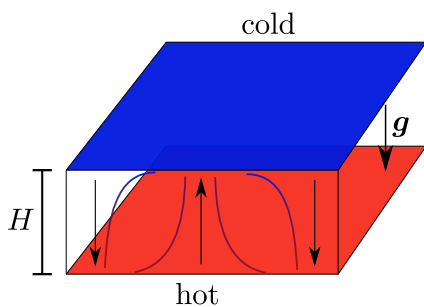


Figure 2.1: Sketch of RBC. The fluid is heated from below and cooled from above. The warm fluid rises and the cold fluid falls.

Additionally, convection plays a major role in many technological applications, e.g. the circulation of air in rooms and passenger cabins [71–75]. A paradigmatic system to study convection is Rayleigh-Bénard convection. This system has been thoroughly investigated and is described in several reviews [54, 58–60] and textbooks [53, 55, 56, 76] in great detail. In RBC a fluid is confined between a heated bottom plate and a cooled top plate, and subject to gravity [53] (figure 2.1). Though this setup is arguably very simple, RBC exhibits a plethora of different phenomena ranging from instability to pattern formation, chaos, turbulence, and turbulent superstructures. Therefore, RBC is not only a well studied fluid dynamics problem but also an interesting nonequilibrium system in general

[49]. In the following, I will give a basic introduction to the governing equations and review some of the phenomena relevant to this work. In this regard, I refrain from a review of classical turbulent RBC, which is not at the heart of this thesis. Instead I refer the reader to the excellent reviews of Siggia [57], Ahlers et al. [59], Verma et al. [77], and Lohse and Xia [60] as well as the textbooks of Ching [55] and Verma [56].

Let me start with an introduction to the basic physical principles following Cross and Greenside [49]. Assume that initially the temperature difference between bottom (T_{bottom}) and top (T_{top}) vanishes, $\Delta = T_{\text{bottom}} - T_{\text{top}} = 0$, and that the system is in thermodynamic equilibrium. The fluid is at rest, and the temperature is constant everywhere. Let us now increase $\Delta > 0$, such that the bottom wall has a higher temperature than the top wall. In this case, fluid parcels at the bottom will be heated, expand in volume, and accordingly decrease in density. At the same time, fluid parcels at the top will be cooled, shrink in volume, and increase

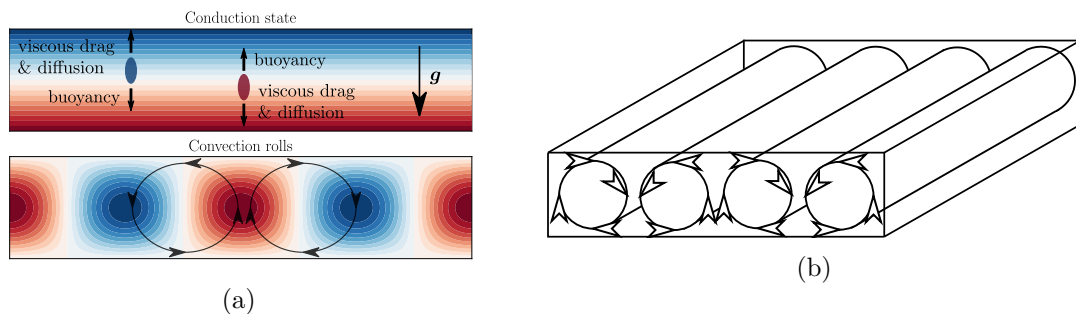


Figure 2.2: (a) Sketch of the temperature in the time-independent conduction state and deviations from it when convection rolls are present. For the latter, fluid parcels rise in regions of warm updraughts (red) and fall in cold downdraughts (blue). (b) Schematic visualization of convection rolls in three dimensions present at the onset of convection.

in density [49]. In this case cold, dense fluid is on top of warmer and lighter fluid. As a result, buoyancy accelerates warm fluid upward and cold fluid downward, see figure 2.2a. However, this is counteracted by viscous drag and thermal diffusion. The former mechanism decreases any spatial variation of the velocity, and the latter tends to equilibrate the temperature of the fluid parcels with its surrounding [49]. Hence, a warm fluid parcel will only start to rise if the buoyancy force overcomes the viscous drag and thermal diffusion [54]. If the buoyancy forces are too weak, the fluid stays at rest, and heat is transported by conduction from top to bottom, and a linear temperature profile develops [76], see figure 2.2a. This fluid flow in RBC is governed by three non-dimensional control parameters. These are the Rayleigh number Ra , characterizing the competition of buoyancy with drag and thermal diffusion, the Prandtl number Pr , governing the fluid properties in terms of the ratio of kinematic viscosity to thermal diffusivity, and the aspect ratio Γ , which is the ratio of the system length to its height. Here, the Rayleigh number is proportional to the temperature difference and determines the stability of the system. If the Rayleigh number exceeds the critical threshold, warm fluid rises and cold fluid falls, and the heat is transported by convection. The fluid parcels organize into patterns, which are steady parallel convection rolls in the simplest case very close to onset of convection, see figure 2.2. As the Rayleigh number, or equivalently the temperature difference, is increased further, the motion becomes increasingly unsteady and complex.

2.2 Governing equations

How can we describe this system mathematically to achieve a quantitative description? In principle, we need to start with a compressible fluid [54, 55]. The evolution of the density ϱ is then described by the continuity equation

$$\partial_t \varrho + \nabla \cdot (\varrho \mathbf{u}) = 0 \quad (2.1)$$

and is a function of pressure and temperature $\varrho = \varrho(T, p)$. This needs to be supplemented with the Navier-Stokes equations for the velocity field \mathbf{u} of a compressible fluid [78]

$$\varrho (\partial_t \mathbf{u} + \mathbf{u} \cdot \nabla \mathbf{u}) = \nabla \cdot \boldsymbol{\sigma} - \varrho g \hat{\mathbf{z}}, \quad (2.2)$$

in which g is the acceleration due to gravity and $\boldsymbol{\sigma}$ the stress tensor. However, we can make use of the Oberbeck-Boussinesq approximation [53, 54, 56]. Here, first the fluid density is assumed

to be independent of the pressure and to vary linearly with temperature [53, 55, 56]

$$\varrho(T, p) = \varrho(T) = \varrho_0 (1 - \alpha(T - T_0)), \quad (2.3)$$

in which α is the thermal expansion coefficient, T_0 is the mean temperature of the system, and $\varrho_0 = \varrho(T_0)$. Physically, this means that the pressure only varies around a hydrostatic equilibrium [54]. All further fluid parameters are assumed to be independent of temperature and pressure. Then for slow processes, the density can be considered as being constant everywhere in (2.1) and (2.2), with the exception that the density variation with temperature needs to be retained in the buoyancy term [53, 54]. Physically, this holds if the speed of sound is much larger than the characteristic velocity of the convective flow [54]. With these assumptions, the stress tensor reduces to the standard form for an incompressible fluid [79] and the velocity field is solenoidal. More details on the approximations can be found, e.g., in Getling [53], Verma [56], and Chillà and Schumacher [54].

To close the equations, we need to complement them with an evolution equation for the temperature. The temperature T obeys the thermal transport equation [54, 55, 79, 80]

$$\partial_t T + \mathbf{u} \cdot \nabla T = \kappa \nabla^2 T, \quad (2.4)$$

in which κ is the thermal diffusivity. It states that the change of temperature of a fluid particle is equal to the heat transferred from the neighbouring fluid parcel. For more details on the derivation, I refer the reader to Guyon et al. [79] and Tritton [80].

Oberbeck-Boussinesq equations As a result of the above assumptions, (2.2) reduces to the standard Navier-Stokes equations for an incompressible fluid with a variable density of the form (2.3) only in the buoyancy term. The density on the left-hand side of (2.2) and in (2.1) is set to be equal to the constant ϱ_0 . The following set of equations is eventually obtained from (2.1), (2.2), and (2.4) [54, 55]

$$\begin{aligned} \nabla \cdot \mathbf{u} &= 0 \\ \partial_t \mathbf{u} + \mathbf{u} \cdot \nabla \mathbf{u} &= -\frac{1}{\varrho_0} \nabla p^* + \nu \nabla^2 \mathbf{u} + \alpha g \theta \hat{\mathbf{z}} \\ \partial_t \theta + \mathbf{u} \cdot \nabla \theta &= \kappa \nabla^2 \theta, \end{aligned}$$

in which ν is the kinematic viscosity, $\theta = T - T_0$ the temperature deviation from the mean, and $p^* = p + \varrho_0 g z$ the pressure variation about the hydrostatic equilibrium profile. This set of partial differential equations (PDEs) is named Oberbeck-Boussinesq equations (OBEs). They are conveniently non-dimensionalized with the temperature difference between top and bottom Δ , the height of the fluid layer H , the free-fall time $t_f = \sqrt{H/(\alpha g \Delta)}$ and free-fall velocity $u_f = H/t_f$,

$$\nabla \cdot \mathbf{u} = 0 \quad (2.5a)$$

$$\partial_t \mathbf{u} + \mathbf{u} \cdot \nabla \mathbf{u} = -\nabla p^* + \sqrt{\frac{Pr}{Ra}} \nabla^2 \mathbf{u} + \theta \hat{\mathbf{z}} \quad (2.5b)$$

$$\partial_t \theta + \mathbf{u} \cdot \nabla \theta = \frac{1}{\sqrt{RaPr}} \nabla^2 \theta. \quad (2.5c)$$

Note that we use the same symbols for dimensionless quantities for ease of notation. These equations contain two control parameters, namely the Rayleigh number,

$$Ra = \frac{\alpha g \Delta H^3}{\nu \kappa}, \quad (2.6)$$

and Prandtl number,

$$Pr = \frac{\nu}{\kappa}, \quad (2.7)$$

already introduced above. These equations now mark the starting point for all further theoretical analyses. In the subsequent chapters, I review some phenomena relevant for this work. I start with hydrodynamic instability and pattern formation, supplemented by an introduction to reduced models. This is followed by a review of turbulent superstructures.

2.3 Pattern formation

Above onset of convection, hot and cold fluid in RBC organize into complex spatiotemporal patterns in large aspect ratio systems. This makes RBC a paradigmatic system to study classical pattern formation [58]. Close to onset, many theoretical techniques such as linear stability and weakly nonlinear analysis can be applied successfully [48, 53, 58] and the results thereof have been confirmed and complemented by numerical and experimental studies [58].

2.3.1 Linear stability analysis

We already know that the Rayleigh number has to exceed a certain threshold before the fluid is set in motion. The first task is to determine this critical parameter value by means of a linear stability analysis. This can be performed fairly easily for free-slip boundary conditions [53, 56, 76]. However, for no-slip boundary conditions the calculations become more involved and are not analytically solvable any longer. A classical reference is given by Chandrasekhar [81] and comprehensive presentations are found in Getling [53], Manneville [76], as well as a modern treatment in Hoyle [48] and Verma [56].

2.3.1.1 General procedure of a linear stability analysis

In the following, I highlight the basic procedure of a linear stability analysis, which is relevant later in this thesis, see section 4.1. Detailed introductions to linear stability analysis can be found, e.g., in Hoyle [48] and Cross and Greenside [49]. Here, I only summarize the basics from Cross and Greenside [49]. Let us consider a generic pattern forming system with translational symmetry in the lateral direction and confined in the vertical direction. The lateral direction is set to have infinite extent or to be spatially periodic. Accordingly, the lateral direction is called extended and the vertical one confined. We assume that the system can be described by some (vector) field $\mathbf{q}(\mathbf{x}, t)$ and that a spatially uniform and time-independent base state exists. To study when this base state becomes unstable to small perturbations, we perform a linear stability analysis in the following way:

- (i) Write down the evolution equation for $\mathbf{q}(\mathbf{x}, t)$.
- (ii) Non-dimensionalize the evolution equation to reduce the number of control parameters p .

- (iii) Choose extended (lateral) directions \mathbf{x}_\perp with infinite or periodic boundary conditions consistent with translational symmetry.
- (iv) Find at least one uniform time-independent base state $\mathbf{q} = \mathbf{q}_b(\mathbf{x}_\parallel)$, which only depends on the confined (vertical) coordinates \mathbf{x}_\parallel and is independent of \mathbf{x}_\perp .
- (v) Linearise the equations around the uniform base state $\mathbf{q} = \mathbf{q}_b(\mathbf{x}_\parallel) + \mathbf{q}_p(\mathbf{x})$ to obtain the evolution equations for small perturbation $\mathbf{q}_p(\mathbf{x})$.
- (vi) Find particular solutions of the form

$$\mathbf{q}_p = \mathbf{q}_k(\mathbf{x}_\parallel) e^{\sigma_k t} e^{i\mathbf{k} \cdot \mathbf{x}_\perp}.$$

to solve the linearised equations. From this, the growth rate σ_k can be determined. It might be nontrivial to find $\mathbf{q}_k(\mathbf{x}_\parallel)$ and numerical calculations might be necessary.

- (vii) Analyse the real part of the growth rate $\Re(\sigma_k)$. Determine the stability of the uniform base state by analysing the growth rate. It is stable if $\max_k \Re(\sigma_k) < 0$. The base state is linearly unstable to perturbations with wavevector \mathbf{k} if $\Re(\sigma_k) > 0$.
- (viii) For a control parameter p of particular interest find the critical value obtained from $\max_k \Re(\sigma_k) = 0$ and the corresponding critical wavevector (or wavenumber for systems that are isotropic in the extended direction) \mathbf{k}_c and frequency $\omega_c = \Im(\sigma_k(\mathbf{k}_c))$, if any exists. They characterize at which value of the control parameter the base state first becomes unstable to perturbations with spatial variations \mathbf{k}_c .

Based on the properties of the growth rate we can define different types of instabilities [49].

2.3.1.2 Types of instabilities

In the following we focus on systems in which the growth rate is a function of the wavenumber of the perturbation and one control parameter p , $\sigma_k(p)$. The growth rate only depends on the magnitude of the wavevector if the system is isotropic in the extended direction, i.e. the governing equations are invariant under rotations about any axis perpendicular to this direction. Above a critical parameter p_c the real part of the growth rate $\Re(\sigma_k)$ takes positive values and spatial structure emerges from perturbations to the base state. Instabilities can be characterized based on the properties of the growth rate. First, they are classified by where the maximum growth rate passes through zero if the control parameter is varied, i.e. at zero or a nonzero wavenumber. Second, we distinguish if the imaginary part of the growth rate at onset, i.e. $\Im(\sigma_k(k_c))$, vanishes or not. The former leads to a classification in three classes: type I, type II or type III. Each individual class is then characterized as stationary or oscillatory, depending on the imaginary part of the growth rate $\Im(\sigma_k(k_c)) = \omega_c$. The case $\omega_c = 0$ is denoted by I/II/III-s and $\omega_c \neq 0$ as I/II/III-o [49]. Therefore, this classification tells us how the instability of the system first sets in. We focus on the wavenumbers close to the maximum of $\Re(\sigma_k)$, which first passes through zero. The wavenumber for which the maximum of $\Re(\sigma_k)$ first becomes positive with varying control parameter p is called critical wavenumber. Finally, we introduce a reduced control parameter $\epsilon = \frac{p-p_c}{p_c}$ to characterize the deviations from onset.

Type-I instability For a type-I instability, the instability is first observed at a nonzero wavenumber. For $p > p_c$ the base state is unstable to perturbations from a band of wavenumbers, which is found e.g. from the neutral stability curve. The key aspects are captured by the following non-dimensional functional form [49]

$$\Re(\sigma_k) \approx \epsilon - (k - k_c)^2, \quad (2.8)$$

see figure 2.3.

Type-II instability A type-II instability is characterized by the fact that the growth rate at $q = 0$ always vanishes. Conserved order parameters, i.e. the field integrated over the full volume is constant in time, are typical examples for such an instability. A parametrization of the growth rate capturing this behaviour is given as [49]

$$\Re(\sigma_k) \approx \epsilon k^2 - k^4/2, \quad (2.9)$$

shown in figure 2.3. In contrast to a type-I instability, the characteristic length of the pattern diverges for $\epsilon \rightarrow 0$ because modes close to wavenumber zero still have a growth rate with positive real part.

Type-III instability If the growth rate has its maximum at $k = 0$ for all p , the instability is of type III. This can be given as [49]

$$\Re(\sigma_k) \approx \epsilon - k^2 \quad (2.10)$$

near onset, sketched in figure 2.3. This type is often found with an oscillatory instability. Here, already close to onset a spatial structure with a large extent may be observed. We make use of this classification in chapter 4 and to compare RBC with reduced models.

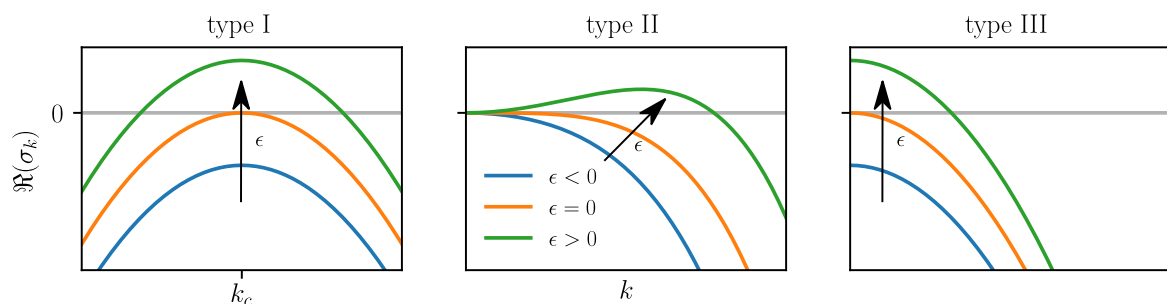


Figure 2.3: Sketch of the growth rates corresponding to the different types I-III.

2.3.1.3 Linear stability analysis for Rayleigh-Bénard convection

To give an explicit example of the procedure of a linear stability analysis, we now consider the OBEs. The following presentation is adapted from Hoyle [48]. The starting point for the

linear stability analysis are the OBEs in the following form

$$\begin{aligned}\nabla \cdot \mathbf{u} &= 0 \\ \partial_t \mathbf{u} + \mathbf{u} \cdot \nabla \mathbf{u} &= -\nabla p^* + \sqrt{\frac{Pr}{Ra}} \nabla^2 \mathbf{u} + \theta \hat{\mathbf{z}} \\ \partial_t \theta + \mathbf{u} \cdot \nabla \theta &= \frac{1}{\sqrt{RaPr}} \nabla^2 \theta.\end{aligned}$$

We are interested in the stability of the conduction solution, i.e. for which control parameters this solution becomes unstable to small perturbations. Therefore, we start with the stationary conduction solution, for which the velocity vanishes

$$\mathbf{u} = \mathbf{0}.$$

From the temperature equation we then find

$$\begin{aligned}\nabla^2 \theta &= 0 \\ \Rightarrow \theta &= \theta_c(z) \equiv \frac{1}{2} - z\end{aligned}$$

and from the equation for the vertical velocity [48]

$$\begin{aligned}\partial_z p^* &= \theta_c \\ \Rightarrow p^* &= p_c(z) \equiv p_0 + \int_0^z \theta_c(z') dz' .\end{aligned}$$

To determine the stability we now consider perturbations around this state. Hence, we rewrite

$$\begin{aligned}p^* &= p_c(z) + \hat{p} \\ \theta &= \theta_c(z) + \vartheta.\end{aligned}$$

This is inserted into the OBEs and we find

$$\begin{aligned}\partial_t \mathbf{u} + \mathbf{u} \cdot \nabla \mathbf{u} &= -\nabla \hat{p} + \sqrt{\frac{Pr}{Ra}} \nabla^2 \mathbf{u} + \vartheta \hat{\mathbf{z}} \\ \partial_t \vartheta + \mathbf{u} \cdot \nabla \vartheta - u_z &= \frac{1}{\sqrt{RaPr}} \nabla^2 \vartheta.\end{aligned}$$

To eliminate the pressure we take the curl of the momentum equation [48]

$$\begin{aligned}\partial_t \boldsymbol{\omega} + \mathbf{u} \cdot \nabla \boldsymbol{\omega} - \boldsymbol{\omega} \cdot \nabla \mathbf{u} &= \nabla \vartheta \times \hat{\mathbf{z}} + \sqrt{\frac{Pr}{Ra}} \nabla^2 \boldsymbol{\omega} \\ \boldsymbol{\omega} &= \nabla \times \mathbf{u},\end{aligned}$$

in which $\boldsymbol{\omega}$ is the vorticity. These equations mark the starting point for the general procedure outlined in section 2.3.1.1.

Linearisation We now choose the base state $\mathbf{u}_b = \boldsymbol{\omega}_b = 0, \vartheta_b = 0$, which describes the conduction solution. Here, the extended directions are the horizontal directions $\mathbf{x}_h = (x, y)^\top$, and the base state is independent of these coordinates. We now linearise the equations around this state, resulting in [48]

$$\begin{aligned}\partial_t \boldsymbol{\omega} &= \nabla \vartheta \times \hat{\mathbf{z}} + \sqrt{\frac{Pr}{Ra}} \nabla^2 \boldsymbol{\omega} \\ \partial_t \vartheta - u_z &= \frac{1}{\sqrt{RaPr}} \nabla^2 \vartheta.\end{aligned}$$

The final manipulation of the equations is to act with the operator $\hat{\mathbf{z}} \cdot \nabla \times$ on the vorticity equation to rewrite the equations in terms of the vertical velocity. We end up with the following set of equations for ϑ and u_z only

$$\partial_t \nabla^2 u_z = \nabla_h^2 \vartheta + \sqrt{\frac{Pr}{Ra}} \nabla^4 u_z \quad (2.11a)$$

$$\partial_t \vartheta - u_z = \frac{1}{\sqrt{RaPr}} \nabla^2 \vartheta, \quad (2.11b)$$

in which $\nabla_h = (\partial_x, \partial_y, 0)^\top$. These equations need to be supplemented with boundary conditions. We consider a laterally infinite system. The top and bottom plate are held at fixed temperature, which is why

$$\vartheta = 0 \quad \text{at } z = 0, 1.$$

Additionally, we use free-slip boundary conditions

$$u_z = 0, \quad \partial_z \mathbf{u}_h = 0 \quad \text{at } z = 0, 1.$$

The first one states that the top and bottom boundaries are impenetrable and the second one results from the vanishing of tangential stresses. The latter implies that the fluid can move freely in the horizontal directions at the boundaries. Differentiating the incompressibility condition with respect to z then gives

$$\partial_z^2 u_z = 0 \quad \text{at } z = 0, 1.$$

Solving the PDE In this case the solution can be sought as a superposition of Fourier modes with wavenumber $n\pi$

$$\begin{aligned}u_z^{(n)} &= u_n \sin(n\pi z) e^{i\mathbf{k}_h \cdot \mathbf{x}_h + \sigma_k t} + c.c. \\ \vartheta^{(n)} &= \vartheta_n \sin(n\pi z) e^{i\mathbf{k}_h \cdot \mathbf{x}_h + \sigma_k t} + c.c.,\end{aligned}$$

where $c.c.$ denotes the complex conjugate, the subscript h the horizontal directions and σ_k the growth rate of the eigenmode. We insert one mode into (2.11) and obtain

$$\begin{aligned}-\sigma_k (k^2 + n^2 \pi^2) u_n &= -k^2 \vartheta_n + \sqrt{\frac{Pr}{Ra}} (k^2 + n^2 \pi^2)^2 u_n \\ \sigma_k \vartheta_n - u_n &= -\frac{1}{\sqrt{RaPr}} (k^2 + n^2 \pi^2) \vartheta_n,\end{aligned}$$

with $k = |\mathbf{k}_h|$. From this, we can eliminate ϑ_n and u_n to find

$$\sigma_k^2(k^2 + n^2\pi^2) + \sigma_k \frac{(1 + Pr)}{\sqrt{RaPr}}(k^2 + n^2\pi^2)^2 + \frac{1}{Ra}(k^2 + n^2\pi^2)^3 - k^2 = 0.$$

This is a quadratic equation for σ_k , for which one solution

$$\sigma_k = -\frac{1 + Pr}{2\sqrt{RaPr}}(k^2 + n^2\pi^2) + \frac{1}{2}\sqrt{\frac{(1 - Pr)^2}{RaPr}(k^2 + n^2\pi^2)^2 + \frac{4k^2}{k^2 + n^2\pi^2}}$$

is shown in figure 2.4a, cf. [53]. The other solution is always negative [53].

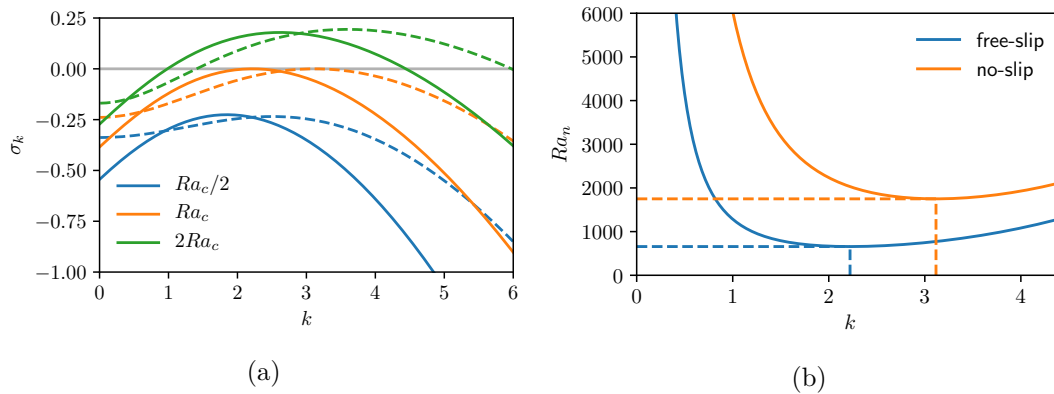


Figure 2.4: (a) Comparison of the growth rate σ_k for free-slip (solid lines) and no-slip (dashed lines) boundary conditions for different Ra and $Pr = 1$. (b) Neutral stability curve $\sigma_k = 0$ for $n = 1$ with free-slip boundary conditions (2.12) and an approximate solution for no-slip boundary conditions (2.15). The dashed lines in the right plot highlight the critical parameters Ra_c , k_c .

Analysing the growth rate We are interested in the wavenumber and Rayleigh number for which the base state becomes first unstable and, therefore, consider the case $\sigma_k = 0$. This results in

$$Ra_n(k) = \frac{(k^2 + n^2\pi^2)^3}{k^2}. \quad (2.12)$$

This curve is also called neutral stability curve and is shown in figure 2.4b. Stable states (Ra, k) corresponds to the region below the curve and unstable ones to the one above the curve. The corresponding eigenmode grows if $Ra > Ra_n(k)$. The minimal Ra_n is obtained for $n = 1$ and $k = k_c = \frac{\pi}{\sqrt{2}}$ and is called the critical Rayleigh number Ra_c , which is given by the classic result [48, 53, 76]

$$Ra_c = \frac{27}{4}\pi^4. \quad (2.13)$$

The critical wavenumber k_c sets the horizontal scale of the perturbation growing at onset. Notably, the critical values are independent of the Prandtl number, i.e. the ratio of fluid viscosity to thermal diffusivity. If the Rayleigh number exceeds this threshold, buoyancy

forces overcome the viscous drag and diffusion, and any mode $Ra > Ra_n(k) \geq Ra_c$ can grow irrespectively of the Prandtl number. However, very close to onset only the mode $n = 1$ is unstable [48]. Then, only a small band of wavenumbers with width $\sqrt{Ra - Ra_c}$ centred around k_c [76] can grow, and we expect a pattern which consists of a superposition of these modes close to k_c from the linear analysis [48]. But, only a small number of modes is selected by the nonlinearity [48]. The prominent stripe solutions consists only of a single pair of wavevectors $\pm \mathbf{k}_h$. The corresponding fields are real and, therefore, the solutions always consist of pairs of wavevectors. The corresponding wavenumber $k \approx k_c$ gives a prediction for the size of the convection rolls at onset. However, the numerical value of this scale k_c and also of the critical Rayleigh number Ra_c depend on the boundary conditions for the velocity.

No-slip boundary conditions In the more realistic case of no-slip boundary conditions ($\mathbf{u} = 0$ at $z = 0, 1$) the calculations are more involved and result in a transcendental equation, from which the neutral stability curve can be obtained [56, 82]. An accurate numerical solution gives

$$k_c \approx 3.117 \quad (2.14a)$$

$$Ra_c \approx 1708, \quad (2.14b)$$

see e.g. Verma [56], Manneville [76] for details. We can calculate an approximate solution for the linearised equations with no-slip boundary conditions with the so-called *Galerkin method* [76]. Here, first a set of orthogonal basis functions is chosen, which fulfill the boundary conditions. Then the exact solution can be represented as a series expansion. In order to make the calculations feasible the series expansion is typically truncated to the lowest order. Yet, the resulting equations still depend on the confined coordinate, which is finally removed by a projection technique. Since the basis functions are orthonormal, we can project on single modes by taking a scalar product. This results in a linear homogeneous algebraic problem with the growth rate σ_k , wavenumber k and control parameters as variables. In the case of RBC, an approximate solution in terms of polynomials can be found. Compared to the free-slip calculations, the procedure is identical up to (2.11). In the remaining part of the linear stability analysis only the additional projection is needed, but the general approach is identical. We outline the approach here and more details are found in [76]. We start with Fourier modes in horizontal directions as previously

$$\begin{aligned} u_z &= V(z)e^{i\mathbf{k}_h \cdot \mathbf{x}_h + \sigma_k t} \\ \vartheta &= \Theta(z)e^{i\mathbf{k}_h \cdot \mathbf{x}_h + \sigma_k t} \end{aligned}$$

and need to specify the vertical dependence. A representation compatible with the boundary conditions in a domain $z \in [-0.5, 0.5]$ is given as [76]

$$\begin{aligned} V(z) &= \left(\frac{1}{4} - z^2\right)^2 P_v(z) \\ \Theta(z) &= \left(\frac{1}{4} - z^2\right) P_\Theta(z) \\ P_q &= \sum_0^\infty q_n z^n \end{aligned}$$

in terms of a series expansion in polynomials. We truncate the series to the lowest order $n = 0$ for simplicity

$$\begin{aligned} u_z &= u_A \left(\frac{1}{4} - z^2 \right)^2 e^{i\mathbf{k}_h \cdot \mathbf{x}_h + \sigma_k t} \\ \vartheta &= \vartheta_A \left(\frac{1}{4} - z^2 \right) e^{i\mathbf{k}_h \cdot \mathbf{x}_h + \sigma_k t}. \end{aligned}$$

This is inserted into (2.11) and a set of equations which still depend on z are obtained. The momentum equation is multiplied by $(1/4 - z^2)^2$ and the temperature equation by $(1/4 - z^2)$ and we integrate over the height to remove the vertical dependence. This results in a system of algebraic equations, which can be solved for the growth rate σ_k and the neutral stability curve $\sigma_k = 0$. In figure 2.4a the resulting growth rates for different Ra and $Pr = 1$ are shown and in 2.4b the neutral stability curve [76]

$$Ra = \frac{28(k^4 + 24k^2 + 504)(k^2 + 10)}{27k^2}. \quad (2.15)$$

From the latter curve the critical Rayleigh number and corresponding critical wavenumber are given by the minimum. The approximate values are

$$k_c \approx 3.1165 \quad (2.16)$$

$$Ra_c \approx 1750, \quad (2.17)$$

which are close to the more accurate numerical solution (2.14). The results for the free-slip and no-slip boundary conditions are qualitatively similar and only the numerical values differ. However, the fluid is often confined by horizontal impervious solid walls at which the fluid molecules adhere [76]. This is described by no-slip boundary conditions, and the given critical wavenumber for the no-slip case is, therefore, closer to real situations. It gives a very good approximation of the size of convection rolls observed in experiments [83, 84] and simulations [22, 30] at onset which is close to $\pi/k_c \approx 1$, i.e. equal to the height of the system.

Let me finally note, that the instability in RBC is of type I-s, for which $\Re(\sigma_k)$ passes through zero at $k_c > 0$ and is locally parabolic around the maximum.

2.3.2 Type of patterns

In RBC a plethora of interesting patterns emerge, depending on the cell geometry, the control parameters, the boundary conditions, the initial conditions, and also on variations of fluid parameters in the system (i.e. non-Oberbeck-Boussinesq effects) [30, 58, 61]. Already close to onset many interesting different patterns are observed. One of the most prominent patterns are ideal straight convection rolls as predicted by linear stability analysis. Interestingly, they appear in cylindrical as well as rectangular setups [49] with only little difference due to the circular confinement. They typically have a wavenumber close to the critical one $k_c \approx 3.117$ [58], and their stability has been investigated theoretically and experimentally in great detail by Busse and co-workers [85, 86]. These efforts resulted in the prominent *Busse balloon*, which describes the stability of straight rolls in the $Ra - k - Pr$ space. As the Rayleigh number is increased further away from onset, experimental, numerical, and naturally observed patterns become increasingly disordered and time-dependent. They exhibit spatio-temporal chaos and are irregular in the horizontal plane [58]. However, their vertical structure is comparably

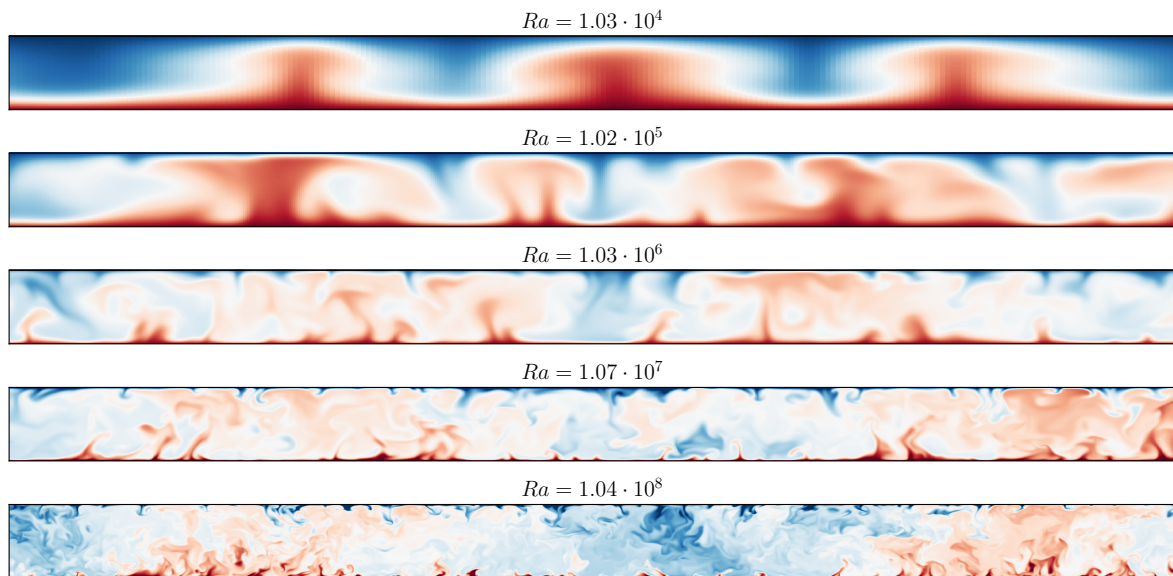


Figure 2.5: Part of the domain of a vertical cut through a snapshot of the temperature field for different Ra and $Pr = 1$, see chapter 3 for details on the numerical simulations. Note that the color ranges are chosen differently to highlight the respective structure.

simple, which contrasts them from fully developed turbulence. In figure 2.5 the height dependence of the temperature field is shown from numerical simulations for $Pr = 1$, see chapter 3 for details. It can be seen that for the lowest Rayleigh number, the temperature field is rather homogeneous in the vertical direction before the boundaries are reached. In contrast, with increasing Rayleigh number, the vertical structure becomes increasingly complicated. However, not only the vertical structure becomes more complex, but the horizontal patterns vary too. In figure 2.6 the temperature field in the midplane is shown for $Pr = 1$. For small Ra , a regular large-scale flow pattern is visible. In contrast, with increasing Rayleigh number, more and more smaller-scale fluctuations emerge. Notably, a large-scale flow pattern superposed by smaller-scale fluctuations is still present for large Ra [22, 27, 30, 31, 35, 61–63]. These patterns, named turbulent superstructures, will be at the centre of this thesis and are described in more detail in section 2.5.

RBC can be loosely separated into different regimes [53, 56, 85, 87], which depend on the Rayleigh and Prandtl number. A sketch of the different regimes is shown in figure 2.7, cf. Getling [53], Busse [85], and Verma [56] for a more detailed description. In general, at small Pr the transition to a time-dependent flow is already observed at smaller Ra close to the critical Rayleigh number. At higher Pr steady rolls are still present for larger Ra as well [53, 85]. I refer the reader to Hartlep et al. [61] for an overview of emerging patterns in numerical simulations of RBC for a wide range of Ra, Pr from parameters close to onset up to the turbulent regime.

Spiral defect chaos A particularly interesting time-dependent pattern is called spiral defect chaos (SDC) [49], see figure 2.8b. Here, spirals and stripes coexist and evolve in a complex way. The spirals move around the system, sometimes annihilate with other spirals and sometimes trigger the emergence of new spirals and defects, i.e. local imperfections [49]. But there is also

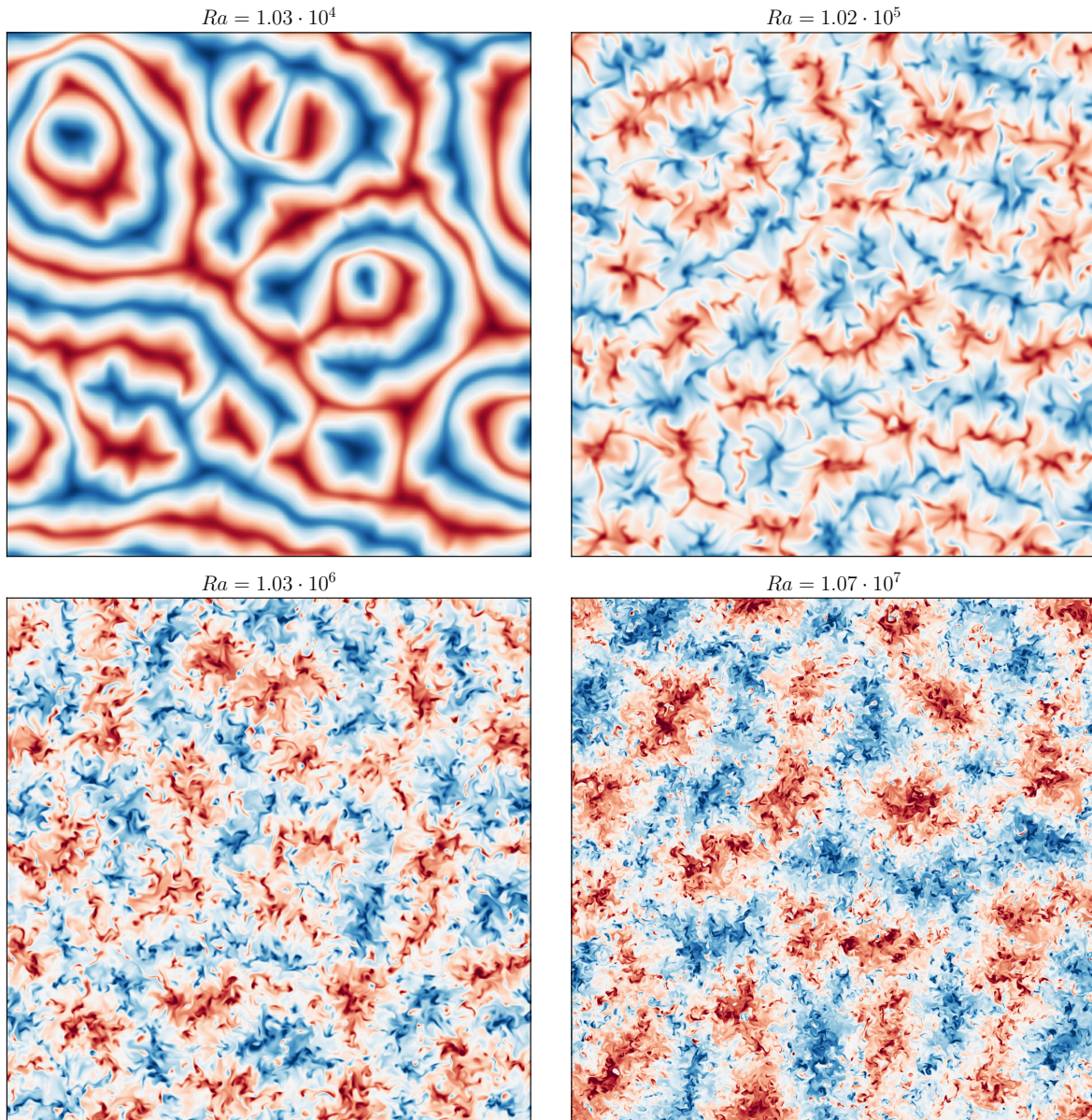


Figure 2.6: Snapshot of the temperature field in the midplane for different Ra and $Pr = 1$ (see chapter 3 for details on the numerical simulations). Note that the color ranges are chosen differently to highlight the large-scale flow.

evidence that spirals can be considered to a reasonable degree as being independent of each other [58]. This results from the fact that the number of spirals roughly follows a Poisson distribution [58]. SDC is present for small Pr in large-enough aspect ratio systems in experiments with rectangular as well as circular cells and in numerical solutions of the OBEs [53, 58]. It is generally believed that SDC is an intrinsic state of RBC for fluids with $Pr \approx 1$. Notably, this state is found experimentally and numerically in the same parameter regime as the stripe state [49, 88], see figure 2.8. This means that there are two dynamical attractors and which one is selected is determined by the initial conditions [49, 88]. Typically, ideal straight rolls

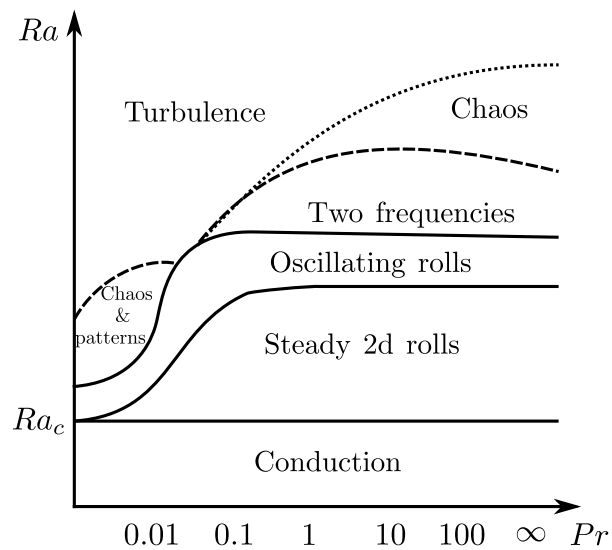


Figure 2.7: Qualitative sketch of the different convective regimes as a function of Ra , Pr . Reproduced following Verma [56], cf. Busse [85], Krishnamurti and Howard [87], and Getling [53].

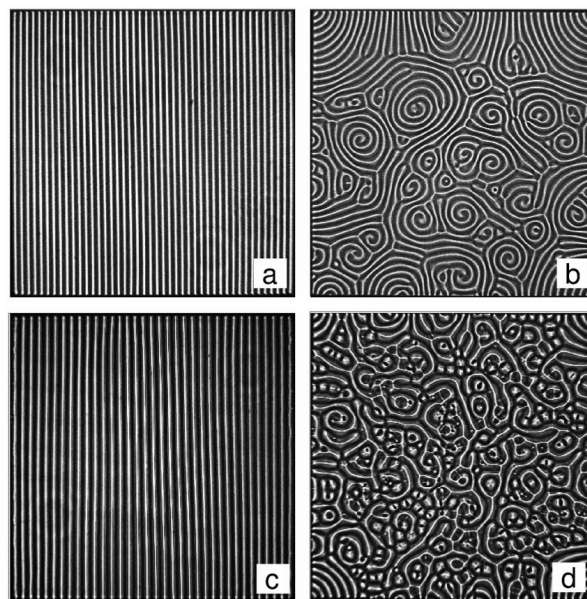


Figure 2.8: Shadowgraph visualization of patterns found in RBC experiments in rectangular cells close to onset of convection for different temperature differences from [88]. Dark regions show warm upflow and bright region cold downflow. For similar parameters, ideal straight rolls (a,c) and spiral defect chaos is found (b,d) depending on the initial conditions. The parameter $\epsilon = \Delta/\Delta_c - 1$ characterizes the deviation from onset at the critical temperature difference Δ_c . (a,b) $\epsilon = 0.92$, (c) $\epsilon = 2.99$, (d) $\epsilon = 3.0$. Reprinted figure 1 a-d with permission from [Reha V. Cakmur et al., Phys. Rev. Lett., 79, 1853 (1997).] Copyright (2020) by the American Physical Society.

need specifically designed initial conditions, e.g. with a preferred direction, while SDC emerges from random initial conditions [58, 89]. In addition, the onset value of SDC Ra_s decreases with increasing aspect ratio [58]. There is evidence that a so-called mean flow plays an important role for the occurrence of SDC [58, 90]. Here, mean flow refers to a horizontal velocity field with a nonzero mean, if averaged over the depth of the cell, see e.g. [50, 91–95]. This remark will become important in the next section on reduced models. A detailed description of spiral defect chaos can be found in Getling [53], Bodenschatz et al. [58], and references therein. I also refer the reader to these references for a more detailed review of pattern formation in RBC.

2.4 Reduced model equations

The theoretical treatment of the OBEs becomes increasingly complicated as one considers parameters away from the onset of convection and goes beyond linear stability analysis. Therefore, early on researchers focused on reduced models of the OBEs to advance the theoretical analysis. The seminal work by Swift and Hohenberg [66], resulting in the nowadays called Swift-Hohenberg (SH) equation [49], is the foundation for many models that are still widely used today, see e.g. [48–50, 53, 58] for reviews and textbooks. A modified version of this model is also the foundation for the theoretical and numerical analysis in chapter 4.

Swift-Hohenberg equation The SH equation can be justified based on projection techniques which eventually eliminates the dependence on the vertical coordinate in the OBEs. In Swift and Hohenberg [66], this was done in Fourier-space, but real-space techniques can also be used [82], cf. Bodenschatz et al. [58]. The Swift-Hohenberg equation is given in non-dimensional form by [49]

$$\partial_t \theta(x, y) = \left[r - (\nabla^2 + 1)^2 \right] \theta(x, y) - \theta(x, y)^3, \quad (2.18)$$

in which θ is a two-dimensional field and can be considered as a superposition of temperature and vertical velocity, and r is a control parameter describing the deviation from onset. Effectively, the field θ describes the temperature or vertical velocity in RBC in the midplane [53]. This equation is considerably simpler than the original OBEs, though still captures relevant features of RBC close to onset. For example, the SH equation has the same type of instability as RBC [49]. A particular example is that the SH equation reproduces the stripes of RBC for small r , see figure 2.9a. At larger r , disordered patterns can be observed. A disordered, though almost time-independent, pattern is shown in figure 2.9b.

Potential dynamics The SH equation (2.18) exclusively results in stationary patterns due to a special property. In the given form the SH equation has a potential dynamics [49]. Here, a potential which is a functional of the field θ exists. This potential is also called *Lyapunov functional* and given by

$$V[\theta] = \iint dx dy \left(-\frac{1}{2} r \theta^2 + \frac{1}{4} \theta^4 + \frac{1}{2} [(\nabla^2 + 1) \theta]^2 \right).$$

The temporal change of this potential results from the evolution equation (2.18), and for, e.g., periodic boundary conditions it holds

$$\frac{dV}{dt} = - \iint dx dy (\partial_t \theta)^2,$$

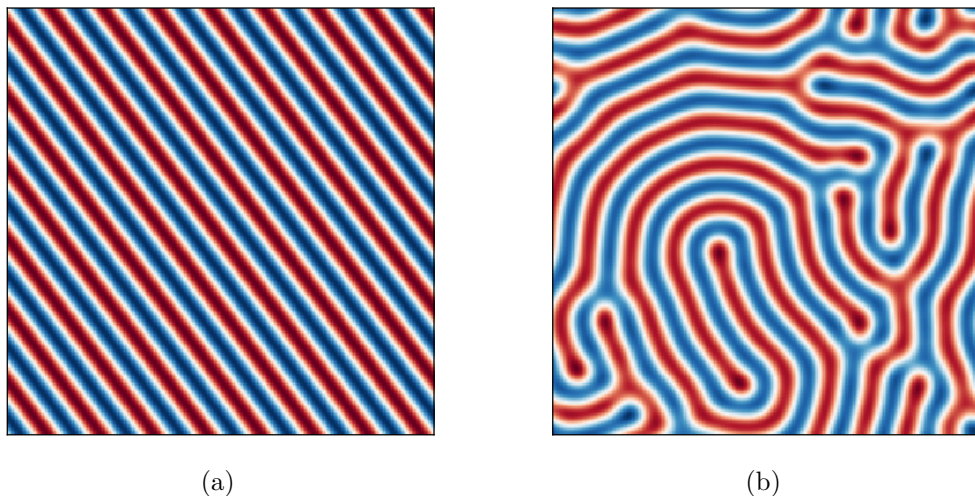


Figure 2.9: Examples for different patterns (scaled to unit maximum amplitude) in the SH model from a numerical solution of (2.18) with $N = 256^2$ grid points in a domain of size $20\pi \times 20\pi$, time stepping $\Delta t = 0.1$, and (a) $r = 0.01$, and (b) $r = 0.9$, see section 4.3.1.2 for details on the numerical method. Random initial conditions have been used.

see Cross and Greenside [49] for details on the derivation. In addition, it can be shown that the potential is bounded from below [49]. This potential, therefore, decreases monotonically in time until it reaches a local minimum. Furthermore, the evolution equation of θ is directly linked to the potential by a functional derivative [49]

$$\partial_t \theta = -\frac{\delta V}{\delta \theta}. \quad (2.19)$$

Starting from an arbitrary state, the field can, accordingly, only change such that a local minimum of the potential is reached. There, the potential is extremal with respect to θ and the variation vanishes. Hence, the pattern becomes time-independent according to (2.19). This explains why only stationary patterns are obtained for the SH model. Let me refer the reader to Greenside and Coughran [96] for a detailed study of the SH equation and to Hoyle [48], Cross and Greenside [49].

As we have learned before, the dynamics of RBC can become time-dependent already close to onset. This is, therefore, not represented by (2.18). However, there are several modifications to the model to include time-dependent states, see e.g. Cross and Greenside [49] for an overview. First, nonpotential dynamics is necessary to observe a time-dependent state but not sufficient. Time-independent states are also found in nonpotential models [49]. A specific model proposed by Greenside and Cross [97] that includes time-dependence is presented in section 2.4.4.

In the next step, I will review the linear stability analysis for the SH equation, which is relevant for section 4.1, and compare it to RBC. This comparison shows how the reduction of the OBEs simplifies the analysis.

2.4.1 Linear stability analysis of the SH equation

The SH model (2.18) has a simple uniform time-independent solution $\theta_b = 0$. This solution corresponds to the conduction state in a RBC setup. In contrast to RBC, the SH model only

consists of extended coordinates. The confined coordinate, i.e. the vertical direction in RBC, is removed here. The control parameter r corresponds to a reduced Rayleigh number and we are interested in the value of r at which the base state becomes unstable to small perturbations. The following presentation is adapted from Cross and Greenside [49].

Linearisation To perform the linear stability analysis, we linearise (2.18) around θ_b . For this, we introduce the fluctuations around the base state

$$\theta_p = \theta - \theta_b.$$

Thus, the evolution of θ_p is given by

$$\begin{aligned}\partial_t \theta_p &= \hat{N}[\theta_p + \theta_b] - \hat{N}[\theta_b] \\ \hat{N}[q] &= \left[r - (\nabla^2 + 1)^2 \right] q(x, y) - q(x, y)^3.\end{aligned}$$

We assume that the perturbations θ_p are small and, accordingly, only keep terms that are linear in θ_p

$$\partial_t \theta_p = \left[r - (\nabla^2 + 1)^2 \right] \theta_p - \theta_b^2 \theta_p.$$

Inserting the base state $\theta_b = 0$ explicitly, we obtain

$$\partial_t \theta_p = \left[r - (\nabla^2 + 1)^2 \right] \theta_p,$$

which is a linear partial differential equation with constant coefficients. For a vanishing base state, this result could have been obtained immediately by only keeping the linear terms of (2.18).

Solving the PDE A particular solution to the linearised equation is

$$\theta_p = e^{\sigma_k t} e^{i\mathbf{k}\cdot\mathbf{x}}$$

and inserting this into the above equation gives

$$\sigma_k = r - (1 - k^2)^2 \tag{2.20}$$

with $k = |\mathbf{k}|$. This equation describes whether a small-amplitude, spatially periodic perturbation with wavenumber k grows in time. In this example the growth rate is real. Accordingly, there are no oscillating perturbations. If $\sigma_k < 0$ the perturbation decays exponentially and the system returns to the base state. If $\sigma_k > 0$ the perturbation grows.

Analysing the growth rate In the following, we determine the properties of the growth rate (2.20). Depending on r and k , σ_k can be positive or negative valued. Let us first determine at which parameters r_c and k_c the growth rate first becomes positive. Similar to the approach in RBC, we calculate the neutral stability curve

$$0 = r - (1 - k^2)^2 \tag{2.21}$$

$$r = (1 - k^2)^2 \tag{2.22}$$

and determine the minimum to find r_c and k_c . The extrema are found as

$$\begin{aligned}\partial_k r = 0 &= -4k(1 - k^2) \\ \Rightarrow k &= 0 \vee k = 1.\end{aligned}$$

Here, $k = 0$ corresponds to a maximum and, therefore, the critical wavenumber is $k_c = 1$. From this we find

$$r_c = 0. \quad (2.23)$$

This means that the base state is stable for $r < 0$, unstable for $r > 0$, and that σ_k first takes a positive value at $k_c = 1$. The maximum of the growth rate σ_k is always at $k_c = 1$,

$$\partial_k \sigma_k(r, k_c) = 0,$$

independent of r . Thus, the maximum-growth wavenumber is identical to the critical one. This is in contrast to RBC in which the maximum-growth wavenumber changes with the Rayleigh number, see figure 2.4a. We can learn more about the growth rate if we plot σ_k for different r , see figure 2.10a. Here, we see that the growth rate is negative for all k for $r < 0$. Furthermore, this confirms that there is a maximum at $k = k_c$ independent of r . For $r > 0$ there is a small band of wavenumbers

$$\sqrt{1 - \sqrt{r}} < k < \sqrt{1 + \sqrt{r}}$$

around the maximum for which the growth rate is positive. Therefore, in principle, perturbations with a wavenumber from that range grow exponentially. The neutral stability curve (2.22) is shown in figure 2.10b. Perturbations to the base state with (r, k) above the curve are unstable and the ones below are stable. The curve, hence, shows the range of perturbations with wavenumber k that are unstable. The minimum is given by the critical parameters calculated above, r_c and k_c .

From the previous considerations we can see that the SH model has the same type of instability (I-s) as RBC. The growth rates have a comparable form, see figure 2.4a and 2.10a and are locally parabolic around the critical wavenumber. However, the analysis is considerably less involved and the resulting growth rate has a simpler functional form.

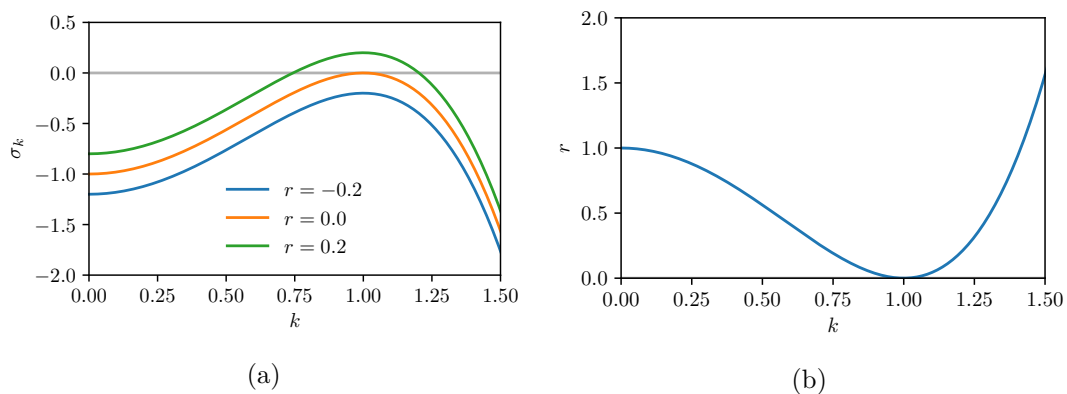


Figure 2.10: (a) Growth rate σ_k for model (2.18) for different control parameters r . (b) Neutral stability curve $\sigma_k = 0$.

2.4.2 Nonlinear stripe state

Previously, we have considered only a linear stability analysis close to onset for RBC and the SH model. This only predicts an exponential growth of perturbations of the base state with certain wavenumbers. Though, a physically relevant solution cannot grow indefinitely. In addition, we have already seen that solutions of the SH equation finally become stationary due to its potential dynamics. The saturation, accordingly, has to set in due to the nonlinearity. In the following, we present a nonlinear solution which becomes important in chapter 4. A straightforward generalization of the linear approach close to onset is

$$\theta(\mathbf{x}, t) = A(t)e^{i\mathbf{k}_c \cdot \mathbf{x}} + c.c., \quad (2.24)$$

which preserves the periodicity of the perturbation and only relaxes the constraint for the time-dependence. This makes use of the fact that close to onset, only perturbations with the critical mode k_c are unstable. Inserting this into (2.18) results in

$$\dot{A}e^{i\mathbf{k}_c \cdot \mathbf{x}} - rAe^{i\mathbf{k}_c \cdot \mathbf{x}} + 3|A|^2Ae^{i\mathbf{k}_c \cdot \mathbf{x}} + A^3e^{3i\mathbf{k}_c \cdot \mathbf{x}} + c.c. = 0.$$

In the next step, we use that the Fourier modes are linearly independent and, therefore, the coefficient of each mode must vanish

$$\dot{A} - rA + 3A^3 = 0 \quad (2.25)$$

$$A^3 = 0, \quad (2.26)$$

where we assumed that $A \in \mathbb{R}$ for simplicity. For a stationary state, we obtain from the first equation, in addition to the base state $A_b = 0$,

$$A = \pm \sqrt{\frac{r}{3}} \quad (2.27)$$

$$\sqrt{\overline{\theta^2}} = \sqrt{\frac{2}{3}}r = \sqrt{2}|A|, \quad (2.28)$$

in which the overbar denotes a spatial average. This seems to fix the final amplitude of a nonlinear stripe state close to onset for small r . However, from the second equation we obtain

$$A = 0,$$

which is obviously a contradiction. The nonlinear term generates a higher harmonic with wavenumber $3\mathbf{k}_c$ and there is no additional term balancing this mode. Hence, (2.24) is incomplete. It can be shown [49] that all odd modes must be included into the Ansatz

$$\theta(x) = \sum_{n \text{ odd}} a_n \cos(nx)$$

with $\mathbf{k}_c = (1, 0)^\top$ to resolve the inconsistency for all modes. However, it holds

$$a_n \propto r^{n/2},$$

and, therefore, for small enough r

$$\theta(x) \approx \pm \sqrt{\frac{4}{3}}r \cos(x) + O(r^{3/2}) \cos(3x)$$

is a reasonable approximation. This shows analytically that a stationary nonlinear stripe solution exists for the SH equation close enough to onset with a critical wavenumber k_c . The nonlinear stripe state consists of a dominant term with the same spatial variation as the linear mode supplemented with higher harmonic spatial corrections with a significantly smaller amplitude close enough to onset. Far away from onset, the nonlinear solutions can only be calculated numerically.

Validation of the nonlinear stripe state How accurate is the description of θ in terms of an amplitude close to onset? From (2.25) we expect that $A(t)$ initially follows an exponential growth $\propto \exp rt$, which is saturated by the nonlinearity at $\sqrt{r/3}$. This can be compared to the numerical solution of the full eq. (2.18), if started from $\theta_0 = 2A_0 \cos(x)$ with $\mathbf{k}_c = (1, 0)^\top$. A comparison of the theoretical expectation and the numerical solutions of (2.18) and (2.25) is shown in figure 2.11 for $r = 0.1$. Here, for the simulations of the SH equation the amplitude $A(t)$ is calculated from (2.28). This confirms that close to onset eq. (2.25) gives an accurate representation of the evolution of the amplitude of θ and that the critical wavenumber is the dominant contribution.

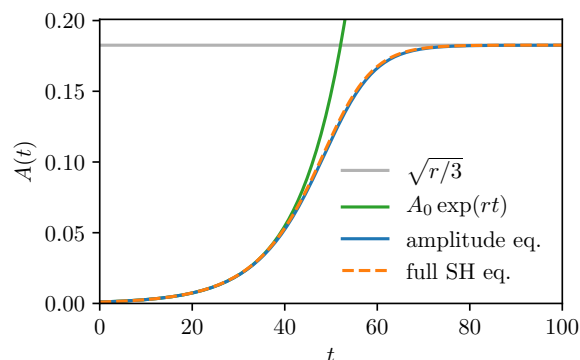


Figure 2.11: Comparison of the amplitude $A(t)$ obtained from eq. (2.25) with the full SH eq. (2.18) for $r = 0.1$, $A_0 = 10^{-3}$. In the latter case $A(t)$ is obtained from (2.28) The green solid line shows the initial expected exponential growth, the blue line depicts the numerical solution of (2.25), the dashed orange line the one of (2.18) and the gray line the expected amplitude in the stationary state.

Bifurcation analysis Let me mention that this amplitude equation describes a so-called supercritical pitchfork bifurcation [48, 49]. The equation has three fixed points

$$A = 0, \pm \sqrt{\frac{r}{3}}.$$

The first fixed point is stable for $r < 0$ and unstable for $r > 0$. The latter two only exist for $r > 0$ and are stable in this regime. This is sketched in figure 2.12. For the full OBEs a similar amplitude equation (2.25) can be derived [56, 98]

$$\dot{A} = rA - A^3 \tag{2.29}$$

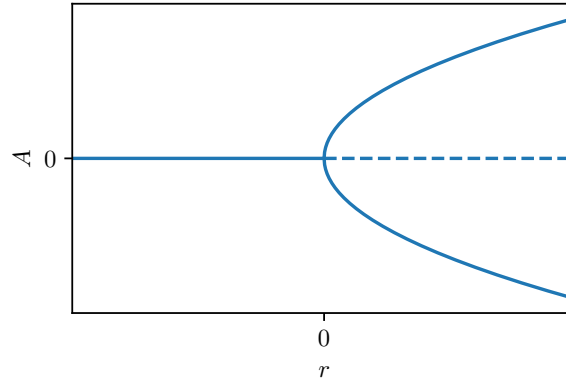


Figure 2.12: Bifurcation diagram for (2.25). Solid lines denote stable fixed points and dashed lines unstable ones.

in rescaled units with $r = \frac{Ra - Ra_c}{Ra_c}$. Hence, the transition from the conduction state to the convective state in RBC can be described as a supercritical pitchfork bifurcation and the exponential growth is saturated by the nonlinearity. For an introduction to bifurcation theory, I refer to Hoyle [48], Strogatz [99].

2.4.3 Envelope equations

The presented linear stability analysis for RBC and the SH model is valid very close to onset. Additionally, for the nonlinear stripe state shown in section 2.4.2 only the critical mode was considered and the solution still obeys the same periodicity as the linear solution. However, directly above onset a small range of wavenumbers becomes unstable and may initially grow. Which modes survive or decay is eventually determined by nonlinear effects. These wavenumbers modulate the envelope of the carrier wave $\exp(i\mathbf{k}_c \cdot \mathbf{x})$ slowly in space and time [48]. This opens the possibility to apply a multiple-scales expansion which results in a partial differential equation for the amplitude alone in terms of slowly varying variables [48]. Such equations offer a simplified description of the flow in weakly nonlinear situations and are called envelope or amplitude equations. Equation (2.25) is a basic version of such an equation, in which the amplitude is not spatially varying. The form of the envelope equation is strongly linked to the type of instability and linear solution, i.e. stripes for RBC and the SH model.

The general procedure to derive envelope equations is as follows. First, a small parameter $\epsilon \ll 1$ is introduced for which different choices are possible. Close to the bifurcation point, this parameter can, e.g., be $(Ra - Ra_c)/Ra_c$ in RBC [53] or r in the SH model [49]. Slow variables can then be introduced as scaled versions of the original coordinates, $X = \epsilon^{s_x} x$; $Y = \epsilon^{s_y} y$; $T = \epsilon^{s_t} t$, in which the positive exponents are initially either left as unknowns or fixed by phenomenological arguments [48, 49]. Here, the capital coordinates (T, X, Y) denote the slow variables and $(\tilde{x}, \tilde{y}, \tilde{t}) = (x, y, t)$ the fast ones. A change in the former coordinates corresponds to a large variation in the physical coordinates (x, y, t) . Subsequently, the relevant field (e.g. the vertical velocity in RBC)

$$\mathbf{q}_p(\tilde{x}, \tilde{y}, \tilde{t}; X, Y, T) = \epsilon^{s_1} \mathbf{q}_0 + \epsilon^{s_2} \mathbf{q}_1 + \dots$$

as well as the derivatives

$$\begin{aligned}\partial_x &= \partial_{\bar{x}} + \epsilon^{sx} \partial_X \\ \partial_y &= \partial_{\bar{y}} + \epsilon^{sy} \partial_Y \\ \partial_t &= \partial_{\bar{t}} + \epsilon^{st} \partial_T\end{aligned}$$

are expanded. Inserting this into the evolution equation and collecting terms of the same order in ϵ yields the amplitude equation from a solvability condition [100], see, e.g., Hoyle [48] and Cross and Greenside [49] for details. For the SH equation and the OBEs, a similar amplitude equation can be derived [96, 101, 102]. This equation is called Newell-Whitehead-Segel equation [48, 53, 58] and given here for completeness in a rescaled version as

$$\partial_T A(X, Y, T) = \mu A - |A|^2 A + \left(\partial_X - \frac{i}{2} \partial_Y^2 \right)^2 A,$$

in which μ is a rescaled control parameter. This amplitude equation can be used to study the stability of rolls and stripes, resulting in so-called stability balloons [49]. In RBC the stability of ideal rolls is characterized by the famous *Busse balloon*, see e.g. Getling [53], Busse [85, 103], and Bodenschatz et al. [58]. Going into more detail would go beyond the scope of this work and I refer the reader to Cross and Greenside [49], Bodenschatz et al. [58], Manneville [76], and Hoyle [48].

2.4.4 Spiral defect chaos

Up to here, I have shown that the SH equation has some basic similarities with the OBEs. It has the same type of instability and ideal stripes are observed close to onset. However, because the SH model has a potential dynamics, time-dependent states cannot be observed. In order to overcome this drawback, the SH equation has to be modified such that it becomes nonpotential [49]. Yet, this is only a sufficient condition and does not necessarily result in time-dependent states or even spatiotemporal chaos. A prominent modification of the SH model includes a mean flow [49, 53, 58, 82, 97], which is motivated from the fact that such a flow is believed to play an important role for SDC in RBC. In this case, a horizontal velocity field is induced by the curvature of the field, which in turn couples back to the field itself in form of an advection term. Though, a little modification at the first sight, it complicates the theoretical analysis dramatically. This equation not only results in time-dependent states, but SDC is found as well [104, 105]. A particularly simple form of the equation is [49, 50, 53]

$$\partial_t \theta(x, y) + \mathbf{U} \cdot \nabla \theta = \left[r - (\nabla^2 + 1)^2 \right] \theta(x, y) - \theta(x, y)^3 \quad (2.30a)$$

$$\mathbf{U} = \nabla \times (\zeta \hat{\mathbf{z}}) \quad (2.30b)$$

$$\nabla_h^2 \zeta = g \hat{\mathbf{z}} \cdot \left[\nabla \left(\nabla_h^2 \theta \right) \times \nabla \theta \right]. \quad (2.30c)$$

Here, ζ is the stream function and $-\nabla_h^2 \zeta = \omega_z$ gives the vertical vorticity. Note that the right-hand side of (2.30c) is the simplest form which is consistent with the symmetries of the SH equation, i.e. rotational invariance and inversion symmetry ($\theta \rightarrow -\theta$) [49]. In Greenside et al. [106] it was shown that a similar model allows for chaotic flows. Two specific fields resulting from numerical simulations are shown in figure 2.13 at different times. Here, differently sized spirals and disordered regions are observed. The comparison of both times shows that the

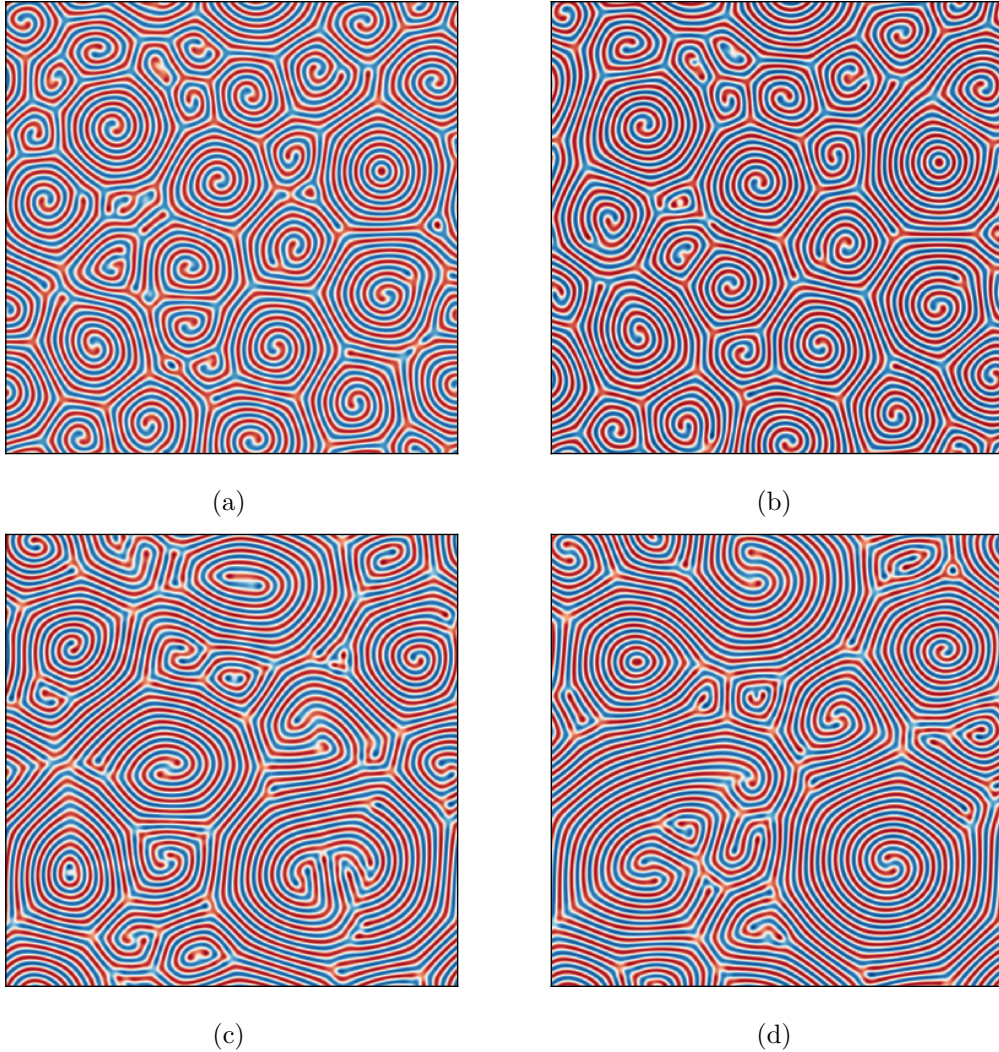


Figure 2.13: Resulting θ from a numerical solution of (2.30) in a domain of size $80\pi \times 80\pi$ with $N = 1024^2$, $\Delta t = 0.1$ for two different times. (a,c) $t = 2500$; (b,d) $t = 5000$; (a,b) $r = 0.9$, $g = 10$; (c,d) $r = 0.5$, $g = 10$

spirals slowly migrate through the system. In summary, modified versions of the SH model are capable of reproducing more complex patterns similar to those observed in RBC. However, the similarities are not exact and it was found that SDC in SH models for typically used parameters only occurs as a (long) transient state [107].

2.4.5 Wavelength selection

A problem I have not discussed so far is how the final wavenumber of a pattern is chosen above onset. Close enough to onset, the base state is almost solely unstable to perturbations with the critical wavenumber, which in turn gives the characteristic scale of patterns at onset. As we already know, above onset the base state becomes unstable to perturbations from a range of wavenumbers. In contrast, experiments and numerical simulations show that the resulting

patterns still only have a narrow distribution around a dominant wavenumber [49]. How this wavenumber emerges is an extremely difficult question to answer and depends on a plethora of factors, see e.g. Cross and Greenside [49], Getling [53]. Currently, there is no universal selection mechanism known [49].

Starting from random initial conditions the fastest growing mode will dominate at the beginning, however as the amplitude increases the nonlinear terms become increasingly important and a different dominant wavenumber may be found [49]. In the SH model, the critical wavenumber is equal to the maximum-growth wavenumber. It is known that in this model patterns with a narrow wavenumber distribution centred around the critical wavenumber are observed [96]. There are possibly several reasons for this observation, e.g. because k_c is the fastest growing mode or because it minimizes the Lyapunov functional [96]. Notably, the width of the observed wavenumber band in simulations is significantly smaller than the width of the stability band predicted theoretically [96]. In contrast, in RBC, the characteristic length scale deviates from the maximum-growth wavenumber already closely after onset, cf. [58, 83]. A detailed discussion is given in Cross and Greenside [49], Cross and Hohenberg [50] and Getling [53].

The problem of predicting the emerging characteristic pattern length scale is not even settled in the weakly nonlinear regime of RBC. Additionally, the problem is more difficult if the control parameter is increased further such that turbulence emerges. In the next section, we turn to turbulent RBC and consider large aspect ratio systems and the emerging flow states and characteristic wavelengths.

2.5 Turbulent superstructures

As described in the previous sections, in RBC pattern formation is observed in large-aspect-ratio cells. These patterns become increasingly unsteady and chaotic and the flow becomes finally turbulent as the Rayleigh number is increased. Chaotic states, e.g. SDC, are typically observed in the horizontal directions but have a simple vertical structure, which is not true in the turbulent regime. Surprisingly, a horizontally extended large-scale flow pattern can still be observed in turbulent RBC, however, now superposed by small-scale fluctuations (see figure 2.14). Such a horizontally extended coherent large-scale flow is named turbulent superstructure. These large-scale patterns have first been reported in the midplane of RBC in the seminal work by Hartlep et al. [22] in a large-aspect-ratio system and have been studied extensively since then [27, 30–33, 35, 61–64]. These studies on turbulent superstructures have been primarily computational [27, 30, 31, 33, 35, 61–64]. Only little work has been devoted to theoretical approaches [108–110] or experimental studies [32, 84].

Turbulent superstructures and SDC Interestingly, it was found that the large-scale patterns in the turbulent regime are reminiscent of patterns close to onset of convection [22, 30, 61, 111], namely SDC [27]. The large-scale flow persists for very long times and can, therefore, be revealed by time-averaging the temperature and vertical velocity fields in the midplane. This removes the fast fluctuations and extracts the slowly evolving large-scale pattern [27, 30]. In Emran and Schumacher [27], turbulent Rayleigh and Prandtl numbers are inferred from a Boussinesq closure to characterize the large-scale flow state. In such a closure, the turbulent stresses and fluxes are linearly related to the mean gradients with the so-called turbulent viscosity and diffusivity as proportionality constant. Effectively, the fluid motion induced by

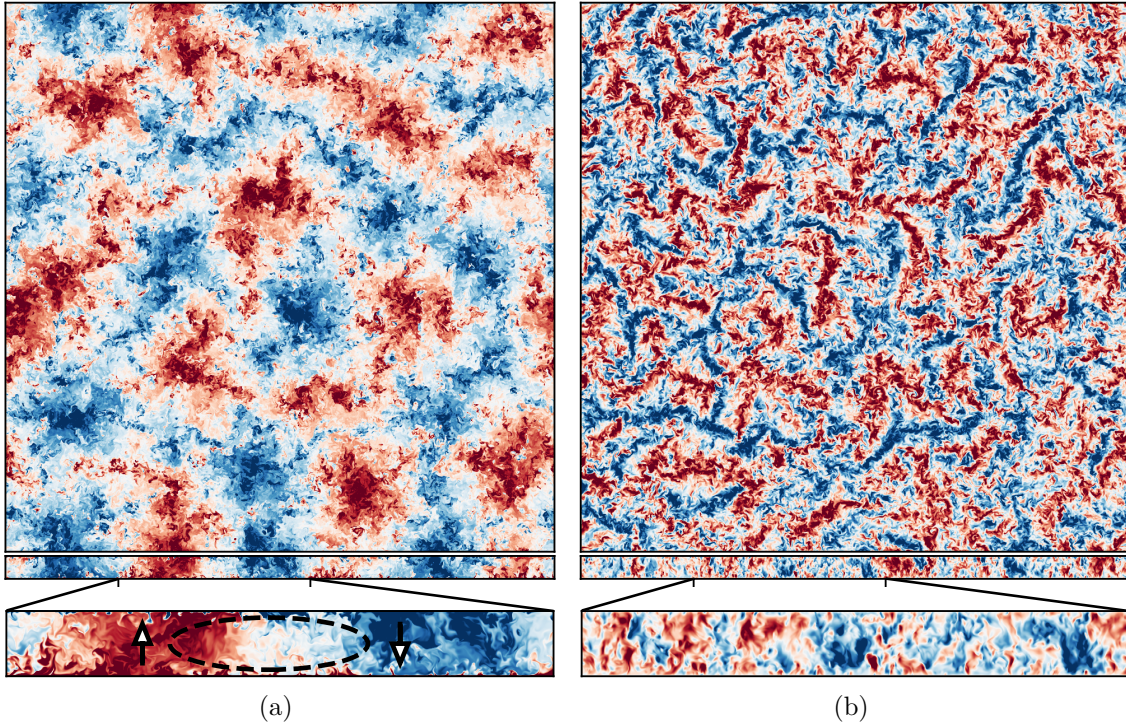


Figure 2.14: Snapshot of the (a) temperature and (b) vertical velocity field in the midplane and from a front view from DNS for $Ra = 1.04 \times 10^8$. Clustered small-scale plumes form effective large-scale convection rolls consisting of large-scale warm updraughts and cold downdraughts extending from top to bottom as indicated by the black dashed ellipse and arrows. See chapter 2 for details on the DNS.

the turbulence is described by increasing the viscous and thermal diffusion. These diffusivities are used to calculate new turbulent Rayleigh and Prandtl numbers. The resulting reduced parameters indeed fall in the SDC range and are, hence, consistent with the observations. Additionally, the averaged pattern in simulations with the reduced parameters compare visually well with the original patterns. However, the formation mechanisms of the large-scale flow could not be described theoretically in detail since then. The patterns close to onset are understood in detail with the help of linear stability analysis and order parameter equations (e.g. amplitude equations) [48, 49, 53, 56, 58, 76], which is why a mapping of the turbulent superstructure to effective parameters, which fall back to this regime, seems promising to make theoretical progress.

Characteristics of superstructures Observational studies give insights into the formation of the superstructures. With increasing driving, smaller-scale structures, called (thermal) plumes, emerge. The horizontal width of these plumes is comparable to the boundary layer thickness [62]. In large-aspect-ratio systems these plumes cluster into effective large-scale up- and downdraughts forming the turbulent superstructures [30, 62, 64, 112] (see figure 2.14). Consistent with this picture, turbulent superstructures exist in both the temperature field and the vertical velocity field [35]. This observation also reveals that there is a close connection between the large-scale pattern in the midplane and the boundary layer dynamic [30, 31, 35, 62].

Specifically, the ridges of the hot and cold plumes close to the plates are at the same position as the maxima and minima of the temperature in the midplane [30, 31]. This observation has recently been supported by Krug et al. [35], who showed that turbulent superstructures extend through the whole cell and do not vary significantly with height. This can already be confirmed visually, see figure 2.14. There, clustered plumes forming effective large-scale up- and downdraughts extending from top to bottom are visible in the temperature field.

Characteristic length scale A particular interest in the studies on superstructures has been the characteristic size of the pattern and how it changes with the control parameters, i.e. the Rayleigh and Prandtl number as well as the aspect ratio. The consistent finding is that the scale increases with Rayleigh number, see e.g. [22, 30, 35, 64, 84], as shown in figure 2.15. The characteristic scale of the superstructures is, therefore, larger than the scale of the regular patterns at onset and much larger than the characteristic dimension of the system, the height. In contrast, there is no simple trend for varying Prandtl number [22, 30]. Notably, it was found that large-aspect-ratio systems are needed to see a geometry independent size [31, 35, 63]. At small aspect ratios the largest possible size in the system is selected [62]. Different measures have been used to define the size of the turbulent superstructures. The early study of Hartlep et al. [22] used the cross-spectrum $E_{\theta u_z}(k, z)$ of the vertical velocity and temperature and, later, also the spectra of the temperature and vertical velocity fields individually are considered [30, 31]. The different measures may result in different length scales of the turbulent superstructures. However, it was shown by Krug et al. [35] that turbulent superstructures of the same size exist in both the temperature and vertical velocity fields. They suggest to extract the corresponding size from the linear coherence spectrum of θ and

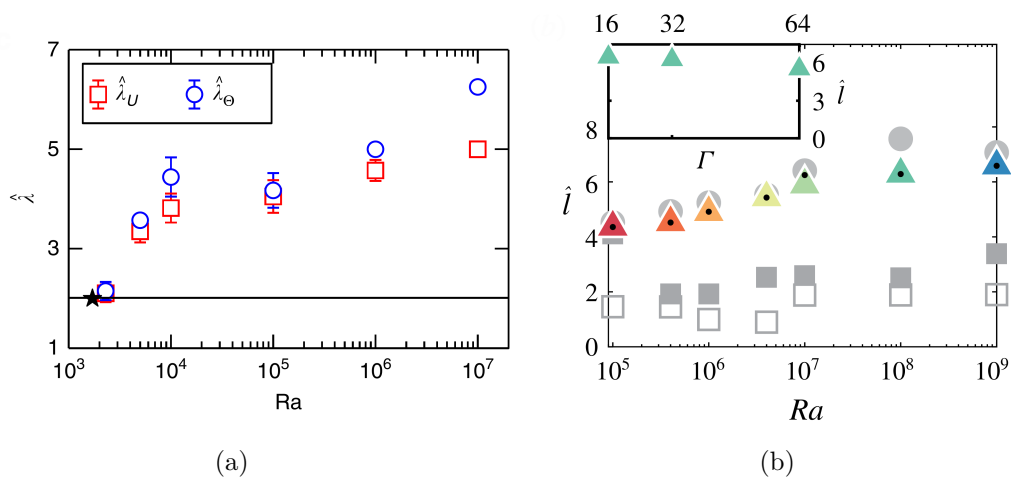


Figure 2.15: Wavelength of the turbulent superstructures as a function of Rayleigh number from (a) Pandey et al. [30] and (b) Krug et al. [35]. In (a) the size $\hat{\lambda}_\theta$ is extracted from the temperature spectrum and $\hat{\lambda}_U$ from the vertical velocity spectrum and in (b) from the linear coherence spectrum of θ and u_z (triangles). (b) The circles show the wavelength obtained from the temperature spectrum and the filled squares from the vertical velocity spectrum. The open squares are obtained from the pre-multiplied vertical velocity spectrum and the dots from the pre-multiplied cross-spectrum of the vertical velocity and temperature. Reprinted with permission.

u_z , which for $Pr = 1$ almost perfectly coincides with the size obtained from the cross-spectrum. Both characterize the correlation between temperature and vertical velocity at a certain scale, though the former is normalized to remove the influence of the magnitudes [35]. Currently, there is no theory that can predict the observed wavelengths.

Another important observation is that the turbulent fluctuations and superstructures are separated in spectral space [22, 35]. This scale separation results in a bimodal temperature spectrum and the separation increases with increasing driving [22, 35]. This results from the fact that increasingly smaller scales emerge with increasing driving while simultaneously the characteristic size of the large-scale flow grows.

Summary To summarize, turbulent superstructures exist on length scales much larger than the height of the fluid layer and are composed of clustered plumes, which themselves only have a horizontal extent comparable to the thickness of the boundary layers. This leads to the question how the large and small scales interact. This is naturally related to inter-scale energy transfers and is the main focus of the first part of this thesis, see chapter 3. Second, it is not understood why the length scale of turbulent superstructures increases with increasing driving. I will address this problem in the second part, see chapter 4. Explicitly, we consider if we can qualitatively understand the effect of the presence of small-scale fluctuations on a generic large-scale pattern in a modified SH equation. Finally, it was observed that turbulent superstructures are reminiscent of SDC, a phenomenon present in the weakly nonlinear regime. In addition, turbulent superstructures do not vary significantly with height. Is it, therefore, possible to model turbulent superstructures based on two-dimensional reduced models similar to the ones presented in section 2.4, which are capable of producing SDC? In chapter 5, I present an *a priori* study on how such a model can be systematically obtained from currently available DNS.

Part I

—
Manuscript I

Resolved energy budget of superstructures in Rayleigh-Bénard convection

J. Fluid Mech. (2020), vol. 887, A21. © The Author(s), 2020.

887 A21-1

Published by Cambridge University Press

This is an Open Access article, distributed under the terms of the Creative Commons Attribution licence (<http://creativecommons.org/licenses/by/4.0/>), which permits unrestricted re-use, distribution, and reproduction in any medium, provided the original work is properly cited.
doi:10.1017/jfm.2019.1008

Resolved energy budget of superstructures in Rayleigh–Bénard convection

Gerrit Green^{1,2}, Dimitar G. Vlaykov^{1,3}, Juan Pedro Mellado^{4,‡}
and Michael Wilczek^{1,2,†}

¹Max Planck Institute for Dynamics and Self-Organization (MPI DS), Am Faßberg 17,
37077 Göttingen, Germany

²Faculty of Physics, University of Göttingen, Friedrich-Hund-Platz 1, 37077 Göttingen, Germany

³Astrophysics Group, College of Engineering, Mathematics and Physical Sciences, University of Exeter,
Exeter EX4 4QL, UK

⁴Max Planck Institute for Meteorology, Bundesstraße 53, 20146 Hamburg, Germany

(Received 24 May 2019; revised 17 October 2019; accepted 28 November 2019)

Figure 3.1: Title header of [67].

By now we have learned about RBC in general, turbulent superstructures, and some open questions regarding the latter. Here, we address the problem of the interaction of smaller-scale

fluctuations and superstructures. We are particularly interested in the energetic interaction and study them by means of DNS. In this part I reproduce the paper [67]: "G. Green, D. G. Vlaykov, J. P. Mellado, and M. Wilczek, [Resolved energy budget of superstructures in Rayleigh-Bénard convection](#). *J. Fluid Mech.*, 887:A21, 2020. doi: 10.1017/jfm.2019.1008"(see figure 3.1). This article is published under the Creative Commons Attribution licence (<http://creativecommons.org/licenses/by/4.0/>).

Author contributions MW designed the study. JPM provided the simulation code. GG wrote the post processing routines, performed the simulations, analysed the data and performed the analytical calculations. DV supported the simulations, analyses and interpretation. All authors discussed and interpreted the results and wrote the manuscript. The code used for the simulations presented in this manuscript is freely available at <https://github.com/turbulencia/tlab> and all numerical methods are documented there in detail. Further information can be found in [113, 114].

Abstract

Turbulent superstructures, i.e. large-scale flow structures in turbulent flows, play a crucial role in many geo- and astrophysical settings. In turbulent Rayleigh-Bénard convection, for example, horizontally extended coherent large-scale convection rolls emerge. Currently, a detailed understanding of the interplay of small-scale turbulent fluctuations and large-scale coherent structures is missing. Here, we investigate the resolved kinetic energy and temperature variance budgets by applying a filtering approach to direct numerical simulations of Rayleigh-Bénard convection at high aspect ratio. In particular, we focus on the energy transfer rate between large-scale flow structures and small-scale fluctuations. We show that the small scales primarily act as a dissipation for the superstructures. However, we find that the height-dependent energy transfer rate has a complex structure with distinct bulk and boundary layer features. Additionally, we observe that the heat transfer between scales mainly occurs close to the thermal boundary layer. Our results clarify the interplay of superstructures and turbulent fluctuations and may help to guide the development of an effective description of large-scale flow features in terms of reduced-order models.

3.1 Introduction

Many turbulent flows in nature, for example in the atmosphere or in the interior of stars and planets, are driven by thermal gradients, which lead to convection. A characteristic feature of these flows is the coexistence of large-scale order and smaller-scale fluctuations. Prominent examples are cloud streets in the atmosphere [1] or solar granulation [2]. Currently, little is known about the interplay of small-scale fluctuations and large-scale order, but a detailed understanding is important for the development of reduced-order models, e.g. in climate science, as well as in geo- and astrophysical settings. Better understanding the coexistence of this large-scale order and turbulence in convective flows is one motivation for the current work.

Rayleigh-Bénard convection (RBC), a confined flow between a heated bottom plate and a cooled top plate, is an idealized system to study convection and has been successfully employed to understand various phenomena such as pattern formation, spatio-temporal chaos [53, 58] and turbulence [54, 60]. Rayleigh-Bénard convection is governed by three non-dimensional parameters, the Rayleigh number Ra , characterizing the strength of the thermal driving, the Prandtl number Pr , which is the ratio between kinematic viscosity and thermal diffusivity, and

the aspect ratio Γ of the system's width to its height. Above the onset of convection, at which the heat transfer changes from conduction to convection, a rich dynamics can be observed (see, e.g. Bodenschatz et al. [58]). Close to onset, the flow organizes into regular convection rolls. As the Rayleigh number is increased, the flow becomes increasingly complex. At moderate Rayleigh numbers in high aspect ratio RBC, the dynamics of the convection rolls becomes chaotic, exhibiting spiral defect chaos (SDC) (see, e.g. Morris et al. [115] for an early study, or Bodenschatz et al. [58] and references therein for an overview). At much higher Rayleigh numbers, the flow becomes turbulent and features prominent smaller-scale flow structures such as thermal plumes [57, 60, 116, 117].

As visualized in figure 3.2, even in the turbulent regime, horizontally extended large-scale convection rolls, so-called turbulent superstructures, have been observed in direct numerical simulations of large aspect ratio systems [22, 27, 30, 31, 62–64, 118]. Their large-scale structure and dynamics can be revealed, for example, by time averaging [27, 30], and they are composed of clustered plumes [62]. The presence of the large-scale flow has important consequences for the temperature statistics in RBC, see Stevens et al. [31], Lülff et al. [119, 120] as well as the heat transport [31, 111]. Turbulent superstructures vary on time scales much larger than the characteristic free-fall time [30], and their length scale increases with Ra [22, 30, 61, 64, 118], which is visualized in figure 3.2. Additionally, they appear to have a close connection to the boundary layer dynamics [30, 31], e.g. the local maxima and minima of the temperature in the midplane coincide with the position of hot and cold plume ridges in the boundary layer.

For moderate Rayleigh numbers, the superstructure dynamics is reminiscent of SDC in the weakly nonlinear regime [27]. This points to the possibility of establishing connections to flows at much lower Rayleigh number, which are theoretically tractable by methods such as linear stability analysis and order parameter equations [58, 76]. This is of considerable interest because, so far, only a few attempts exist to theoretically understand these turbulent large-scale patterns. Elperin et al. [108, 109, 110] found large-scale instabilities based on a mean field theory combined with a turbulence closure. Ibbeken et al. [68] studied the effect of small-scale fluctuations on large-scale patterns in a generalized Swift-Hohenberg model and showed that the fluctuations lead to an increased wavelength of the large-scale patterns. Still, the precise mechanism of the formation of the large-scale pattern and the selection of their length scale is not fully understood in turbulent RBC, and the emergence of large-scale rolls in the turbulent regime leaves many open questions. In particular, the interplay between superstructures and small-scale turbulence is currently largely unexplored. Thus, the main aim of this article is to clarify the impact of small-scale fluctuations and to characterize the energy budget of the large-scale convection rolls. With a focus on superstructures, this complements previous studies on the scale-resolved energy and temperature variance budgets of convective flows: Togni et al. [121] focused on the impact of thermal plumes and the scale dependence at different heights, Kimmel and Domaradzki [122] and Togni et al. [123, 124] aimed at improving large eddy simulations, Valori et al. [125] focused on small scales and Faranda et al. [126] studied atmospheric flows.

Here, we investigate RBC by means of direct numerical simulations (DNS) in large aspect ratio systems from the weakly nonlinear regime close to onset up to the turbulent regime covering a Rayleigh number range from $Ra = 10^4$ to $Ra = 10^8$ at $Pr = 1$. To separate the scales, we apply a filtering approach [127] and isolate the superstructure dynamics. We then determine the energy and temperature variance budgets of the superstructures and the corresponding transfer rates between large-scale flow structures and small-scale fluctuations.

The remainder of the article is structured as follows. We first present the relevant theoretical

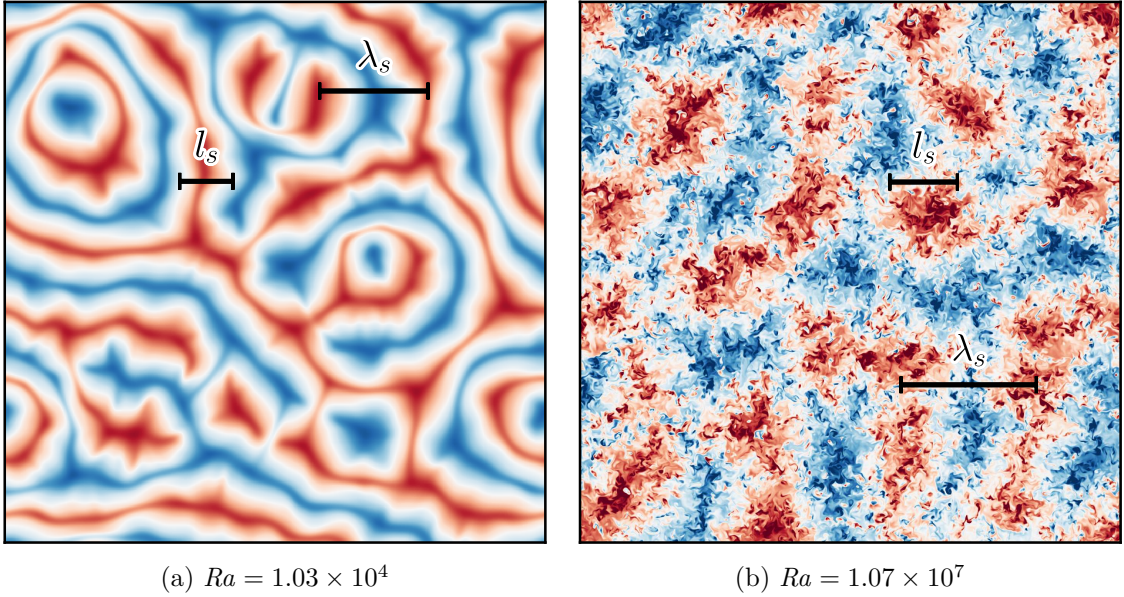


Figure 3.2: Temperature fields in the midplane for two different Rayleigh numbers with $Pr = 1$ and aspect ratio 24. Red indicates hot rising fluid, and blue cold descending fluid. (a) Close to onset in the weakly nonlinear regime, regular patterns with wavelength λ_s emerge. (b) Connected large-scale structures are present in the turbulent regime as well, and their length scale λ_s is increased compared to onset. The small-scale fluctuations can be removed with a filter of width l_s , which preserves the large-scale rolls. For similar visualizations of turbulent superstructures, see also Stevens et al. [31], Hartlep et al. [61] and Pandey et al. [30].

and numerical background in section 3.2. In section 3.3, the results are presented. Here, we find that at the scale of the superstructures the time- and volume-averaged resolved energy input into the large scales is primarily balanced by the energy transfer rate to small scales instead of the direct dissipation. To understand the role of the boundary layers, we supplement the volume-averaged analysis with a study of the height profiles of the different contributions to the resolved energy budget obtained from horizontal and time averages. We find that these profiles exhibit a complex near-wall structure and interpret the form of the profiles in terms of the plume dynamics. We complement the analysis of the resolved energy budget with that of the resolved temperature variance budget. This reveals that the averaged heat transfer rate is exceeded by the averaged direct thermal dissipation for all Rayleigh numbers, a qualitatively different behaviour than that of the energy transfer rate. Also, a substantial part of the heat transfer rate is limited to the boundary layers. Finally, we conclude in section 3.4.

3.2 Theoretical and numerical background

To begin with, we introduce the underlying equations and methods. We present the filtering approach as well as the resolved energy and temperature variance budgets used to study the transfer rates between scales. We then describe the numerical data used for our analysis.

3.2.1 Governing equations

RBC is governed by the Oberbeck-Boussinesq equations (OBEs), which describe the evolution of the velocity \mathbf{u} and the temperature fluctuation θ , i.e. the deviation from the mean temperature. In this set-up, it is assumed that the density varies linearly with temperature with only small variations, such that the fluid can still be considered as incompressible [54]. Explicitly, the non-dimensionalized, three-dimensional equations are

$$\nabla \cdot \mathbf{u} = 0 \quad (3.1a)$$

$$\partial_t \mathbf{u} + \mathbf{u} \cdot \nabla \mathbf{u} = -\nabla p^* + \sqrt{\frac{Pr}{Ra}} \nabla^2 \mathbf{u} + \theta \hat{\mathbf{z}} \quad (3.1b)$$

$$\partial_t \theta + \mathbf{u} \cdot \nabla \theta = \frac{1}{\sqrt{RaPr}} \nabla^2 \theta, \quad (3.1c)$$

in which p^* is the kinematic pressure including gravity, which points in the negative z -direction. Here, $\hat{\mathbf{z}}$ is the unit vector in the vertical direction. The equations are non-dimensionalized with the temperature difference between top and bottom Δ , the free-fall time $t_f = \sqrt{H/(\alpha g \Delta)}$ and the velocity $u_f = H/t_f$, where H is the height of the system. The system is subject to two control parameters, the Prandtl number $Pr = \nu/\kappa$, which is the ratio of kinematic viscosity to thermal diffusivity and the Rayleigh number $Ra = g\alpha\Delta H^3/(\nu\kappa)$, the ratio between the strength of the thermal driving and damping by dissipation. Here, g is the acceleration due to gravity and α the thermal expansion coefficient. These equations are supplemented with Dirichlet boundary conditions for the temperature as well as no-slip boundary conditions for the velocity at the top and bottom wall, and periodic boundary conditions at the side walls. Strong thermal driving leads to a turbulent convective flow at sufficiently high Ra far above the onset of convection.

In a statistically stationary state, exact relations between forcing and dissipation can be derived from the kinetic energy and temperature variance budgets [128],

$$\langle \varepsilon \rangle = \langle u_z \theta \rangle = \frac{1}{\sqrt{RaPr}} (Nu - 1), \quad \text{where} \quad \varepsilon = \frac{1}{2} \sqrt{\frac{Pr}{Ra}} (\nabla \mathbf{u} + (\nabla \mathbf{u})^\top)^2, \quad (3.2)$$

$$\text{and } \langle \chi \rangle = \frac{1}{\sqrt{RaPr}} Nu, \quad \text{where} \quad \chi = \frac{1}{\sqrt{RaPr}} (\nabla \theta)^2, \quad (3.3)$$

i.e. the averaged energy input $\langle u_z \theta \rangle$ is balanced by the averaged dissipation $\langle \varepsilon \rangle$, and the dimensionless heat transport $Nu = \sqrt{RaPr} \langle u_z \theta \rangle + 1$ is balanced by the thermal dissipation $\langle \chi \rangle$. Here, $\langle \cdot \rangle$ denotes an average over time and volume, which we simply refer to as volume averaged and $^\top$ stands for transpose. For more details, see also Chillà and Schumacher [54], Siggia [57] and Ching [55]. These statements for the averaged relation between forcing and dissipation are generalized to scale-dependent budgets in the following section.

3.2.2 Filtering

In order to separate small-scale fluctuations and large-scale structures, we use low-pass filtering. In this study, we only filter horizontally to extract the horizontally extended superstructures. Compared to three-dimensional filtering, this approach avoids complications in the interpretation of results introduced by the inhomogeneity in the vertical direction, especially near the boundaries [129]. Note also that, besides a few exceptions, e.g. Fodor et al. [33], this approach

is widely used in the study of wall-bounded flows, see, e.g. Bauer et al. [43], Togni et al. [123, 124], Cimarelli and De Angelis [130] and Valori et al. [125]. The filtering operator is a locally weighted average given by a convolution with a filter kernel G_l ,

$$\bar{\mathbf{u}}_l(\mathbf{x}) = G_l * \mathbf{u} = \frac{1}{l^2} \int_{x-l/2}^{x+l/2} \int_{y-l/2}^{y+l/2} \mathbf{u}(x', y', z) dx' dy'. \quad (3.4)$$

For our study, we choose a standard two-dimensional box filter. The large-scale velocity $\bar{\mathbf{u}}_l$ encodes the velocity on scales larger than the scale l in the horizontal directions. The large-scale temperature $\bar{\theta}_l$ is defined analogously. In the following, we refer to scales below the filter width as unresolved and scales above it as resolved or large scale. The evolution of the resolved scales is given by filtering (3.1)

$$\nabla \cdot \bar{\mathbf{u}}_l = 0 \quad (3.5a)$$

$$\partial_t \bar{\mathbf{u}}_l + \bar{\mathbf{u}}_l \cdot \nabla \bar{\mathbf{u}}_l = -\nabla \bar{p}_l^* + \sqrt{\frac{Pr}{Ra}} \nabla^2 \bar{\mathbf{u}}_l + \bar{\theta}_l \hat{z} - \nabla \cdot \boldsymbol{\tau}_l \quad (3.5b)$$

$$\partial_t \bar{\theta}_l + \bar{\mathbf{u}}_l \cdot \nabla \bar{\theta}_l = \frac{1}{\sqrt{RaPr}} \nabla^2 \bar{\theta}_l - \nabla \cdot \boldsymbol{\gamma}_l, \quad (3.5c)$$

in which

$$\boldsymbol{\tau}_l = \overline{(\mathbf{u}\mathbf{u})}_l - \bar{\mathbf{u}}_l \bar{\mathbf{u}}_l \quad (3.6)$$

$$\text{and } \boldsymbol{\gamma}_l = \overline{(\mathbf{u}\theta)}_l - \bar{\mathbf{u}}_l \bar{\theta}_l. \quad (3.7)$$

Here additional terms involving $\boldsymbol{\tau}_l$ and $\boldsymbol{\gamma}_l$ appear due to the nonlinearity of the OBEs. The turbulent stress tensor $\boldsymbol{\tau}_l$ and turbulent heat flux $\boldsymbol{\gamma}_l$ effectively describe the impact of the unresolved scales on the resolved ones.

A few words on the limiting cases $l \rightarrow 0$ and $l \rightarrow \infty$ are in order. For any field q

$$\lim_{l \rightarrow 0} G_l * q = q, \quad (3.8)$$

see, e.g. Sagaut [129]. On the other hand, for $l \rightarrow \infty$ the filtering is essentially a horizontal average, which we shall denote by $\langle \cdot \rangle_A$, i.e.

$$\lim_{l \rightarrow \infty} G_l * q = \langle q \rangle_A. \quad (3.9)$$

This means that the filtering procedure applied in this work smoothly interpolates between the fully resolved and the height-dependent, horizontally averaged fields. Using the above definitions, we derive the resolved energy budget in the next section. In particular, we focus on the resolved budgets at the scale of the turbulent superstructures.

3.2.3 Resolved energy budget

To derive the resolved energy budget, (3.5b) is multiplied with $\bar{\mathbf{u}}_l$, cf. Sagaut [129], Eyink [131, 132], Eyink and Aluie [133], Aluie and Eyink [134] and Togni et al. [124]. We obtain

$$\partial_t e_l + \nabla \cdot \mathbf{J}_l = -\varepsilon_l + Q_l - \Pi_l, \quad (3.10)$$

and the individual terms are explicitly given by

$$\varepsilon_l = \frac{1}{2} \sqrt{\frac{Pr}{Ra}} (\nabla \bar{\mathbf{u}}_l + (\nabla \bar{\mathbf{u}}_l)^\top)^2, \quad (3.11)$$

$$Q_l = \bar{\theta}_l \bar{\mathbf{u}}_l \cdot \hat{\mathbf{z}}, \quad (3.12)$$

$$\Pi_l = -(\nabla \bar{\mathbf{u}}_l) : \boldsymbol{\tau}_l, \quad (3.13)$$

$$\text{and } \mathbf{J}_l = (e_l + \bar{p}_l^*) \bar{\mathbf{u}}_l - \sqrt{\frac{Pr}{Ra}} \nabla e_l + \boldsymbol{\tau}_l \cdot \bar{\mathbf{u}}_l - \sqrt{\frac{Pr}{Ra}} \bar{\mathbf{u}}_l \cdot \nabla \bar{\mathbf{u}}_l. \quad (3.14)$$

Here, $e_l = \bar{\mathbf{u}}_l^2/2$ is the resolved kinetic energy, ε_l denotes the direct large-scale dissipation and Q_l is the energy input rate into the resolved scales by thermal driving. Compared to the unfiltered energy budget, an additional contribution Π_l appears. It originates from the nonlinear term in the momentum equation and captures the transfer rate of kinetic energy between scales. It can act, depending on its sign, as a sink or source for the resolved scales. In the following, we refer to Π_l as the energy transfer. The evolution equation also contains a large-scale spatial flux term \mathbf{J}_l , which redistributes energy in space. As we focus on the energy transfer between scales in this study, we refrain from characterizing the individual contributions to the spatial flux. For a detailed study of the corresponding unfiltered spatial flux terms, we refer to Petschel et al. [135].

In a nutshell, (3.10) describes the change of the resolved energy e_l by spatial redistribution, direct dissipation, large-scale thermal driving and energy transfer between scales. Complementary to spectral analysis techniques (see, e.g. Lohse and Xia [60], Verma et al. [77], Domaradzki et al. [136] and Verma [56]), this approach allows the spatially resolved study of the energy transfer between superstructures and small-scale fluctuations. In the following, spatial and temporal averages of the resolved energy balance are considered.

3.2.3.1 Averaged resolved energy budget

To derive a scale-resolved generalization of (3.2), we average (3.10) over space and time. In a statistically stationary state, $\langle \partial_t e_l \rangle$ vanishes. The averaged flux $\langle \nabla \cdot \mathbf{J}_l \rangle$ vanishes as well because of the no-slip boundary conditions for the velocity. The resulting balance

$$\langle Q_l \rangle = \langle \varepsilon_l \rangle + \langle \Pi_l \rangle \quad (3.15)$$

shows that, at each scale, the energy input is balanced by the direct dissipation and the energy transfer between scales. Note that the latter is not present in the unfiltered energy balance (3.2). As presented in Appendix 3.A, (3.15) can also be related to the Nusselt number.

Because the energy dissipation primarily occurs at the smallest scales in three-dimensional turbulence [47], the introduced energy has to be transferred to the dissipative scales for a statistically stationary state to exist. Since RBC is forced on all scales by buoyancy, including the largest scales, the volume-averaged energy transfer above the dissipative range is *a priori* expected to be down-scale. Accordingly, the volume-averaged energy transfer has to act as a sink in the resolved energy budget.

To understand the scale dependence of the different contributions, we first determine the two limits $l \rightarrow 0$ and $l \rightarrow \infty$, for which we make use of (3.8) and (3.9). For $l \rightarrow 0$, Π_l vanishes and

$$\lim_{l \rightarrow 0} \langle Q_l \rangle - \langle \varepsilon_l \rangle - \langle \Pi_l \rangle = \langle Q \rangle - \langle \varepsilon \rangle = 0, \quad (3.16)$$

i.e. the unfiltered balance is recovered with $Q = u_z \theta$. In the limit $l \rightarrow \infty$, the filtering is equivalent to a horizontal average. In an infinitely extended domain, $\langle \mathbf{u} \rangle_A = 0$, and therefore, all terms in the budget vanish individually

$$\lim_{l \rightarrow \infty} \langle Q_l \rangle = \lim_{l \rightarrow \infty} \langle \varepsilon_l \rangle = \lim_{l \rightarrow \infty} \langle \Pi_l \rangle = 0. \quad (3.17)$$

The detailed scale dependence and the balance between the different terms at the length scale corresponding to superstructures are investigated numerically and presented in subsequent sections.

To complete this section, we present the horizontally and time-averaged resolved kinetic energy budget

$$\langle \nabla \cdot \mathbf{J} \rangle_A = - \langle \varepsilon_l \rangle_A - \langle \Pi_l \rangle_A + \langle Q_l \rangle_A, \quad (3.18)$$

in which $\langle \cdot \rangle_A$ from now on describes a horizontal and time average. This will be used to determine the role of the boundary layers and to refine the picture based on the volume average. Compared to the volume-averaged resolved energy budget, the spatial flux term $\langle \nabla \cdot \mathbf{J} \rangle_A$ does not vanish. The limiting behaviour is very similar to that of the volume-averaged balance. As $l \rightarrow 0$, the energy transfer vanishes, whereas the other terms recover the unfiltered balance

$$\langle \nabla \cdot \mathbf{J} \rangle_A = - \langle \varepsilon \rangle_A + \langle Q \rangle_A, \quad (3.19)$$

$$\text{where } \mathbf{J} = (e + p^*) \mathbf{u} - \sqrt{\frac{Pr}{Ra}} \nabla e - \sqrt{\frac{Pr}{Ra}} \mathbf{u} \cdot \nabla \mathbf{u}. \quad (3.20)$$

As $l \rightarrow \infty$, all terms vanish individually for the same reason as above.

In the work of Petschel et al. [135], the unfiltered budget (3.19) has been studied. It was shown that most of the energy is typically dissipated near the wall and energy input occurs in the bulk, from where it is transported to the wall. The generalization to a resolved energy budget allows us to investigate these processes as a function of scale, and in particular at the scale of the turbulent superstructures.

3.2.4 Resolved temperature variance budget

To complete the theoretical background, we consider the budget of the resolved temperature variance $e_l^\theta = \bar{\theta}_l^2 / 2$:

$$\partial_t e_l^\theta + \nabla \cdot \mathbf{J}_l^\theta = -\chi_l - \Pi_l^\theta, \quad (3.21)$$

where the individual terms are given by

$$\chi_l = \frac{1}{\sqrt{RaPr}} \left(\nabla \bar{\theta}_l \right)^2, \quad (3.22)$$

$$\mathbf{J}_l^\theta = \bar{\mathbf{u}}_l e_l^\theta - \frac{1}{\sqrt{RaPr}} \nabla e_l^\theta + \gamma_l \bar{\theta}_l, \quad (3.23)$$

$$\text{and } \Pi_l^\theta = -\gamma_l \cdot \nabla \bar{\theta}_l. \quad (3.24)$$

Equation (3.22) describes the direct thermal dissipation of the resolved scales, (3.23) the spatial redistribution of temperature variance and (3.24) the transfer rate between resolved and unresolved scales. We will refer to the latter as the heat transfer in the following.

3.2.4.1 Averaged resolved temperature variance budget

As before, we consider the time- and volume-averaged budget

$$\langle \chi_l \rangle + \langle \Pi_l^\theta \rangle = \frac{1}{\sqrt{RaPr}} Nu = \langle \chi \rangle, \quad (3.25)$$

see Appendix 3.B for the derivation. This budget shows that the total heat transport is balanced by the direct thermal dissipation and the heat transfer between scales. Because $\langle \chi_l \rangle \leq \langle \chi \rangle$, the averaged heat transfer between scales is down-scale, i.e. $\langle \Pi_l^\theta \rangle > 0$. This is consistent with classical theories, in which a direct temperature variance cascade is proposed [60]. The horizontally averaged budget is given by

$$\langle \nabla \cdot \mathbf{J}_l^\theta \rangle_A = -\langle \chi_l \rangle_A - \langle \Pi_l^\theta \rangle_A, \quad (3.26)$$

which shows that the spatial redistribution of the resolved temperature variance is balanced by the direct thermal dissipation and the heat transfer between scales.

3.2.5 Numerical simulations

The OBEs (3.1) are solved numerically, using a compact sixth-order finite-difference scheme in space and a fourth-order Runge-Kutta scheme for time stepping [137]. The grid is non-uniform in the vertical direction for $Ra \geq 5 \times 10^4$, with monotonically decreasing grid spacing towards the wall. The pressure equation is solved with a factorization of the Fourier-transformed Poisson equation to satisfy the solenoidal constraint [113]. The filter used in

Input		Output						Time scales		
Ra	$N_x N_y N_z$	Nu	Nu_ε	Nu_χ	Re	λ_s	l_s	T_t	τ	t_s
1.03×10^4	$448^2 \times 64$	2.26	2.26	2.26	17.8	4.8	2.4	1954	1303	91
5.01×10^4	$768^2 \times 96$	3.55	3.55	3.55	47.3	4.8	2.4	1092	728	76
1.02×10^5	$1280^2 \times 140$	4.36	4.37	4.36	69.2	4.8	2.4	701	467	74
1.03×10^6	$2560^2 \times 208$	8.37	8.38	8.37	222.6	4.8	2.4	752	451	73
1.07×10^7	$3200^2 \times 256$	16.04	16.06	16.04	685.9	6.0	3.0	1151	765	90
1.04×10^8	$7200^2 \times 416$	30.95	30.99	30.94	2004.2	6.0	3.0	362	196	96

Table 3.1: Input and reference output parameters of the simulations with $Pr = 1$. The number of grid points in the vertical direction is N_z and in the horizontal directions N_x and N_y . Nu , Nu_χ and Nu_ε are Nusselt numbers calculated based on the thermal driving, thermal and viscous dissipation, respectively. Here, the Reynolds number $Re = \sqrt{\langle \mathbf{u}^2 \rangle} Ra / Pr$ is based on the root-mean-square velocity. Additionally, λ_s characterizes the wavelength of the turbulent superstructures, which is determined from the cross-spectrum of u_z and θ , and l_s represents the filter width to separate the superstructures from turbulent fluctuations. Lastly, T_t is the total runtime, τ the time window over which the averages are taken after the initial transient, and t_s the characteristic time scale of the evolution of the superstructures. We adopt the definition of t_s from Pandey et al. [30] but base it on λ_s .

our analysis is implemented using a trapezoidal rule. The code is also freely available at <https://github.com/turbulencia/tlab>.

We study the Rayleigh number regime from $Ra \approx 10^4$ up to $Ra \approx 10^8$ in a large aspect ratio domain with $\Gamma \approx 24$ for $Pr = 1$. The full simulation details are provided in table 3.1. The Nusselt numbers shown are calculated based on the thermal driving $Nu = \sqrt{RaPr} \langle u_z \theta \rangle + 1$, the viscous dissipation $Nu_\varepsilon = \sqrt{RaPr} \langle \varepsilon \rangle + 1$ and the thermal dissipation $Nu_\chi = \sqrt{RaPr} \langle \chi \rangle$. Their mutual consistency serves as a resolution check of the simulations [138]. For our simulations, the different Nusselt numbers agree to 99% or better. Furthermore, the resolution requirements have been estimated *a priori* as proposed in Shishkina et al. [139], and the relevant scale, i.e. the Kolmogorov scale η for $Pr = 1$, has been compared to the grid resolution *a posteriori*. In all cases we find that the maximum grid step h is smaller than the Kolmogorov scale η , and that the vertical grid spacing Δz is smaller than the height-dependent Kolmogorov scale based on $\langle \varepsilon \rangle_A$ at the corresponding height. Together with the consistency of the Nusselt number, this shows that our simulations are sufficiently resolved. Further resolution studies can be found in Mellado [114]. As a test for stationarity, we computed all terms in (3.15) and (3.25) individually. We find from our simulations that the left-hand sides agree with the right-hand sides to 99% for all considered filter widths.

3.3 Results

In the following, we present numerical results to examine the scale dependence of the resolved energy budget as well as the resolved temperature variance budget. We focus on the scale of the superstructures, for which we first have to characterize their scale.

3.3.1 Determining the superstructure scale

In order to extract the length scale of the superstructures, we compute azimuthally and time-averaged spectra in horizontal planes (cf. Hartlep et al. [22], Pandey et al. [30] and Stevens et al. [31]). Specifically, we choose the azimuthally averaged cross-spectrum $E_{\theta u_z}(k)$ of the vertical velocity and the temperature in the midplane for the definition of the superstructure scale [22]. Here, $E_{\theta u_z}(k)$ is normalized in such a way that it integrates to $\langle Q \rangle_A (z = 0.5)$. A representative example is shown in figure 3.3. The peak of the spectrum characterizes the wavelength of the superstructures $\lambda_s = 2\pi/k_{\lambda_s}$. The corresponding length scale λ_s is listed in table 3.1 for all simulations. The wavelength increases compared to the theoretical expectation for onset $\lambda_0 = 2.016$ [53] and is largest for the highest Rayleigh numbers. The observed length scales are comparable with the ones obtained in previous studies of superstructures [22, 30, 31, 33, 63]. Since a superstructure consists of a pair of a warm updraft and a cold downdraft, we choose the filter width $l_s \approx \lambda_s/2$ to investigate the energy and temperature variance budgets at the scale of the superstructure. The values are given in table 3.1. We tested that small variations do not affect the outcome significantly. With this choice the individual large-scale up- and downdrafts are retained and the small-scale fluctuations are removed. We can then use (3.10) and (3.21) to characterize the energetics of the large-scale convection rolls and the associated superstructures and filter out the smaller-scale fluctuations.

Previous studies indicated that the length scales for the temperature and velocity field differ at high Rayleigh numbers [30, 31] when they are determined from the peak in the corresponding spectrum. However, recently Krug et al. [118] studied linear coherence spectra of the vertical velocity and temperature field to argue that superstructures of the same size exist in both

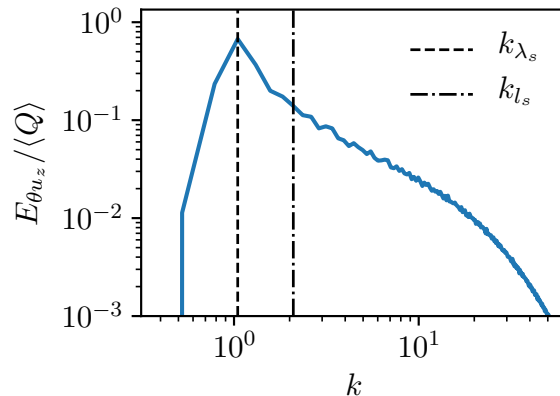


Figure 3.3: Cross spectrum of the temperature and the vertical velocity in the midplane for $Ra = 1.07 \times 10^7$. The maximum wavenumber, which characterizes the large-scale rolls, is highlighted by the dashed line. The filter width (dash-dotted line) to separate superstructures and small-scale fluctuations is given by $k_{l_s} \approx 2k_{\lambda_s}$. This choice removes the small-scale fluctuations and preserves the large-scale hot updrafts and cold downdrafts, which form the superstructures. The corresponding wavelengths are indicated in the snapshot of the temperature field in the midplane in figure 3.2b.

fields for $Pr = 1$ also at high Ra . They found that the resulting scale essentially coincides with the peak of the cross-spectrum, which justifies the use of a single length scale for both fields. Note also that we use a single filter scale for all heights. This can be justified from the fact that the size of the superstructures does not noticeably vary with height and is closely connected to characteristic large scales close to the wall [30, 31, 62, 63, 118]. The spectra of the temperature and the heat flux have a second maximum at larger wavenumbers close to the wall, which characterize smaller-scale fluctuations [118, 140, 141]. For completeness, we discuss the choice of the superstructure scale in more detail in Appendix 3.C.

3.3.2 Volume-averaged resolved energy budget

In this section, we study the volume-averaged resolved energy budget. We first consider a wide range of filter widths before focusing on the specific scale of the superstructures. We begin our discussion with the scale dependence of the stationary resolved energy budget (3.15). The different contributions are shown in figure 3.4a as a function of the filter width for $Ra = 1.07 \times 10^7$. The average energy input into the resolved scales $\langle Q_l \rangle$ and the direct dissipation $\langle \varepsilon_l \rangle$ decrease monotonically with increasing l . In contrast to that, the average energy transfer $\langle \Pi_l \rangle$ has a maximum at intermediate scales. For all shown filter widths $\langle \Pi_l \rangle > 0$, i.e. the energy transfer acts on average as an energy sink as expected for three-dimensional turbulence (see discussion in section 3.2.3.1). In other words, there is a net energy transfer from the large to the small scales.

How can we understand the functional form of $\langle \Pi_l \rangle$? At large scales, dissipation is comparably small and the energy transfer primarily balances the resolved thermal driving. With decreasing filter scale the energy input through thermal driving accumulates, which is why it increases with decreasing filter width. It is mostly balanced by the energy transfer, which

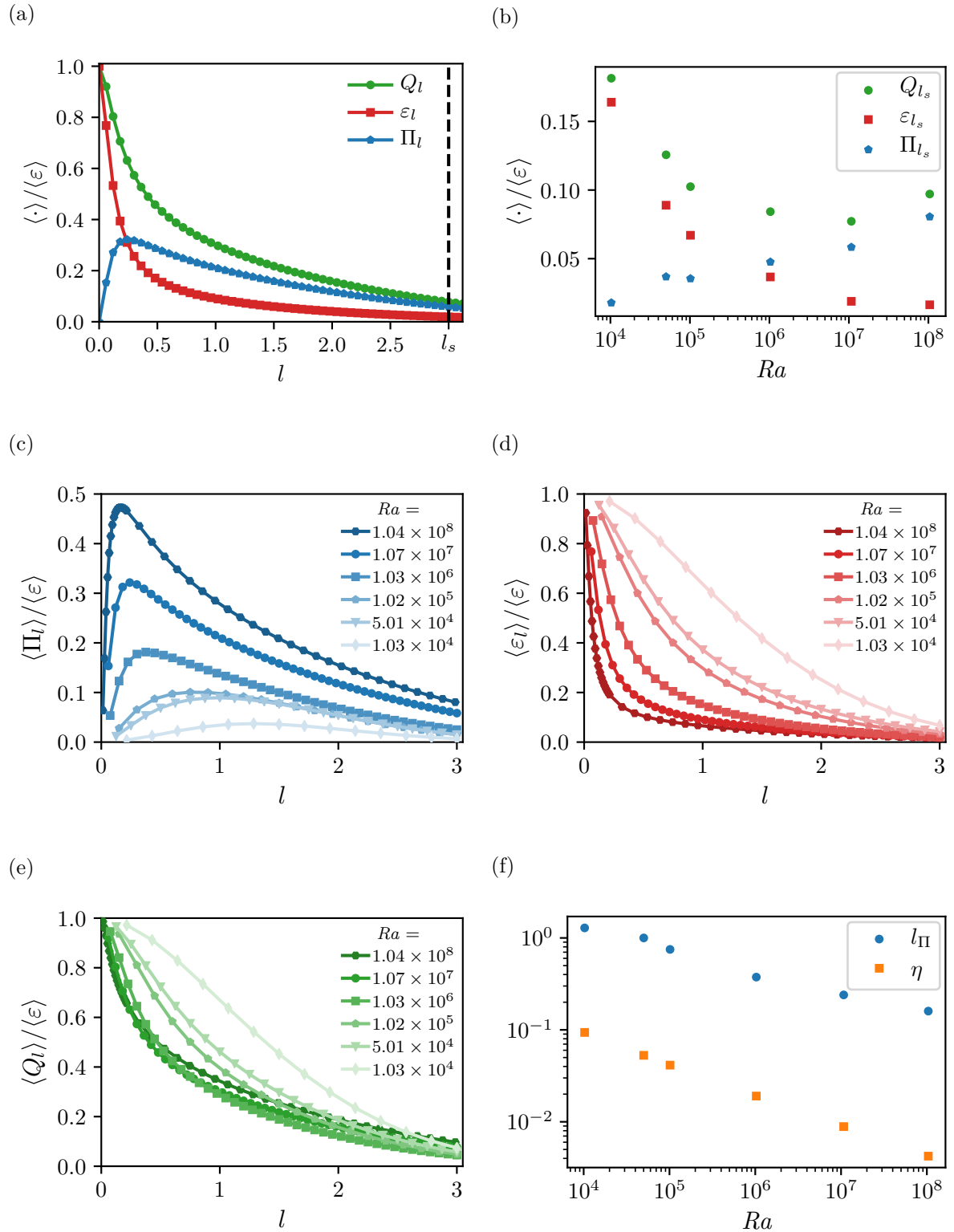


Figure 3.4: (a) Contributions to the volume-averaged resolved energy budget for a range of filter scales l for $Ra = 1.07 \times 10^7$. (b) Different contributions to the budget (3.15) at the superstructure scale l_s as a function of Ra . (c,d,e) Comparison of $\langle \Pi_l \rangle$, $\langle \varepsilon_l \rangle$ and $\langle Q_l \rangle$ for different Ra . (f) Scale l_{Π} of the maximum of $\langle \Pi_l \rangle$ compared to the Kolmogorov scale η as a function of Ra .

increases accordingly. When the filter scale reaches the dissipative regime, the direct dissipation $\langle \varepsilon_l \rangle$ begins to dominate, and the energy transfer starts to decay and finally vanishes at $l = 0$, as expected from the analytical limits derived above. The functional form of the energy transfer at small filter width is comparable to three-dimensional turbulence, see, e.g., Ballouz and Ouellette [142], Buzzicotti et al. [143]. Notably, at the superstructure scale l_s , only a small fraction, roughly 8%, of the total energy input $\langle Q \rangle$ is injected into the resolved scales. Out of that approximately 76% are transferred to unresolved scales, and approximately 24% are directly dissipated.

In figure 3.4b, we compare $\langle \Pi_{l_s} \rangle$, $\langle Q_{l_s} \rangle$ and $\langle \varepsilon_{l_s} \rangle$, respectively, at the scale of the superstructure l_s for different Rayleigh numbers. The energy transfer becomes increasingly important compared to the direct dissipation at larger Rayleigh numbers. For $Ra \geq 1.07 \times 10^7$ it is of the same order as the energy input, hence being crucially important for the energy budget of the turbulent superstructures. We associate the relative increase of the energy transfer to an increase in turbulence for higher Ra .

Figures 3.4c, 3.4d and 3.4e show $\langle \Pi_l \rangle$, $\langle Q_l \rangle$ and $\langle \varepsilon_l \rangle$ as a function of filter width. In general, the energy transfer between scales acts as a sink and increases with Ra , see figure 3.4c. In contrast, the direct dissipation decreases, see figure 3.4d, for all considered scales. For the resolved energy input we do not observe simple trends, see figure 3.4e. It is more constrained to small scales, yet there is still a non-vanishing energy input into the largest scales.

The scale l_{Π} at which $\langle \Pi_l \rangle$ is maximal decreases with Ra , as shown in figure 3.4f. We expect this to be related to the shift of the dissipative range to smaller scales with increasing Ra , since the energy transfer decays when the filter scale reaches the dissipative regime. The Kolmogorov scale η characterizes the dissipative scale. As shown in figure 3.4f, l_{Π} follows a similar trend as η .

3.3.3 Horizontally averaged resolved energy budget

In RBC the flow in the boundary layers and the bulk region is qualitatively different, as long as the boundary layers are not fully turbulent [54, 59, 60]. To analyse the difference between these distinct regions in the resolved energy budget, we present results for the horizontally averaged energy budget (3.18). This helps to understand the role of the boundary layers for the different contributions of the resolved energy budget in more detail. Compared to the volume-averaged budget, there is an additional spatial flux term $\langle \nabla \cdot \mathbf{J}_l \rangle_A$, which redistributes energy vertically. The profiles of all the height-dependent contributions of (3.18) at the superstructure scale l_s are presented in figure 3.5a for a simulation with $Ra = 1.07 \times 10^7$ as an example from the turbulent regime. They are compared to the unfiltered profiles in 3.5b. The shown flux terms are calculated from the right-hand sides of (3.18) and (3.19), respectively. The energy input into the resolved scales takes place mainly in the bulk and decays towards the wall. In contrast, the direct dissipation primarily occurs near the wall and decays towards the bulk. The energy transfer is positive in a layer in the bulk, i.e. it acts as a sink. Therefore, it effectively increases the dissipation, as it does for the volume-averaged balance. However, we also find an inverse energy transfer from the unresolved to the resolved scales near the wall in agreement with previous results for RBC [121, 124] and other wall-bounded flows [43, 130, 136, 144–146].

A comparison of the energy transfer profiles for different Rayleigh numbers (see figure 3.5c) shows that their form depends strongly on Ra . The energy transfer peaks always in the bulk and is exclusively a sink in this region, i.e. it acts as an additional dissipation. Thus the bulk determines the behaviour of the volume-averaged energy transfer. With increasing Ra the

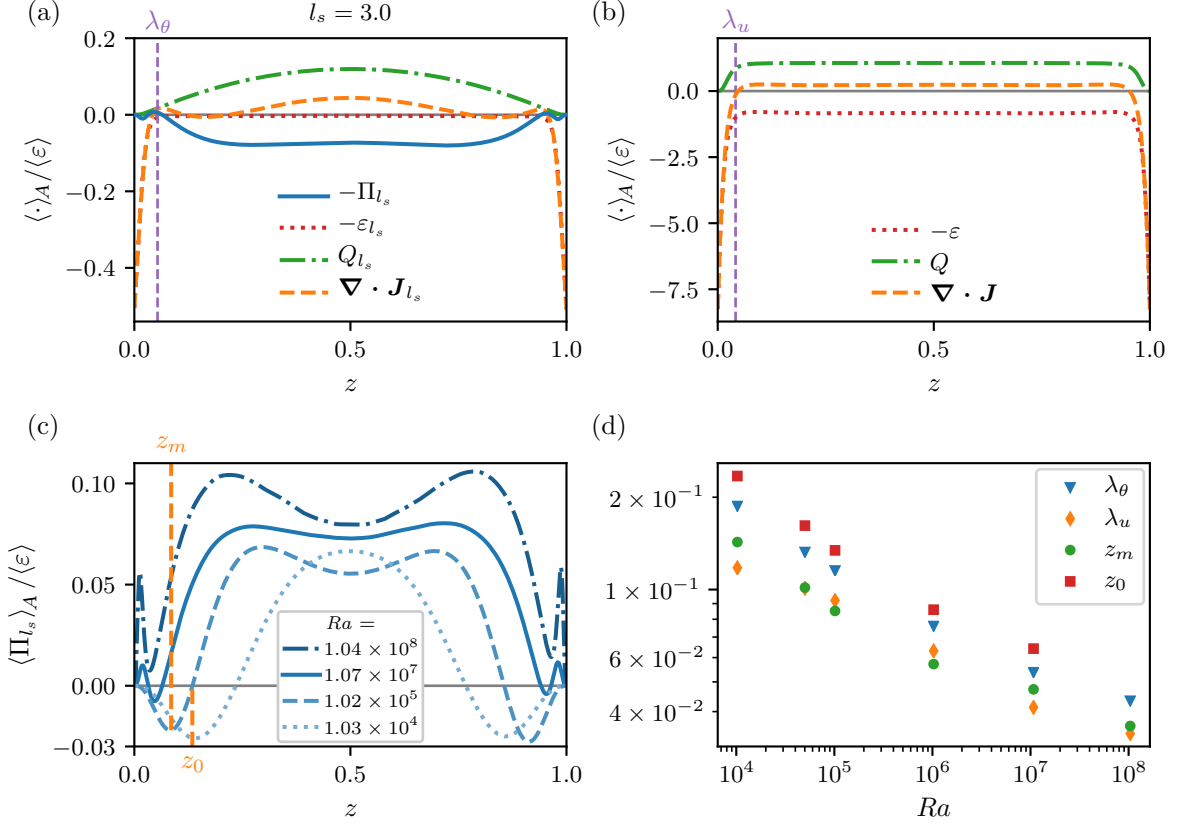


Figure 3.5: (a) Different contributions to the horizontally averaged resolved energy budget at the superstructure scale l_s and (b) unfiltered energy budget for $Ra = 1.07 \times 10^7$ normalized by the total dissipation. (c) Energy transfer term at l_s for different Ra normalized by the corresponding total dissipation. (d) Comparison of the distance from the wall to the first minimum z_m and zero crossing z_0 of $\langle \Pi_{l_s} \rangle_A$ with the boundary layer thicknesses of the temperature and the velocity fields as a function of Ra .

width of the plateau of $\langle \Pi_{l_s} \rangle_A$ in the bulk increases. For $Ra < 10^7$ the energy transfer close to the wall is characterized by a negative minimum, which means that there is a near-wall layer contributing to the driving of the resolved scales. With increasing Ra the near-wall structure of $\langle \Pi_{l_s} \rangle_A$ changes and the inverse layer vanishes at the largest Rayleigh number. Here, it turns into a positive minimum. However, locally there are still regions of upscale transfer present. This illustrates that the boundary layers play a different role for the dynamics of the superstructures than the bulk. We present an interpretation of this layer structure in terms of the plume dynamics in section 3.3.5. Note that the profiles are scale dependent, particularly at high Ra . Therefore, the energy transfer close to the wall depends on the considered filter scale as well as the Rayleigh number and has to be interpreted carefully for this reason. We present a description of the dependence on the filter scale l in Appendix 3.D.

We shall make the first attempt to link the scale-resolved layer structure revealed in figure 3.5c with the boundary layer structure of RBC. Figure 3.5d shows the thickness of the thermal dissipation layer λ_θ and viscous dissipation layer λ_u as a function of Ra . The layers are defined as the distance to the wall at which the horizontally averaged thermal, respectively viscous,

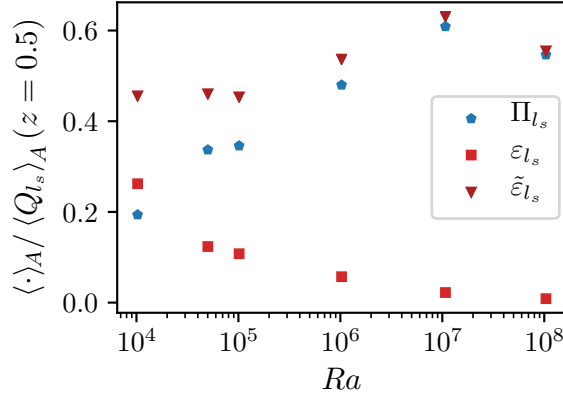


Figure 3.6: Comparison of the direct dissipation ε_{l_s} , the energy transfer Π_{l_s} , and the effective dissipation $\tilde{\varepsilon}_{l_s} = \varepsilon_{l_s} + \Pi_{l_s}$ in the midplane normalized by the resolved energy input in the midplane as a function of Ra . The energy transfer is significantly larger than the direct dissipation at high Rayleigh numbers.

dissipation equals its volume average. Petschel et al. [147] originally introduced these layers to study and compare boundary layers for different boundary conditions in RBC. They also compared their scaling as a function of Pr with classical boundary layer definitions. For an investigation of the Rayleigh number dependence of the different boundary layers we refer to Scheel and Schumacher [148], who showed that the scaling of the dissipation-based boundary layers differ from the classical ones. The boundary layers are indicated in figure 3.5a and 3.5b to present their relative position compared to the profiles. In figure 3.5d, the distance of the first local minimum of $\langle \Pi_{l_s} \rangle_A$ to the lower wall z_m and that of the subsequent zero crossing to the lower wall z_0 , where the transfer changes from inverse to direct, are presented as a function of Ra . (They are also highlighted for clarity in figure 3.5c for $Ra = 1.02 \times 10^5$.) All scales decrease with increasing Ra and follow a similar trend. Interestingly, z_m appears to be bounded by the thermal layer. This means that the inverse energy transfer mostly happens inside the thermal boundary layer, i.e. close to the wall. We associate the decrease of its extent with the well-known shrinking of the boundary layers [59, 148]. For the highest Ra , the inverse transfer layer vanishes, which we will discuss in section 3.3.5. The minimum at z_m now describes a direct transfer in contrast to the smaller Ra but is still inside the thermal boundary layer. Overall, this shows that the differences in the flow between the bulk and close to the wall are also represented in the structure of the transfer term.

3.3.4 Effective resolved dissipation and implications for reduced models

Emran and Schumacher [27] and Pandey et al. [30] have pointed out similarities between the turbulent superstructures and patterns close to the onset of convection. In this regime, analytical techniques are feasible [58]. Combined with the filtering approach, this could enable future developments of effective large-scale equations for RBC at high Ra . To discuss these similarities and their implications, we draw comparisons between the resolved profiles at large Ra to the unfiltered profiles for a small Ra from the weakly nonlinear regime. As we have seen in the previous section, the energy transfer primarily contributes to the resolved energy

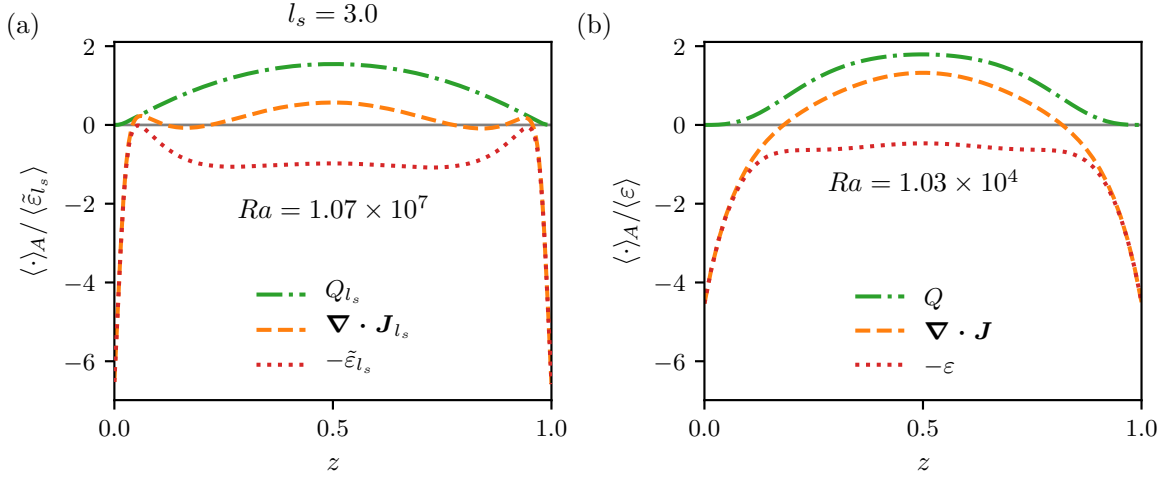


Figure 3.7: (a) Resolved energy budget at the superstructure scale l_s in terms of the effective dissipation $\tilde{\epsilon}_{l_s}$ normalized with the total effective dissipation $\langle \tilde{\epsilon}_{l_s} \rangle$ for $Ra = 1.07 \times 10^7$. (b) Unfiltered energy budget normalized with the total dissipation for $Ra = 1.03 \times 10^4$, close to onset in the weakly nonlinear regime of convection.

budget as a sink term, resulting in an additional dissipation. We therefore consider the effective resolved dissipation $\tilde{\epsilon}_l = \epsilon_l + \Pi_l$ at the superstructure scale. In figure 3.6, the averaged effective dissipation in the midplane is shown as a function of Ra normalized by the resolved energy input in the midplane. We observe that the effective dissipation slightly increases until $Ra = 10^7$. It removes roughly half of the energy input in the midplane. The comparison with the energy transfer and the direct dissipation reveals that at high Rayleigh number, the transfer of energy to small scales is primarily responsible for the effective dissipation of the energy. The direct dissipation, in comparison, is negligible at high Ra .

Figure 3.7 shows the resolved profiles at the scale of the superstructures compared to the unfiltered profiles from the weakly nonlinear regime. Close to the wall, the effective resolved dissipation and the redistribution differ from the corresponding profiles close to onset. Close to the midplane, the height-dependent profiles from the resolved budget and the original budget compare quite well, although some quantitative differences are visible. This indicates that an effective dissipation may capture the effect of the energy transfer on the superstructures in the bulk. The more complex near-wall behaviour of the superstructures at high Ra requires more elaborate approaches.

3.3.5 Energy transfer rate and plume dynamics

In RBC plumes play a crucial role in the dynamics and are essential parts of the superstructures. Using the filtering approach we can connect flow structures and their contribution to the energy budget. To gain insight into their role in the energy transfer, we discuss the local energy budget. Figure 3.8 shows vertical cuts through the system for the energy transfer field and the temperature field for different Ra . Especially in the weakly nonlinear regime, we observe a spatial correlation between plume impinging and detaching and the direction of the energy transfer. Regions of plume detachment correspond to regions of energy transfer to the unresolved scales, whereas regions of plume impinging correspond to regions of energy transfer

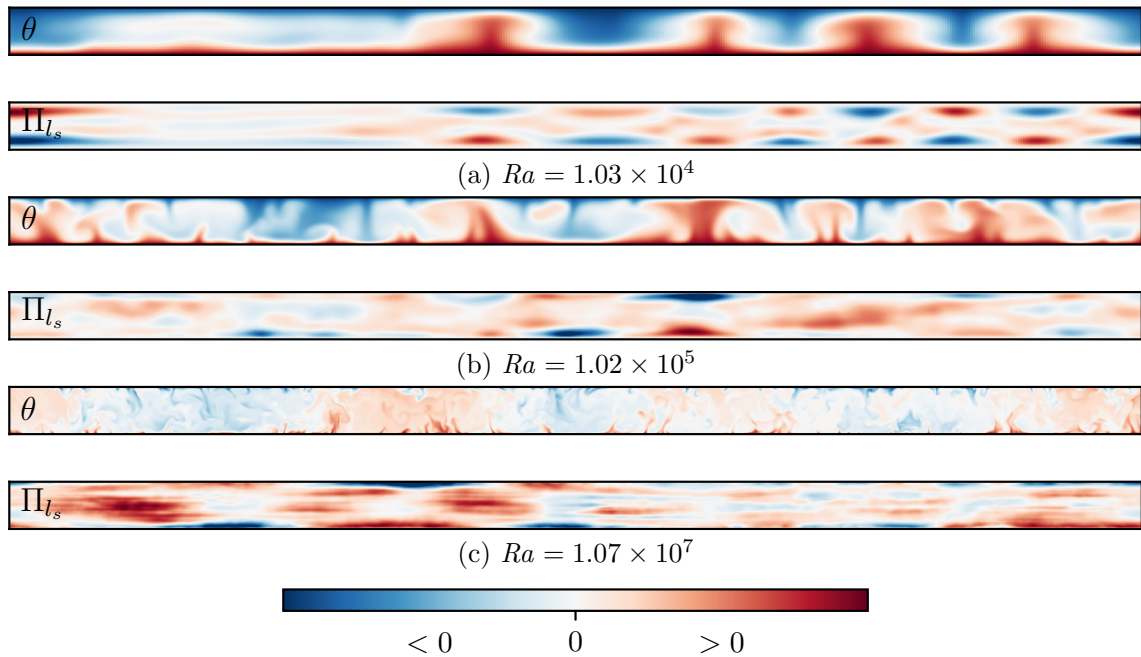


Figure 3.8: Comparison of an instantaneous snapshot of the temperature field and the energy transfer (normalized to unit maximum amplitude) between scales for (a) $Ra = 1.03 \times 10^4$, (b) $Ra = 1.02 \times 10^5$, and (c) $Ra = 1.07 \times 10^7$ at the superstructure scale l_s . Close to onset in the weakly nonlinear regime, a direct connection between the plume dynamics, i.e. impinging and detachment, and the direction of the energy transfer is present. On impinging the plume heads enlarge, which is accompanied by an inverse energy transfer. During detachment the plumes shrink and there is a direct energy transfer.

from the small to the large scales. Similar observations have been made by Togni et al. [121], who also found an inverse transfer from small to large scales connected to plume impinging. Due to the increasingly complex and three-dimensional motions at larger Ra , see figure 3.8b and 3.8c, this spatial correlation is weakening. This is due to the fact that fewer plumes extend throughout the entire cell and are more likely to be deflected on their way from the top to the bottom plate or *vice versa*. Hence they do not experience the sharp temperature gradient at the boundary layers. Instead, they release their temperature in the bulk and do not impinge on the boundary layers. This prevents the strong enlargement of individual plumes and the corresponding energy transfer to the large scales. However, clustered plumes, which effectively form large-scale plumes, still impinge on the walls and cause an inverse energy transfer. From the horizontally averaged energy transfer, see figure 3.5c, we conclude that the inverse transfer caused by plume impinging exceeds the direct transfer caused by plume detaching, at least in the weakly nonlinear regime. However, at the largest Rayleigh number, the layer of inverse transfer vanishes. Here, the direct transfer caused by plume detaching exceeds the inverse transfer.

How can the above considerations be related to the findings for the volume-averaged energy budget? At small Rayleigh numbers the direct transfer in the bulk and the inverse transfer close to the wall almost balance, resulting on average in a small direct transfer. At larger Ra

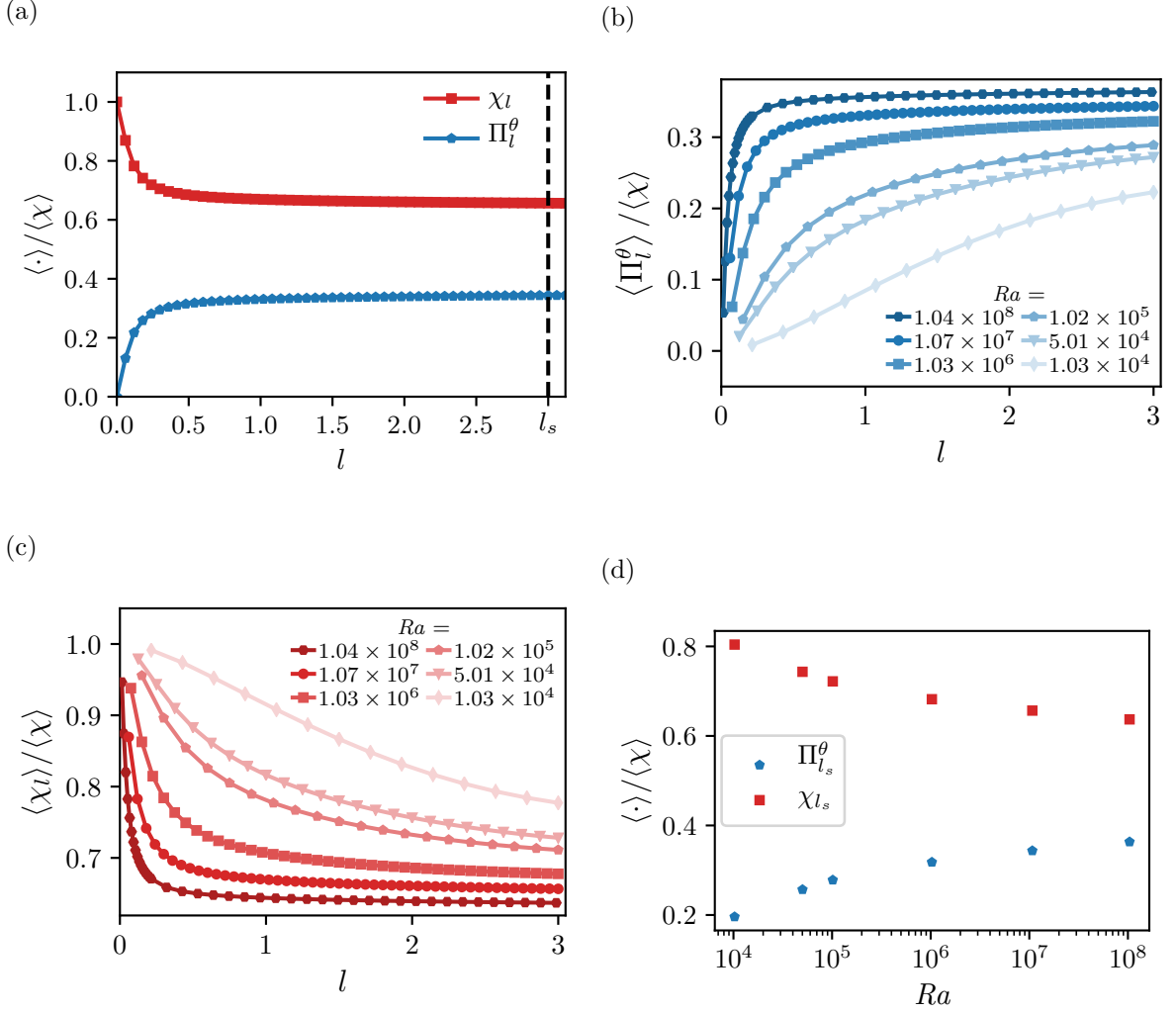


Figure 3.9: (a) Volume-averaged temperature variance budget for $Ra = 1.07 \times 10^7$. (b) Heat transfer $\langle \Pi_l^\theta \rangle$ and (c) thermal dissipation $\langle \chi_l \rangle$ for different Ra as a function of filter scale. (d) $\langle \Pi_{l_s}^\theta \rangle$ and $\langle \chi_{l_s} \rangle$ at the scale of the superstructures as a function of Ra .

the inverse transfer caused by impinging is reduced because only a fraction of the released plumes reaches the opposite boundary layer. Here, the width of the inverse transfer layer is reduced. At the same time, the direct transfer increases and the corresponding layer becomes larger. The direct transfer consequently grows on average with Ra . For a discussion of the scale dependence of plume dynamics connected to the direction of the energy transfer see Appendix 3.D. There, we discuss Π_l and the profiles $\langle \Pi_l \rangle_A$ for varying filter scales l .

3.3.6 Volume-averaged resolved temperature variance budget

For completeness, we here complement the previous section with the consideration of the budget of the resolved temperature variance. The balance (3.25) shows that the total thermal

dissipation is split into two contributions: the resolved dissipation $\langle \chi_l \rangle$ and the heat transfer $\langle \Pi_l^\theta \rangle$. As illustrated in figure 3.9a, the resolved thermal dissipation exceeds the heat transfer at all scales, including the scale of the superstructure for the considered Rayleigh number. This is qualitatively different from the behaviour observed for the contributions to the kinetic energy balance. The heat transfer and direct dissipation both approach a constant value after an initial increase for small filter width. At these scales, they are approximately scale independent and the transfer of temperature variance is down-scale. This is important for the phenomenology of RBC. In fact, both the Obukhov-Corrsin theory as well as the Bolgiano-Obukhov theory rest on a direct cascade picture for the temperature variance, consistent with our observations. A more detailed treatment of these considerations is beyond the scope of our work, and we refer the reader to Ching [55], Lohse and Xia [60], Verma et al. [77] and Verma [56] and references therein. Similarly to the energy transfer, the heat transfer increases with increasing Ra and the resolved thermal dissipation decreases, see figure 3.9b, 3.9c, and 3.9d. The heat transfer is always positive and, therefore, acts as a thermal dissipation for the resolved scales.

3.3.7 Horizontally averaged resolved temperature variance budget

The profiles of all the contributions to the horizontally averaged resolved temperature variance budget are shown in figure 3.10a for $Ra = 1.07 \times 10^7$ and compared to the unfiltered profiles in figure 3.10b as an example from the turbulent regime. Here, the unfiltered flux is given by $\mathbf{J}^\theta = \mathbf{u}e^\theta - \nabla e^\theta / \sqrt{RaPr}$, which can be obtained from (3.23) in the limit of a vanishing filter width l . The resolved thermal dissipation follows a very similar form as the original thermal dissipation. It almost vanishes in the bulk and strongly increases towards the walls in the boundary layers. The heat transfer is positive for almost all heights and also vanishes in the bulk. It has a strong peak close to the walls and acts exclusively as a thermal dissipation. This is similar for different Ra as shown in figure 3.10c. A notable exception is at small Ra , where it is slightly negative, i.e. up-scale, close to the midplane. The peak of $\langle \Pi_{l_s}^\theta \rangle_A$ increases in magnitude with increasing Ra and its distance to the wall z_m^θ decreases. The peak almost coincides with the height of the thermal boundary layer λ_{Nu} , see figure 3.10d. In this region, the temperature variance deposited by the resolved heat flux is partly transferred to smaller scales and mainly dissipated.

Comparing the resolved energy with the resolved temperature variance budget, there are qualitatively similar scale dependencies. The transfers between scales increase with increasing Ra and act on average as a dissipation. However, the volume-averaged heat transfer is roughly constant after an initial increase at small scales, whereas the energy transfer decays after a maximum at small scales. At the scale of the superstructures, the volume-averaged heat transfer is smaller than the corresponding direct thermal dissipation for all Ra . In contrast, the volume-averaged energy transfer exceeds the direct dissipation at large Ra . Additionally, the profiles at the superstructure scale show qualitative differences, i.e. the heat transfer is almost exclusively down-scale for all heights while the energy transfer shows a layer of up-scale energy transfer as well.

3.4 Summary

We investigated the scale-resolved kinetic energy and temperature variance budgets of RBC at Rayleigh numbers in the range $1.03 \times 10^4 \leq Ra \leq 1.04 \times 10^8$ for a fixed $Pr = 1$ and a

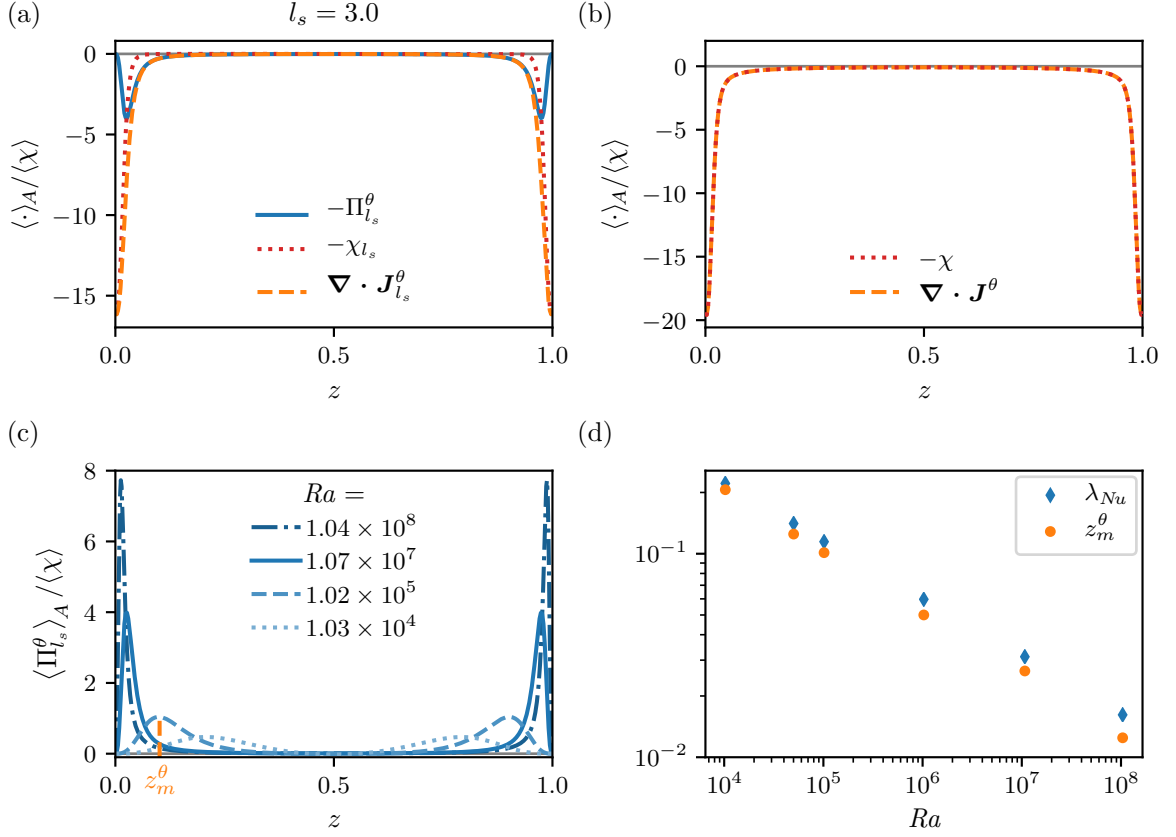


Figure 3.10: (a) Different contributions to the horizontally averaged resolved temperature variance budget at the superstructure scale l_s and (b) unfiltered temperature variance budget for $Ra = 1.07 \times 10^7$, normalized by the total thermal dissipation. (c) Profile of the heat transfer $\langle \Pi_{l_s}^\theta \rangle_A$ at the superstructure scale for different Ra . (d) Distance z_m^θ from the wall to the maximum of $\langle \Pi_{l_s}^\theta \rangle_A$ compared to the thermal boundary layer thickness λ_{Nu} as function of Ra . z_m^θ is also highlighted in (c) for $Ra = 1.02 \times 10^5$.

high aspect ratio ($\Gamma \approx 24$) with a focus on the interplay of turbulent superstructures and turbulent fluctuations. As a starting point, we generalized the volume-averaged kinetic energy and temperature variance budgets to scale-dependent budgets of the resolved fields. For the kinetic energy budget, this results in a balance between the resolved energy input, the direct large-scale dissipation and an energy transfer to the unresolved scales. It shows that the small-scale fluctuations play an important role for the energy balance of the large scales. For our simulations at the highest Rayleigh numbers under consideration, we find that the energy transfer to the smaller scales is of comparable magnitude to the resolved energy input at the superstructure scale. This means that the generation of small-scale turbulence acts as a dissipation channel for the large scales, which qualitatively confirms the classic picture that small-scale turbulence introduces an effective dissipation.

When resolving the energy transfer with respect to height, a more complex picture emerges which, in particular, reveals the role of the boundary layers. The height-dependent balance of

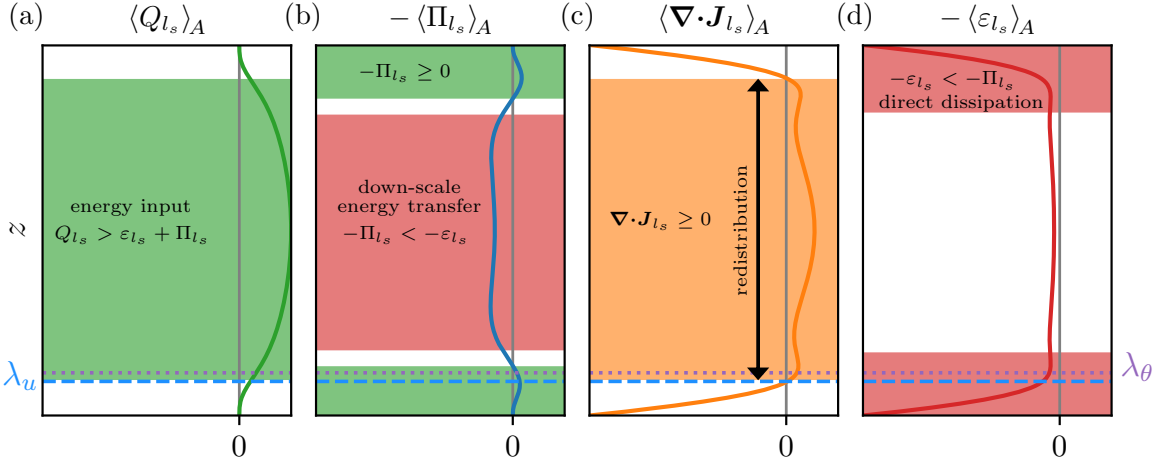


Figure 3.11: Sketch of the resolved energy balance at the scale of the superstructure, highlighting the distinct structure of the bulk and boundary layer. The profiles are obtained from a simulation at $Ra = 1.02 \times 10^5$ as an illustrative example for the moderately turbulent regime. The dissipation layer λ_u and the thermal dissipation layer λ_θ are indicated by the dashed and dotted lines, respectively. Energy input regions are highlighted in green, direct dissipation and down-scale energy transfer in red, and spatial redistribution in orange.

the distinct terms is summarized in figure 3.11 at the superstructure scale. Panel (a) shows that most of the energy input due to thermal driving takes place in the bulk. From there, energy is transferred to smaller scales, see panel (b), and transported towards the wall, see panel (c). While the direct large-scale dissipation is comparably small in the bulk, its main contribution stems from regions close to the wall, see panel (d). There, the situation is more complex. We find an additional inverse energy transfer from the small to the large scales for $Ra < 10^8$ and a minimum for the largest considered Rayleigh number. This illustrates that the boundary layers play a distinct role for the energy budget of the superstructures.

Consistent with previous studies [27, 30], we find qualitative similarities between the energy budget of turbulent superstructures and that of patterns in the weakly nonlinear regime. The resolved energy budget of the superstructures and the standard energy budget at the onset of convection show qualitative similarities in the midplane when the energy transfer to smaller scales is interpreted as an effective dissipation. This may open possibilities for modelling the large-scale structure of turbulent convection at high Rayleigh numbers.

In order to gain insight into the origin of the inverse energy transfer, we studied the spatially resolved energy transfer. At small Ra , there is a direct correspondence between plume impinging and plume detaching and the direction of the energy transfer. The enlargement of the plume head during impinging is accompanied by an energy transfer to the large scales. Conversely, the small scales are fed during plume detachment. A stronger inverse transfer caused by plume impinging can therefore result in the layer of inverse transfer observed close to the wall. However, in the turbulent regime, the lateral motion of the plumes is increased, which prevents the impinging on the boundary layers and the corresponding inverse energy transfer. Finally, at the largest Rayleigh number, the inverse layer vanishes.

We complemented the investigations of the resolved energy budget with the study of the re-

solved temperature variance budget. We find that the heat transfer between scales is roughly scale independent at large scales in the turbulent regime. Here, at the scale of the superstructures, the averaged direct thermal dissipation exceeds the averaged heat transfer for all considered Ra . This is different from the behaviour of the energy transfer, and the direct thermal dissipation is more relevant for the balance of the temperature variance of the superstructures. Furthermore, the study of the height-dependent profiles showed that the heat transfer acts as a thermal dissipation at all heights for large Rayleigh numbers and is strongly peaked close to the boundary layers.

In summary, our investigations reveal the impact of turbulent fluctuations on the large-scale convection rolls in turbulent Rayleigh-Bénard convection. In future investigations, it will be interesting to see whether the turbulent effects reach an asymptotic state at sufficiently high Reynolds numbers. This could open the possibility for universal effective large-scale models for Rayleigh-Bénard convection at high Rayleigh numbers.

Acknowledgments

This work is supported by the Priority Programme SPP 1881 Turbulent Superstructures of the Deutsche Forschungsgemeinschaft. D.V. gratefully acknowledges partial support by ERC grant No 787361-COBOM. Computational resources of the Max Planck Computing and Data Facility and support by the Max Planck Society are gratefully acknowledged.

Declaration of Interests

The authors report no conflict of interest.

3.A Connection between volume-averaged resolved energy budget and original budget

Under the assumptions that the filtered fields obey the same boundary conditions as the unfiltered ones, and that the filter preserves volume averages, the statistically stationary energy and temperature variance budgets can be related to the Nusselt number. First, we can reformulate the resolved energy input

$$\langle \overline{u_{z_l} \bar{\theta}_l} \rangle = \langle \overline{(u_z \theta)_l} \rangle - \langle \gamma_l \cdot \hat{z} \rangle = \langle u_z \theta \rangle - \langle \gamma_l \cdot \hat{z} \rangle, \quad (3.27)$$

where we have used (3.7) and that the filter preserves the volume average. Then we find with $Nu = \sqrt{RaPr} \langle u_z \theta \rangle + 1$ that

$$\langle \overline{u_{z_l} \bar{\theta}_l} \rangle = \langle Q_l \rangle = \frac{1}{\sqrt{RaPr}} (Nu - 1) - \langle \gamma_l \cdot \hat{z} \rangle.$$

This is inserted into (3.15), and combined with (3.2) we obtain

$$\langle \varepsilon_l \rangle + \langle \Pi_l \rangle + \langle \gamma_l \cdot \hat{z} \rangle = \frac{1}{\sqrt{RaPr}} (Nu - 1) = \langle \varepsilon \rangle. \quad (3.28)$$

This shows that the total kinetic energy dissipation $\langle \varepsilon \rangle$ is split into energy transfer between scales $\langle \Pi_l \rangle$, direct dissipation of the resolved scales $\langle \varepsilon_l \rangle$ and the thermal driving of the unresolved scales $\langle \gamma_l \cdot \hat{z} \rangle$. With (3.15) and (3.2), we can write equation (3.28) also as

$$\langle Q_l \rangle + \langle \gamma_l \cdot \hat{z} \rangle = \frac{1}{\sqrt{RaPr}} (Nu - 1) = \langle Q \rangle, \quad (3.29)$$

in which the total energy input is split into the resolved energy input and the turbulent heat flux. If we introduce the resolved Nusselt number $Nu_l = \sqrt{RaPr} \langle Q_l \rangle + 1$, this relation can be written as

$$Nu_l + \sqrt{RaPr} \langle \gamma_l \cdot \hat{z} \rangle = Nu, \quad (3.30)$$

which shows that Nu is split into Nu_l and the heat flux into the unresolved scales $\sqrt{RaPr} \langle \gamma_l \cdot \hat{z} \rangle$.

3.B Volume-averaged resolved temperature variance budget

Here we derive the volume-averaged resolved temperature variance budget (3.25). We take the volume average of (3.21),

$$\langle \nabla \cdot \mathbf{J}_l^\theta \rangle = -\langle \chi_l \rangle - \langle \Pi_l^\theta \rangle, \quad (3.31)$$

in which the temporal derivative vanishes in the statistically stationary state. In contrast to the kinetic energy budget, the flux term does not vanish for the temperature variance. We obtain

$$\langle \nabla \cdot \mathbf{J}_l^\theta \rangle = \left\langle \nabla \cdot \left(\bar{\mathbf{u}}_l e_l^\theta - \frac{1}{\sqrt{RaPr}} \nabla e_l^\theta + \gamma_l \bar{\theta}_l \right) \right\rangle = -\frac{1}{\sqrt{RaPr}} \langle \nabla^2 e_l^\theta \rangle, \quad (3.32)$$

since the contributions containing $\bar{\mathbf{u}}_l$ vanish because of the boundary conditions. To relate the flux term to the Nusselt number, we write the volume integral in the form

$$\int_V \nabla^2 e_l^\theta dV = \int_V \nabla \cdot (\bar{\theta}_l \nabla \bar{\theta}_l) dV = \int_{\partial V} (\bar{\theta}_l \nabla \bar{\theta}_l) \cdot \hat{\mathbf{n}} dA. \quad (3.33)$$

In the last integral the contributions from the sidewalls vanish because of the periodic boundary conditions. Therefore only the integration over the top and bottom wall remains, at which the temperature is constant, i.e. $\bar{\theta}_l(z = 0, 1) = \pm 1/2$. This gives

$$\int_{\partial V} (\bar{\theta}_l \nabla \bar{\theta}_l) \cdot \hat{\mathbf{n}} dA = -\frac{1}{2} \left(\partial_z \int_{z=0} \theta dA + \partial_z \int_{z=1} \theta dA \right), \quad (3.34)$$

where we used the fact that θ is constant at the top and bottom wall, and therefore $\bar{\theta}_l(z = 0, 1) = \theta(z = 0, 1)$. The Nusselt number is defined as

$$Nu = \sqrt{RaPr} \langle u_z \theta \rangle_A - \partial_z \langle \theta \rangle_A, \quad (3.35)$$

which is independent of z (see, e.g. Scheel and Schumacher [148]). At the top and bottom wall $\mathbf{u} = 0$ and $Nu(z = 0, 1) = -\partial_z \langle \theta \rangle_A(z = 0, 1)$, and we find

$$\langle \nabla^2 e_l^\theta \rangle = -\frac{1}{2} [\partial_z \langle \theta \rangle_A(z = 0) + \partial_z \langle \theta \rangle_A(z = 1)] = Nu. \quad (3.36)$$

Substituting this back into (3.31) results in the volume-averaged balance (3.25).

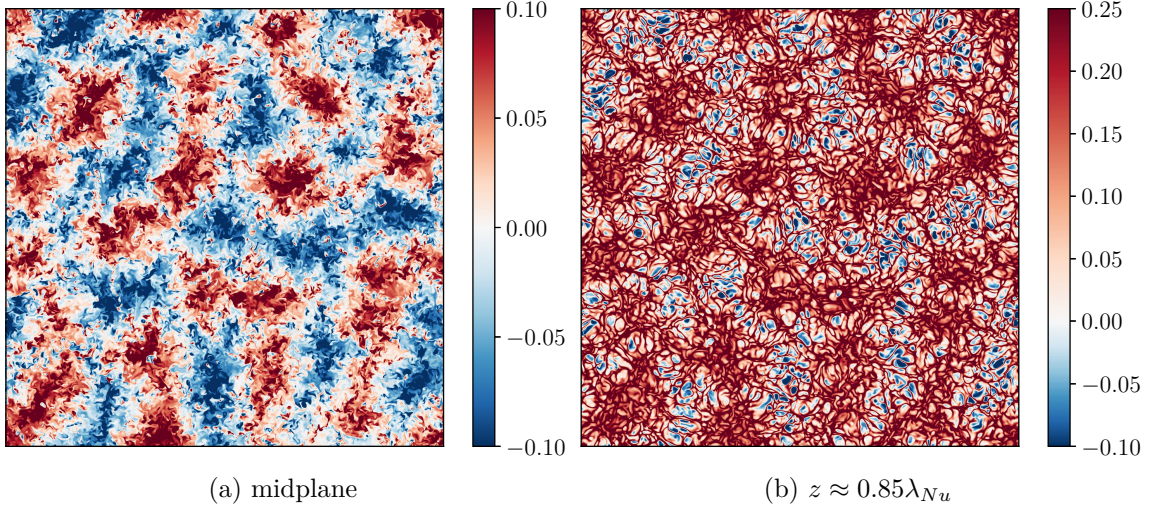


Figure 3.12: Comparison of the temperature in (a) the midplane and (b) close to the wall for $Ra = 1.07 \times 10^7$. A footprint of the large-scale pattern in the midplane is visible close to the bottom wall.

3.C Height-dependent spectra

Here, we discuss the height dependence of the spectrum $E_{\theta u_z}(k, z)$ first introduced in section 3.3.1. Because of the lack of statistical homogeneity in the vertical direction, it is not *a priori* clear that there is a single characteristic large scale at all heights. However, it was already shown by Pandey et al. [30], Stevens et al. [31], Parodi et al. [62], von Hardenberg et al. [63] and Krug et al. [118] that the turbulent superstructures leave an imprint in the boundary layers. Figure 3.12 shows a comparison of the temperature field in the midplane and at boundary layer height close to the wall, which visually confirms the connection between the bulk flow and the boundary layer (see also Stevens et al. [31]).

To verify this quantitatively, we consider the height-dependent azimuthally averaged cross-spectrum $E_{\theta u_z}(k, z)$ of the vertical velocity and temperature. The spectrum is shown in figure 3.13 in pre-multiplied form for two different Ra and different heights as well as height averaged. In the midplane a single maximum is present, which characterizes the size of the superstructure. However, closer to the wall a second maximum forms [118, 140, 141], which is related to the small-scale turbulent fluctuations. As expected, this maximum is more pronounced at the higher Rayleigh number. Still, we observe a local maximum at the scale of the superstructure, corresponding to the wavenumber of the maximum in the midplane. This shows that the size of the superstructure is indeed independent of height, and can also be inferred from the single peak of the height-averaged spectrum.

3.D Horizontally averaged Π_l for varying filter scale

Here we discuss the scale dependence of Π_l and the corresponding profiles $\langle \Pi_l \rangle_A$. The profiles of the energy transfer term Π_l are strongly scale dependent, as can be expected. Figure 3.14 shows the horizontally averaged energy transfer profiles for different filter widths and different Ra . For $Ra = 1.02 \times 10^5$ and $Ra = 1.03 \times 10^6$, the inverse transfer layer grows in size and

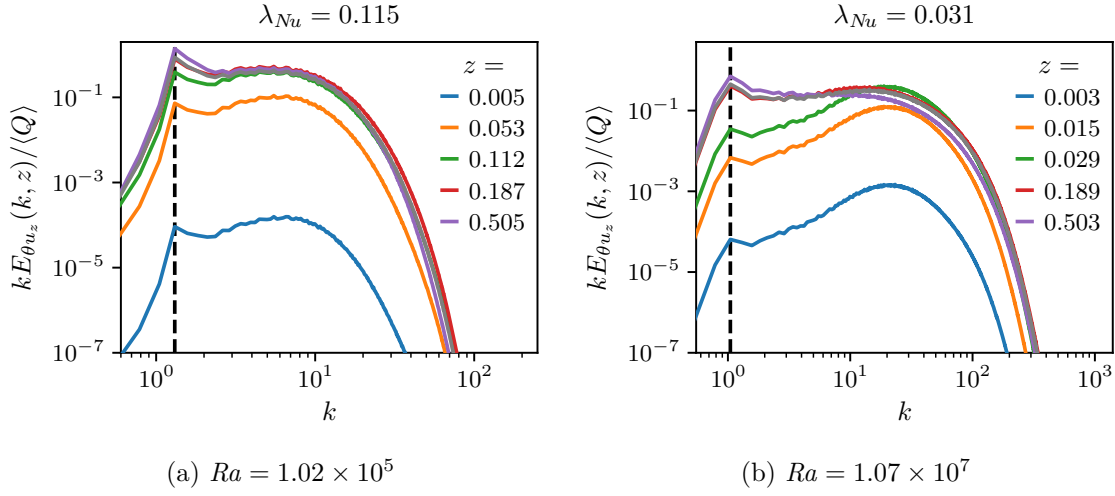


Figure 3.13: Pre-multiplied spectra, $kE_{\theta_{u_z}}(k, z)$, for (a) $Ra = 1.02 \times 10^5$ and (b) $Ra = 1.07 \times 10^7$, and different heights z . The height-averaged spectrum is shown in dark gray. The thermal boundary layer thickness λ_{Nu} is given for reference. A peak at the same position k is present at all heights, also in the boundary layer, characterizing the size of the superstructure. However, close to the boundary layer a second maximum emerges. This is related to small-scale fluctuations. The maximum at small scales is highlighted through the presentation in pre-multiplied form.

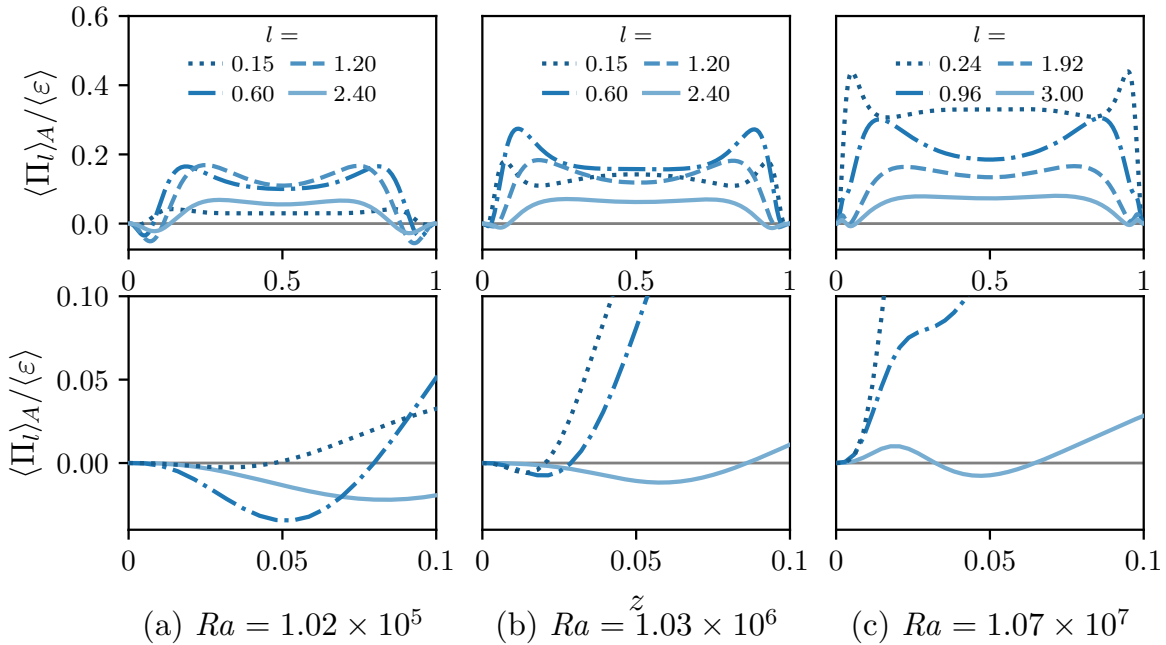
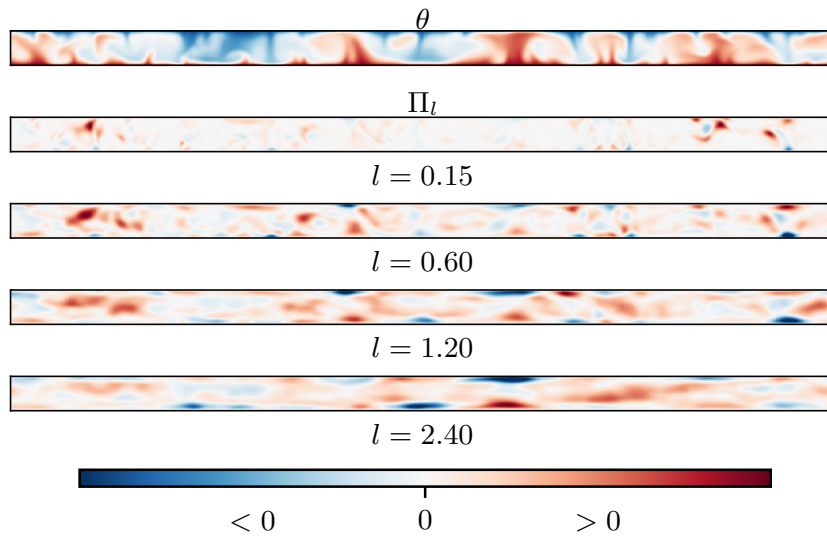


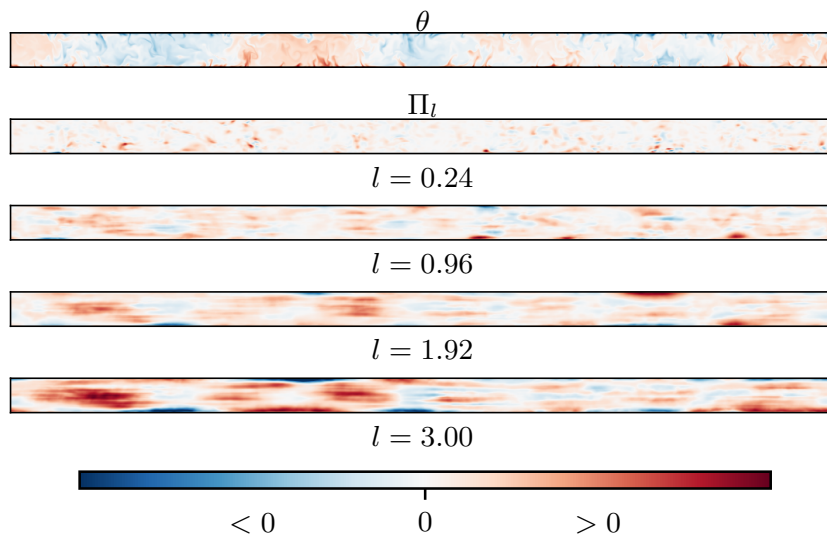
Figure 3.14: Profile of the energy transfer $\langle \Pi_l \rangle_A$ for three different Ra and different filter width l . The largest filter scale corresponds to the scale of the superstructures l_s . The bottom row shows a zoom into the region close to the wall.

magnitude with increasing filter width. For $Ra = 1.07 \times 10^7$, the inverse energy transfer close to the wall only occurs for large filter widths. For small filter widths, the profiles are consistent with the ones for $Ra = 10^7$ reported by Togni et al. [123, 124], who obtained the height-dependent budgets for small filter width ($l < 0.25$) and smaller aspect ratio ($\Gamma = 8$) with a spectral cutoff filter in the horizontal directions. They found that the energy transfer acts as a dissipation for all heights throughout the layer, consistent with our findings at small filter width. The inverse transfer at large scales reported here indicates the need for different modelling approaches for the large-scales dynamics compared to the one at smaller scales.

In section 3.3.5, we related the direction of the energy transfer to the plume dynamics. Here, we discuss the inverse transfer layer at different filter widths. In figure 3.15a, a vertical cut through Π_l is shown for different filter widths and compared to the corresponding temperature field for $Ra = 1.02 \times 10^5$. Differently sized plumes extend through the whole cell and impinge on the wall. This causes an inverse transfer at small and large filter width. In contrast, for $Ra = 1.07 \times 10^7$ in figure 3.15b, it can be seen that only few isolated small-scale plumes extend throughout the whole cell and impinge on the wall. They only cause little inverse energy transfer at small filter widths, which is why on average the direct transfer dominates and there is no inverse transfer layer. However, clustered plumes form larger-scale structures, which contribute to the inverse transfer at larger scales when they impinge on the wall. This results in an inverse transfer layer in the profiles at large filter widths.



(a) $Ra = 1.02 \times 10^5$



(b) $Ra = 1.07 \times 10^7$

Figure 3.15: Comparison of vertical cuts through the temperature fields θ and the energy transfer field Π_l (normalized to unit maximum amplitude) for different filter widths and two Ra .

Part II

—
Manuscript II

Large-Scale Pattern Formation in the Presence of Small-Scale Random Advection

PHYSICAL REVIEW LETTERS **123**, 114501 (2019)

Large-Scale Pattern Formation in the Presence of Small-Scale Random Advection

Gregor Ibbeken,^{1,2} Gerrit Green,^{1,2} and Michael Wilczek^{1,2,*}

¹Max Planck Institute for Dynamics and Self-Organization (MPI DS), Am Faßberg 17, 37077 Göttingen, Germany

²Faculty of Physics, University of Göttingen, Friedrich-Hund-Platz 1, 37077 Göttingen, Germany


 (Received 9 July 2018; published 13 September 2019)

Figure 4.1: Section of the title header of [68].

Previously, we studied the full RBC system with DNS. In order to understand the influence of small-scale fluctuations on generic large-scale patterns in more detail, we consider a reduced model to gain insights into general mechanisms. Here, we make use of a modified SH equation, which allows us to make analytical progress. The following article is reproduced with permission of the American Physical Society from the original paper Ibbeken et al. [68]: "G. Ibbeken, G. Green, and M. Wilczek, [Large-Scale Pattern Formation in the Presence Of Small-Scale Random Advection](#). Phys. Rev. Lett., 123:114501, 2019. doi: 10.1103/PhysRevLett.123.114501"(see figure 4.1). The work has been started as the Bachelor thesis of Gregor Ibbeken [149]. During Gregor's work at the MPIDS I started to co-supervise him with Michael, which ultimately led to the final results and the manuscript [68].

Author contributions MW designed the study. GI wrote the simulation code. GG performed the simulations. GI and GG wrote the post processing routines and analysed the data. All authors contributed to the analytical calculations. All authors discussed and interpreted

the results and wrote the manuscript. GI and GG contributed equally to this work (shared first author).

4.1 Main text

Abstract

Despite the presence of strong fluctuations, many turbulent systems such as Rayleigh-Bénard convection and Taylor-Couette flow display self-organized large-scale flow patterns. How do small-scale turbulent fluctuations impact the emergence and stability of such large-scale flow patterns? Here, we approach this question conceptually by investigating a class of pattern forming systems in the presence of random advection by a Kraichnan-Kazantsev velocity field. Combining tools from pattern formation with statistical theory and simulations, we show that random advection shifts the onset and the wave number of emergent patterns. As a simple model for pattern formation in convection, the effects are demonstrated with a generalized Swift-Hohenberg equation including random advection. We also discuss the implications of our results for the large-scale flow of turbulent Rayleigh-Bénard convection.

DOI: [10.1103/PhysRevLett.123.114501](https://doi.org/10.1103/PhysRevLett.123.114501)

Many turbulent systems show a remarkable degree of large-scale coherence, despite the presence of strong fluctuations. Large-scale convection patterns in the atmosphere and in the oceans are among the most fascinating examples. Rayleigh-Bénard convection (RBC) [57–60], the flow between two plates heated from below and cooled from above, is a prototypical model for such flows and displays a range of phenomena—the emergence of laminar large-scale rolls close to the onset of convection, transitions to increasingly complex flow patterns as the temperature difference is increased, and finally, the emergence of turbulence. Close to onset, techniques like linear stability analysis as well as amplitude and phase equations explain the emergence and stability of convection patterns [50, 85, 93, 150–153]. Further away from the onset of convection, the flow becomes increasingly difficult to describe, especially when it becomes turbulent. Both experiments and, in particular, numerical simulations have provided insights into these complex flow regimes [57–59]. Remarkably, coherent large-scale flow patterns, so-called turbulent superstructures, have been reported in the presence of small-scale turbulence [22, 27, 30, 31, 61–63]. Using suitable averaging techniques, the topology and dynamics of the superstructures have been extracted from the turbulent flow fields, demonstrating, e.g., large-scale dynamics reminiscent of spiral-defect chaos [27]. Extensive experimental and numerical investigations revealed that the length scale of the emerging patterns increases as a function of Rayleigh and Prandtl numbers as the flow becomes increasingly unsteady [83, 154, 155] and, finally, turbulent [30, 61]. Investigations of RBC close to onset suggest that there is no universal scale selection mechanism, see, e.g., [49, 53] for an overview. As soon as turbulence sets in, the issue is even more delicate: so far there is no conclusive explanation for the increased wavelength of turbulent superstructures. Interestingly, similar issues remain in explaining turbulent Taylor Couette flow [25], i.e. the flow between two rotating cylinders. Also here, the length scale of Taylor rolls increases with the Reynolds number [26], and the coexistence of large-scale flow states points at complex interactions between coherent flow and fluctuations [24].

On a more general level, this raises the fundamental question of how small-scale turbulent fluctuations impact the emergence and stability of large-scale flow patterns. Because of their

complexity, a comprehensive explanation of these phenomena based on the full hydrodynamic equations appears formidable. However, as we demonstrate in this Letter, the role of turbulent fluctuations for pattern formation can be conceptually clarified by analyzing a much simpler, analytically tractable problem. We investigate a general class of pattern forming systems, in which the order parameter field is advected by a Kraichnan-Kazantsev velocity field [156, 157]—a spatially correlated, white-in-time Gaussian field. Advection problems involving such fields have unveiled the role of small-scale fluctuations on the dynamo effect [157], and led to a better understanding of passive scalar turbulence (see [158] for a review). Coupling such a random advection field to a pattern-forming order parameter field allows us to analytically quantify its impact on the onset as well as the length scales of the emerging patterns. As a prototypical model for the emergence of large-scale patterns in convection, we illustrate our findings at the example of the Swift-Hohenberg (SH) equation [66], which we generalize to feature random advection. We find that random advection shifts the onset of pattern formation and effectively increases the pattern’s wavelength by turbulent diffusion, offering a qualitative explanation for recent observations in turbulent RBC [30, 31].

To start with, we consider a scalar order parameter field $\theta(\mathbf{x}, t)$ that exhibits pattern formation in two dimensions. Its nondimensionalized evolution equation takes the form

$$\partial_t \theta + \mathbf{u} \cdot \nabla \theta = \mathcal{L}[\nabla] \theta + \mathcal{N}[\theta, \nabla]. \quad (4.1)$$

Here, \mathcal{L} and \mathcal{N} denote linear and nonlinear operators, respectively. Additionally, the order parameter field is advected by a two-dimensional, zero-mean Gaussian velocity field $\mathbf{u}(\mathbf{x}, t)$ which is white in time and incompressible. As the Kraichnan-Kazantsev velocity field acts as a multiplicative advective noise, the resulting equation is a stochastic partial differential equation, which we interpret in the Stratonovich sense [159]; i.e., the velocity field is considered as rapidly varying in time in the limit of vanishing correlation time. The Gaussian random field has the correlation structure $\langle u_i(\mathbf{x}, t) u_j(\mathbf{x}', t') \rangle = R_{ij}(\mathbf{x} - \mathbf{x}') \delta(t - t')$, where the spatial covariance tensor takes the form $R_{ij}(\boldsymbol{\rho}) = 2Q [f(\boldsymbol{\rho}) \delta_{ij} + \varrho [\partial_{\boldsymbol{\rho}} f(\boldsymbol{\rho})] \{ \delta_{ij} - \hat{\rho}_i \hat{\rho}_j \}]$ as the result of homogeneity ($\boldsymbol{\rho} = \mathbf{x} - \mathbf{x}'$), isotropy, and incompressibility. Here, Q is the amplitude of the fluctuations, and f denotes the longitudinal velocity correlation function with $f(0) = 1$.

Within this setting, analytical statements can be made for the ensemble-averaged field. To obtain such a description, we average Eq. (4.1) with respect to realizations of the random advection. The mean advection term can be evaluated using the Furutsu-Donsker-Novikov identity (or Gaussian integration by parts) [160–162]:

$$\partial_i \langle u_i(\mathbf{x}, t) \theta(\mathbf{x}, t) \rangle = \partial_i \int d\mathbf{x}' R_{ij}(\mathbf{x} - \mathbf{x}') \left\langle \frac{\delta \theta(\mathbf{x}, t)}{\delta u_j(\mathbf{x}', t)} \right\rangle. \quad (4.2)$$

The mean response function is readily evaluated from the integral representation of Eq. (4.1) resulting in $\langle \delta \theta(\mathbf{x}, t) / \delta u_j(\mathbf{x}', t) \rangle = -\frac{1}{2} \delta(\mathbf{x} - \mathbf{x}') \partial_j \langle \theta \rangle$. Therefore, we obtain

$$\langle \mathbf{u}(\mathbf{x}, t) \cdot \nabla \theta(\mathbf{x}, t) \rangle = -Q \Delta \langle \theta \rangle(\mathbf{x}, t), \quad (4.3)$$

where $\Delta = \nabla^2$. On the level of the averaged field, only the random advection amplitude, and not the shape of the correlation function, plays a role. As a result, the averaged equation takes the form

$$\partial_t \langle \theta \rangle = (\mathcal{L}[\nabla] + Q \Delta) \langle \theta \rangle + \langle \mathcal{N}[\theta, \nabla] \rangle. \quad (4.4)$$

The important implication of this result is that the advection term contributes linearly to the averaged equation, adding an additional “turbulent” diffusion. This means that eddy-diffusivity type closures, which have been proposed phenomenologically for RBC (see, e.g., [27]),

are exact for Kraichnan-Kazantsev velocity fields. Considering an ensemble-averaged field is only meaningful if a stationary large-scale pattern is achieved as its amplitude otherwise decays over time. As detailed in the Supplemental Material [163], this exact result based on ensemble averaging can be generalized to temporal coarse-graining, provided the coarse-graining scale is large compared to the scales of the random fluctuations but still smaller than the scales of the pattern formation. As a result, order parameter fields which vary slowly in time are also captured by this theoretical result.

To continue, we decompose the order parameter field into mean and fluctuations, $\theta = \langle \theta \rangle + \theta'$. If the random advection is comparably small in scale and amplitude, the assumption $\langle \mathcal{N}[\theta, \nabla] \rangle \approx \mathcal{N}[\langle \theta \rangle, \nabla]$ can be justified on the basis that the averages involving the fluctuations are small compared to the averaged field. This leads to a closed equation for the averaged field. The validity of this assumption is explicitly tested with simulations below, see Fig. 4.3. If fluctuations around the averaged field need to be taken into account, they potentially yield additional linear and nonlinear contributions which can be treated separately.

We proceed with a linear stability analysis by Fourier-expanding the averaged field. As is evident from Eq. (4.4), the linear dispersion relation acquires an additional term $-Qk^2$, which shifts the position of the maximal linear growth rate. This can be made more transparent at the example of type-I and type-II instabilities [49, 50]. Both are characterized by a control parameter ϵ and a maximum-growth wave number k_c . For type-I instabilities, as in RBC, the linear dispersion relation is locally parabolic around the maximum-growth wave number. In the presence of random advection, the real part of the linear growth rate σ_k takes the nondimensionalized form $\text{Re}(\sigma_k) \approx \epsilon - (k - k_c)^2 - Qk^2$. As a result, the critical control parameter is shifted from $\epsilon_c = 0$ to $\epsilon_c = k_c^2 Q / (1 + Q)$, and the critical wave number is shifted to a lower value $k_c^* = k_c / (1 + Q)$. For type-II instabilities, as they, for example, occur for conserved order parameters, the growth rate takes the form $\text{Re}(\sigma_k) \approx \epsilon k^2 - k^4 / 2 - Qk^2$, which shifts the critical control parameter from $\epsilon_c = 0$ to $\epsilon_c = Q$ and implies a shifted maximum-growth wave number of $k_c^* = \sqrt{\epsilon - Q}$. A sketch of the two types of instabilities is shown in Fig. 4.2, which illustrates the effect of the fluctuations. As is evident from these considerations, random advection reduces the maximal linear growth rate and the corresponding wave number. For sufficiently strong advection, the onset of pattern formation can even be suppressed. The next step is a weakly nonlinear analysis in terms of amplitude equations. Provided the contributions

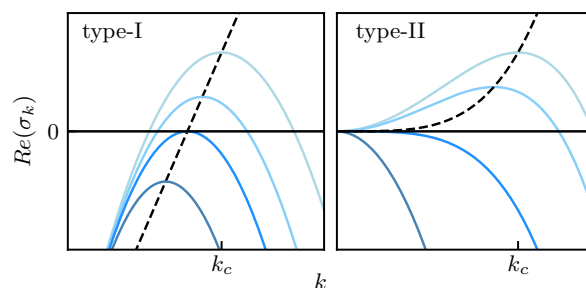


Figure 4.2: Effect of random advection on type-I (left) and type-II (right) instabilities. As the random advection amplitude Q is increased (from light to dark blue) for a fixed r , both the maximum growth rate and the corresponding wave number of the linear dispersion relation are shifted. Here, k_c denotes the maximum-growth wave number of the case without advection ($Q = 0$). The dashed line shows the maximum growth rate as a function of k and Q .

of the fluctuations to the averaged equation are small, the structure of the amplitude equations is identical to the case without random advection, only the control parameter and the wave number need to be renormalized. Note that, depending on the specific model, the nonlinear pattern formation does not necessarily select the linearly predicted wave number [49]. In such cases, a more elaborate analysis is necessary.

To provide a concrete example relevant for convection and to further corroborate the analytical results, we investigate a generalized SH equation with random advection. The original SH equation has been introduced to model the onset of convection in the midplane of RBC in terms of an order parameter field, which can be interpreted as a linear combination of the temperature fluctuations and the vertical velocity [66]. Although dramatically simplified compared to the Oberbeck-Boussinesq equations, it features the same type of instability and amplitude equations when only the slowest evolving modes of the full problem are considered [101, 102]. By including random advection, we introduce a model for the fast, turbulent modes to the dynamics. The main motivation for this approach is the observation that the time-averaged patterns in the turbulent regime in RBC are reminiscent of the patterns close to onset, despite the presence of fluctuations [27, 30, 31]. Therefore the underlying assumption is that a description in terms of an order parameter field, superposed by fluctuations, remains valid in the turbulent case. As we will see in the following, such a simple model suffices to conceptually explain recent observations on turbulent superstructures [22, 27, 30, 31]. Suitably nondimensionalized, the SH equation with random advection takes the form

$$\partial_t \theta + \mathbf{u} \cdot \nabla \theta = [r - (\Delta + 1)^2] \theta - \theta^3. \quad (4.5)$$

Here, r denotes the control parameter, which effectively models the Rayleigh number. In this nondimensionalization $k_c = 1$, i.e. $\lambda_c = 2\pi/k_c = 2\pi$. For the longitudinal velocity correlation we choose $f(\varrho) = \exp[-\pi\varrho^2/(4\lambda^2)]$ for simplicity. Therefore, the fluctuations are characterized by a single length scale λ . Alternative choices, e.g., correlation functions corresponding to velocity fields with inertial-range scaling, are also possible. The spatial scales of the random fluctuations should be significantly smaller than the length scale of the large-scale pattern formation. Therefore, we choose $\lambda = \lambda_c/10$, which implies a scale separation, consistent with RBC in the soft-turbulence regime [22].

Assuming that the unclosed terms are small, we obtain the averaged equation

$$\partial_t \langle \theta \rangle \approx \left[r^* - (\Delta + k_c^{*2})^2 \right] \langle \theta \rangle - \langle \theta \rangle^3. \quad (4.6)$$

In this approximation, the averaged equation takes exactly the form of the SH equation without advection, however, with renormalized control parameter and critical wave number. Consistent with the above discussion on the effects of random advection on type-I instabilities, we obtain a growth rate of $\sigma_k = r - (k^2 - 1)^2 - Qk^2$, which implies a shifted critical wave number $k_c^* := \sqrt{1 - Q/2}$ and a shifted control parameter $r^* := r - Q + Q^2/4$. Corrections due to non-negligible fluctuations can be introduced by inclusion of the terms proportional to $\langle \theta^2 \rangle$ and $\langle \theta^3 \rangle$, which require additional closure. This can become necessary, for example, in the absence of scale separation between the random fluctuation and the large-scale pattern, leading to a breakdown of the approximation $\langle \mathcal{N}[\theta, \nabla] \rangle \approx \mathcal{N}[\langle \theta \rangle, \nabla]$. We characterize these limitations in the Supplemental Material [163].

The emergence of a pattern in the averaged field can be investigated by a single-mode amplitude equation which is readily derived from Eq. (4.6) with the ansatz $\langle \theta \rangle(\mathbf{x}, t) = A(t)e^{ik_c^* \cdot \mathbf{x} + \text{c.c.}}$,

where the direction of the renormalized wave vector \mathbf{k}_c^* is arbitrary. The amplitude equation takes the form $\dot{A}(t) = r^*A(t) - 3|A(t)|^2A(t)$, which has the usual stationary solutions $|A(t)| = 0$ for $r^* < 0$ and $|A(t)| = \sqrt{r^*/3}$ for $r^* \geq 0$, just with a renormalized control parameter. This implies that the bifurcation curves for different random advection amplitudes can be collapsed on one master curve, a prediction which we verify with simulations.

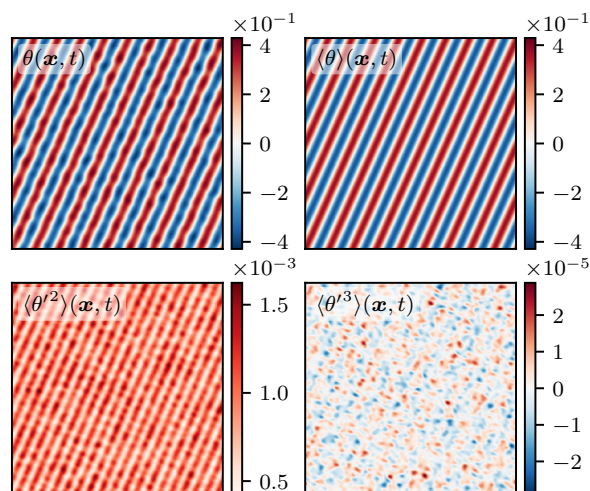


Figure 4.3: Formation of a stripe pattern in the Swift-Hohenberg equation with random advection. Single realization (top left), ensemble-averaged field (top right), mean squared fluctuations (bottom left) and mean cubed fluctuations (bottom right) from simulations of Eq. (4.5) in the statistically stationary state. Parameters are $\lambda = \lambda_c/10$, $Q = 0.1$, and $r = 0.2$. The simulations have been conducted on a periodic domain with $L = 20\pi$ on a 256×256 grid. A comparison of the field amplitudes shows that the fluctuations are negligible compared to the averaged field.

To this end, we rewrite Eq. (4.5) in its Itô formulation by applying the Itô drift correction formula [164] and solve it by means of a pseudospectral method with a semi-implicit Itô integrator for time stepping [159] with $\Delta t = 0.1$. Figure 4.3 shows an example realization with $\lambda = \lambda_c/10$, $Q = 0.1$, and $r = 0.2$ along with the ensemble-averaged field and the mean squared and mean cubed fluctuations. The results for the ensemble-averaged field have been obtained by initializing 192 simulations of Eq. (4.5) with identical initial conditions and letting them evolve with different realizations of the random advection field. Here, the initial conditions are stripe patterns with wave number k_c^* , which we let evolve under random advection to a statistically stationary state before we perform our analysis. While the realization and the averaged field are similar in amplitude, the unclosed terms involving fluctuations are orders of magnitude smaller, which gives an *a posteriori* justification for neglecting them in Eq. (4.6).

The theoretical predictions for the bifurcation in the presence of random advection are tested in Fig. 4.4. Plotted against the original, uncorrected order parameter, the onset of a large-scale pattern is shifted towards larger values of the control parameter. Renormalizing the control parameter confirms our theoretical result that the bifurcation scenario can be mapped onto the master curve $\sqrt{\langle \theta \rangle^2} = \sqrt{2r^*/3}$, where the overbar denotes spatial averaging. The factor of 2 compared to the amplitude equation result is a consequence of spatially averaging the order parameter field.

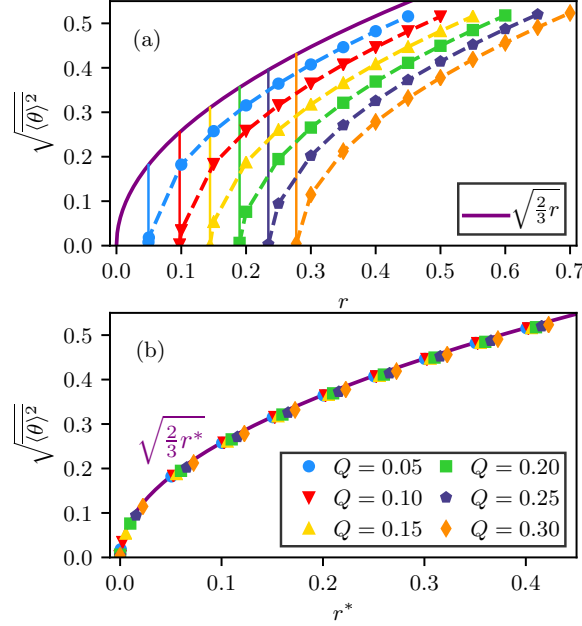


Figure 4.4: (a) Root mean squared amplitude in stationary state as a function of control parameter r for varying amplitude Q of the random advection field. All other simulation parameters are chosen as in Fig. 4.3. Compared to the bifurcation curve without random advection (purple line), the onset is shifted. The theoretically predicted shift of onset (indicated with vertical lines) agrees well with the numerical results. (b) For the renormalized control parameter r^* , all cases collapse on the theoretically predicted master curve.

So far, the theoretical discussion has focused on the averaged order parameter field. To test the predicted wave-number shift for a wider range of random advection amplitudes and to establish its validity beyond the ensemble with identical initial conditions, we investigate the randomly advected SH system significantly above onset ($r = 0.9$) with random initial conditions. Figure 4.5 demonstrates excellent agreement of the theoretically predicted wave-number shift with simulation results. Analogous to the procedure established for RBC in [30], the average wave number is obtained from the simulations from time-averaged spectra in the statistically stationary state, which corroborates that the characteristic shift is a feature of the individual realizations. This is also confirmed by the sample visualizations for various random advection amplitudes shown in the insets.

In conclusion, we have investigated the implications of random advection in the form of a Kraichnan-Kazantsev velocity field on a general class of pattern formation systems. We have shown that both the onset as well as the maximum-growth wave number are shifted in the presence of such fluctuations, which effectively introduce a turbulent diffusion. This effect is a direct consequence of the random advection and cannot be generated by standard additive or multiplicative noise.

Motivated by recent observations of turbulent superstructures in RBC, we investigated a generalized SH equation with random advection to mimic the impact of small-scale turbulent fluctuations on the emergence of large-scale patterns. Sufficiently close to onset, the bifurcations for various random advection amplitudes can be collapsed onto one master curve if

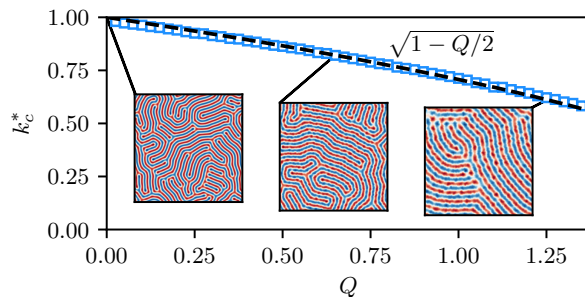


Figure 4.5: Numerically obtained dominant wave number of the individual realizations (blue squares, simulations with $L = 40\pi$ on a 512×512 grid with $\lambda = \lambda_c/10$ and $r = 0.9$) shown along with the theoretically predicted shifted critical wave number k_c^* (dashed black line). As an illustration, the insets show individual realizations (scaled to unit maximum amplitude) for different Q .

the control parameter and the critical wave number are renormalized. We also confirmed our theoretical prediction of a renormalized critical wave number significantly above onset.

Let us briefly set our findings into the context of previous work on stochastic SH models. Additive noise, which has previously been considered [66, 165, 166], for example, to account for the impact of thermal fluctuations, does not yield any contribution on the level of the averaged equation. Multiplicative noise in the form of a fluctuating control parameter leads to a variety of effects [167]: For example, García-Ojalvo et al. [168] observed a noise-induced onset of pattern formation, i.e. an effective shift of the critical control parameter to smaller values, for noise which rapidly fluctuates in space and time. For spatially constant multiplicative noise, on-off intermittency [169, 170] has been observed in SH models [171]. Random advection to model turbulent fluctuations, as considered here, adds a fundamentally different aspect: The critical wave number of the arising pattern is shifted to smaller values, and the critical control parameter is shifted to larger ones.

In RBC, the Reynolds number is a function of the Rayleigh number and the Prandtl number [57, 59]. In contrast to that, the control parameters r (modeling the Rayleigh number) and Q (amplitude of turbulent fluctuations) can be varied independently in our model. This allowed the detailed investigation of the role of fluctuations on the emergence of patterns, which cannot be directly studied in RBC. With turbulent diffusion leading to a larger wavelength of the emerging pattern, our model offers a qualitative explanation for the wavelength growth of the turbulent superstructures with an increasing Rayleigh number [30, 31, 61]. Therefore, the presented results may guide future quantitative investigations of the role of turbulent fluctuations in RBC and other turbulent flows with emergent large-scale patterns.

Acknowledgments This work is supported by the Priority Programme SPP 1881 Turbulent Superstructures of the Deutsche Forschungsgemeinschaft. We thank Wouter J. T. Bos, Ragnar Fleischmann, Martin James and Stephan Weiss for helpful discussions and the anonymous referees for their comments, which helped to improve the manuscript.

G.I. and G.G. contributed equally to this work.

4.2 Supplemental Material

In this Supplemental Material, we discuss a generalization of the ensemble averaging approach presented in the main text to running time averages, which allows the application to slowly evolving patterns. Furthermore, we provide more insights into the limitations of our approach.

Generalization to time averaging

In the following, we show numerically that the same results as for the ensemble average can be obtained using a running time average. This allows us to extend our analysis to large-scale patterns that vary slowly in time. This is an important generalization since turbulent superstructures, e.g., in Rayleigh-Bénard convection, also slowly evolve with time [27, 30]. Here, we limit ourselves to the Swift-Hohenberg equation with random advection since the generalization to other pattern-forming systems is straightforward.

To start with, we introduce the time-averaged order parameter field

$$\langle \theta \rangle_T(\mathbf{x}, t) = \frac{1}{T} \int_{t-T/2}^{t+T/2} \theta(\mathbf{x}, s) ds. \quad (\text{S1})$$

Here, T is the time scale over which the running average is taken. In order to remove the fluctuations, T has to be chosen significantly larger than their characteristic time scale. Time-averaging Eq. (5) from the main text leads to

$$\partial_t \langle \theta \rangle_T + \nabla \cdot \langle \mathbf{u} \theta \rangle_T = [r - (\Delta + 1)^2] \langle \theta \rangle_T - \langle \theta^3 \rangle_T, \quad (\text{S2})$$

where we have used the incompressibility condition $\nabla \cdot \mathbf{u} = 0$. Because the random velocity field evolves rapidly in time (it is delta-correlated) while the large scales evolve slowly, we assume that the time average can be replaced by an ensemble average. This allows to apply the Furutsu-Donsker-Novikov identity [160–162], which, of course, leads to precisely the same evolution equation as for the case of the ensemble average.

Similar to the procedure discussed in the main text, the order parameter field can be decomposed into its mean and fluctuations, $\theta = \langle \theta \rangle_T + \theta'$. For the cases considered, one can confirm from the simulations that the unclosed fluctuations in Eq. (S2), originating from the cubic nonlinearity in the Swift-Hohenberg equation, are small compared to the time-averaged field (see also discussion in the following section). This justifies $\langle \theta^3 \rangle_T \approx \langle \theta \rangle_T^3$, and, therefore, we obtain

$$\partial_t \langle \theta \rangle_T \approx [r^* - (\Delta + k_c^{*2})^2] \langle \theta \rangle_T - \langle \theta \rangle_T^3, \quad (\text{S3})$$

where $r^* = r - Q + Q^2/4$. As a result, the following analysis is analogous to the one presented in the main text. Accordingly, we find that the onset is shifted from $r_c = 0$ to $r_c = Q - Q^2/4$ and that the critical wave number is reduced to $k_c^* = \sqrt{1 - Q/2}$. For the amplitude, we also obtain $\sqrt{\langle \theta \rangle_T^2} = \sqrt{2r^*/3}$, as expected. To verify this result, we perform simulations like the ones presented in the main text with $N_x = N_y = 256$, $L = 20\pi$, and $\Delta t = 0.1$. The averaging window is $T = 500$, and the time difference is $\Delta s = 1$ between snapshots for the evaluation of Eq. (S1). In contrast to the simulations in the main text, these simulations are started from random initial conditions instead of an ideal stripe pattern. It is important to note that the temporal averaging window has to be chosen carefully. It has to be long enough in order to remove the small-scale fluctuations but significantly shorter than the time scale on

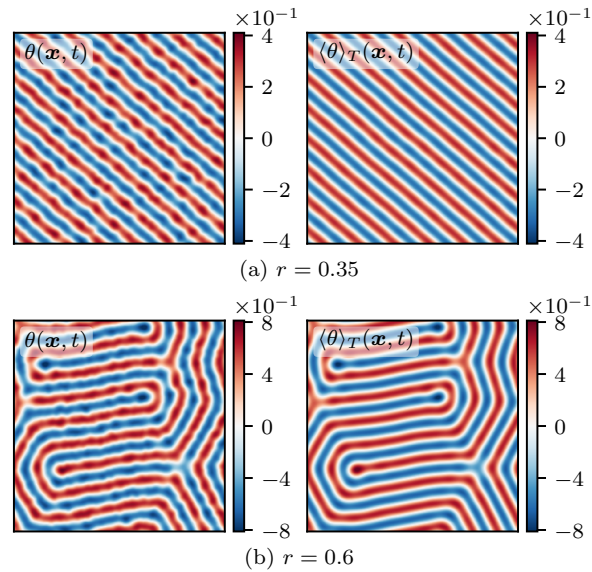


Figure S1: Formation of a large-scale pattern in the Swift-Hohenberg equation with random advection. Single realization (left), time-averaged field (right). Parameters are $\lambda = \lambda_c/10$, $Q = 0.3$, (a) $r = 0.35$ and (b) $r = 0.6$. The simulations are conducted on a periodic domain starting from random initial conditions. Because of the random initial condition, a complex large-scale pattern emerges in (b).

which the large-scale pattern evolves. This is similar to the procedure applied to Rayleigh-Bénard convection [27, 30]. Example snapshots and averaged fields for different r are shown in Fig. S1. Even when started from random initial conditions, a non-vanishing large-scale pattern emerges in the time-averaged field. We then obtain the full bifurcation diagram from time-averaged simulations and confirm that it matches the theoretical prediction, see Fig. S2. Compared to the theoretical expectation, only minor deviations can be seen due to the random initial conditions. Therefore, we conclude that our findings can be generalized to running time averages of fields with slowly evolving large scales.

Limitations of the approach

In this section, we discuss the limitations of our approach. To this end, consider the approximation made in the main text:

$$\langle \mathcal{N}[\theta, \nabla] \rangle \approx \mathcal{N}[\langle \theta \rangle, \nabla]. \quad (\text{S4})$$

Here, $\langle \cdot \rangle$ denotes an ensemble average. When we introduce the decomposition $\theta = \langle \theta \rangle + \theta'$ and average the Swift-Hohenberg equation with random advection, we obtain

$$\partial_t \langle \theta \rangle = \left[r^* - \left(\Delta + k_c^{*2} \right)^2 \right] \langle \theta \rangle - \langle \theta^3 \rangle, \quad (\text{S5})$$

where

$$\langle \theta^3 \rangle = \langle \theta \rangle^3 + 3 \langle \theta'^2 \rangle \langle \theta \rangle + 3 \langle \theta' \rangle \langle \theta \rangle^2 + \langle \theta'^3 \rangle. \quad (\text{S6})$$

The term $3 \langle \theta' \rangle \langle \theta \rangle^2$ vanishes because $\langle \theta' \rangle = 0$, but $3 \langle \theta'^2 \rangle \langle \theta \rangle$ and $\langle \theta'^3 \rangle$ remain. However, as

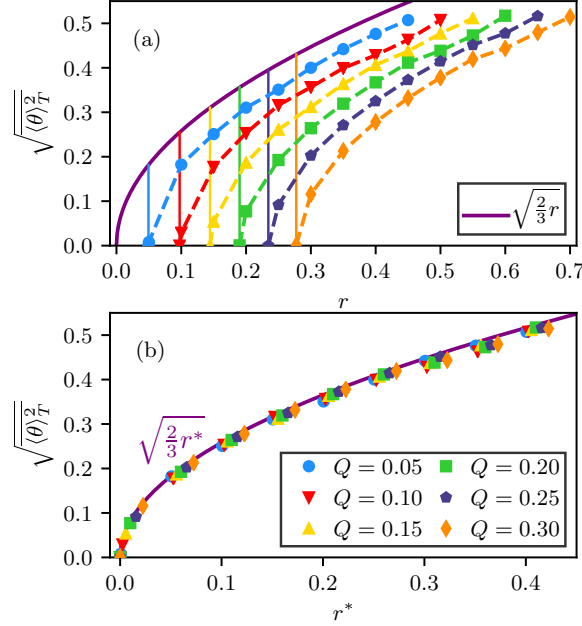


Figure S2: (a) Root mean squared amplitude of the time-averaged order parameter field in the stationary state as a function of control parameter r for varying amplitude Q of the random advection field. (b) For the renormalized control parameter r^* , all cases collapse on a master curve, matching the theoretically predicted curve very well.

illustrated in Fig. 2 of the main text, these terms are very small in all cases of relevance, which justifies our approximation (S4). This is also reflected in the remarkable overall agreement between the theoretical prediction and the numerical results in Fig. 3 of the main text as well as in Fig. S3. Compared to the main text, Fig. S3(c) additionally shows a zoom into the region very close to onset whereas panels (a) and (b) are identical to Fig. 3.

Deviations close to onset The root mean squared amplitude of the averaged field is $\sqrt{2r^*/3}$ and, therefore, is small itself close to onset. This may very well lead to the breakdown of the approximation (S4) as the previously neglected fluctuation terms gain importance. To check the validity of the approximation close to the bifurcation point ($r_c^* = 0$), we map out the bifurcation diagram in this regime, which is presented in Fig. S3(c). Minor systematic deviations can be observed. For small random advection amplitudes, these can be accounted for by including the neglected fluctuations. However, given the still excellent agreement, we choose to apply the approximation (S4) which leads to a closed equation for the averaged field and allows to derive the renormalized control parameter and wave number in a predictive manner.

More generally, the breakdown of our ensemble averaging approach is reflected by the fact that a stationary non-vanishing averaged field does not develop. As illustrated by Fig. S4(a), this is the case very close to onset for $Q = 0.3$. Here, a slow decay of the averaged field's amplitude can be observed. However, this is only the case for the largest amplitudes of the random advection field and very close to onset, where the amplitude of the order parameter field is small. For smaller Q , the amplitude is stationary even close to onset, see Fig. S4(b)

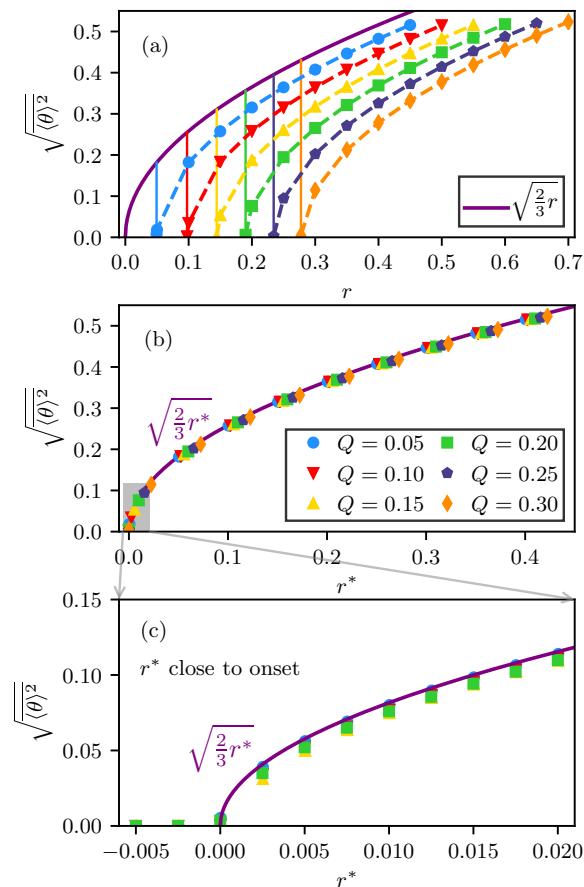


Figure S3: Root mean squared amplitude of the ensemble-averaged field as a function of (a) r and (b) r^* . Panels (a) and (b) are identical to Fig. 3 in the main text. Panel (c) shows a zoom into the range close to onset with additional data from longer simulations, cf. Fig. S4. Simulation details are given in the main text.

for $Q = 0.1$. For the cases considered in our main text, the amplitude is stationary even close to onset. In Fig. S3(c), we only show data for random advection amplitudes Q , for which the root mean squared amplitudes of the ensemble-averaged fields are stationary for all r . As a result, we exclude the cases $Q = 0.3$ and $Q = 0.25$, for which the points corresponding to the two values of r^* directly above onset are not stationary.

Large velocity correlation length Finally, we briefly discuss the influence of the length scale λ (see main text for details) characterizing the correlation length of the velocity fluctuations. The approximation (S4) requires scale separation between fluctuations and the large-scale pattern. If this scale separation is absent, the unclosed terms in the averaged equation play a crucial role and cannot be neglected *a priori*. In extreme cases, stationary or slowly evolving large-scale patterns do not even develop. Different realizations then vary strongly and, therefore, cancel on average, prohibiting an application of our theoretical results. Indications for this can be seen in Fig. S5, in which a comparison for different length scales λ is shown. Here, the large-scale pattern smears out at large λ . In order to quantify the scale separation,

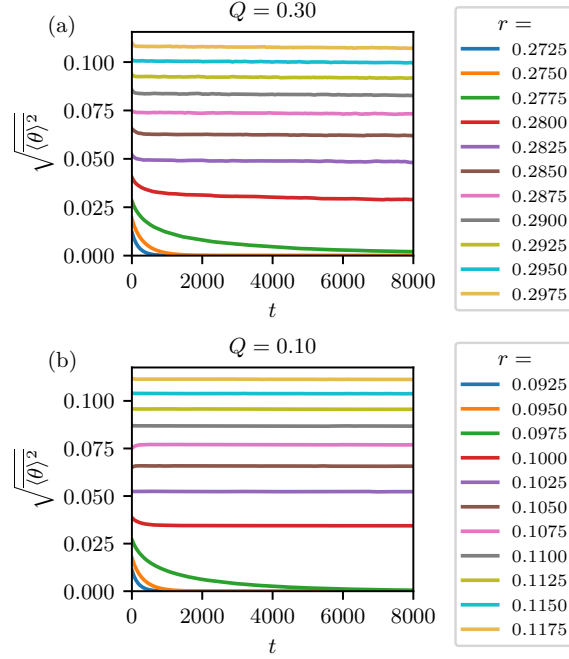


Figure S4: Time dependence of the root mean squared amplitude of the ensemble-averaged field for different r with (a) $Q = 0.3$ and (b) $Q = 0.1$ very close to onset from long-time simulations. (a) For large $Q = 0.3$, the amplitude of the unclosed fluctuations is not small compared to the order parameter field. Here, an extremely slow decay of the amplitude of the averaged field can be observed. The three curves with the fastest decay correspond to the cases for which $r^* \leq 0$, in agreement with our theoretical prediction. (b) For small $Q = 0.1$, the mean amplitude does not decay over time for all parameters above onset. Only for the cases with $r^* \leq 0$, the amplitudes decay, as expected.

we compare the azimuthally averaged spectrum $S(k)$ of θ with $E(k)$, the prescribed spectrum of the Gaussian random velocity field, in Fig. S5. The spectra $S(k)$ show a single peak for all λ , but their width grows with λ . In contrast, the velocity spectrum $E(k)$ becomes narrower. For the smallest considered correlation length λ , the peak of the spectrum of θ is at k_c^* , separated from the peak of $E(k)$ at much larger wave numbers. Here, a stationary large-scale pattern emerges. This illustrates how scale separation between the large-scale pattern and the most intense small-scale fluctuations is essential.

To summarize, in this Supplemental Material we have shown that our results are not limited to the case of ensemble averaging, but also hold for running time averages. Additionally, we have provided insights into the limitations of our approach and showed that it only starts to fail very close to onset and for a large correlation length of the random velocity field.

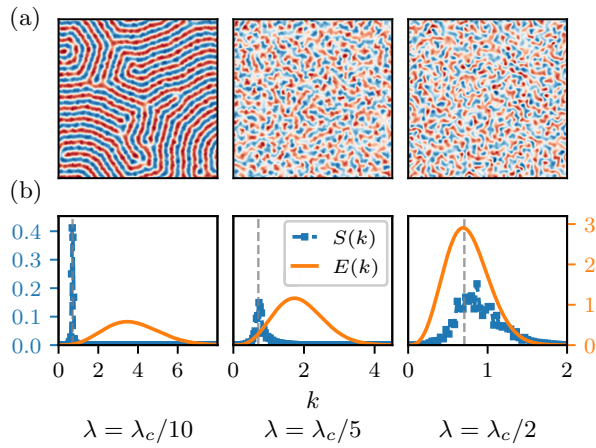


Figure S5: (a) Realization of θ (scaled to unit maximum amplitude) for $r = 0.9$, $Q = 1.0$, and different λ . With increasing length scale, the fluctuations suppress the emergence of a large-scale pattern. (b) Corresponding azimuthally averaged spectrum $S(k)$ of θ compared to the energy spectrum $E(k)$ of the Gaussian random velocity field. A clear scale separation between the spectra is visible for $\lambda = \lambda_c/10$, which vanishes with increasing λ . The theoretical expectation for the location of the peak, k_c^* , is indicated by the dashed line. For the largest length scale λ , we observe a deviation of the peak from the theoretical expectation. Simulations are performed on a 512×512 grid with $L = 40\pi$ and started from random initial conditions.

4.3 Additional supplementary information

In order to complete the documentation of the results in Ibbeken et al. [68], I provide further information on the methods here. The following has already been documented in Ibbeken [149], which is, however, not published. This complements the supplementary material from the previous section published alongside the original paper [68].

4.3.1 Numerical methods

There are two parts in the article, which may need further clarification. First, we need to supplement the numerical simulations with a Gaussian random field which is white in time. The form is prescribed by the theoretical analysis and, here, we document the implementation. Second, the numerical procedure is given in detail.

4.3.1.1 Generation of the random field

Our model is built to study the effect of small-scale fluctuations on a large-scale pattern and motivated by the observation of superstructures in turbulent RBC. For an introduction to turbulence, I refer the reader to Davidson [46], Pope [47], Sagaut and Cambon [78], Bailly and Comte-Bellot [172]. The random velocity field should represent a two-dimensional incompressible homogeneous isotropic velocity field, which requires a statistical description. Here, I only focus briefly on the relevant aspects.

A specific function which characterizes the randomness in space and time is the correlation

$$\langle u_i(\mathbf{x}, t) u_j(\mathbf{x}', t') \rangle.$$

In our model this takes the form

$$\langle u_i(\mathbf{x}, t) u_j(\mathbf{x}', t') \rangle = R_{ij}(\mathbf{x} - \mathbf{x}') \delta(t - t'), \quad (4.7)$$

where $R_{ij}(\mathbf{x} - \mathbf{x}')$ contains information about the spatial correlation. In the case of a two-dimensional homogeneous isotropic field, the two-point correlation is fully determined by a single scalar function [46]

$$R_{ij}(\boldsymbol{\varrho}) = 2Q [f(\varrho) \delta_{ij} + \varrho [\partial_{\varrho} f(\varrho)] \{\delta_{ij} - \hat{\varrho}_i \hat{\varrho}_j\}],$$

in which Q characterizes the amplitude of the fluctuations and $\boldsymbol{\varrho} = \mathbf{x} - \mathbf{x}'$. Here, $f(\varrho)$ is the longitudinal velocity correlation function [47]

$$f(\varrho) = \frac{R_{11}(\hat{\mathbf{e}}_1 \varrho)}{R_{11}(\mathbf{0})}.$$

The two-point correlation is directly related to its spectrum [46, 47, 172] by a Fourier transformation, which gives a simpler description in terms of a scalar function. First, we start with the spectrum tensor

$$\phi_{ij}(\mathbf{k}) = \frac{1}{(2\pi)^2} \int_{-\infty}^{\infty} \int_{-\infty}^{\infty} d^2 \varrho R_{ij}(\boldsymbol{\varrho}) \exp \{-i\mathbf{k} \cdot \boldsymbol{\varrho}\}.$$

From this, the spectrum is obtained by removing all directional information

$$E(k) = \oint \frac{1}{2} \phi_{ii}(\mathbf{k}) dS(k),$$

in which the integral is over the surface of a sphere with radius k [47], respectively a circle in two dimensions. For a two-dimensional homogeneous isotropic velocity field this results in [172]

$$\begin{aligned} \phi_{ij}(\mathbf{k}) &= \frac{E(k)}{\pi k} \left(\delta_{ij} - \frac{k_i k_j}{k^2} \right) \\ E(k) &= \pi k \phi_{ii}(\mathbf{k}). \end{aligned}$$

Therefore, we only need to choose $f(\varrho)$ to fix the spatial correlation and subsequently the spectrum. With the given $f(\varrho) = \exp[-\pi\varrho^2/(4\lambda^2)]$, straightforward calculations results in

$$E(k) = \frac{4\lambda^4 Q}{\pi^2} k^3 \exp\left\{-k^2 \lambda^2 / \pi\right\}.$$

From this, we can calculate

$$E = \int dk E(k) = 2Q,$$

which shows that the parameter Q indeed characterizes the amplitude of the fluctuations. From $E(k)$ we can generate a Gaussian random field \mathbf{v} numerically with the prescribed spatial correlation R_{ij} in the following way [149]

$$\begin{pmatrix} \hat{v}_x \\ \hat{v}_y \end{pmatrix}(\mathbf{k}) = \sqrt{\frac{4\pi}{kL^2} E(k)} \frac{1}{k} \begin{pmatrix} k_y \\ -k_x \end{pmatrix} X_1, \quad (4.8)$$

where X_1 is a complex Gaussian random number with zero mean and standard deviation $\sigma_{X_1} = 1$, L is the length of the system, and $\hat{\mathbf{v}}(\mathbf{k})$ is the discrete Fourier transform of the random field. Since the field is real, the Fourier transformation has to be Hermitian, which has to be prescribed in the numerical implementation. The random field is obtained by an inverse Fourier transform and is automatically incompressible and Gaussian through this implementation. The resulting field can be tested by, e.g., computing

$$E = \left\langle \frac{\mathbf{v}^2}{2} \right\rangle \stackrel{!}{=} 2Q.$$

This random field has to be generated at every time step independently, such that the field is white in time.

4.3.1.2 Pseudo-spectral simulation

The model (4.5) is a stochastic partial differential equation. I do not intend to give an introduction to stochastic partial differential equations (SPDEs) here, but refer the reader to Gardiner [159], Garcia-Ojalvo and Sancho [167], Paul and Baschnagel [173], and Øksendal [174]. I only consider an important subtlety which regards the interpretation of the stochastic

partial differential in the Stratonovich or the Itô sense. Note, however, that both formulations can be converted to each other. We start with our model

$$d\theta(\mathbf{x}, t) = f^S[\theta](\mathbf{x}, t)dt - \partial_j\theta(\mathbf{x}, t) \circ dU_j(\mathbf{x}, t) \quad (4.9)$$

$$f^S[\theta](\mathbf{x}, t) = [r - (\Delta + 1)^2]\theta - \theta^3, \quad (4.10)$$

which we interpret in the Stratonovich sense. This equation contains a multiplicative noise term $\partial_j\theta(\mathbf{x}, t) \circ dU_j(\mathbf{x}, t)$ for which \circ denotes the Stratonovich sense of a stochastic integral. It can be formally related to the velocity field \mathbf{u} as [159]

$$\int_0^t dt' \mathbf{u}(t') = \int_0^t d\mathbf{U}(t') \\ d\mathbf{U} = \mathbf{u}dt.$$

In contrast to the Itô interpretation, the mean of the multiplicative noise term in a Stratonovich SPDE does not vanish [167]. The results can, however, be mapped onto each other. Additionally, a significant difference is that in the Stratonovich sense the stochastic terms follow the usual rules of calculus. For the Itô interpretation, this is not the case. Therefore, the Stratonovich interpretation is especially useful for analytical calculations. However, the numerical simulation is typically more natural in the Itô interpretation. To numerically solve (4.5) we, hence, make use of a pseudospectral method with a semi-implicit Itô integrator for time stepping [159]. For this, we first need to apply the Itô drift correction formula to convert (4.9) to the Itô interpretation. For a random advection multiplicative noise the conversion is [164]

$$f^I[\theta](\mathbf{x}, t) = f^S[\theta](\mathbf{x}, t) + \frac{1}{2}\nabla \cdot (\mathbf{R}(\mathbf{0})\nabla\theta),$$

with $\mathbf{R} = (R_{ij})$. In its Itô formulation the equation then reads

$$d\theta(\mathbf{x}, t) = f^I[\theta](\mathbf{x}, t)dt - \partial_j\theta(\mathbf{x}, t)dU_j(\mathbf{x}, t) \\ f^I[\theta](\mathbf{x}, t) = f^S[\theta](\mathbf{x}, t) + Q\Delta\theta(\mathbf{x}, t),$$

with $R_{ij}(0) = 2Q\delta_{ij}$. Here, an additional linear term is present in contrast to the Stratonovich version. For the numerical solution of the above equation, we use the Gaussian fields \mathbf{v} introduced in the previous section. The full numerical time stepping scheme is

$$\hat{\theta}_{i+1} = (1 - \Delta t \hat{\mathcal{L}}^I[k])^{-1} \left[\hat{\theta}_i + \Delta t \mathcal{F} \{ \mathcal{N}[\theta_i] \} - \sqrt{\Delta t} \mathcal{F} \{ \mathbf{v} \cdot \nabla \theta_i \} \right], \\ \mathcal{N}[\theta_i] = -\theta_i^3 \\ \hat{\mathcal{L}}^I[k] = r - (1 - k^2)^2 - Qk^2,$$

in which \mathcal{F} and $\hat{\cdot}$ denote Fourier transformation. In this we used the Itô interpretation of the stochastic integral

$$\int_{t_i}^{t_{i+1}} d\mathbf{U} \cdot \nabla\theta = (\mathbf{U}_{i+1} - \mathbf{U}_i) \cdot \nabla\theta_i = \Delta\mathbf{U}_i \cdot \nabla\theta_i.$$

Similar to a Wiener process, the velocity increments are obtained as $\Delta \mathbf{U}_i = \mathbf{v} \sqrt{\Delta t}$, in which \mathbf{v} is a Gaussian random field with a prescribed spatial correlation $\langle v_i(\mathbf{x}) v_j(\mathbf{x}') \rangle = R_{ij}(\mathbf{x} - \mathbf{x}')$ and is obtained from (4.8) independently at each time step. In the numerical implementation the linear terms and derivatives are evaluated in Fourier space and the nonlinear terms in real space. To account for aliasing errors the 2/3–dealiasing rule [175] is used in Fourier space after each quadratic nonlinear multiplication, i.e. twice in the cubic nonlinearity. It is implemented with a mask

$$D_{ij} = \begin{cases} 1 & \text{for } k = \sqrt{k_i^2 + k_j^2} < 2/3 k_i^{\max} \\ 0 & \text{for } k \geq 2/3 k_i^{\max} \end{cases},$$

in which k_i^{\max} is the largest resolved wavenumber.

4.3.2 Furutsu-Donsker-Novikov identity

In the theoretical analysis of the modified Swift-Hohenberg equation, we make use of ensemble averaging the equation (4.1). Here, the calculation of the ensemble average of the advection term needs additional clarification. This term is evaluated with the Furutsu-Donsker-Novikov identity [160–162, 167], which results in (4.2). The functional derivative can be evaluated by formally solving eq. (4.1) by the integration

$$\theta(\mathbf{x}, t) = \theta(\mathbf{x}, 0) + \int_0^t ds [\mathcal{L}[\nabla]\theta + \mathcal{N}[\theta, \nabla] - u_k \partial_k \theta](\mathbf{x}, s), \quad (4.11)$$

where \mathcal{L} denotes the linear operator of the evolution equation. Thus, the functional derivative can be taken as

$$\begin{aligned} \frac{\delta \theta(\mathbf{x}, t)}{\delta u_j(\mathbf{y}, t)} &= \frac{\delta \theta(\mathbf{x}, 0)}{\delta u_j(\mathbf{y}, t)} + \int_0^t ds \frac{\delta}{\delta u_j(\mathbf{y}, t)} [\mathcal{L}[\nabla]\theta(\mathbf{x}, s) + \mathcal{N}[\theta, \nabla](\mathbf{x}, s)] \\ &\quad - \int_0^t ds \frac{\delta}{\delta u_j(\mathbf{y}, t)} [u_k(\mathbf{x}, s) \partial_k \theta(\mathbf{x}, s)]. \end{aligned} \quad (4.12)$$

The first term vanishes since the initial condition $\theta(\mathbf{x}, 0)$ is independent of the random field. The first integral vanishes for reasons of causality. To see this, we rewrite the expression as

$$\begin{aligned} &\lim_{t' \rightarrow t} \int_0^t ds \frac{\delta}{\delta u_j(\mathbf{y}, t')} [\mathcal{L}[\nabla]\theta(\mathbf{x}, s) + \mathcal{N}[\theta(\mathbf{x}, s), \nabla]] \\ &\stackrel{(*)}{=} \lim_{t' \rightarrow t} \left[\int_0^{t'} ds \underbrace{\frac{\delta}{\delta u_j(\mathbf{y}, t')} \{ \mathcal{L}[\nabla]\theta(\mathbf{x}, s) + \mathcal{N}[\theta(\mathbf{x}, s), \nabla] \}}_{=0 \text{ for } s < t'} \right] \\ &\quad + \int_{t'}^t ds \frac{\delta}{\delta u_j(\mathbf{y}, t')} \{ \mathcal{L}[\nabla]\theta(\mathbf{x}, s) + \mathcal{N}[\theta(\mathbf{x}, s), \nabla] \} = 0. \end{aligned} \quad (4.13)$$

In (*) the fact, that the field $\theta(\mathbf{x}, s)$ is independent of future realizations of the random field $\mathbf{u}(\mathbf{y}, t')$ is exploited and, therefore, the first integrand vanishes for $s < t'$. Afterwards we take the limit $t' \rightarrow t$ for which the second integral vanishes since the integrand is bounded. The second integral of (4.12) is evaluated by the product rule, giving

$$\begin{aligned}
 & - \int_0^t ds \left[\frac{\delta u_k(\mathbf{x}, s)}{\delta u_j(\mathbf{y}, t)} \partial_k \theta(\mathbf{x}, s) + u_k(\mathbf{x}, s) \frac{\delta \{\partial_k \theta(\mathbf{x}, s)\}}{\delta u_j(\mathbf{y}, t)} \right] \\
 &= - \int_0^t ds \delta_{jk} \delta(\mathbf{x} - \mathbf{y}) \delta(t - s) \partial_k \theta(\mathbf{x}, s) \\
 &= - \int_0^t ds \delta(t - s) \delta(\mathbf{x} - \mathbf{y}) \partial_j \theta(\mathbf{x}, s) = -\frac{1}{2} \delta(\mathbf{x} - \mathbf{y}) \partial_j \theta(\mathbf{x}, t).
 \end{aligned} \tag{4.14}$$

In eq. (4.14) the integrand's second summand vanishes, again, for reasons of causality. In the last step, evaluating Dirac's delta function at the integral's limits adds the factor of $\frac{1}{2}$. Inserting $R_{ij}(0) = 2Q\delta_{ij}$, we obtain (4.3)

$$\langle u_i \partial_i \theta \rangle(\mathbf{x}, t) = -\frac{1}{2} \partial_i \int d\mathbf{y} R_{ij}(\mathbf{x} - \mathbf{y}) \delta(\mathbf{x} - \mathbf{y}) \partial_j \langle \theta \rangle(\mathbf{x}, t) = -Q \partial_i^2 \langle \theta \rangle(\mathbf{x}, t).$$

Note that this result is identical to the average of the Itô drift correction. Therefore, consistently the resulting averaged equations are identical in the Itô and Stratonovich interpretation, since the mean of the multiplicative noise in the former case vanishes [167]. The result has already been given in (4.3) and this concludes the theoretical calculations presented in the main article.

Part III

Effective description of turbulent
superstructures

Height-averaged Oberbeck-Boussinesq equations

Abstract

The phenomena of turbulent superstructures cover a wide range of spatial and temporal scales ranging from turbulent fluctuations to coherent large-scale flows. Therefore, the study of superstructures is computationally very expensive and theoretically demanding. To gain insights into, e.g., their long time dynamics, reduced models offer the possibility of feasible (long time) investigations. However, the models need to quantitatively reproduce the correct behaviour. In this article, we develop a reduced model for turbulent superstructures in Rayleigh-Bénard convection in an *a priori* study. We average the governing equations over height to reduce the dimensionality and spatially coarse-grain to separate the turbulent fluctuations from the large-scale flow. For the resulting unclosed equations, we propose closure models based on theoretical arguments and observations from direct numerical simulations for a single Rayleigh number. Given an appropriately chosen coarse-graining scale, the closure models and the unclosed terms agree remarkably well overall. The resulting equations are evolution equations for the averaged temperature and vertical velocity in two dimensions, which are advected by a horizontal mean flow. This study paves the way to obtain a quantitative reduced model of turbulent superstructures in RBC.

5.1 Introduction

The phenomenon of turbulent superstructures is associated with a wide range of spatial and temporal scales, cf. Pandey et al. [30] and Krug et al. [35]. Turbulent fluctuations, which are small-scale and rapidly varying in time, are observed superposed to slowly evolving large-scale superstructures (figure 5.1a). Currently, theoretical and computational studies are, therefore, limited, because they are either very demanding or very expensive. To advance the understanding of turbulent superstructures, reduced models are promising. They may reduce the computational cost considerably and allow investigations on long time scales as well as facilitating the theoretical analysis. Yet, the models need to accurately represent the turbulent superstructures quantitatively and, at present, such a model does not exist.

In the previous part, we introduced a phenomenological model for turbulent superstructures in the horizontal directions, which qualitatively explains the increasing wavelength observed in

Rayleigh-Bénard convection. However, the model (4.5) does not make contact with the governing equations, the Oberbeck-Boussinesq equations, and, therefore, prohibits a quantitative study. In the following, we aim to obtain a reduced model from the fundamental governing equations to come closer to a quantitative description of turbulent superstructures. For this, we use the fact that superstructures extend through the whole cell, are roughly height independent [30, 35, 62, 63], and evolve on long time scales (compared to the small-scale fluctuations) [27, 30]. In the literature, there are suggestions to separate small and large scales with, e.g., asymptotic expansions [30] or mapping the flow back to onset of convection [27]. Here, we combine both ideas to derive a reduced model for turbulent superstructures. We average the OBEs over height to reduce the dimensionality and spatially coarse-grain to remove the fluctuations. This procedure reveals the regular two-dimensional large-scale pattern only, see figure 5.1 and, thus, maps the flow effectively closer to onset. However, due to the nonlinearity and

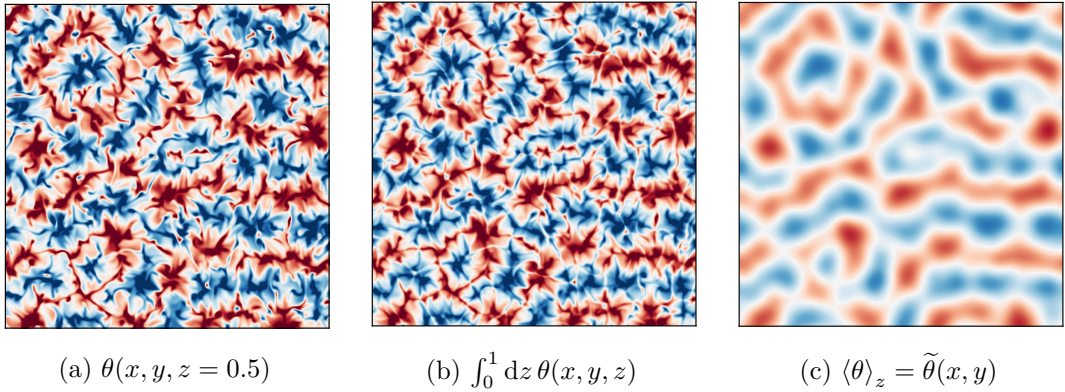


Figure 5.1: The full temperature field for $Ra = 1.02 \times 10^5$, $Pr = 1$ (a) shown in the midplane is (b) height-averaged and finally (c) filtered to reveal a two-dimensional large-scale pattern. A Gaussian filter with standard deviation $\sigma_l = \frac{\lambda_s}{8}$ is used. Here, λ_s is the superstructure size as described in chapter 3.

the solid top and bottom walls, the resulting equations contain unclosed terms that effectively capture the effect of the small-scale fluctuations. These terms need to be modelled to obtain a reduced description of superstructures. The elimination of the vertical coordinate has been employed with projection techniques to model RBC at onset [66, 82] resulting in (generalized) Swift-Hohenberg equations describing the temperature and vertical velocity in the midplane. They are described in section 2.4. Though, these models only capture RBC close to onset. In contrast, we consider the turbulent regime far away from onset. Let me note for completeness that so-called bulk averages are used in the atmospheric sciences. These are averages over the depth of the atmospheric boundary layer and, e.g., used to parametrize this layer in larger-scale models [176]. However, different from our RBC setup with a fixed height, the depth of the layer is a function of time and horizontal directions.

Outline In the following, we initially apply the averaging procedure to the OBEs and derive the averaged Oberbeck-Boussinesq equations. These equations are unclosed, and closure models are needed. Here, we split the averaged equations into different parts. Turbulent superstructures are present in the temperature and vertical velocity field. Therefore, we primarily focus on the evolution equations for these quantities. In this part, we propose closure models

for the unclosed terms in the averaged evolution equations based on theoretical arguments and insights from DNS. In contrast, we do not yet propose closures for the terms in the evolution equation of the horizontal velocity. Instead, we use a simplified model for the horizontal velocity field known from onset of convection [49, 53]. It is based on the observation that the dynamics of turbulent superstructures is reminiscent of SDC [27]. For SDC, a mean flow with respect to an average over height (see e.g. [50, 91–95]), i.e. a non-vanishing mean horizontal velocity field, has been shown to be important [58, 90]. Such a mean flow can be effectively described by linking it to the curvature of the large-scale pattern [49, 53] and we suggest to use such a model for turbulent superstructures as well. We then validate the proposed closure models quantitatively and study the dependence on time and the coarse-graining scale. The resulting reduced model is finally studied theoretically in terms of a linear stability analysis.

5.2 Derivation of averaged equation

To begin with, we apply the average to the full governing equations, the Oberbeck-Boussinesq equations. They describe the evolution of the velocity \mathbf{u} and temperature fluctuations θ and are given in non-dimensionalized form as [55]

$$\nabla \cdot \mathbf{u} = 0 \quad (5.1a)$$

$$\partial_t \mathbf{u} + \mathbf{u} \cdot \nabla \mathbf{u} = -\nabla p + \sqrt{\frac{Pr}{Ra}} \nabla^2 \mathbf{u} + \theta \hat{\mathbf{z}} \quad (5.1b)$$

$$\partial_t \theta + \mathbf{u} \cdot \nabla \theta = \frac{1}{\sqrt{RaPr}} \nabla^2 \theta. \quad (5.1c)$$

Here, p is the kinematic pressure including gravity, Pr the Prandtl number, and Ra the Rayleigh number. The average is given as

$$\tilde{q} \equiv \langle q \rangle_z(\mathbf{x}_h, t) = \int_A d^2 r_h G_l(\mathbf{r}_h - \mathbf{x}_h) \int_0^1 dz q(\mathbf{r}_h, z, t) = G_l * \int_0^1 dz q, \quad (5.2)$$

in which the subscript h denotes the horizontal directions and G_l is the filter kernel with filter width l . To keep the presentation simple, we use the notion \tilde{q} and $\langle q \rangle_z$ interchangeable as needed. For the numerical computations, we evaluate the height average with a trapezoidal rule [177] and choose a truncated Gaussian filter [178]. The filter width is given by its standard deviation σ_l

$$G_l(\mathbf{x}_h) = \frac{1}{N} \exp\left(-\frac{\mathbf{x}_h^2}{2\sigma_l^2}\right),$$

and N is a normalization constant such that $\int_A d^2 x_h G_l = 1$. If we apply the average to the OBEs we obtain

$$\langle \nabla \cdot \mathbf{u} \rangle_z = 0 \quad (5.3a)$$

$$\partial_t \langle \mathbf{u} \rangle_z + \langle \mathbf{u} \cdot \nabla \mathbf{u} \rangle_z = -\langle \nabla p \rangle_z + \langle \theta \rangle_z \hat{\mathbf{z}} + \sqrt{\frac{Pr}{Ra}} \langle \Delta \mathbf{u} \rangle_z \quad (5.3b)$$

$$\partial_t \langle \theta \rangle_z + \langle \mathbf{u} \cdot \nabla \theta \rangle_z = \frac{1}{\sqrt{PrRa}} \langle \Delta \theta \rangle_z. \quad (5.3c)$$

In the following, we consider the different terms individually and focus on the nonlinear terms as well as vertical derivatives. Before we continue, the equations need to be supplemented with boundary conditions. We use

$$\begin{aligned} 0 &\leq z \leq 1 \\ \mathbf{u}|_{z=0,1} &= 0 \\ \theta|_{z=0} &= \frac{1}{2} \\ \theta|_{z=1} &= -\frac{1}{2}. \end{aligned}$$

Together with the incompressibility condition this also implies for the vertical velocity w

$$\partial_z w|_{z=0,1} = 0,$$

which will be important in the following.

Continuity equation Let us begin with the continuity equation

$$\begin{aligned} \langle \nabla \cdot \mathbf{u} \rangle_z &= \nabla_h \cdot \tilde{\mathbf{u}}_h + \langle \partial_z w \rangle_z = 0 \\ \nabla_h &= (\partial_x, \partial_y)^\top. \end{aligned}$$

Here, we have used that we can exchange horizontal derivatives and averaging

$$\langle \partial_i q \rangle_z = \partial_i \langle q \rangle_z \quad \text{for } i = x, y.$$

Now we consider the vertical derivative. We find

$$\int_0^1 dz \partial_z \mathbf{u} = \mathbf{u}(z=1) - \mathbf{u}(z=0) = 0,$$

due to the no-slip boundary conditions. Hence, the average of the vertical derivative vanishes

$$\langle \partial_z \mathbf{u} \rangle_z = 0,$$

and we get from the incompressibility condition

$$\langle \nabla \cdot \mathbf{u} \rangle_z = \nabla_h \cdot \tilde{\mathbf{u}}_h = 0.$$

This means that the averaged horizontal velocity is solenoidal.

Advection term The advection term can be written as

$$\begin{aligned} \langle \mathbf{u} \cdot \nabla \mathbf{u} \rangle_z &= \tilde{\mathbf{u}} \cdot \nabla \tilde{\mathbf{u}} + \langle \nabla \cdot (\mathbf{u}\mathbf{u}) \rangle_z - \nabla \cdot (\tilde{\mathbf{u}}\tilde{\mathbf{u}}) \\ \langle \mathbf{u} \cdot \nabla \theta \rangle_z &= \tilde{\mathbf{u}} \cdot \nabla \tilde{\theta} + \langle \nabla \cdot (\mathbf{u}\theta) \rangle_z - \nabla \cdot (\tilde{\mathbf{u}}\tilde{\theta}). \end{aligned}$$

We can simplify this and evaluate the height average of the vertical derivatives

$$\begin{aligned} \langle \partial_z (w u_i) \rangle_z &= G_l * [(w u_i)(z=1) - (w u_i)(z=0)] = 0 \\ \langle \partial_z (w \theta) \rangle_z &= G_l * [(w \theta)(z=1) - (w \theta)(z=0)] = 0, \end{aligned}$$

because of the no-slip boundary condition. In addition, the averaged quantities are independent of z and the respective derivatives vanish. Thus, the advection term reads

$$\begin{aligned}\langle \mathbf{u} \cdot \nabla \mathbf{u} \rangle_z &= \tilde{\mathbf{u}} \cdot \nabla_h \tilde{\mathbf{u}} + \nabla_h \cdot (\overline{\mathbf{u}\mathbf{u}} - \tilde{\mathbf{u}}\tilde{\mathbf{u}}) \\ \langle \mathbf{u} \cdot \nabla \theta \rangle_z &= \tilde{\mathbf{u}} \cdot \nabla_h \tilde{\theta} + \nabla_h \cdot (\overline{\mathbf{u}\theta} - \tilde{\mathbf{u}}\tilde{\theta}),\end{aligned}$$

in which we only need to consider the horizontal gradients. Finally, we introduce the turbulent stress tensor $\tilde{\boldsymbol{\tau}}$ and the turbulent heat flux $\tilde{\boldsymbol{\gamma}}$ to simplify the notation

$$\begin{aligned}\langle \mathbf{u} \cdot \nabla \mathbf{u} \rangle_z &= \tilde{\mathbf{u}} \cdot \nabla_h \tilde{\mathbf{u}} - \nabla_h \cdot \tilde{\boldsymbol{\tau}} \\ \langle \mathbf{u} \cdot \nabla \theta \rangle_z &= \tilde{\mathbf{u}} \cdot \nabla_h \tilde{\theta} - \nabla_h \cdot \tilde{\boldsymbol{\gamma}}_h \\ \tilde{\tau}_{ij} &= \tilde{u}_i \tilde{u}_j - \overline{u_i u_j} \\ \tilde{\gamma}_i &= \tilde{u}_i \tilde{\theta} - \overline{u_i \theta}.\end{aligned}$$

The turbulent stress tensor and heat flux are unclosed terms which originate from the nonlinearity of the OBEs. They effectively capture the effect of the (unresolved) fluctuations on the (resolved) averages.

Laplace term We proceed with the Laplacians. To rewrite the Laplacians we use that we can exchange horizontal derivatives and averaging

$$\begin{aligned}\langle \Delta \mathbf{u} \rangle_z &= \langle \partial_z^2 \mathbf{u} \rangle_z + \Delta_h \tilde{\mathbf{u}} \\ \langle \Delta \theta \rangle_z &= \langle \partial_z^2 \theta \rangle_z + \Delta_h \tilde{\theta} \\ \Delta_h &= \partial_x^2 + \partial_y^2.\end{aligned}$$

We can further reduce the Laplacian of the vertical velocity because $\partial_z w|_{z=0,1} = 0$. The latter results in

$$\langle \partial_z^2 w \rangle_z = G_l * (\partial_z w(z=1) - \partial_z w(z=0)) = 0.$$

Thus, only the horizontal Laplacian needs to be considered

$$\langle \Delta w \rangle_z = \Delta_h \tilde{w}.$$

Therefore, we end up with

$$\begin{aligned}\langle \Delta \mathbf{u}_h \rangle_z &= \langle \partial_z^2 \mathbf{u}_h \rangle_z + \Delta_h \tilde{\mathbf{u}}_h \\ \langle \Delta w \rangle_z &= \Delta_h \tilde{w} \\ \langle \Delta \theta \rangle_z &= \langle \partial_z^2 \theta \rangle_z + \Delta_h \tilde{\theta}.\end{aligned}$$

Averaged OBEs Collecting the previous results we, eventually, obtain

$$\nabla_h \cdot \tilde{\mathbf{u}}_h = 0 \quad (5.4a)$$

$$\partial_t \tilde{\mathbf{u}}_h + \tilde{\mathbf{u}}_h \cdot \nabla_h \tilde{\mathbf{u}}_h = -\nabla_h \tilde{p} + \sqrt{\frac{Pr}{Ra}} \left(\Delta_h \tilde{\mathbf{u}}_h + \left\langle \partial_z^2 \mathbf{u}_h \right\rangle_z \right) + \nabla_h \cdot \tilde{\boldsymbol{\tau}}_h \quad (5.4b)$$

$$\partial_t \tilde{w} + \tilde{\mathbf{u}}_h \cdot \nabla_h \tilde{w} = -\langle \partial_z p \rangle_z + \tilde{\theta} + \sqrt{\frac{Pr}{Ra}} \Delta_h \tilde{w} + \nabla_h \cdot \tilde{\boldsymbol{\tau}}_z \quad (5.4c)$$

$$\partial_t \tilde{\theta} + \tilde{\mathbf{u}}_h \cdot \nabla_h \tilde{\theta} = \frac{1}{\sqrt{Pr Ra}} \left(\Delta_h \tilde{\theta} + \left\langle \partial_z^2 \theta \right\rangle_z \right) + \nabla_h \cdot \tilde{\boldsymbol{\gamma}}_h. \quad (5.4d)$$

This is an averaged form of the OBEs, which has not been presented before to the best of our knowledge. The set of equations is still exact, though it contains unclosed terms. It is in spirit similar to classical Reynolds averages [179, 180] and coarse-graining approaches [129, 181, 182] but results in very different equations due to the reduction of the dimensionality. In contrast to the classical averages, not only the nonlinear advection term results in unclosed terms but also the linear terms contribute additional unclosed terms. These originate from the fact that we average over the total domain height. Therefore, averages of derivatives with respect to z have to be treated separately and the boundary conditions need to be incorporated. Thus, we can characterize the unclosed terms by their origin. The nonlinear advection results in

$$\begin{aligned} & \nabla_h \cdot \tilde{\boldsymbol{\tau}}_h \\ & \nabla_h \cdot \tilde{\boldsymbol{\tau}}_z \\ & \nabla_h \cdot \tilde{\boldsymbol{\gamma}}_h \\ & \tilde{\tau}_{ij} = \tilde{u}_i \tilde{u}_j - \widetilde{u_i u_j} \\ & \tilde{\gamma}_i = \tilde{u}_i \tilde{\theta} - \widetilde{u_i \theta}. \end{aligned}$$

Note that only the horizontal components of $\tilde{\boldsymbol{\gamma}}$ and 5 components of the turbulent stress tensor, $\tilde{\tau}_{xy} = \tilde{\tau}_{yx}, \tilde{\tau}_{xz}, \tilde{\tau}_{yz}, \tilde{\tau}_{yy}, \tilde{\tau}_{xx}$, are present in the averaged equations because vertical gradients vanish. Additionally, the unclosed terms originating from the boundary terms are

$$\begin{aligned} & \left\langle \partial_z^2 \mathbf{u}_h \right\rangle_z \\ & \left\langle \partial_z^2 \theta \right\rangle_z \\ & \left\langle \partial_z p \right\rangle_z. \end{aligned}$$

The unclosed terms need to be modelled to proceed. The problem of finding a closure model for the unclosed terms is very similar to classical large-eddy simulations (LES) and Reynolds-averaged Navier-Stokes equation (RANS) type of problems [129, 179–191], however, there the boundary terms are not present.

5.3 Development of closure models

In this section, we use theoretical considerations and modelling to gain insights into the structure of the unclosed terms and to obtain closure models. The resulting closure models are compared to DNS with $Ra = 1.02 \times 10^5$, $Pr = 1$ visually for one snapshot in time as a proof of concepts, before we evaluate them quantitatively in the subsequent section. The DNS data have

already been used in chapter 3 and are described there in detail. We split the considerations in two parts. We begin with the unclosed terms in the evolution equations for the temperature and vertical velocity. Here, we first consider the boundary terms, and subsequently the turbulent heat flux and stress tensor. In the second part, we deal with the evolution equation for the horizontal velocity.

5.3.1 Hydrostatic balance

We start with the unclosed boundary term $\langle \partial_z p \rangle_z$ present in the evolution equation for the averaged vertical velocity.

Turbulent superstructures are observed in large-aspect-ratio systems. In geophysical flows, this typically leads to the so-called hydrostatic balance [19]. Let us consider the consequences of a large aspect ratio here. We start with the equations for the velocity

$$\begin{aligned}\nabla \cdot \mathbf{u} &= 0 \\ \partial_t \mathbf{u}_h + \mathbf{u} \cdot \nabla \mathbf{u}_h &= -\nabla_h p + \sqrt{\frac{Pr}{Ra}} \Delta \mathbf{u}_h \\ \partial_t w + \mathbf{u} \cdot \nabla w &= -\partial_z p + \theta + \sqrt{\frac{Pr}{Ra}} \Delta w.\end{aligned}$$

We now decompose the different quantities in characteristic scales [19], where we choose horizontal velocity and length scales U, L as well as vertical velocity and length scales W, H

$$\begin{aligned}\mathbf{u}_h &= U \bar{\mathbf{u}}_h, \\ (x, y) &= (L\bar{x}, L\bar{y}), \\ w &= W \bar{w}, \\ z &= H \bar{z}, \\ p &= P \bar{p}, \\ \theta &= \Phi \bar{\theta} \\ t &= \frac{L}{U} \bar{t}.\end{aligned}$$

Here, we can deduce a time scale from the velocity and length scales as well. Initially, the pressure and temperature scale are unspecified. This is inserted into continuity equation and we find

$$\frac{U}{L} \bar{\nabla} \cdot \bar{\mathbf{u}}_h = -\frac{W}{H} \partial_{\bar{z}} \bar{w}.$$

If we only consider the contributions from the large-scale flow, the characteristic length scale L on which the horizontal velocity varies is the width of a convection roll, and for the vertical velocity it is the height H . Here, the latter is roughly equal to the system size. Therefore, in order for the continuity equation to be fulfilled, we can estimate the magnitude of the vertical velocity

$$\Rightarrow W \sim \frac{H}{L} U,$$

because the gradients are rescaled to the same magnitude. Thus, we also find that $t = \frac{H}{W}\bar{t} = \frac{H}{HU/L}\bar{t} = \frac{L}{U}\bar{t}$. Hence, the scaling of t in terms of the vertical or horizontal characteristic scales is identical. The relation for W can be used in the evolution equations for the velocity and we obtain

$$\begin{aligned}\frac{U^2}{L}\partial_{\bar{t}}\bar{\mathbf{u}}_h + \frac{U^2}{L}\bar{\mathbf{u}} \cdot \bar{\nabla}\bar{\mathbf{u}}_h &= -\frac{P}{L}\bar{\nabla}_h\bar{p} + \frac{U}{L^2}\sqrt{\frac{Pr}{Ra}}\bar{\Delta}_h\bar{\mathbf{u}}_h + \frac{U}{H^2}\sqrt{\frac{Pr}{Ra}}\partial_{\bar{z}}^2\bar{\mathbf{u}}_h \\ \frac{HU^2}{L^2}\partial_{\bar{t}}\bar{w} + \frac{HU^2}{L^2}\bar{\mathbf{u}} \cdot \bar{\nabla}\bar{w} &= -\frac{P}{H}\partial_{\bar{z}}\bar{p} + \Phi\bar{\theta} + \frac{HU}{L^3}\sqrt{\frac{Pr}{Ra}}\bar{\Delta}_h\bar{w} + \frac{U}{HL}\sqrt{\frac{Pr}{Ra}}\partial_{\bar{z}}^2\bar{w}.\end{aligned}$$

Here, we assume that the pressure varies on the same length scales as the horizontal and vertical velocity, respectively. After averaging over height and spatially coarse-graining, we neglect the Laplace terms here, since they are small-scale and we only consider the large-scale flow. In other words, we assume that the Rayleigh number is large and, therefore, the Laplacians are small and can be neglected for this argument. However, we still keep them in the averaged equations (5.4). We obtain for the horizontal velocity

$$\frac{U^2}{L}\partial_{\bar{t}}\langle\bar{\mathbf{u}}_h\rangle_z + \frac{U^2}{L}\langle\bar{\mathbf{u}} \cdot \bar{\nabla}\bar{\mathbf{u}}_h\rangle_z = -\frac{P}{L}\bar{\nabla}_h\langle\bar{p}\rangle_z.$$

From this we estimate the magnitude of the pressure

$$P \sim U^2,$$

such that all terms are of the same order and balance. Then, the evolution equation for the vertical velocity reads

$$\begin{aligned}\frac{HU^2}{L^2}\partial_{\bar{t}}\langle\bar{w}\rangle_z + \frac{HU^2}{L^2}\langle\bar{\mathbf{u}} \cdot \bar{\nabla}\bar{w}\rangle_z &= -\frac{U^2}{H}\langle\partial_{\bar{z}}\bar{p}\rangle_z + \Phi\langle\bar{\theta}\rangle_z \\ \Rightarrow \frac{H^2}{L^2}\partial_{\bar{t}}\langle\bar{w}\rangle_z + \frac{H^2}{L^2}\langle\bar{\mathbf{u}} \cdot \bar{\nabla}\bar{w}\rangle_z &= -\langle\partial_{\bar{z}}\bar{p}\rangle_z + \Phi\frac{H}{U^2}\langle\bar{\theta}\rangle_z.\end{aligned}$$

The width of a convection roll exceeds its height several times $L = \bar{\alpha}H$ for turbulent superstructures [35]. For a large aspect ratio $\bar{\alpha}$ we find

$$\Rightarrow 0 \approx \bar{\alpha}^{-2}\partial_{\bar{t}}\langle\bar{w}\rangle_z + \bar{\alpha}^{-2}\langle\bar{\mathbf{u}} \cdot \bar{\nabla}\bar{w}\rangle_z = -\langle\partial_{\bar{z}}\bar{p}\rangle_z + \Phi\frac{H}{U^2}\langle\bar{\theta}\rangle_z.$$

Finally, we need to estimate Φ . We assume for the magnitude of the temperature $\Phi \sim U^2/H$ [19] to match the right-hand side of the equation. Then the hydrostatic balance follows [19]

$$\begin{aligned}\langle\bar{\theta}\rangle_z - \langle\partial_{\bar{z}}\bar{p}\rangle_z &\approx 0 \\ \Rightarrow \langle\partial_{\bar{z}}\bar{p}\rangle_z &= \langle\bar{\theta}\rangle_z.\end{aligned}$$

We use this as a motivation to formulate the following closure model in terms of the original quantities

$$\langle\partial_z p\rangle_z = p_0\langle\theta\rangle_z \quad (5.5)$$

for the unclosed pressure term in (5.4), in which p_0 accounts for deviations from ideal hydrostatic balance ($p_0 = 1$). In figure 5.2 the model assumptions are tested with DNS data. A comparison to the unclosed term shows a very good agreement. Thus, we obtained a closure model for the first unclosed term originating from the solid walls. In the next step, we proceed with the boundary term in the evolution equation for the temperature.

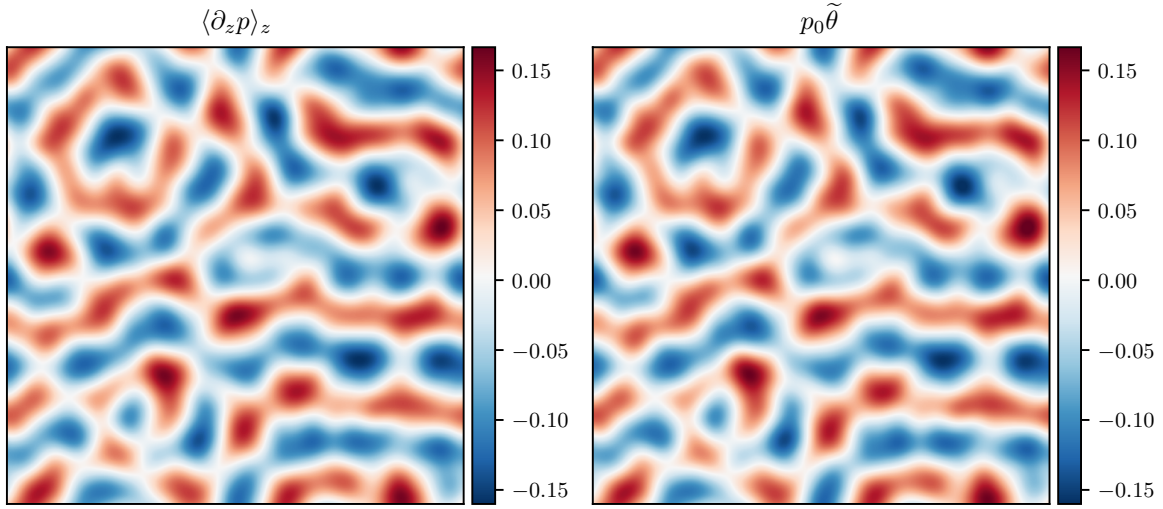


Figure 5.2: Comparison of the unclosed term with the closure model (5.5) from DNS with a filter width $\sigma_l = \lambda_s/8$. The prefactor p_0 is obtained from curve fitting.

5.3.2 Height dependence of the temperature

We now turn to the boundary term $\langle \partial_z^2 \theta \rangle_z$ and seek a closure model. How can we represent the dependence of the temperature on the vertical coordinate? Here, we make use of a decomposition of the temperature in the (linear) conduction solution θ_c and fluctuations ϑ around it

$$\begin{aligned}\theta &= \vartheta + \theta_c \\ \theta_c &= \frac{1}{2} - z.\end{aligned}$$

In general, the temperature fluctuations can be represented exactly by a series expansion

$$\vartheta(\mathbf{x}, t) = \sum_{n=1}^{\infty} \vartheta_n(x, y, t) \sin(n\pi z),$$

which is compatible with the boundary conditions $\vartheta(z = 0, 1) = 0$, cf. Pesch [192]. For practical applications, the series has to be truncated

$$\vartheta \approx \sum_n^{N_{\text{cut}}} \vartheta_n(x, y) \sin(n\pi z), \quad (5.6)$$

in which we omit the time dependence. Thus, this representation is not exact and, depending on the cut-off N_{cut} , it is more or less accurate, see figure 5.3. We now use this expansion to evaluate the height average

$$\begin{aligned}\langle \theta \rangle_z &= \langle \vartheta \rangle_z \approx \sum_n^{N_{\text{cut}}} \langle \vartheta_n(x, y) \sin(n\pi z) \rangle_z \\ &= \sum_{n \text{ odd}}^{N_{\text{cut}}} G_l * \vartheta_n(x, y) \frac{2}{n\pi}\end{aligned}$$

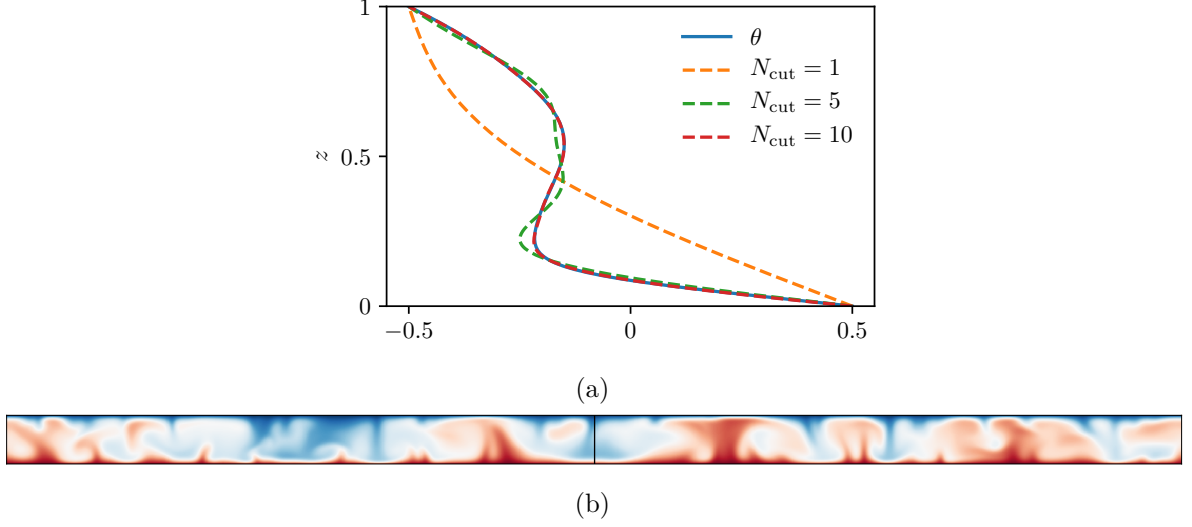


Figure 5.3: (a) Comparison of the vertical dependence of the full temperature field θ with a series expansion (5.6) for $\theta = \vartheta + \theta_c$ for different cut-offs, and (b) vertical cut through temperature field θ for $Ra = 1.02 \times 10^5$, $Pr = 1$. The black line highlights the position from which $\theta(z)$ in (a) is taken.

with

$$\int_0^1 dz \sin(n\pi z) = \frac{1 - \cos(n\pi)}{n\pi} = \begin{cases} 0 & \text{for } n \text{ even} \\ \frac{2}{n\pi} & \text{for } n \text{ odd.} \end{cases}$$

This shows that the contributions from higher order modes are reduced with the factor $1/n$ compared to the first mode. Therefore, we assume that the average is dominated by the first non-vanishing odd mode. We can proceed and calculate the height average of

$$\begin{aligned} \langle \partial_z^2 \theta \rangle_z &= \langle \partial_z^2 \vartheta \rangle_z \\ &\approx - \sum_n^{N_{\text{cut}}} \langle \vartheta_n(x, y) (n\pi)^2 \sin(n\pi z) \rangle_z \\ &= - \sum_{n \text{ odd}}^{N_{\text{cut}}} 2n\pi G_l * \vartheta_n(x, y). \end{aligned}$$

Here, the contributions from higher order modes grow with n .

In the turbulent regime, the small-scale plumes cluster in effective large-scale convection rolls, forming the turbulent superstructures. Since our approach removes the fluctuations by filtering we are left with a regular large-scale pattern. Such a flow can be described by a low number of modes. We assume that we only need to consider a single mode $n = 1$ to capture the averaged temperature

$$\begin{aligned} \langle \theta \rangle_z &\approx \frac{2}{\pi} G_l * \vartheta_1(x, y) \\ \langle \partial_z^2 \theta \rangle_z &\approx -2\pi G_l * \vartheta_1(x, y). \end{aligned}$$

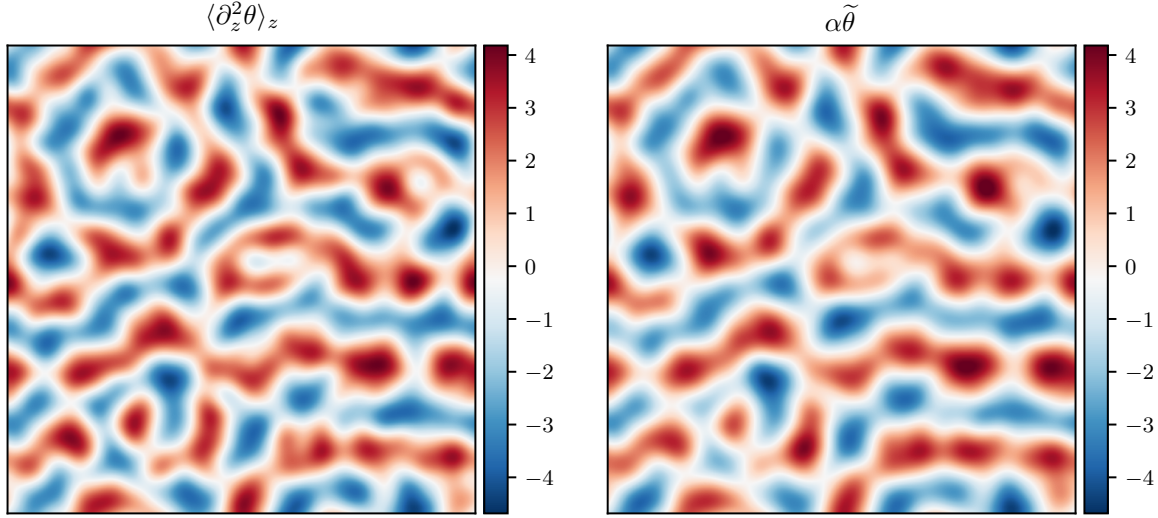


Figure 5.4: Comparison of the unclosed term with the closure model (5.7) from DNS with a filter width $\sigma_l = \lambda_s/8$. The prefactor α is obtained from curve fitting.

From this we obtain

$$\langle \partial_z^2 \theta \rangle_z \approx -\pi^2 \langle \theta \rangle_z.$$

However, contributions from higher order modes to the unclosed term $\langle \partial_z^2 \theta \rangle_z$ are generally larger due to the second derivative. Therefore, they may still contribute to the average even though they are small in the representation of $\langle \theta \rangle_z$. We assume that this can be effectively captured by rescaling the prefactor

$$\begin{aligned} \langle \partial_z^2 \theta \rangle_z &\approx -\pi^2 \langle \theta \rangle_z - 6\pi G_l * \vartheta_3(x, y) - \dots \\ &\approx (-\pi^2 + \dots) \langle \theta \rangle_z. \end{aligned}$$

Thus, we formulate a closure model

$$\langle \partial_z^2 \theta \rangle_z = \alpha \tilde{\theta}. \quad (5.7)$$

This hypothesis is validated in figure 5.4. The model reproduces the unclosed term remarkably well, which supports our assumptions.

This concludes the closure models for the boundary terms in the evolution equation for the temperature and vertical velocity. In the subsequent sections, we approach the unclosed terms originating from the nonlinearity.

5.3.3 Turbulent heat flux

We now turn to the turbulent heat flux $\tilde{\gamma}_h$. Initially, we deal with the consequences of a background temperature profile for this term.

Background temperature profile In RBC the temperature has a background profile, i.e. the horizontally averaged temperature $\langle \theta \rangle_A$ does not vanish

$$\langle \theta \rangle_A \equiv \Theta_{nl}(z).$$

Here, Θ_{nl} is a nonlinear function of height above onset of convection and is generally different from the conduction solution presented previously. Only below onset it is identical to the linear conduction solution. The profile is shown exemplarily in figure 5.5. This can be used to

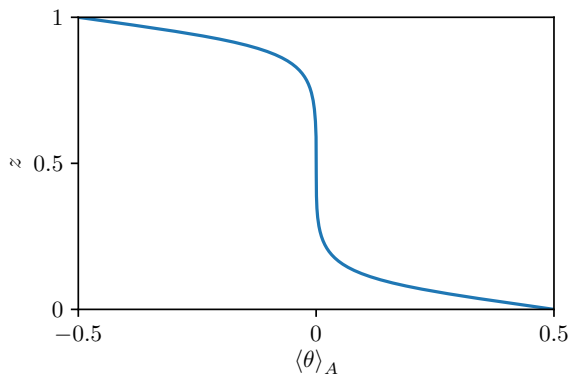


Figure 5.5: Example of a temperature profile in RBC from $Ra = 1.02 \times 10^5$, $Pr = 1$.

decompose the temperature field

$$\theta = \vartheta + \Theta_{nl},$$

in which ϑ is not identical to the one in the previous section. Here, Θ_{nl} has to be symmetric around $z = 1/2$ due to the symmetries of the system,

$$\begin{aligned} \xi &= z - \frac{1}{2} \\ \Theta_{nl}(\xi) &= -\Theta_{nl}(-\xi). \end{aligned}$$

Therefore, it holds

$$\langle \Theta_{nl} \rangle_z \equiv \tilde{\Theta}_{nl} = 0.$$

We use this decomposition for the turbulent heat flux

$$\begin{aligned} \nabla_h \cdot \tilde{\gamma}_h &= \nabla_h \cdot (\tilde{\mathbf{u}}_h \tilde{\theta} - \widetilde{\mathbf{u}}_h \theta) \\ &= \nabla_h \cdot (\tilde{\mathbf{u}}_h \tilde{\vartheta} - \langle \mathbf{u}_h (\vartheta + \Theta_{nl}) \rangle_z) \\ &= \nabla_h \cdot (\tilde{\mathbf{u}}_h \tilde{\vartheta} - \widetilde{\mathbf{u}}_h \vartheta) - \langle \Theta_{nl} \nabla_h \cdot \mathbf{u}_h \rangle_z \\ &= \nabla_h \cdot (\tilde{\mathbf{u}}_h \tilde{\vartheta} - \widetilde{\mathbf{u}}_h \vartheta) + \langle \Theta_{nl} \partial_z w \rangle_z. \end{aligned}$$

Note that we employed that Θ_{nl} is independent of the horizontal coordinates and the incompressibility condition

$$\begin{aligned} \nabla_h \Theta_{nl} &= 0 \\ \nabla \cdot \mathbf{u} &= 0 \\ \Leftrightarrow \nabla_h \cdot \mathbf{u}_h &= -\partial_z w. \end{aligned}$$

Let us consider the last term, which contains the background profile. We decompose the vertical velocity field into mean and fluctuations $w = \tilde{w} + w'$ to find

$$\begin{aligned}\langle \Theta_{nl} \partial_z w \rangle_z &= \langle \Theta_{nl} \partial_z w' \rangle_z \\ &= \langle \partial_z (\Theta_{nl} w') \rangle_z - \langle w' \partial_z \Theta_{nl} \rangle_z.\end{aligned}$$

We can simplify the first term and evaluate the height average

$$\begin{aligned}\langle \partial_z (\Theta_{nl} w') \rangle_z &= G_l * (\Theta_{nl} w'|_0^1) = -\frac{1}{2} G_l * (w'(z=1) + w'(z=0)) \\ &= G_l * \tilde{w}.\end{aligned}$$

Here, we have used the no-slip boundary conditions from which we find for the fluctuations

$$\begin{aligned}w(z=0) = 0 &= w(z=1) = \tilde{w} + w'(z=0,1) \\ \Rightarrow w'(z=0,1) &= -\tilde{w}.\end{aligned}$$

For a generic filter $G_l * G_l * q \neq G_l * q$ [129], which is why $G_l * \tilde{w} \neq \tilde{w}$. The equality only holds if the filter is idempotent [129]. To account for this, we assume $G_l * \tilde{w} \propto \tilde{w}$ to relate the divergence of the turbulent heat flux to the averaged vertical velocity

$$\Rightarrow \nabla_h \cdot \tilde{\gamma}_h = \alpha_2 \tilde{w} + \nabla_h \cdot \tilde{\gamma}_h^\vartheta - \langle w' \partial_z \Theta_{nl} \rangle_z \quad (5.8)$$

$$\tilde{\gamma}_h^\vartheta = \tilde{\mathbf{u}}_h \tilde{\vartheta} - \langle \mathbf{u}_h \vartheta \rangle_z. \quad (5.9)$$

This means that due to the presence of the background profile the divergence of the turbulent heat flux is linked to the averaged vertical velocity directly. Note that this result is exact if the filter is idempotent including the case where only a height average is considered, i.e. if the filter is a delta function $G_l(\mathbf{x}) = \delta(\mathbf{x})$. This result, therefore, helps to find a closure model for the turbulent heat flux. This is because we already know from the above calculation that \tilde{w} contributes to the unclosed term. Note that a similar approach for the velocity does not work because $\langle \mathbf{u} \rangle_A = \mathbf{0}$ in horizontally infinite systems.

Closure model We previously found that the divergence of the turbulent heat flux is closely connected to the averaged vertical velocity (5.8). Yet, (5.8) still contains unclosed terms. A well-known approach to find closure models is to make use of tensor representation theory [193–195]. This was established by Pope [186] and is nowadays a well-known method [129, 179, 183–185, 196]. The theory allows us to expand isotropic tensor-valued functions exactly in terms of generators, given that we know the functional dependency. If the latter is not given exactly, we can still deduce an approximate representation. In section 5.A we give a brief summary of the relevant theoretical basis. To proceed, we now make use of this theory. We assume that the turbulent heat flux is a function of the gradients of the averaged temperature and vertical velocity

$$\tilde{\gamma}_h^\vartheta = \tilde{\gamma}_h^\vartheta(\nabla_h \tilde{\theta}, \nabla_h \tilde{w}).$$

From tensor representation theory (see table 5.3) we get the possible generators for such an approach, which are simply the gradients $\nabla_h \tilde{\theta}$ and $\nabla_h \tilde{w}$ themselves. The generators are inserted into the representation (5.24b) to obtain

$$\tilde{\gamma}_h^\vartheta(\nabla_h \tilde{\theta}, \nabla_h \tilde{w}) = \alpha_1 \nabla_h \tilde{\theta} + \alpha_3 \nabla_h \tilde{w}.$$

In general, the coefficients can be arbitrarily complicated functions of the invariants of the basis vectors $\nabla_h \tilde{\theta}$ and $\nabla_h \tilde{w}$. For simplicity, we assume that the α_i 's are constant coefficients. Then

$$\Rightarrow \nabla_h \cdot \tilde{\gamma}_h^\vartheta = \alpha_1 \nabla_h^2 \tilde{\theta} + \alpha_3 \nabla_h^2 \tilde{w}.$$

We combine this with (5.8) and get

$$\nabla_h \cdot \tilde{\gamma}_h = \alpha_1 \nabla_h^2 \tilde{\theta} + \alpha_2 \tilde{w} + \alpha_3 \nabla_h^2 \tilde{w} - \langle w' \partial_z \Theta_{nl} \rangle_z.$$

To obtain a closure model, we neglect the last term

$$\nabla \cdot \tilde{\gamma}_h = \alpha_1 \nabla^2 \tilde{\theta} + \alpha_2 \tilde{w} + \alpha_3 \nabla^2 \tilde{w}. \quad (5.10)$$

This can be justified based on two observations, cf. figure 5.5. First, in the bulk the background profile is almost constant. Therefore, $\partial_z \Theta_{nl} \approx 0$. Second, in the boundary layers, the profile is close to linear and the average is proportional to the averaged fluctuations $\propto \langle w' \rangle_z$. The fluctuations are small-scale, and if the filter width is large enough $G_l * w'$ is small. In combination, the contribution of $\langle w' \partial_z \Theta_{nl} \rangle_z$ is expected to be negligible.

The closure model is shown in figure 5.6. Given the simplicity of the model, the unclosed term is represented quite accurately, which supports our closure model. Specifically, the pattern is captured well. Interestingly, the unclosed term consists of a clear footprint of the superstructure pattern, compare figure 5.1c.

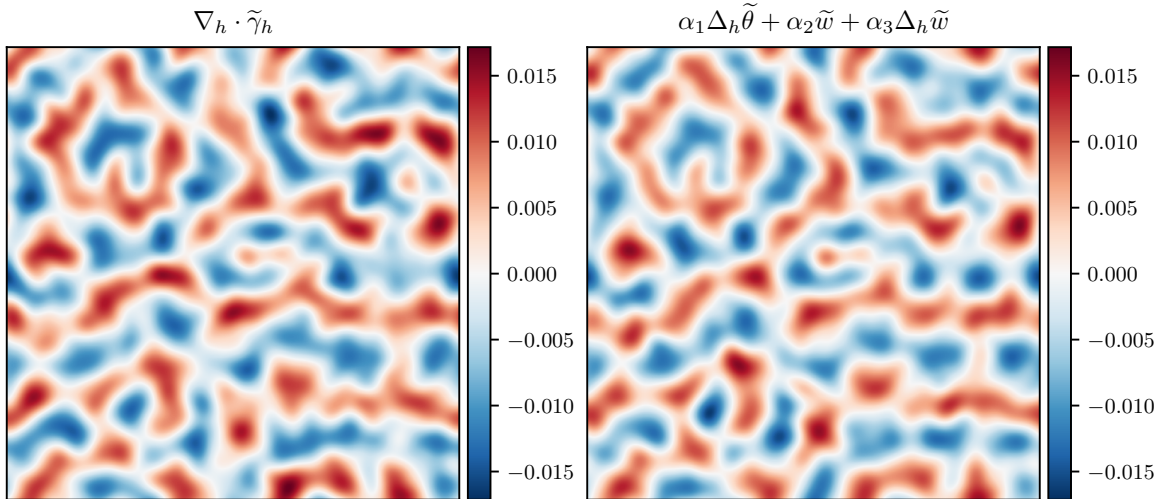


Figure 5.6: Comparison of the unclosed term with the closure model (5.10) from DNS with a filter width $\sigma_l = \lambda_s/8$. The prefactors α_1 , α_2 and α_3 are obtained from curve fitting.

5.3.4 Turbulent stress tensor

The equation for the vertical velocity also contains an unclosed term resulting from the non-linearity. In this section, we deal with the respective term, the z -component of the turbulent stress tensor. We continue in the same way as in the previous section and assume that the

z -component of the turbulent stress tensor is a function of the gradients of the averaged temperature and vertical velocity

$$\tilde{\tau}_z = \tilde{\tau}_z(\nabla_h \tilde{\theta}, \nabla_h \tilde{w}).$$

This results in

$$\tilde{\tau}_z(\nabla_h \tilde{\theta}, \nabla_h \tilde{w}) = \beta_0 \nabla_h \tilde{\theta} + \beta_1 \nabla_h \tilde{w},$$

where the β_i 's are again set as constant coefficients for simplicity. From this we obtain

$$\nabla_h \cdot \tilde{\tau}_z = \beta_0 \nabla_h^2 \tilde{\theta} + \beta_1 \nabla_h^2 \tilde{w}. \quad (5.11)$$

In figure 5.7 the closure model is determined from DNS. The structural form of the unclosed term is reproduced closely. However, locally there are deviations in magnitude. The pattern is also reminiscent of the superstructure pattern, although the closure only consists of Laplacians of $\tilde{\theta}$ and \tilde{w} .

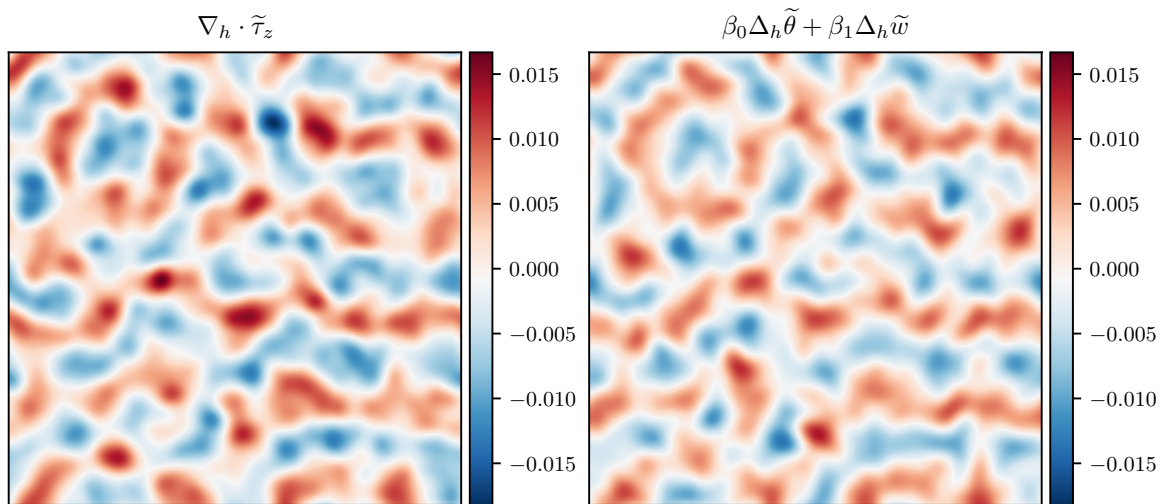


Figure 5.7: Comparison of the unclosed term with the closure model (5.11) from DNS with a filter width $\sigma_l = \lambda_s/8$. The prefactors β_0 and β_1 are obtained from curve fitting.

So far, we proposed closure models for the relevant terms related to the vertical velocity and temperature. Though rather simple, the closures represent the unclosed terms quite accurately, at least visually. As a proof of concept, we evaluate the closure models for a higher Rayleigh number for a single snapshot in the appendix 5.D. Before introducing quantitative measures to assess the closure models, we consider the horizontal velocity.

5.3.5 Large-scale velocity field

In order to complement the reduced model, we need to represent (5.4b) in a closed form. Let me first note that the vectorial equation can be reduced to one scalar equation for the vertical

vorticity

$$\tilde{\omega}_z = \partial_x \tilde{u}_y - \partial_y \tilde{u}_x \quad (5.12)$$

$$\begin{aligned} \left(\partial_t - \sqrt{\frac{Pr}{Ra}} \Delta_h \right) \tilde{\omega}_z = & \partial_y (\tilde{\mathbf{u}}_h \cdot \nabla_h \tilde{u}_x) - \partial_x (\tilde{\mathbf{u}}_h \cdot \nabla_h \tilde{u}_y) + \sqrt{\frac{Pr}{Ra}} \langle \partial_z^2 \omega_z \rangle_z \\ & + \partial_x \nabla_h \cdot \tilde{\boldsymbol{\tau}}_y - \partial_y \nabla_h \cdot \tilde{\boldsymbol{\tau}}_x. \end{aligned} \quad (5.13)$$

The horizontal velocity field can then be reconstructed from $\tilde{\omega}_z$, cf. Guyon et al. [79]. This equation is very similar to the model derived in Manneville [82], however, the present equation is still exact. Though, the equation contains three unclosed terms

$$\begin{aligned} & \langle \partial_z^2 \omega_z \rangle_z \\ & \partial_x \nabla_h \cdot \tilde{\boldsymbol{\tau}}_y \\ & \partial_y \nabla_h \cdot \tilde{\boldsymbol{\tau}}_x, \end{aligned}$$

which need to be modelled. The unclosed terms are presented in figure 5.8 for which we combined the components from the unclosed stress tensor. In contrast to the previously considered unclosed terms, the patterns are not reminiscent of the superstructure pattern. This prohibits a simple closure in terms of \tilde{w} , $\tilde{\theta}$ or their gradients. However, the evolution of the horizontal velocity needs to depend on the vertical velocity or temperature to describe the evolution of superstructures consistently. However, we initially only consider the effective influence of the horizontal velocity field on the turbulent superstructures. Therefore, we refrain from proposing closures at this point. We follow a simplified approach here and make use of the observation that the large-scale flow in the turbulent regime is reminiscent of SDC. We employ the observation that a mean flow is particularly important for SDC, see e.g. [90]. As discussed in section 2.4.4, the mean flow can be effectively captured by a coupling to the curvature of the temperature field in SH models [82]. The mean flow can be introduced to the equations in

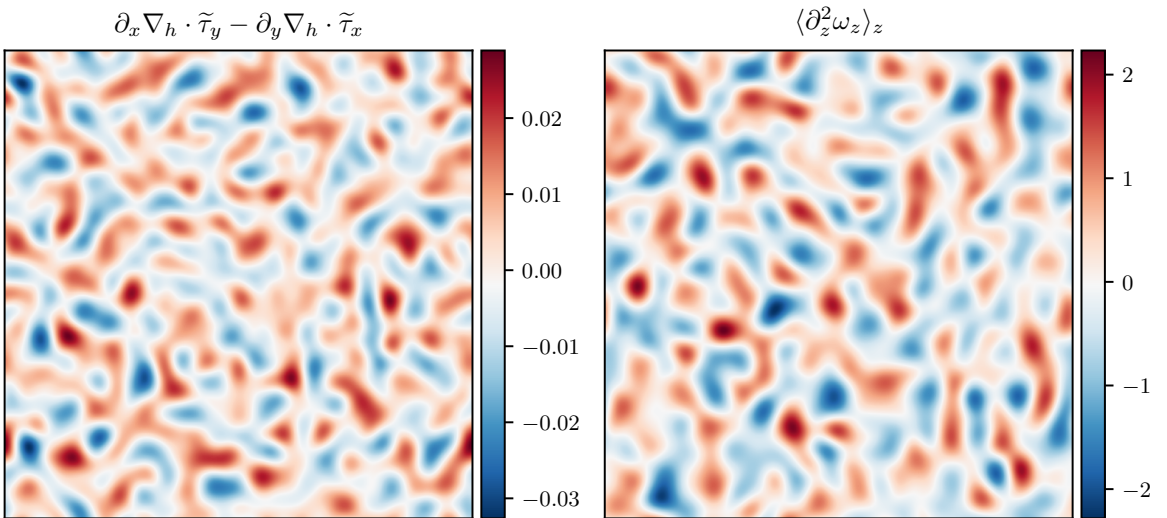


Figure 5.8: Unclosed term of (5.13) from DNS with a filter width $\sigma_l = \lambda_s/8$.

several variants, see e.g. [49, 53]. We follow the same approach and choose a simple model similar to (2.30), introduced in chapter 2. We propose the following model

$$\tilde{\mathbf{u}}_h = \nabla \times (\zeta \hat{\mathbf{z}}) \quad (5.14a)$$

$$\tilde{\omega}_z = -\nabla_h^2 \zeta \quad (5.14b)$$

$$\nabla_h^2 \zeta = g G_l * \hat{\mathbf{z}} \cdot [\nabla (\nabla_h^2 \tilde{\theta}) \times \nabla \tilde{\theta}], \quad (5.14c)$$

in which the horizontal velocity field is obtained from a stream function ζ , and we add an additional filter G_l to obtain a large-scale velocity field, cf. [49, 82, 97, 197]. We take the filter to be identical to the one in the average (5.2). The horizontal velocity is determined by the stream function ζ , which is directly linked to the vertical vorticity. Therefore, (5.14c) is a simplified phenomenological alternative to (5.13). In figure 5.9 the model is shown and

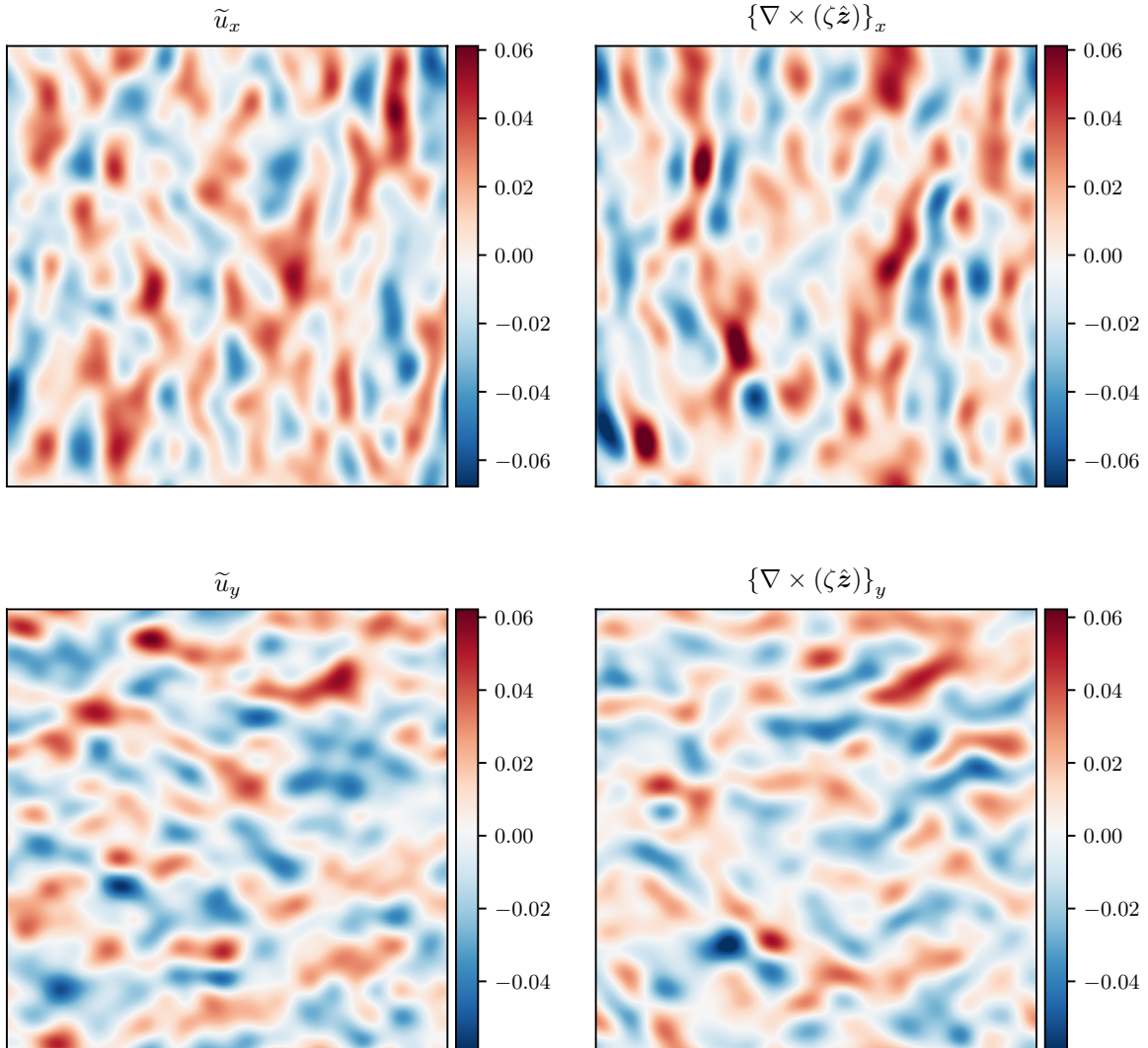


Figure 5.9: Comparison of the averaged horizontal velocity with the model (5.14) from DNS with a filter width $\sigma_l = \lambda_s/8$.

compared to DNS. The model is only designed to reproduce a similar velocity field but not to match the velocity exactly. Indeed, the model results in a qualitatively similar velocity field, which is already remarkable. This supports the observation that the large-scale flow in turbulent RBC is reminiscent of SDC and shows that it can be treated as a mean flow in reduced models. This finalizes the set up of the reduced model and we summarize the results in the next section.

5.4 Reduced model of turbulent superstructures

In this section, we combine the previous results and end up with the following reduced model

$$\partial_t \tilde{w} + \tilde{\mathbf{u}}_h \cdot \nabla_h \tilde{w} = p'_0 \tilde{\theta} + \beta_0 \Delta_h \tilde{\theta} + \beta'_1 \Delta_h \tilde{w} \quad (5.15a)$$

$$\partial_t \tilde{\theta} + \tilde{\mathbf{u}}_h \cdot \nabla_h \tilde{\theta} = \alpha' \tilde{\theta} + \alpha'_1 \Delta_h \tilde{\theta} + \alpha_2 \tilde{w} + \alpha_3 \Delta_h \tilde{w} \quad (5.15b)$$

$$\nabla_h^2 \zeta = g G_l * \hat{\mathbf{z}} \cdot \left[\nabla \left(\nabla_h^2 \tilde{\theta} \right) \times \nabla \tilde{\theta} \right] \quad (5.15c)$$

$$\tilde{\mathbf{u}}_h = (\partial_y \zeta, -\partial_x \zeta)^\top, \quad (5.15d)$$

in which we introduced new parameters

$$p'_0 \equiv 1 - p_0 \quad (5.16)$$

$$\beta'_1 \equiv \sqrt{\frac{Pr}{Ra}} + \beta_1 \quad (5.17)$$

$$\alpha' \equiv \frac{\alpha}{\sqrt{Pr Ra}} \quad (5.18)$$

$$\alpha'_1 \equiv \frac{1}{\sqrt{Pr Ra}} + \alpha_1. \quad (5.19)$$

However, the prefactors

$$\boldsymbol{\beta} = (p'_0, \alpha', \alpha'_1, \alpha_2, \alpha_3, \beta_0, \beta'_1, g) \quad (5.20)$$

are still undetermined. The final reduced model consists of coupled evolution equations for the averaged temperature and vertical velocity. Both fields are advected by a horizontal velocity field, which is described as a mean flow. It is obtained from a stream function, which is coupled to the curvature of the averaged temperature. This is a novel approach to describe the evolution of turbulent superstructures and a first step towards a quantitative description in terms of a reduced model. In the next section, I describe how the prefactors are obtained from DNS and how they depend on time and on the filter width.

5.5 Quantitative model evaluation

In the previous section we already validated the model visually but have not specified how the prefactors are determined. We also did not consider their temporal evolution and the dependence on the filter width. The prefactors are obtained from DNS for a single Rayleigh number. The relevant parameters of the DNS are given in table 5.1. We split the available snapshots in two subsets with the ratio 3 : 1. The first part is used to deduce the parameters β_i at every snapshot. From this we obtain a single parameter set

$$\boldsymbol{\beta} = \langle \beta_i \rangle_t \quad (5.21)$$

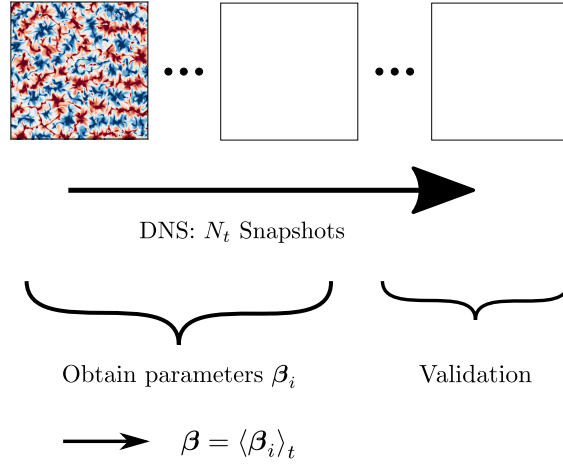


Figure 5.10: Sketch of the method to obtain the parameters β and validate the model (5.15).

Ra	Pr	λ_s	t_s	T_i	T_f	τ	N_s
1.02×10^5	1	4.8	74	467	701	178	201

Table 5.1: Parameters of the DNS. More details on the DNS are given in chapter 3 and in table 3.1. λ_s is the characteristic length scale of the turbulent superstructure obtained from the cross-spectrum and t_s the related characteristic time scale. T_i gives the initial time and T_f the final time from which snapshots are used in this section. The length of the averaging interval is given by τ and the average is taken from T_i to $T_i + \tau$. N_s is the number of snapshots in the given time interval. All parameters are given in free-fall units.

by averaging over time with an average window τ . Note that this set of parameters depends on the filter width. The remaining part serves as a test base to validate the model with the parameters β , see figure 5.10. With this, we test the time dependence of the prefactors and verify that the problem is stationary. Splitting the data set in training and test cases is a typical approach in data science [198]. We remark that for the previous visual assessment of the closure models, we only used data from a single snapshot, i.e. the prefactors are not the averaged ones. In order to validate the model quantitatively, we use two different measures. First, we calculate the relative error

$$\frac{\langle (q - q_m)^2 \rangle}{\langle q^2 \rangle}, \quad (5.22)$$

in which q represents the unclosed term, q_m the respective model, and $\langle \cdot \rangle$ an average over space. This is a measure for the local deviation of the model from the unclosed term. Second, we make use of the correlation coefficient

$$\frac{\langle (q - \langle q \rangle)(q_m - \langle q_m \rangle) \rangle}{\sigma_q \sigma_{q_m}}, \quad (5.23)$$

which quantifies how well the structural form is reproduced by measuring the normalized deviation from the mean. Here, σ_q and σ_{q_m} are the standard deviations of the unclosed term and the model, respectively. In the following, we study these measures as a function of time and filter width.

5.5.1 Temperature and vertical velocity

We start with the closure models (5.5), (5.7), (5.10) and (5.11). Here, the prefactors are obtained by a simple curve fit, i.e. least squares regression [198–200], from the DNS.

Temporal change To begin with, we consider the boundary terms in more detail for a single filter width $\sigma_l = l_s/8$. In figure 5.11, the temporal change of the prefactors p'_0 and α' is shown. Both prefactors vary around a mean value, which is obtained by averaging over the first part of the data set up to the dashed orange line. If the hydrostatic balance would be fulfilled exactly, p'_0 should vanish. But, this is not exactly true and the prefactor deviates from 0. Similarly, α' deviates from a single mode description which would result for the first mode in $\alpha' = -\pi^2/\sqrt{RaPr} \approx -0.031$. The difference can be related to higher modes which can not be neglected. To evaluate the closure models quantitatively, we consider the relative error and correlation coefficient in figure 5.12 as a function of time. Here, we differentiate between the values obtained at each time step after curve fitting (interpolation) and the ones obtained with the averaged parameter (extrapolation) in the second part of the time series. Note that for single parameter closure models the correlation coefficient is identical for interpolation and extrapolation. For both closure models the relative errors are quite small and the correlation coefficients are close to one. This, therefore, quantitatively validates our model. In addition, the extrapolation works as good as the interpolation. This shows that the model is robust in time, that the use of the averaged parameters is reasonable, and that the superstructures are indeed in a stationary state. The temporal change of the remaining prefactors, errors and correlation coefficients for the closure models of the turbulent heat flux and stress tensor are presented in the appendix 5.C, figure 5.16, 5.17 and 5.18 for $\sigma_l = \lambda_s/8$. Here, we focus on the averaged quantities in the following.

Evaluation of averages In figure 5.13a the resulting averaged prefactors are presented as a function of the filter width. All prefactors vary around the average, obtained from the first part of the time series and depend on the filter width. The standard deviation of the temporal average is shown as error bars but almost not visible in the figure. They are, however, given in table 5.5. To evaluate the models, we compare the relative error and correlation coefficient.

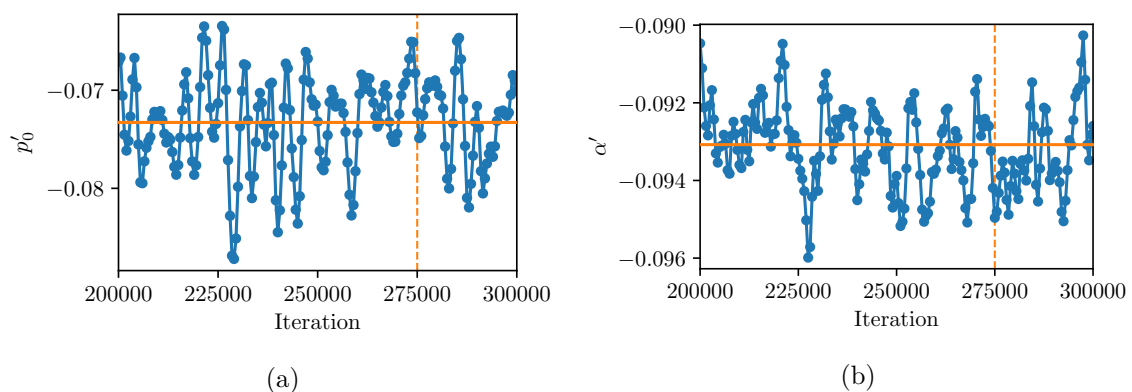


Figure 5.11: Temporal change of the different prefactors in (a) (5.5) and (b) (5.7) for $\sigma_l = \lambda_s/8$. The orange line shows the average over the time range τ . The dashed orange line indicates the end of the average range.

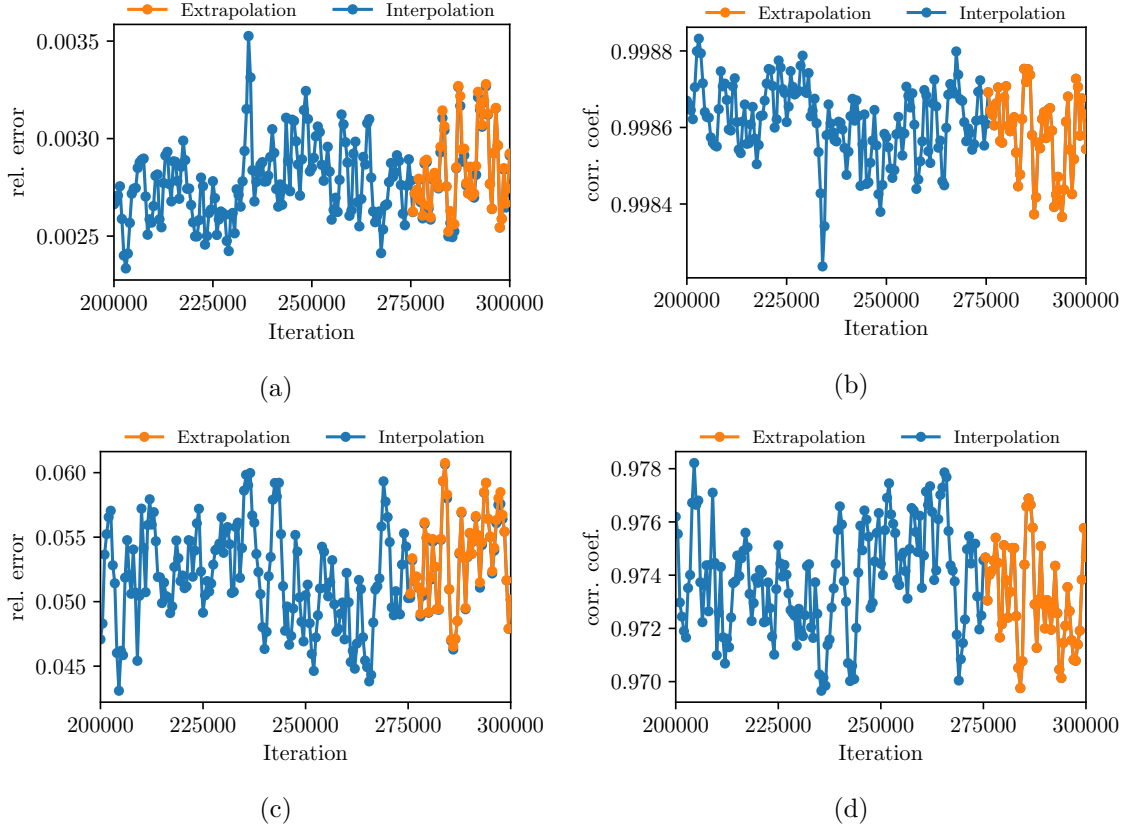


Figure 5.12: Temporal change of the relative error and correlation coefficient of the closure models for (a,b) $\langle \partial_z p \rangle_z$ (5.5) and (c,d) $\langle \partial_z^2 \theta \rangle_z$ (5.7) for $\sigma_l = \lambda_s/8$. The extrapolation results in almost identical errors as the interpolation.

Again, we differentiate between extrapolation and interpolation and average the values in the respective part of the time series. The comparison is presented in figure 5.13b and 5.13c. There is almost no difference between interpolation and extrapolation. Therefore, we conclude that the closure models are robust in time. Though, the quality of the models strongly depend on the filter width. A large enough filter width is necessary to obtain reasonable errors. Specifically, the model for $\nabla \cdot \boldsymbol{\tau}_z$ only results in a small error for $\sigma_l \geq \lambda_s/8$. In contrast, the other models already work remarkably well at smaller filter width.

This concludes the model validation for the temperature and vertical velocity and shows that the different models reproduce the unclosed terms reasonably well, as already seen visually, if the filter width is chosen adequately.

5.5.2 Horizontal velocity

We now turn to the model for the horizontal velocity. In contrast to the previous closure models, the velocity field in the horizontal plane is described by a phenomenological model, i.e. the model is not built based on the OBEs. Therefore, locally the deviation from the real velocity field is expected to be larger. This is why we do not obtain the prefactor g in (5.14) by curve fitting but instead match the energy of the model with that of the original velocity

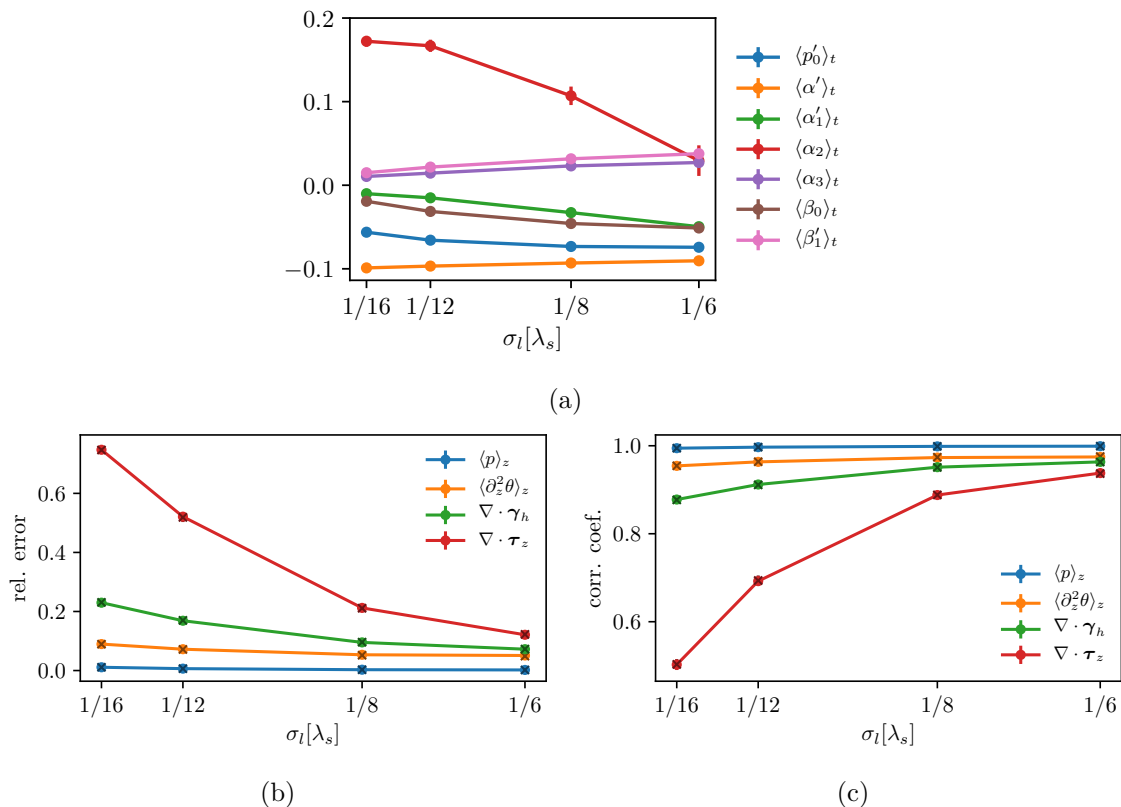


Figure 5.13: (a) Change of the averaged prefactors with the filter width. The errorbars are given by the standard deviation. (b) Relative error and (c) correlation coefficient as a function of the filter width. The circles are obtained from extrapolation and the dark crosses from interpolation.

field

$$\langle \tilde{u}_x^2 + \tilde{u}_y^2 \rangle = \langle (\partial_x \zeta)^2 + (\partial_y \zeta)^2 \rangle,$$

such that the averaged properties are identical. The resulting prefactor is a function of time and the temporal variation shown in the appendix in figure 5.16 for a specific filter width. There, we also present the variation in time of the respective relative error and correlation coefficient in figure 5.17 and 5.18. Here, we focus on time averaged quantities. The results are shown in figure 5.14. The prefactor grows with increasing filter width. As expected, the relative error is high, because the model does not capture the velocity field locally. It decreases with increasing filter width. The correlation coefficient grows with increasing filter width and reaches values above 0.4, which shows that some aspects of the large-scale pattern are captured. Also in this case, the results from extrapolation and interpolation are comparable. In conclusion, as shown visually before in figure 5.9, the model captures the velocity field qualitatively but not quantitatively.

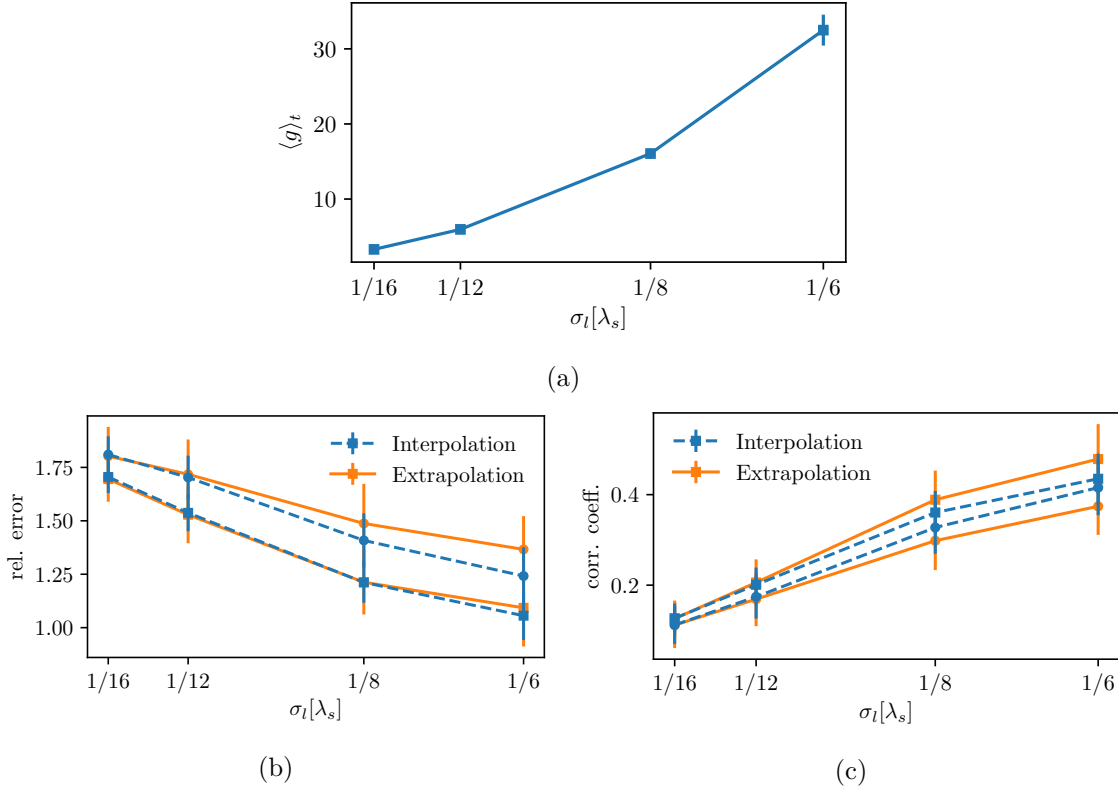


Figure 5.14: (a) Change of the averaged prefactor $\langle g \rangle_t$ with the filter width. The errorbar is given by the standard deviation. (b) Relative error and (c) correlation coefficient as a function of the filter width. The circles are for the x -component and the squares for the y -component.

5.6 Linear stability analysis

In the previous sections, we constructed a reduced model for turbulent superstructures and compared it to DNS with overall good agreement. Therefore, we can now proceed to analyse this equation theoretically. For this, we perform a linear stability analysis as described in the introduction 2.3.1. We study the stability of the base state with respect to small perturbations. The base state, i.e. the conduction solution, is given by $\tilde{\theta}_b = 0$, $\tilde{w}_b = 0$. The linearized equations around this base state that we need to consider are

$$\begin{aligned}\partial_t \tilde{w} &= p'_0 \tilde{\theta} + \beta_0 \Delta_h \tilde{\theta} + \beta'_1 \Delta_h \tilde{w} \\ \partial_t \tilde{\theta} &= \alpha' \tilde{\theta} + \alpha'_1 \Delta_h \tilde{\theta} + \alpha_2 \tilde{w} + \alpha_3 \Delta_h \tilde{w}.\end{aligned}$$

We use the basis functions

$$\begin{aligned}\tilde{w} &= \hat{w} e^{i\mathbf{k}\cdot\mathbf{x}} \\ \tilde{\theta} &= \hat{\theta} e^{i\mathbf{k}\cdot\mathbf{x}},\end{aligned}$$

and insert them into the above equations to obtain

$$\begin{aligned}\partial_t \hat{w} &= p'_0 \hat{\theta} - \beta_0 k^2 \hat{\theta} - \beta'_1 k^2 \hat{w} \\ \partial_t \hat{\theta} &= \alpha' \hat{\theta} - \alpha'_1 k^2 \hat{\theta} + \alpha_2 \hat{w} - \alpha_3 k^2 \hat{w} \\ \Rightarrow \partial_t \begin{pmatrix} \hat{w} \\ \hat{\theta} \end{pmatrix} &= \begin{pmatrix} -\beta'_1 k^2 & p'_0 - \beta_0 k^2 \\ \alpha_2 - \alpha_3 k^2 & \alpha' - \alpha'_1 k^2 \end{pmatrix} \begin{pmatrix} \hat{w} \\ \hat{\theta} \end{pmatrix} = \mathbf{A} \begin{pmatrix} \hat{w} \\ \hat{\theta} \end{pmatrix}.\end{aligned}$$

To determine the stability we need to find the eigenvalues σ_k of the matrix \mathbf{A} which are determined by the trace and determinant

$$\begin{aligned}\sigma_k^\pm &= \frac{1}{2} \left(\text{tr} \mathbf{A} \pm \sqrt{\text{tr} \mathbf{A}^2 - 4 \det \mathbf{A}} \right) \\ \text{tr} \mathbf{A} &= \alpha' - k^2 (\alpha'_1 + \beta'_1) \\ \det \mathbf{A} &= -\beta'_1 k^2 (\alpha' - \alpha'_1 k^2) - (p'_0 - \beta_0 k^2) (\alpha_2 - \alpha_3 k^2) \\ &= k^4 (\beta'_1 \alpha'_1 - \beta_0 \alpha_3) + k^2 (\beta_0 \alpha_2 - \beta'_1 \alpha' + p'_0 \alpha_3) - p'_0 \alpha_2.\end{aligned}$$

This results in

$$\begin{aligned}\Rightarrow \sigma_k^\pm &= \frac{1}{2} \left(\alpha' - k^2 (\alpha'_1 + \beta'_1) \pm \right. \\ &\quad \left. \sqrt{(\alpha' - k^2 (\alpha'_1 + \beta'_1))^2 - 4 \{k^4 (\beta'_1 \alpha'_1 - \beta_0 \alpha_3) + k^2 (\beta_0 \alpha_2 - \beta'_1 \alpha' + p'_0 \alpha_3) - p'_0 \alpha_2\}} \right).\end{aligned}$$

The growth rate contains too many parameters to make useful general predictions. Hence, we insert the parameters β obtained previously to examine the properties of the growth rate. The parameters are given in the appendix in table 5.5 for completeness.

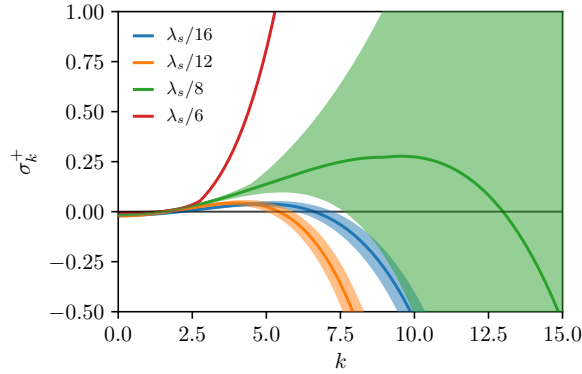


Figure 5.15: Resulting σ_k^+ for different filter width.

The resulting growth rates are shown in figure 5.15. Qualitatively, the growth rates are similar to the one in RBC for $\sigma_l < \lambda_s/6$. However, they strongly depend on the filter width. Specifically, $\sigma_l = \lambda_s/6$ must be excluded, because the resulting growth rate is not parabolic around a maximum-growth wavenumber as in RBC. Notably, the growth rates for $\sigma_l < \lambda_s/6$ take rather small values comparable to the ones for classical RBC close to onset (see figure 2.4a). This shows that our approach maps the flow closer to onset. In the best case, we could extract the turbulent superstructure length scale from the growth rates, e.g. from the

maximum as in the SH model. But, none of the presented growth rates results in a maximum around $k \approx 0.76 = \lambda_s/(2\pi)$, which corresponds to the superstructure size, see table 5.1. Indeed, the growth rates are even negative for $k \approx 0.76$, i.e. do not predict an unstable wavenumber. Note that the growth rate strongly depends on the parameters, specifically at larger wavenumbers. This can be seen in figure 5.15, in which the shaded regions denote the region between $\sigma_k^+(\beta + \sigma_\beta)$ and $\sigma_k^+(\beta - \sigma_\beta)$. Here, σ_β denote the standard deviation of the prefactors. The variation is large, i.e. the growth rate is very sensitive to the choice of the parameters.

5.7 Conclusions

In this part, we derived a reduced model for turbulent superstructures in an *a priori* study. We focused on a single Rayleigh number $Ra = 1.02 \times 10^5$ to begin with. In this model, the fluctuations are removed and the dynamics is reduced to two dimensions by averaging over height and spatially coarse-graining. This procedure reveals the superstructures only. We applied this average to the OBEs and the resulting averaged equations are unclosed due to the nonlinear advection and the solid top and bottom wall. We propose closure models based on theoretical arguments and observations from computational studies and literature. The closure models are validated against DNS and overall excellent agreement is observed. To the best of our knowledge, this is the first closure model for the OBEs averaged over height. Additionally, this is the first attempt to describe turbulent superstructures by a reduced model based on the OBEs. Specifically visually, the large-scale structure of the unclosed terms is reproduced remarkably well. Special attention is, however, given to the horizontal velocity field. The model for this field is set up based on phenomenological arguments, which means that we do not propose closure models for the respective unclosed terms. Instead, we used that turbulent superstructures are reminiscent of SDC. For the latter, the horizontal velocity field can be described as a mean flow, which is coupled to the curvature of the temperature field. This model results in a qualitatively similar velocity field but does not reproduce the original velocity field locally. This is, however, the first attempt to model the horizontal velocity in the turbulent regime in such a way and the qualitative reproduction is already remarkable. This also supports the observation that the dynamics of turbulent superstructures is reminiscent of SDC.

Finally, we analysed the reduced model theoretically. The analysis revealed that the model results in a qualitatively comparable growth rate as in RBC. However, it is sensitive to the choice of the parameters and does not result in a correct prediction for the size of the turbulent superstructure. Yet, it results in a mapping of the flow pattern closer to onset. In subsequent work, therefore, the application of techniques from classical pattern formation may be feasible.

Outlook We presented the first reduced model for turbulent superstructure in RBC and there are still many open questions. First, it needs to be tested if the model represents turbulent superstructures dynamically. This can be done in different ways. For example, initial conditions from DNS can be used to see if the dynamics is comparable and on what time scales. Additionally, the model can be run on its own, from e.g. random initial conditions, in an *a posteriori* study. Does this result in a stable pattern? Does it reproduce turbulent superstructures? What is the characteristic length scale? However, the theoretical analysis showed that the model strongly depends on the choice of the parameters. Therefore, the

prefactors need to be determined robustly, for which improvements to the current method are needed. Finally, the model needs to be validated and possibly revised for larger Rayleigh numbers. Eventually, in order to come closer to a full model of turbulent superstructures based on the governing equations the model for the horizontal velocity field needs to be revised. An ideal starting point is the equation for the averaged vertical velocity. Thus, closure models for the relevant terms in that equations need to be developed.

5.A Representation of two-dimensional isotropic functions

A popular approach pioneered by Pope [186] to find closure models is to make use of tensor representation theory [193–195] and has been used in many instances [129, 179, 183–185, 196]. This theory enables one to represent a tensor-valued function exactly, if the functional dependency is known. In two dimensions the theory is described, e.g., in Korsgaard [193]. We summarize the necessary background briefly based on this article.

Let f be a scalar-valued isotropic function, \mathbf{h} a vector-valued isotropic function and \mathcal{T} a symmetric (two-dimensional) tensor-valued isotropic function of the symmetric (two-dimensional) tensors \mathcal{A}_i ($i = 1, 2, \dots, N$), the vectors \mathbf{v}_m ($m = 1, 2, \dots, M$) and the skew-symmetric tensors \mathcal{W}_p ($p = 1, 2, \dots, P$). Explicitly, this means that they are form-invariant under the full orthogonal group, which is expressed as

$$\begin{aligned} f(\mathcal{Q}\mathcal{A}_i\mathcal{Q}^\top, \mathcal{Q}\mathbf{v}_m, \mathcal{Q}\mathcal{W}_p\mathcal{Q}^\top) &= f(\mathcal{A}_i, \mathbf{v}_m, \mathcal{W}_p), \\ \mathbf{h}(\mathcal{Q}\mathcal{A}_i\mathcal{Q}^\top, \mathcal{Q}\mathbf{v}_m, \mathcal{Q}\mathcal{W}_p\mathcal{Q}^\top) &= \mathcal{Q}\mathbf{h}(\mathcal{A}_i, \mathbf{v}_m, \mathcal{W}_p), \\ \mathcal{T}(\mathcal{Q}\mathcal{A}_i\mathcal{Q}^\top, \mathcal{Q}\mathbf{v}_m, \mathcal{Q}\mathcal{W}_p\mathcal{Q}^\top) &= \mathcal{Q}\mathcal{T}(\mathcal{A}_i, \mathbf{v}_m, \mathcal{W}_p)\mathcal{Q}^\top \quad \forall \mathcal{Q} \in O(2), \end{aligned}$$

where $O(2)$ is the full orthogonal group in the two-dimensional space. This group is the set of all 2×2 real orthogonal matrices

$$\begin{aligned} O(2) &= \{\mathcal{Q} | (Q_{ik}) \in \mathbb{R}^{2 \times 2}, \mathcal{Q}^\top \mathcal{Q} = \mathcal{Q}\mathcal{Q}^\top = \mathbb{I}\} \\ &\Rightarrow \mathcal{Q}^\top = \mathcal{Q}^{-1}, \det \mathcal{Q} = \pm 1 \end{aligned}$$

with matrix multiplication as the group multiplication [201–203]. Explicitly, it contains all rotations \mathcal{R} ($\det \mathcal{R} = 1$) and improper rotations ($\det \mathcal{Q} = -1$), which can be expressed as $\mathcal{Q} = (-\mathbb{I}\mathcal{R})$. The functions $\{f, \mathbf{h}, \mathcal{T}\}$ can then be represented in the following form [193–195]:

$$f(\mathcal{A}_i, \mathbf{v}_m, \mathcal{W}_p) = f(\mathcal{I}_s), \quad (5.24a)$$

$$\mathbf{h}(\mathcal{A}_i, \mathbf{v}_m, \mathcal{W}_p) = \sum_{t=1}^T \varphi_t(\mathcal{I}_s) \mathbf{h}_t, \quad (5.24b)$$

$$\mathcal{T}(\mathcal{A}_i, \mathbf{v}_m, \mathcal{W}_p) = \sum_{r=1}^R \phi_r(\mathcal{I}_s) \mathcal{T}_r, \quad (5.24c)$$

where \mathcal{I}_s ($s = 1, 2, \dots, S$) are the invariants of the functional basis, $\varphi(\mathcal{I}_s)$, $\phi(\mathcal{I}_s)$ are scalar-valued functions of the invariants, \mathbf{h}_t are basic form-invariant symmetric vector-valued isotropic functions (generators), and \mathcal{T}_r are basic form-invariant symmetric tensor-valued isotropic functions (generators). The invariants are given in table 5.2 and the generators in table 5.3 & 5.4, cf. Korsgaard [193]. In order to make use of this, we need to specify the functional dependencies, which fixes the possible generators and, thus, the expansion (5.24). However, the scalar-valued coefficients $f(\mathcal{I}_s)$, $\varphi(\mathcal{I}_s)$, $\phi(\mathcal{I}_s)$ can be arbitrarily complicated functions.

General example To give an explicit example how to apply this in general, we consider two cases in the following. First let us consider a generic vector-valued isotropic function \mathbf{h} , e.g. the turbulent heat flux $\tilde{\gamma}_h$. We assume that it depends on the gradients of the averaged temperature, vertical velocity, and horizontal velocity. We can split the latter into its symmetric and

$\text{tr}\mathcal{A}_i, \text{tr}\mathcal{A}_i^2$	
$\text{tr}\mathcal{A}_i\mathcal{A}_j$	
$\mathbf{v}_m \cdot \mathbf{v}_m$	$i, j = 1, 2, \dots, N; i < j$
$\mathbf{v}_m \cdot \mathbf{v}_n$	$m, n = 1, 2, \dots, M; m < n$
$\text{tr}\mathcal{W}_p^2$	$p, q = 1, 2, \dots, P; p < q$
$\text{tr}\mathcal{W}_p\mathcal{W}_q$	
$\mathbf{v}_m \cdot \mathcal{A}_i\mathbf{v}_m$	
$\mathbf{v}_m \cdot \mathcal{A}_i\mathbf{v}_n$	
$\mathbf{v}_m \cdot \mathcal{W}_i\mathbf{v}_n$	
$\text{tr}\mathcal{A}_i\mathcal{A}_j\mathcal{W}_p$	
$\mathcal{A}_i\mathbf{v}_m \cdot \mathcal{W}_p\mathbf{v}_m$	

Table 5.2: Invariants of the functional basis in two dimensions.

\mathbf{v}_m	$1 = 1, 2, \dots, N$
$\mathcal{A}_i\mathbf{v}_m$	$m = 1, 2, \dots, M$
$\mathcal{W}_p\mathbf{v}_m$	$p = 1, 2, \dots, P$

Table 5.3: Generators of $\mathfrak{h}(\mathcal{A}_i, \mathbf{v}_m, \mathcal{W}_p)$.

\mathbb{I}	
\mathcal{A}_i	$1 = 1, 2, \dots, N$
$\mathbf{v}_m\mathbf{v}_m$	$m, n = 1, 2, \dots, M : m < n$
$\mathbf{v}_m\mathbf{v}_n + \mathbf{v}_n\mathbf{v}_m$	$p = 1, 2, \dots, P$
$\mathbf{v}_m(\mathcal{W}_p\mathbf{v}_m) + \mathcal{W}_p(\mathbf{v}_m\mathbf{v}_m)$	
$\mathcal{A}_i\mathcal{W}_p - \mathcal{W}_p\mathcal{A}_i$	

Table 5.4: Generators of $\mathcal{T}(\mathcal{A}_i, \mathbf{v}_m, \mathcal{W}_p)$.

anti-symmetric parts and write

$$\begin{aligned}\tilde{\mathbf{s}} &= \frac{1}{2}(\nabla_h \tilde{\mathbf{u}}_h + (\nabla_h \tilde{\mathbf{u}}_h)^\top) \\ \tilde{\boldsymbol{\omega}} &= \frac{1}{2}(\nabla_h \tilde{\mathbf{u}}_h - (\nabla_h \tilde{\mathbf{u}}_h)^\top) \\ \mathbf{h} &= \mathbf{h}(\nabla_h \tilde{\theta}, \nabla_h \tilde{w}, \tilde{\mathbf{s}}, \tilde{\boldsymbol{\omega}}).\end{aligned}$$

From table 5.3 we get possible generators

$$\begin{aligned} & \nabla_h \tilde{\theta} \\ & \nabla_h \tilde{w} \\ & \tilde{\mathbf{s}} \nabla_h \tilde{\theta} \\ & \tilde{\mathbf{s}} \nabla_h \tilde{w} \\ & \tilde{\boldsymbol{\omega}} \nabla_h \tilde{\theta} \\ & \tilde{\boldsymbol{\omega}} \nabla_h \tilde{w} \end{aligned}$$

and (5.24b) results in

$$\mathbf{h} = \varphi_1 \nabla_h \tilde{\theta} + \varphi_2 \nabla_h \tilde{w} + \varphi_3 \tilde{\mathbf{s}} \nabla_h \tilde{\theta} + \varphi_4 \tilde{\mathbf{s}} \nabla_h \tilde{w} + \varphi_5 \tilde{\boldsymbol{\omega}} \nabla_h \tilde{\theta} + \varphi_6 \tilde{\boldsymbol{\omega}} \nabla_h \tilde{w}.$$

Second, we can deduce the generators for a tensor-valued function \mathcal{T} if we assume the same functional dependency

$$\mathcal{T} = \mathcal{T}(\nabla_h \tilde{\theta}, \nabla_h \tilde{w}, \tilde{\mathbf{s}}, \tilde{\boldsymbol{\omega}}).$$

Here, the generators are (see table 5.4)

$$\begin{aligned} & \mathbb{I} \\ & \tilde{\mathbf{s}} \\ & \nabla_h \tilde{\theta} \nabla_h \tilde{\theta} \\ & \nabla_h \tilde{w} \nabla_h \tilde{w} \\ & \nabla_h \tilde{\theta} \nabla_h \tilde{w} + \nabla_h \tilde{w} \nabla_h \tilde{\theta} \\ & \nabla_h \tilde{\theta} (\tilde{\boldsymbol{\omega}} \nabla_h \tilde{\theta}) + \tilde{\boldsymbol{\omega}} (\nabla_h \tilde{\theta} \nabla_h \tilde{\theta}) \\ & \nabla_h \tilde{w} (\tilde{\boldsymbol{\omega}} \nabla_h \tilde{w}) + \tilde{\boldsymbol{\omega}} (\nabla_h \tilde{w} \nabla_h \tilde{w}) \\ & \tilde{\mathbf{s}} \tilde{\boldsymbol{\omega}} - \tilde{\boldsymbol{\omega}} \tilde{\mathbf{s}}. \end{aligned}$$

and (5.24c) gives

$$\begin{aligned} \mathcal{T} = & \phi_1 \mathbb{I} + \phi_2 \tilde{\mathbf{s}} + \phi_3 \nabla_h \tilde{\theta} \nabla_h \tilde{\theta} + \phi_4 \nabla_h \tilde{w} \nabla_h \tilde{w} + \phi_5 (\nabla_h \tilde{\theta} \nabla_h \tilde{w} + \nabla_h \tilde{w} \nabla_h \tilde{\theta}) \\ & + \phi_6 (\nabla_h \tilde{\theta} (\tilde{\boldsymbol{\omega}} \nabla_h \tilde{\theta}) + \tilde{\boldsymbol{\omega}} (\nabla_h \tilde{\theta} \nabla_h \tilde{\theta})) + \phi_7 (\nabla_h \tilde{w} (\tilde{\boldsymbol{\omega}} \nabla_h \tilde{w}) + \tilde{\boldsymbol{\omega}} (\nabla_h \tilde{w} \nabla_h \tilde{w})) \\ & + \phi_8 (\tilde{\mathbf{s}} \tilde{\boldsymbol{\omega}} - \tilde{\boldsymbol{\omega}} \tilde{\mathbf{s}}). \end{aligned}$$

This shows that even a simple functional dependency can end up in a quite complicated expansion. In addition, the prefactors φ_t and ϕ_r are functions of the invariants of the generators (\mathcal{I}_s)

$$\begin{aligned} \varphi_t &= \varphi_t(\mathcal{I}_s) \\ \phi_t &= \phi_t(\mathcal{I}_s), \end{aligned}$$

whose functional forms are unspecified and need to be obtained from additional assumptions or empirical information [204]. For this setup, the list of invariants is already quite long and

can be obtained from table 5.2

$$\begin{aligned} \text{tr}\tilde{\mathbf{s}} = 0, \text{tr}\tilde{\mathbf{s}}^2, \text{tr}\tilde{\boldsymbol{\omega}}^2, (\nabla_h\tilde{\boldsymbol{\theta}})^2, (\nabla_h\tilde{w})^2, \nabla_h\tilde{\boldsymbol{\theta}} \cdot \nabla_h\tilde{w}, \\ \nabla_h\tilde{\boldsymbol{\theta}} \cdot (\tilde{\mathbf{s}}\nabla_h\tilde{\boldsymbol{\theta}}), \nabla_h\tilde{w} \cdot (\tilde{\mathbf{s}}\nabla_h\tilde{w}), \nabla_h\tilde{\boldsymbol{\theta}} \cdot (\tilde{\mathbf{s}}\nabla_h\tilde{w}), \nabla_h\tilde{\boldsymbol{\theta}} \cdot (\tilde{\boldsymbol{\omega}}\nabla_h\tilde{w}), \\ (\tilde{\mathbf{s}}\nabla_h\tilde{\boldsymbol{\theta}}) \cdot (\tilde{\boldsymbol{\omega}}\nabla_h\tilde{\boldsymbol{\theta}}), (\tilde{\mathbf{s}}\nabla_h\tilde{w}) \cdot (\tilde{\boldsymbol{\omega}}\nabla_h\tilde{w}). \end{aligned}$$

Therefore, to make practical use of this we assume in the main text that the prefactors are constant coefficients and a simple functional form for the turbulent heat flux. As shown there, this nevertheless results in reasonable representations. These methods have been used before to obtain closure models for turbulent scalar fluxes, see e.g. Wang et al. [184], Younis et al. [185]. Furthermore, they can also be combined with techniques from data science and machine learning [198, 205, 206], cf. Schmelzer et al. [191], Duraisamy et al. [204]. Similar approaches can possibly be employed to advance the current reduced model. For example, the above presented expansions could be a starting point to write down possible terms in the evolution equations. Then, techniques from data science can be applied to reduce the list of terms to obtain a reduced model, cf. Rudy et al. [205], Brunton et al. [206], and Schmelzer et al. [191].

5.B Numerically determined prefactors

$\sigma_l[\lambda_s]$	g	p'_0	β_0	β'_1
1/16	3.3 ± 0.1	-0.056 ± 0.005	-0.0192 ± 0.0007	0.0149 ± 0.0005
1/12	6.0 ± 0.2	-0.066 ± 0.005	-0.031 ± 0.001	0.0217 ± 0.0008
1/8	16.1 ± 0.7	-0.073 ± 0.005	-0.046 ± 0.002	0.0320 ± 0.001
1/6	32 ± 2	-0.074 ± 0.005	-0.051 ± 0.002	0.0380 ± 0.002

(a) Parameters for (5.15c) and (5.15a)

$\sigma_l[\lambda_s]$	α'	α'_1	α_2	α_3
1/16	-0.0989 ± 0.0009	-0.0101 ± 0.0007	0.172 ± 0.006	0.0105 ± 0.0004
1/12	-0.0968 ± 0.0010	-0.015 ± 0.001	0.167 ± 0.007	0.0145 ± 0.0006
1/8	-0.093 ± 0.001	-0.033 ± 0.002	0.11 ± 0.01	0.023 ± 0.001
1/6	-0.090 ± 0.001	-0.050 ± 0.003	0.03 ± 0.02	0.027 ± 0.002

(b) Parameters for (5.15b)

Table 5.5: Numerically determined prefactors. See figure 5.11 and 5.16 for their variation in time.

5.C Temporal change

Here, we present the temporal change of the different prefactors and the corresponding errors and correlation coefficients, see figure 5.16, 5.17 and 5.18. Note that the correlation coefficient is identical by construction for interpolation and extrapolation for single parameter models. It can be seen in the relative error that the extrapolation works almost as good as the interpolation. This, therefore, also shows that the models are actually good, reproduce the unclosed term reasonably, and are robust in time.

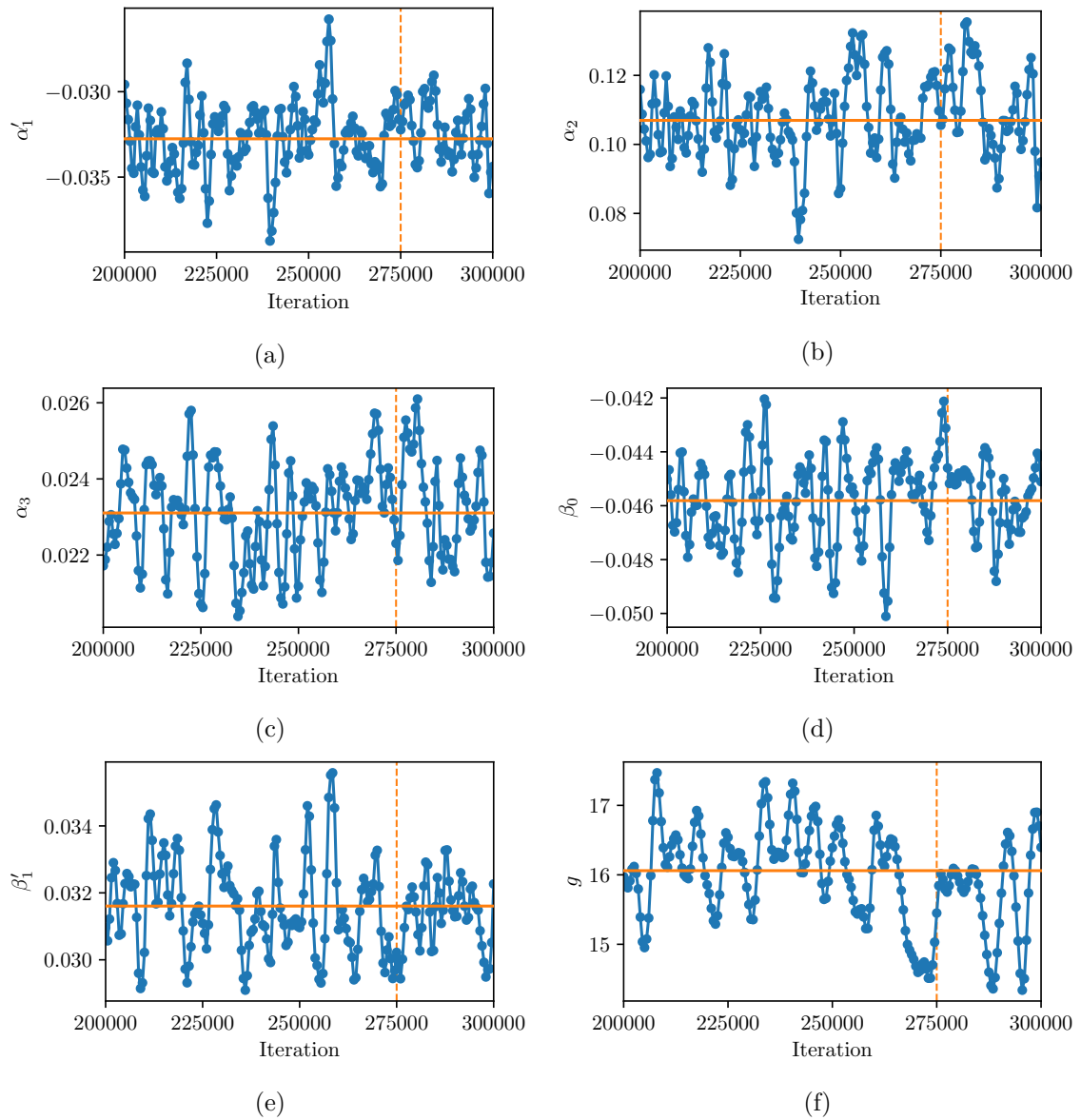


Figure 5.16: Temporal change of the different prefactors in (5.15) for $\sigma_l = \lambda_s/8$. The orange line shows the average over the time range τ . The dashed orange line indicates the end of the average range.

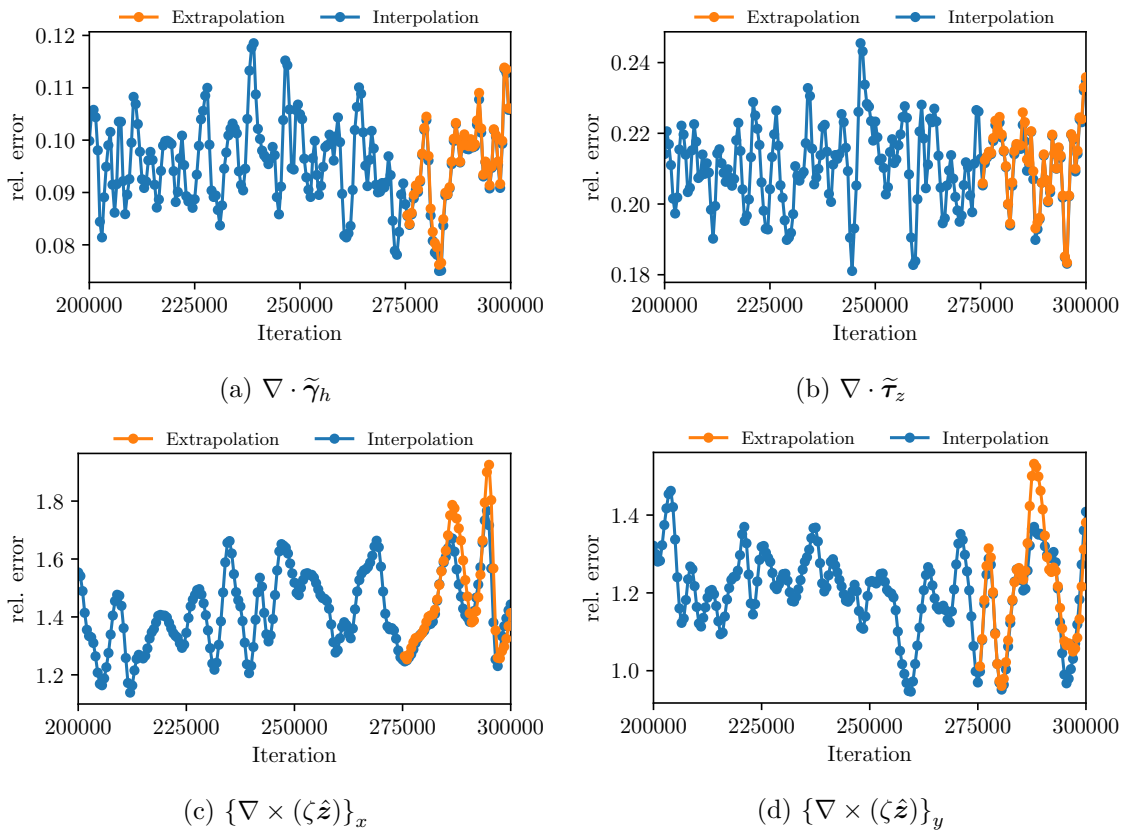


Figure 5.17: Temporal change of the relative error of the different closures for $\sigma_l = \lambda_s/8$. The extrapolation results in almost identical errors as the interpolation.

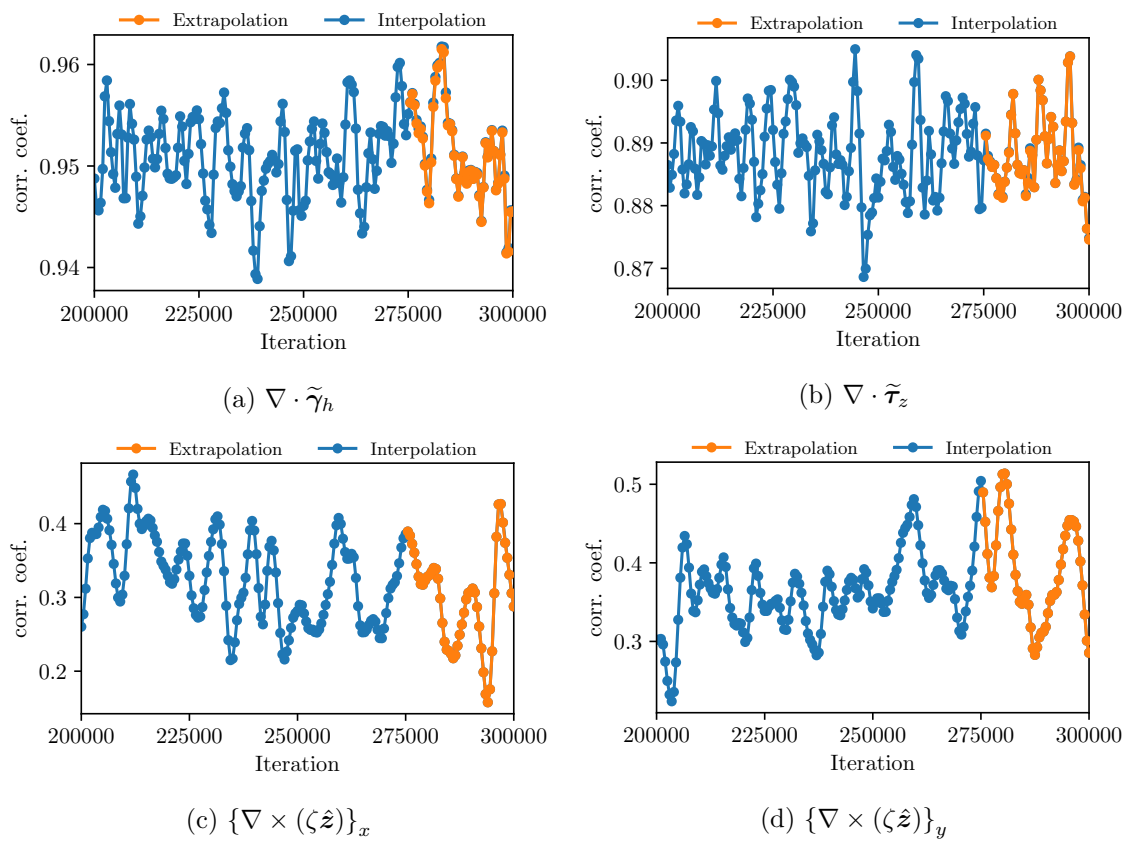


Figure 5.18: Temporal change of the correlation coefficient of the different closures for $\sigma_l = \lambda_s/8$. By construction, the values for extrapolation and interpolation are identical.

5.D Application to higher Rayleigh number

Ra	Pr	λ_s	t_s	t
1.07×10^7	1	6.0	90	964.2

Table 5.6: Parameters of the DNS. More details on the DNS are given in chapter 3 and in table 3.1. Here, t is the time (in free fall units) at which the snapshot is obtained in this section.

Can the proposed closure models (5.5), (5.7), (5.10), and (5.11) be extended to higher Rayleigh numbers? Here, we briefly address this question and visually compare the closure models with the full unclosed terms from DNS for one snapshot in time. The prefactors for the closure models are given in table 5.7. Although not averaged in time, we can see that the prefactors are different from the ones for $Ra = 1.02 \times 10^5$ (table 5.5), and, therefore, depend on the control parameters. In figure 5.19, a comparison of the temperature field in the midplane with the height-averaged and filtered ones is shown. In contrast to the smaller Rayleigh number, the regions close to the walls (figure 5.19b) leave a stronger footprint in the height-averaged field, see figure 5.19c. The comparison reveals that the full averaged field represents the large-scale pattern well again.

$\sigma_l[\lambda_s]$	g	p'_0	β_0	β'_1
1/8	117.7862	-0.0742	-0.0689	0.0219

(a) Parameters for (5.15c) and (5.15a)

$\sigma_l[\lambda_s]$	α'	α'_1	α_2	α_3
1/8	-0.0289	-0.0221	0.02352	0.0083

(b) Parameters for (5.15b)

Table 5.7: Numerically determined prefactors for $Ra = 1.7 \times 10^7$ from a single snapshot.

Boundary terms Let us first consider the closure models for the unclosed terms resulting from the solid top and bottom wall. These are

$$\begin{aligned} \langle \partial_z p \rangle_z &= p_0 \tilde{\theta} \\ \langle \partial_z^2 \theta \rangle_z &= \alpha \tilde{\theta} \end{aligned}$$

and the comparison is shown in figure 5.20. The agreement between the unclosed terms and the proposed closure models is remarkably well. In both cases the correlation coefficient is close to 1 and the relative error below 0.1. This shows that our proposed closure models can be extended to higher Rayleigh numbers, though the prefactors need to be updated.

Nonlinear advection We now turn to the closure models

$$\begin{aligned} \nabla_h \cdot \tilde{\gamma}_h &= \alpha_1 \nabla_h^2 \tilde{\theta} + \alpha_2 \tilde{w} + \alpha_3 \nabla_h^2 \tilde{w} \\ \nabla_h \cdot \tilde{\tau}_z &= \beta_0 \nabla_h^2 \tilde{\theta} + \beta_1 \nabla_h^2 \tilde{w}. \end{aligned}$$

They are shown in figure 5.21 and a good agreement to the full unclosed terms is observed again. Here, the relative error is around 0.2 and the correlation coefficient close to 0.9. Interestingly, the closure model for the turbulent stress tensor is quantitatively better than that for the turbulent heat flux, which is the other way around for the smaller Rayleigh number. Note, however, that this is only the result from a single snapshot.

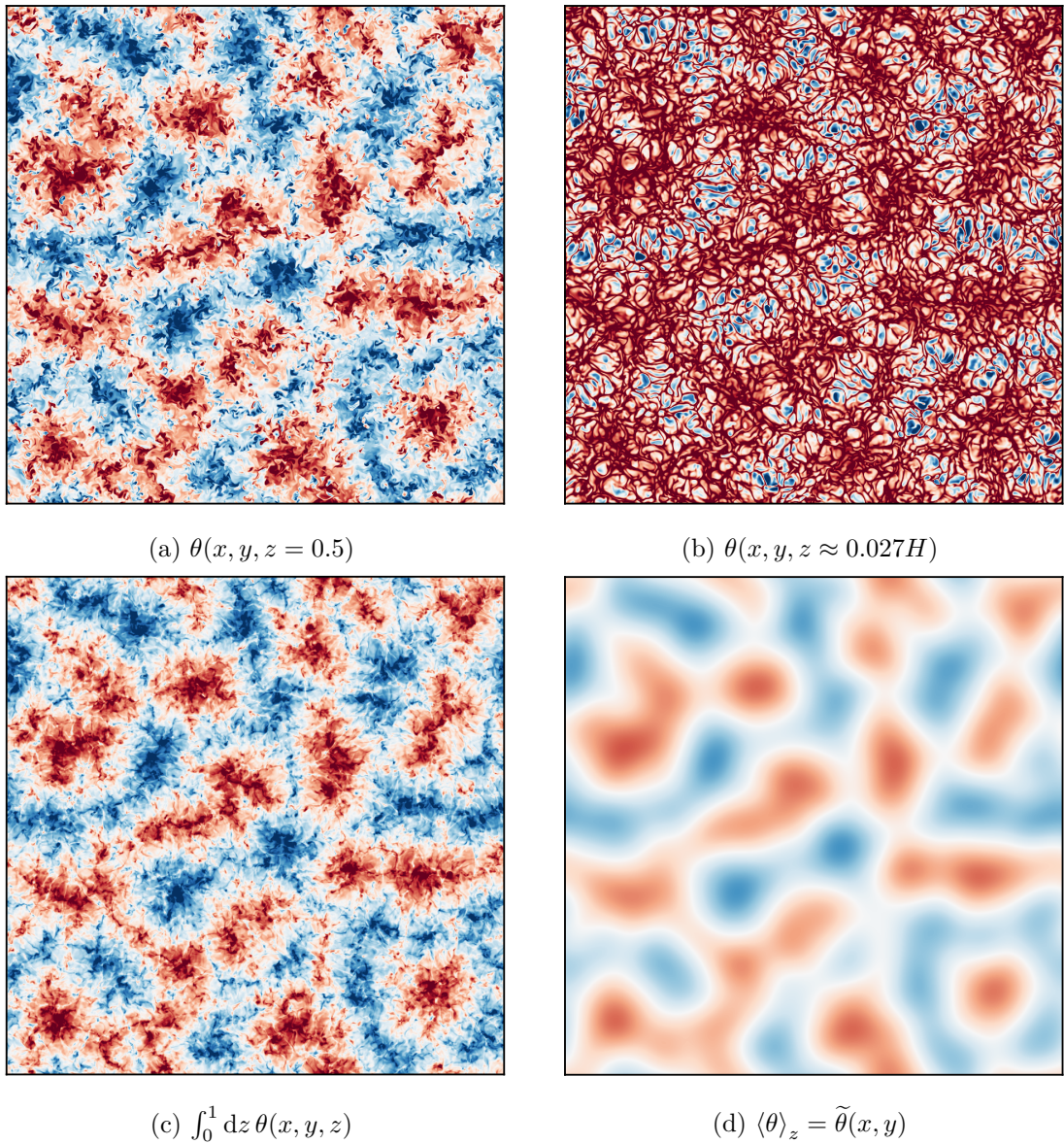


Figure 5.19: The full temperature field for $Ra = 1.07 \times 10^7$, $Pr = 1$ (a) shown in the midplane, (b) close to the bottom wall, (c) height-averaged and (d) filtered. A Gaussian filter with standard deviation $\sigma_l = \frac{\lambda_s}{8}$ is used. Here, λ_s is the superstructure size as described in chapter 3. Note that the color range in (b) is different from the other figures to highlight the fine-scale structure.

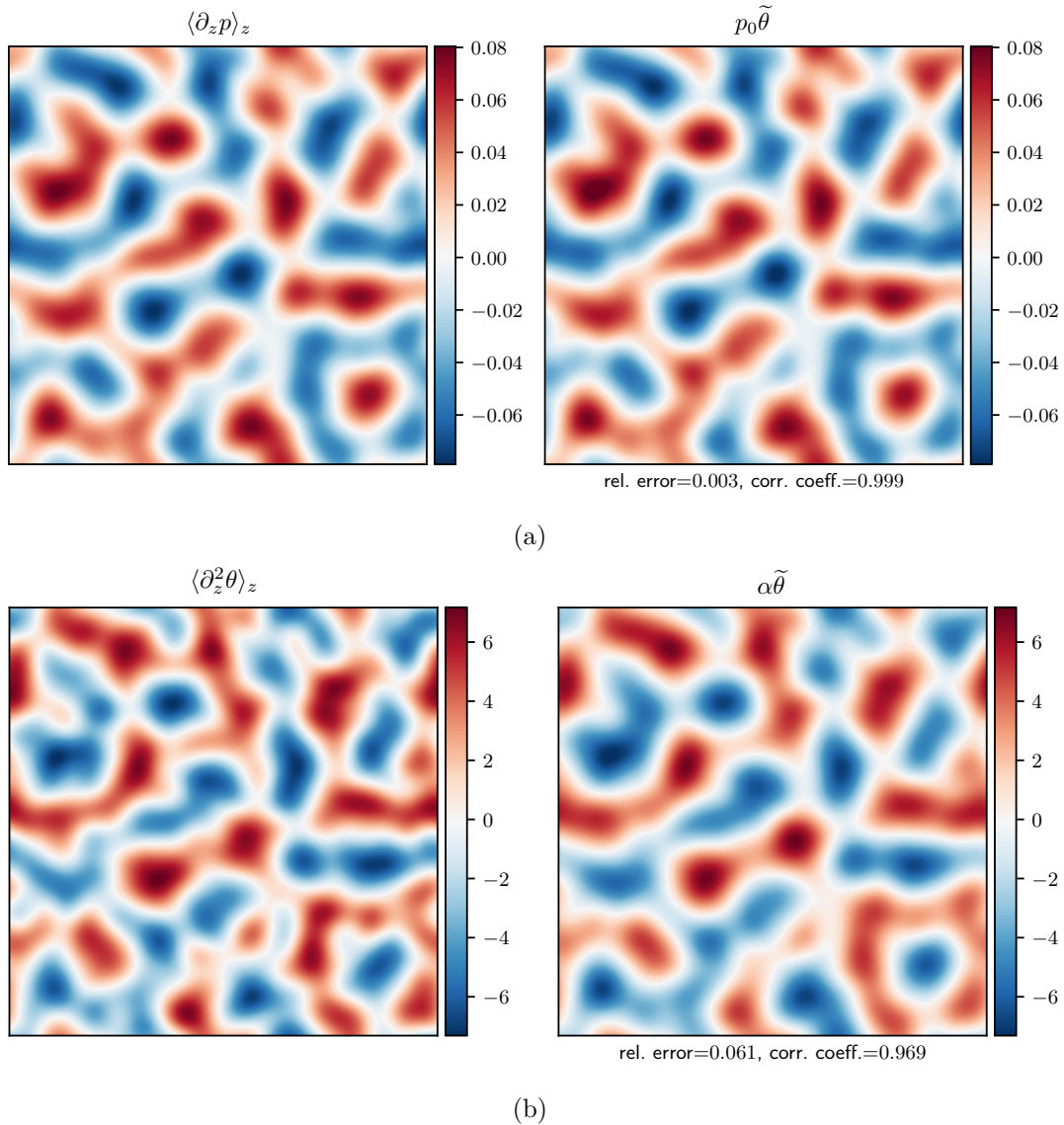


Figure 5.20: Comparison of the closure models (a) (5.5) and (b) (5.7) with the unclosed terms obtained from DNS.

Horizontal velocity Finally, we consider the model for the horizontal velocity field

$$\begin{aligned}\tilde{\mathbf{u}}_h &= \nabla \times (\zeta \hat{\mathbf{z}}) \\ \tilde{\omega}_z &= -\nabla_h^2 \zeta \\ \nabla_h^2 \zeta &= gGl * \hat{\mathbf{z}} \cdot \left[\nabla \left(\nabla_h^2 \tilde{\theta} \right) \times \nabla \tilde{\theta} \right].\end{aligned}$$

Let me stress that this model does not reproduce the velocity field locally. This can be seen in figure 5.22, which shows that the model results in a qualitatively similar velocity field but does not coincide locally.

We conclude that the proposed closure models also work in principle for higher Rayleigh numbers. Here, an advantage may be that the scale separation between the superstructures

and turbulent fluctuations is even larger. Therefore, the fluctuations can be removed more effectively. In future work, this needs to be studied in more detail and, specifically, the dependence of the prefactors on the control parameters needs to be evaluated. An interesting question to consider is, if the superstructures reach an asymptotic state at even higher Rayleigh numbers and if this state can still be captured by the proposed closure models.

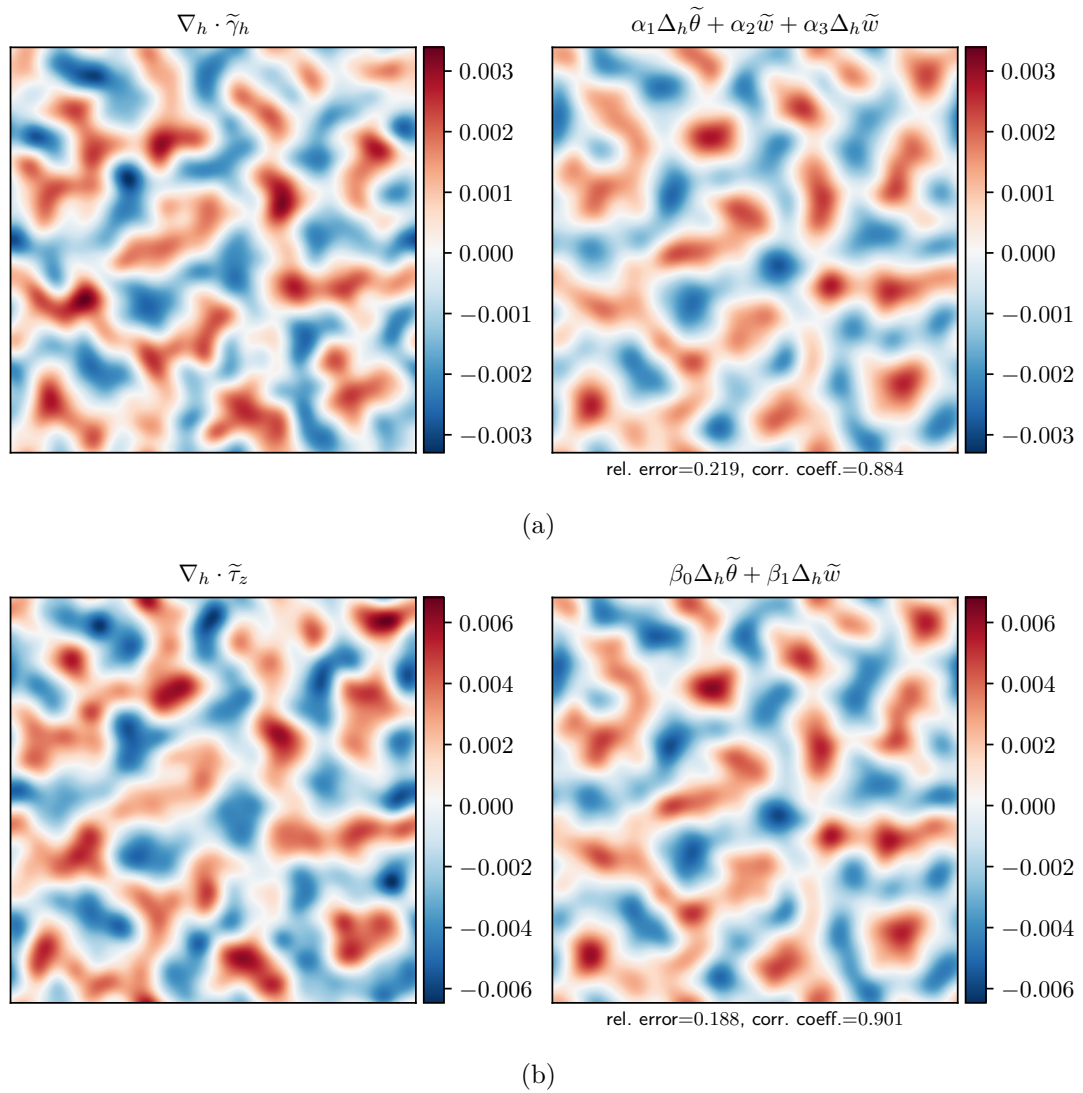


Figure 5.21: Comparison of the closure models (a) (5.10) and (b) (5.11) with the unclosed terms obtained from DNS.

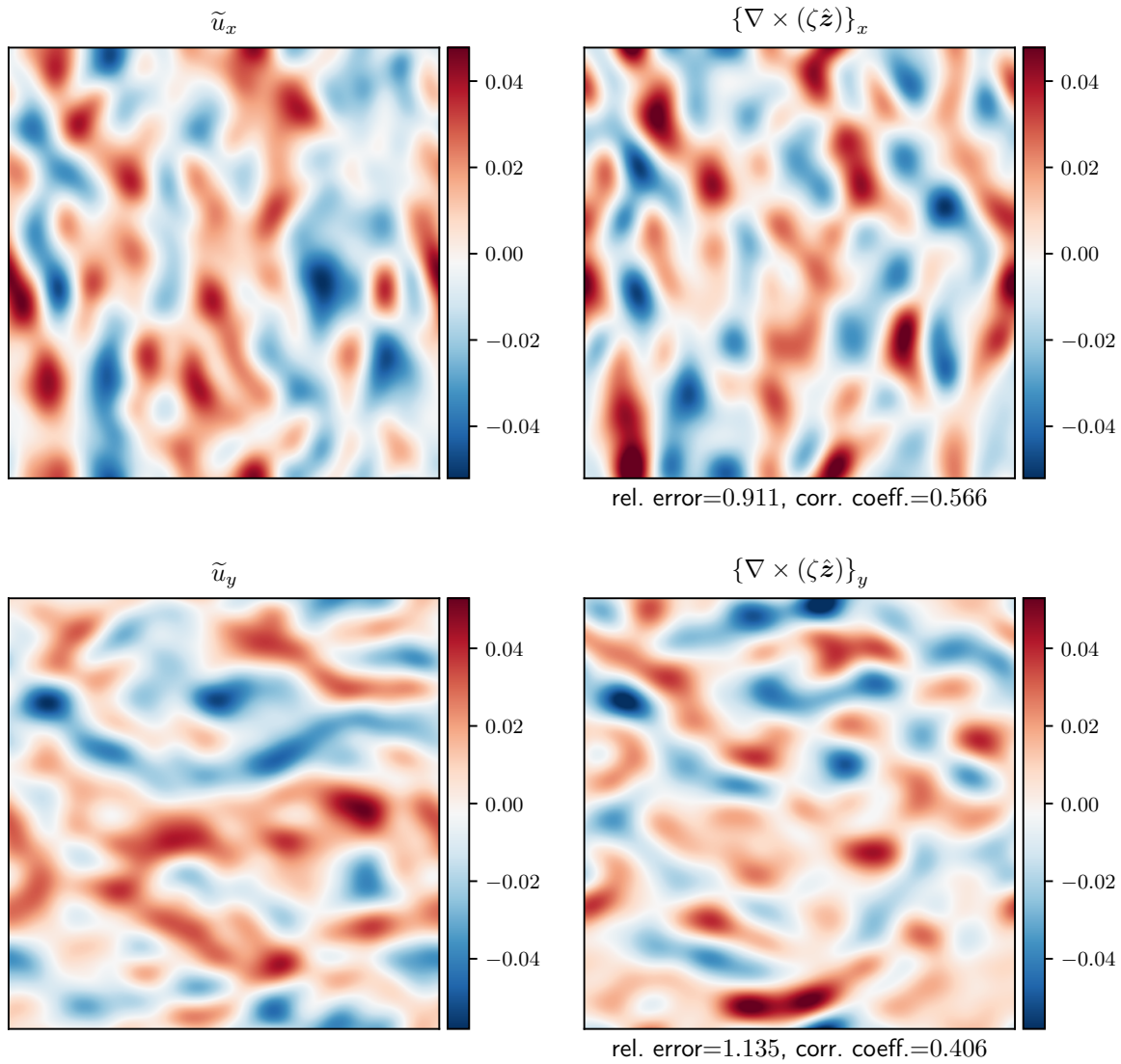


Figure 5.22: Comparison of the averaged horizontal velocity with the model (5.14) from DNS with a filter width $\sigma_l = \lambda_s/8$.

Part IV

—
Conclusions

Summary & discussion

Turbulent superstructures, i.e. coherent large-scale flows in the presence of small-scale fluctuations, are a ubiquitous phenomenon in nature. In order to understand this phenomenon, various idealized model systems have been studied. Among them are generalized Kolmogorov flows and several wall-bounded flows such as Rayleigh-Bénard convection. Though studied in quite some detail, many open questions remain. In this thesis, I studied turbulent superstructures in large-aspect-ratio Rayleigh-Bénard convection.

The initial motivation of this thesis, as reflected in the title, was to find an effective description of turbulent superstructures in Rayleigh-Bénard convection. Ultimately, one aims to obtain this description in the form of reduced model equations to provide a closed description of the large-scale pattern, separated in scale from the turbulent (small-scale) fluctuations. Providing such a model is a formidable task, and we approached this problem from different ends to come closer to such a reduced description. In line with the different approaches, this thesis is split into three projects in which I addressed how the small-scale fluctuations interact with turbulent superstructures, why the characteristic pattern scale is increasing, and how a reduced description of superstructures can be developed. To begin with, the projects are summarized and discussed separately in the following.

Resolved energy budget of superstructures in Rayleigh-Bénard convection

The interaction between the turbulent superstructures and the small-scale fluctuations has been studied in the first part of this thesis. Here, we used fully resolved direct numerical simulations of Rayleigh-Bénard convection in large-aspect-ratio systems to investigate the energetic interaction between superstructures and turbulent fluctuations. We covered a Rayleigh number range from $Ra \approx 10^4$ to $Ra \approx 10^8$ for a fixed Prandtl number, $Pr = 1$, in an aspect ratio $\Gamma \approx 24$ box with periodic boundary conditions in the horizontal directions. A straightforward method to make use of the scale separation between superstructures and fluctuations is to apply a filter (spatial coarse-graining) to the governing equations. With this, a scale-resolved energy and temperature variance budget can be derived from the Oberbeck-Boussinesq equations. From these budgets, valuable information about the energy and temperature variance transfer between resolved and unresolved scales can be obtained from the numerical simula-

tions. The advantage of the filtering approach is that the transfer terms contain spatially resolved information.

The main finding is that the transfer of energy and temperature variance is directed from large to small scales on average, consistent with the classical picture of the direct turbulent cascade. Hence, the small scales act on average as an energy sink for the turbulent superstructures. Specifically at high Rayleigh numbers, the energy transfer is the primary dissipation mechanism at the superstructure scale if compared to the direct dissipation. However, if averaged horizontally, a more complex picture emerges. In the resulting height-dependent profiles, energy is also transferred from small to large scales. The form of these profiles varies with the Rayleigh number, and the inverse transfer vanishes for the highest considered Rayleigh number. In contrast, the horizontally averaged temperature variance transfer acts primarily as a sink for all Rayleigh numbers. Locally, we observed that the direction of the energy transfer is closely related to the dynamics of plumes. At plume detaching, e.g. when a parcel of hot fluid is detached from the bottom boundary layer, we observed a direct energy transfer from large to small scales. In contrast, at plume impinging the plume heads enlarge and we found an inverse energy transfer from small to large scales.

In summary, the results from the first part of this thesis shed light on the energetic interaction of fluctuations and superstructures. They show that there is a complex interaction between turbulent fluctuations and superstructures. On average, the influence of the small-scale fluctuations can be captured by an effective dissipation, e.g. an eddy viscosity model as proposed by Emran and Schumacher [27]. Locally, however, the small scales also provide energy to the large scales which can only be captured by more complex models. This study provides valuable insights for the development of reduced models of turbulent superstructures in the form of large-eddy simulations.

Observations show that small-scale plumes initially emerge homogeneously distributed and subsequently cluster to effective large-scale convection rolls, which are the superstructures [30, 62]. However, it is still not answered satisfactorily why the plumes cluster and if the effective large-scale rolls are a manifestation of this clustering or if they are a reminder of the flow structures at lower Rayleigh number. The results presented above were obtained in the statistically stationary state. In order to understand the formation mechanism of turbulent superstructures and the interaction between different scales better, the scale-resolved energetic analysis supplemented with an investigation of the spectra of temperature and vertical velocity could be applied in the transitional state. This would address the above question and reveal, how the large-scale flow and small-scale plumes, as well as their energetic interaction, develop in time before the statistically stationary state is reached. Furthermore, this could be compared for different idealized systems to study if there are similar generation mechanisms at work.

Large-Scale Pattern Formation in The Presence of Small-Scale Random advection

The form and dynamics of the large-scale pattern representing the turbulent superstructures is reminiscent of patterns close to onset of convection [27, 30, 61]. However, these patterns are superposed by turbulent fluctuations. This opens the question of how small-scale fluctuations affect the large-scale pattern. To tackle this question, we studied the influence of small-scale fluctuations on a generic large-scale flow pattern using a minimal model for pattern formation in this part. To this end, we chose to include a random advection term to the Swift-Hohenberg equation, using a white-in-time Gaussian random velocity field. The Swift-Hohenberg equation

was initially proposed to study convection close to onset [66] but has proven to be a useful tool to study pattern formation in general [49]. The advantage of this study was that analytical techniques were feasible. This approach, hence, combined methods from classical pattern formation with statistical theory.

After a general discussion of the consequences of a random advection term for the onset and emerging wavelength in type I and II instabilities, we focused on the Swift-Hohenberg equation. For this model, we also confirmed numerically that a stationary large-scale pattern with superposed fluctuations emerges. The random advection has two major consequences for the large-scale pattern. First, it shifts the onset of pattern formation to larger drivings. Second, the wavelength of the emerging patterns is increased. These results were shown analytically for the ensemble-averaged equation and confirmed numerically. The averaged random advection term acts as an additional linear diffusion term in the averaged equations. The averaged equation is equivalent to the Swift-Hohenberg equation again, however, with renormalized control parameters. Our results qualitatively reproduce the observation that the wavelength of turbulent superstructures is increasing with increasing driving. Our model is only phenomenological and, hence, quantitative predictions for Rayleigh-Bénard convection cannot be made. Compared to previous stochastic versions of the Swift-Hohenberg equation with multiplicative noise [168], only the random advection term, added for the first time in this study, affects the wavelength.

Can this reduced model be adapted in future work to quantitatively describe turbulent superstructures? For this, first, time and length scales need to be introduced to the (non-dimensional) equation to match Rayleigh-Bénard convection. At onset, these scales are known, see Manneville [76] and Getling [53]. Second, the amplitude of the fluctuations needs to be expressed in terms of the control parameters (Rayleigh and Prandtl number). How this can be achieved is currently an open question. Last, in contrast to turbulent superstructures in Rayleigh-Bénard convection [27, 30] the large-scale flow in our model is stationary. Therefore, temporal evolution needs to be introduced. Similar to variants of the original Swift-Hohenberg equations, a dynamical pattern may be achieved by adding a mean flow term to the equation [49, 53, 58]. Investigating the combined effect of fluctuations and mean flow on the emerging wavelength, the onset of pattern formation, and the temporal evolution of the large-scale pattern is an interesting setting which could lead to further insights into the coupling between the large-scale flow and fluctuations.

Effective description of turbulent superstructures

How can we find a quantitative model for turbulent superstructures? In order to answer this question, we began with the full governing equations, in contrast to the previously considered phenomenological model. In the last part of this thesis, we took advantage of the observation that turbulent superstructures extend through the whole cell and are roughly height independent. Accordingly, we averaged over the complete height of the cell to remove the dependence on the vertical direction. In addition, the scale separation between superstructures and fluctuations suggests a coarse-graining approach, as employed in the first project. This reduces the dimensionality and removes the fluctuations, revealing a two-dimensional large-scale flow pattern. The averaged (and coarse-grained) equations contain unclosed terms. They are the turbulent stress tensor and turbulent heat flux, as well as terms resulting from vertical derivatives. Removing the vertical direction has also been used in deductions of Swift-Hohenberg

models [66, 82]. In contrast to our approach, Swift and Hohenberg [66] as well as Manneville [82] used projection techniques close to onset; here, we extend the idea to the turbulent regime.

We proposed basic closure models for the unclosed terms in the vertical velocity and temperature equation based on theoretical considerations and direct numerical simulations. Here, we made use of the data generated in the numerical simulations for the first project focusing on a single Rayleigh number, $Ra \approx 10^5$. The closure models are formed from the averaged temperature and vertical velocity and consist of linear terms such as Laplacians. We validated the proposed models with the fully resolved simulation data showing very good agreement between the closure models and the full unclosed terms. The model is complemented by a phenomenological closure model for the horizontal velocity field. The form of this evolution equation is motivated by Swift-Hohenberg equations with mean flow in which the velocity is coupled to the curvature of the temperature field. Qualitatively, this indeed leads to a similar velocity field as found in direct numerical simulations of turbulent superstructures. Though being a first step towards an effective description of turbulent superstructures, more work is necessary. Currently, the model is very sensitive to the chosen parameters, such that the outcome needs to be considered with caution. This leads to the question if it is possible to reduce the set of parameters or even relate them to the Rayleigh and Prandtl number.

In summary, we performed an *a priori* study on closure models for the unclosed terms in the height-averaged and coarse-grained Oberbeck-Boussinesq equations. Subsequent studies need to test how the proposed model performs *a posteriori*. Then, the model needs to be validated for different control parameters and possibly adapted. For this, it has to be studied how the parametrisation depends on the Rayleigh and Prandtl number.

Conclusions

In conclusion, with this thesis, I contributed to the understanding of turbulent superstructures using complementary methods—the energetics of the superstructures was studied in fully resolved simulations, the emerging length scale in a minimal model which is analytically accessible, as well as the development of a reduced model in an *a priori* study. Here, the first two projects helped to characterize and understand the influence of fluctuations on the large-scale flow in more detail. Eventually, I proposed a first reduced description in the last part and paved the way towards a quantitative effective description of the superstructures.

Let me return to the initial motivation of this thesis, the effective description of superstructures. The effect of small-scale fluctuations in direct numerical simulations of Rayleigh-Bénard convection in the first part and in the phenomenological model in the second part are similar. In the former, on average, their effect can be captured by an eddy viscosity model, which introduces an additional diffusion term to the equations. In the same way, the averaged random advection term results in a linear contribution to the averaged equation in the latter. In both cases, this results in renormalized control parameters. The derivation of the reduced model in the last part turned out to be a consequent extension of the findings in the previous parts. First, in both parts an additional diffusion term appears to be useful in modelling turbulent superstructures, which is present in the reduced model as well. Second, a simple eddy diffusion type of closure seems to be too simplistic, and the current closures are indeed more advanced. Third, in contrast to the phenomenological model, the reduced model is based on the Oberbeck-Boussinesq equations. The averaged (unclosed) Oberbeck-Boussinesq equations and the proposed closure models offer a first reduced description and are an ideal starting

point for further investigations on effective descriptions of superstructures.

Part V

—
Appendix

Superstructures in two-dimensional convection

To complement this thesis, we consider large aspect ratio RBC in two dimensions. Confining RBC to two dimensions is a common approach to reduce the computational cost. This allows, e.g., to simulate higher Rayleigh numbers, cf. Zhu et al. [207]. However, this does not resemble the three-dimensional case for all parameters [208–210]. The differences are very prominent for Prandtl numbers less than unity, whereas the flows are comparable at large Pr [208, 209]. Besides, reducing the dimensionality may help to shed light on similarities between RBC and Taylor-Couette flow [36] because the flows can be mapped onto each other exactly in two dimensions [37].

Here, I present results from DNS in large aspect ratios $\Gamma = 24$ for Rayleigh numbers in the range $Ra = 5.01 \times 10^4$ to $Ra = 1.05 \times 10^8$ for $Pr = 1$ with no-slip boundary conditions for the velocity and Dirichlet boundary conditions for the temperature. Periodic boundary conditions are used in horizontal directions. The simulations are performed with the same code as in Green et al. [67], cf. table A.1 for details on the simulations. With this, I briefly confirm that superstructures also exist in two-dimensional RBC with similarities to three-dimensional superstructures. We start by considering the temperature field for different Rayleigh numbers, see figure A.1. For a comparable small Rayleigh number, regular large-scale rolls are observed. They are composed of alternating warm updraughts and cold downdraughts. With increasing driving, the horizontal extent of these up- and downdraughts decreases. Furthermore, they start to be deflected on their way to the opposite boundary. However, they are still organized on a large-scale. Between these regions, the temperature is almost uniform at moderate Rayleigh numbers. At the highest Ra , fluctuations start to emerge in these region as well. In contrast to three-dimensional RBC, in which the plumes cluster in effective large-scales rolls [62], the up- and downdraughts only consist of single hot and cold plumes even at the largest Rayleigh numbers in two dimensions. In figure A.2, the temperature field is shown in the midplane. This also shows that the up- and downdraughts emerge alternating in space and are more localized with increasing Rayleigh number. Besides, the variation in magnitude as well as the fluctuations in between up- and downdraughts become stronger. For a comparative study of different flow states in two-dimensional RBC, we also refer the reader to van der Poel et al. [211].

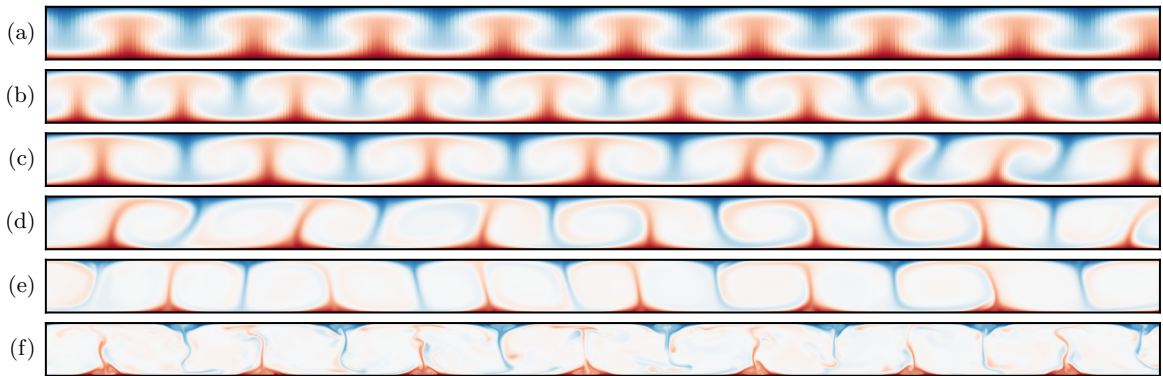


Figure A.1: Temperature field in two-dimensional RBC for different Ra from half of the computational domain. (a) $Ra = 1.06 \times 10^4$, (b) $Ra = 5.01 \times 10^4$, (c) $Ra = 1.04 \times 10^5$, (d) $Ra = 1.03 \times 10^6$, (e) $Ra = 1.07 \times 10^7$, (f) $Ra = 1.05 \times 10^8$

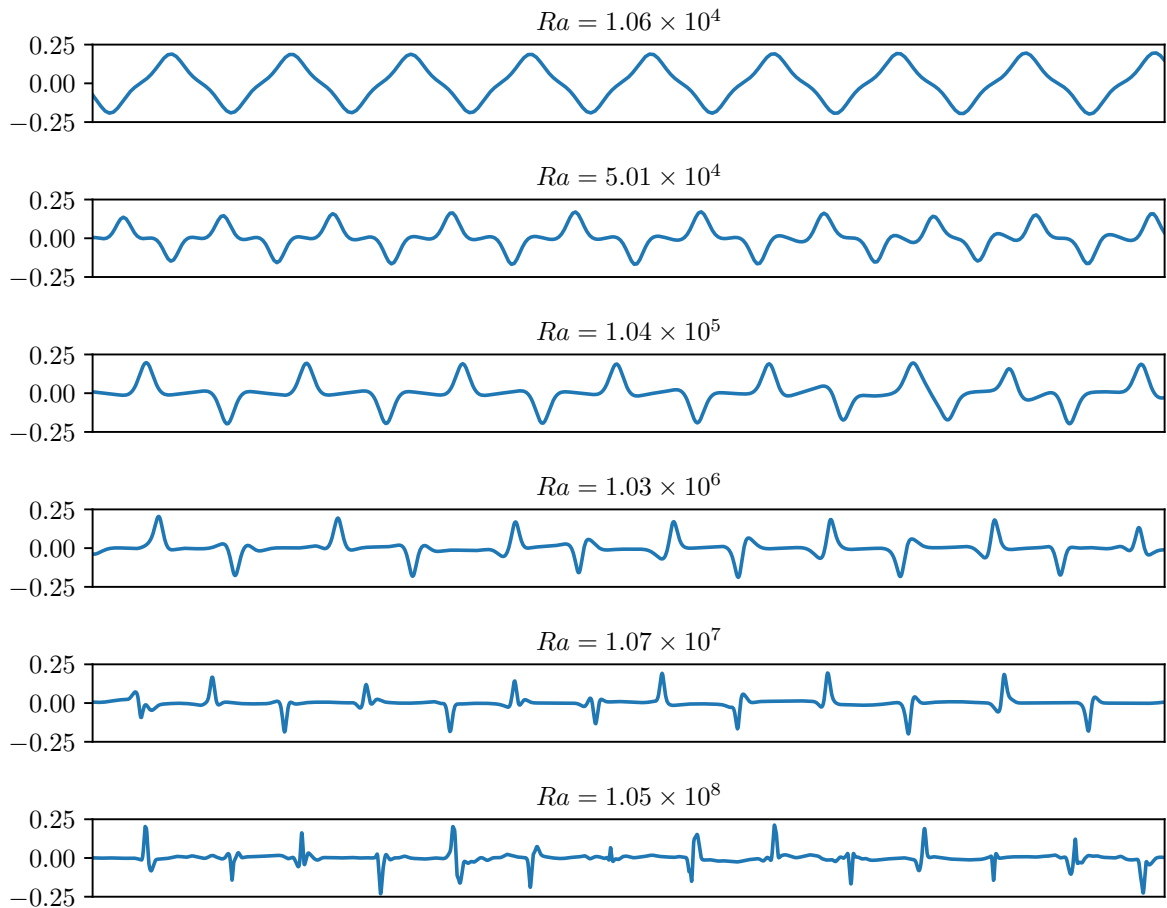


Figure A.2: Temperature field in the midplane of two-dimensional RBC for different Ra from half of the computational domain. The curves represents cuts from figure A.1.

The presence of the large-scale order is readily confirmed by considering, e.g., the cross-spectrum of temperature and vertical velocity as in three dimensions [22, 35]. The cross-spectrum is shown for a single Rayleigh number in figure A.3a. Here, a clear peak is present at small wavenumbers, representing the large-scale flow as in three dimensions. Because of this similarity, we, accordingly, refer to the large-scale flow as superstructure. Besides, also a peak at large wavenumbers is present, which is a result of the small-scale fluctuations. This scale separation is also observed in three dimensions [22, 35]. In figure A.3b, the wavelength corresponding to the peak at small wavenumbers is shown as a function of the Rayleigh number. The wavelength does not follow a clear trend with varying Rayleigh number. Notably, the observed wavelengths are smaller than the wavelength observed at onset $\lambda_c \approx 2$ (cf. Lipps [212] for similar observations closer to onset). This is in contrast to three dimensions, in which the length scale is increasing with Rayleigh number for $Ra > Ra_c$ [22, 30, 35]. However, depending on the initial conditions multiple turbulent states with different number of rolls may emerge in two dimensions [213]. See also Ogura [214] for a numerical study of wavelength selection in two-dimensional RBC for varying initial conditions, and van der Poel et al. [211] for a study of the dependence of the number of rolls on the aspect ratio.

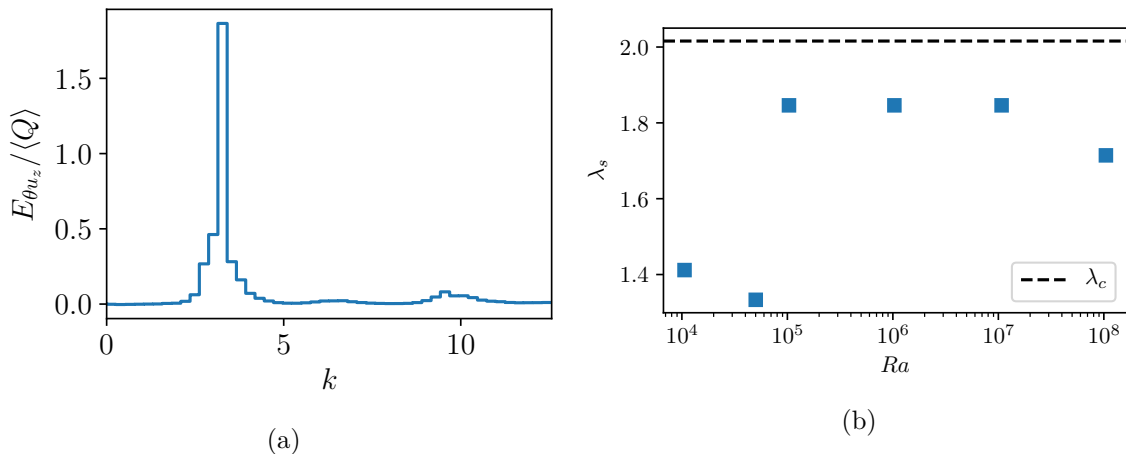


Figure A.3: (a) Cross spectrum of vertical velocity and temperature for $Ra = 1.07 \times 10^7$. (b) Wavelength corresponding to the peak in the cross spectrum as a function of Rayleigh number. Here, $\lambda_c = 2\pi/k_c$ is the critical wavelength for no-slip boundary conditions with $k_c = 3.117$.

How do stronger fluctuations influence the superstructures, and how do they affect the similarities to three dimensions? Investigating these questions in large-aspect-ratio systems is interesting. However, the second question is difficult to address since the simulations in three dimensions are tremendously more expensive and are currently limited to $Ra \sim 10^9$ in large-aspect-ratio systems [31]. In two dimensions, the fluctuations emerge in the form of circular vortices at larger Rayleigh numbers, see figure A.4 for a smaller aspect ratio (or Zhu et al. [207] for visualizations at even higher Rayleigh numbers). While regions of rising and falling fluid are separated at smaller Rayleigh numbers, the vortices move irregularly through the cell, and the different regions mix at larger Rayleigh numbers. However, the regions of plume detaching still appear alternating. Similar to plumes in three dimensions, the vortices cluster during detachment from the boundaries. How and if this flow state changes in larger aspect ratios is an open question.

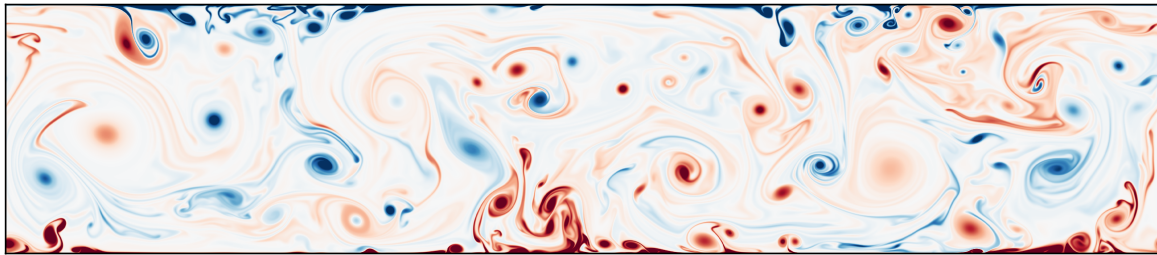


Figure A.4: Temperature field in two-dimensional RBC for $Ra = 1.05 \times 10^{10}$, $Pr = 1$ in an aspect ratio 4 cell.

In conclusion, there is a large-scale flow in large-aspect-ratio two-dimensional RBC that can be called turbulent superstructure. Due to the geometrical confinement, this flow differs from its three-dimensional counterpart in some aspects. Here, the warm and cold plumes do not cluster in the considered Rayleigh number range. But, as in three dimensions the cross-spectrum shows a prominent large-scale peak. This peak characterizes the separation between hot updraughts and cold downdraughts. However, this length scale does not follow a clear trend as a function of the Rayleigh number. In contrast to three dimensions, the corresponding length scale is even smaller compared to onset. To study superstructures in two dimensions in more detail, simulations at larger Rayleigh numbers in large-aspect-ratio cells are necessary. This will clarify, how the emergence of stronger fluctuations, and especially vortices, affect the large-scale flow. Besides, simulations at larger Prandtl number, and comparison with the equivalent three-dimensional case, will reveal if the two-dimensional case resembles the three-dimensional one more closely as previously observed in smaller aspect ratios [208, 209].

A.1 Numerical setup

Input			Output			Time scales	
Ra	Γ	$N_x N_y$	Nu	Nu_ε	Nu_χ	T_t	τ
1.06×10^4	24	512×128	2.676	2.677	2.676	1489.5	930.9
5.01×10^4	24	768×96	4.188	4.192	4.188	2311.2	1540.8
1.04×10^5	24	1280×256	5.120	5.121	5.120	633.9	317.0
1.03×10^6	24	2560×256	8.356	8.360	8.355	1403.6	701.8
1.07×10^7	24	3072×256	14.599	14.666	14.606	3095.1	2481.7
1.05×10^8	24	10240×768	26.687	26.796	26.750	1141.4	575.8
1.05×10^{10}	4	7168×2560	93.976	77.029	93.693	98.4	47.4

Table A.1: Input and reference output parameters of the simulations used in this section. Γ is the aspect ratio, Nu , Nu_ε , and Nu_χ are the Nusselt numbers based on buoyancy, dissipation and thermal dissipation, respectively. T_t is the total runtime of the simulation and τ the length of the average window. Note, that the simulation in aspect ratio 4 is not yet converged, which is why the Nusselt numbers differ.

Backmatter

Bibliography

- [1] B. W. Atkinson and J. Wu Zhang. [Mesoscale shallow convection in the atmosphere](#). *Rev. Geophys.*, 34(4):403–431, 1996. doi: 10.1029/96RG02623.
- [2] Å. Nordlund, R. F. Stein, and M. Asplund. [Solar Surface Convection](#). *Living Rev. Sol. Phys.*, 6(1):2, 2009. doi: 10.12942/lrsp-2009-2.
- [3] A. Hanslmeier. *Einführung in Astronomie und Astrophysik*. Springer Berlin Heidelberg, Berlin, Heidelberg, 2020. doi: 10.1007/978-3-662-60413-7.
- [4] H. Johnston. [Convection cells the size of Texas dazzle with clarity on the Sun](#). *Phys. World*, 33(3):10, 2020. doi: 10.1088/2058-7058/33/3/13.
- [5] How do hurricanes form? <https://spaceplace.nasa.gov/hurricanes/en/>. Viewed on 09.03.2020.
- [6] R. Rotunno. [The Fluid Dynamics of Tornadoes](#). *Annu. Rev. Fluid Mech.*, 45(1):59–84, 2013. doi: 10.1146/annurev-fluid-011212-140639.
- [7] J. P. Terry. *Tropical Cyclones*. Springer New York, New York, NY, 2007. doi: 10.1007/978-0-387-71543-8.
- [8] T. Li and P. Hsu. *Fundamentals of Tropical Climate Dynamics*. Springer Atmospheric Sciences. Springer International Publishing, Cham, 2018. doi: 10.1007/978-3-319-59597-9.
- [9] U. Lohmann, F. Lüönd, and F. Mahrt. *An Introduction to Clouds*. Cambridge University Press, Cambridge, 2016. doi: 10.1017/CBO9781139087513.
- [10] NASA World View. <https://go.nasa.gov/2wkQVM5>. Viewed on 03.03.2020.
- [11] R. A. Brown. [Longitudinal instabilities and secondary flows in the planetary boundary layer: A review](#). *Rev. Geophys.*, 18(3):683, 1980. doi: 10.1029/RG018i003p00683.
- [12] G. S. Young, David A. R. Kristovich, M. R. Hjelmfelt, and R. C. Foster. Rolls, streets, waves, and more: A review of quasi-two-dimensional structures in the atmospheric boundary layer. *Bull. Am. Meteorol. Soc.*, 83(7):997–1001, 2002. doi: 10.1175/1520-0477(2002)083<0997:RSWAMA>2.3.CO;2.
- [13] R. Markson. [Atmospheric Electrical Detection of Organized Convection](#). *Science*, 188(4194):1171–1177, 1975. doi: 10.1126/science.188.4194.1171.

- [14] Cloud streets near Antarctica. <https://earthobservatory.nasa.gov/images/92768/cloud-streets-near-antarctica>, . Viewed on 09.03.2020.
- [15] Winter Cloud Streets, North Atlantic. <https://earthobservatory.nasa.gov/images/49254/winter-cloud-streets-north-atlantica>, . Viewed on 20.07.2020.
- [16] B. Klose. *Meteorologie*. Springer-Lehrbuch. Springer Berlin Heidelberg, Berlin, Heidelberg, 3 edition, 2016. doi: 10.1007/978-3-662-43622-6.
- [17] J. A. Adam. *Mathematics in Nature: Modeling Patterns in the Natural World*. Princeton University Press, 2003.
- [18] W. R. Cotton, G. Bryan, and S. C. van den Heever. *Storm and Cloud Dynamics*. Elsevier Science, 2 edition, 2011.
- [19] G. K. Vallis. *Atmospheric and Oceanic Fluid Dynamics Fundamentals and Large-Scale Circulation*. Cambridge University Press, 2 edition, 2017. doi: 10.1017/9781107588417.
- [20] E. Bodenschatz, S. P. Malinowski, R. A. Shaw, and F. Stratmann. [Can We Understand Clouds Without Turbulence?](#) *Science*, 327(5968):970–971, 2010. doi: 10.1126/science.1185138.
- [21] K. C. Kim and R. J. Adrian. [Very large-scale motion in the outer layer](#). *Phys. Fluids*, 11(2):417–422, 1999. doi: 10.1063/1.869889.
- [22] T. Hartlep, A. Tilgner, and F. H. Busse. [Large Scale Structures in Rayleigh-Bénard Convection at High Rayleigh Numbers](#). *Phys. Rev. Lett.*, 91:064501, 2003. doi: 10.1103/PhysRevLett.91.064501.
- [23] A. J. Smits, B. J. McKeon, and I. Marusic. [High-Reynolds Number Wall Turbulence](#). *Annu. Rev. Fluid Mech.*, 43(1):353–375, 2011. doi: 10.1146/annurev-fluid-122109-160753.
- [24] S.G. Huisman, R.C. Van Der Veen, C. Sun, and D. Lohse. [Multiple states in highly turbulent Taylor–Couette flow](#). *Nat. Commun.*, 5:3820, 2014. doi: 10.1038/ncomms4820.
- [25] S. Grossmann, D. Lohse, and C. Sun. [High-Reynolds Number Taylor-Couette Turbulence](#). *Annu. Rev. Fluid Mech.*, 48(1):53–80, 2016. doi: 10.1146/annurev-fluid-122414-034353.
- [26] R. Ostilla-Mónico, D. Lohse, and R. Verzicco. [Effect of roll number on the statistics of turbulent Taylor-Couette flow](#). *Phys. Rev. Fluids*, 1:054402, 2016. doi: 10.1103/PhysRevFluids.1.054402.
- [27] M. S. Emran and J. Schumacher. [Large-scale mean patterns in turbulent convection](#). *J. Fluid Mech.*, 776:96–108, 2015. doi: 10.1017/jfm.2015.316.
- [28] M. Lee and R. D. Moser. [Extreme-scale motions in turbulent plane Couette flows](#). *J. Fluid Mech.*, 842:128–145, 2018. doi: 10.1017/jfm.2018.131.
- [29] J. Jiménez. [Coherent structures in wall-bounded turbulence](#). *J. Fluid Mech.*, 842:P1, 2018. doi: 10.1017/jfm.2018.144.

- [30] A. Pandey, J. D. Scheel, and J. Schumacher. [Turbulent superstructures in Rayleigh-Bénard convection](#). *Nat. Commun.*, 9(1):2118, 2018. doi: 10.1038/s41467-018-04478-0.
- [31] R. J. A. M. Stevens, A. Blass, X. Zhu, R. Verzicco, and D. Lohse. [Turbulent thermal superstructures in Rayleigh-Bénard convection](#). *Phys. Rev. Fluids*, 3(4):041501, 2018. doi: 10.1103/PhysRevFluids.3.041501.
- [32] C. Kästner, C. Resagk, J. Westphalen, M. Junghähnel, C. Cierpka, and J. Schumacher. [Assessment of horizontal velocity fields in square thermal convection cells with large aspect ratio](#). *Exp. Fluids*, 59(11):171, 2018. doi: 10.1007/s00348-018-2626-9.
- [33] K. Fodor, J. P. Mellado, and M. Wilczek. [On the Role of Large-Scale Updrafts and Downdrafts in Deviations From Monin-Obukhov Similarity Theory in Free Convection](#). *Boundary-Layer Meteorol.*, 172(3):371–396, 2019. doi: 10.1007/s10546-019-00454-3.
- [34] A. Blass, X. Zhu, R. Verzicco, D. Lohse, and R. J. A. M. Stevens. [Flow organization and heat transfer in turbulent wall sheared thermal convection](#). *J. Fluid Mech.*, 897:A22, 2020. doi: 10.1017/jfm.2020.378.
- [35] D. Krug, D. Lohse, and R. J. A. M. Stevens. [Coherence of temperature and velocity superstructures in turbulent Rayleigh-Bénard flow](#). *J. Fluid Mech.*, 887:A2, 2020. doi: 10.1017/jfm.2019.1054.
- [36] H. J. Brauckmann, B. Eckhardt, and J. Schumacher. [Heat transport in Rayleigh-Bénard convection and angular momentum transport in Taylor-Couette flow: a comparative study](#). *Philos. Trans. R. Soc. A Math. Phys. Eng. Sci.*, 375(2089):20160079, 2017. doi: 10.1098/rsta.2016.0079.
- [37] B. Eckhardt, C. R. Doering, and J. P. Whitehead. [Exact relations between Rayleigh-Bénard and rotating plane Couette flow in 2D](#). 2020. arXiv: 2006.09642.
- [38] F. H. Busse. [The twins of turbulence research](#). *Physics*, 5(4), 2012. doi: 10.1103/Physics.5.4.
- [39] C. C. Lalescu and M. Wilczek. Large-scale transitions in fully developed turbulence, 2019. 17th European Turbulence Conference.
- [40] M. Wilczek and C. C. Lalescu. Large-scale transitions of turbulent superstructures in shear flows, 2020. Private communications.
- [41] I. E. Sarris, H. Jeanmart, D. Carati, and G. Winckelmans. [Box-size dependence and breaking of translational invariance in the velocity statistics computed from three-dimensional turbulent Kolmogorov flows](#). *Phys. Fluids*, 19(9):095101, 2007. doi: 10.1063/1.2760280.
- [42] A. M. Obukhov. [Kolmogorov flow and laboratory simulation of it](#). *Russ. Math. Surv.*, 38(4):113–126, 1983. doi: 10.1070/RM1983v038n04ABEH004207.
- [43] C. Bauer, A. von Kameke, and C. Wagner. [Kinetic energy budget of the largest scales in turbulent pipe flow](#). *Phys. Rev. Fluids*, 4(6):064607, 2019. doi: 10.1103/PhysRevFluids.4.064607.

- [44] B. J. Balakumar and R. J. Adrian. [Large- and very-large-scale motions in channel and boundary-layer flows](#). *Philos. Trans. R. Soc. A Math. Phys. Eng. Sci.*, 365(1852):665–681, 2007. doi: 10.1098/rsta.2006.1940.
- [45] N. Hutchins and I. Marusic. [Evidence of very long meandering features in the logarithmic region of turbulent boundary layers](#). *J. Fluid Mech.*, 579:1–28, 2007. doi: 10.1017/S0022112006003946.
- [46] P. Davidson. *Turbulence: An Introduction for Scientists and Engineers*. Oxford University Press, 2 edition, 2015. doi: 10.1093/acprof:oso/9780198722588.001.0001.
- [47] S. B. Pope. *Turbulent Flows*. Cambridge University Press, 2000. doi: 10.1017/CBO9780511840531.
- [48] R. Hoyle. *Pattern Formation: An Introduction to Methods*. Cambridge University Press, 2006. doi: 10.1017/CBO9780511616051.
- [49] M. Cross and H. Greenside. *Pattern Formation and Dynamics in Nonequilibrium Systems*. Cambridge University Press, Cambridge, England, 2009. doi: 10.1017/CBO9780511627200.
- [50] M. C. Cross and P. C. Hohenberg. [Pattern formation outside of equilibrium](#). *Rev. Mod. Phys.*, 65:851–1112, 1993. doi: 10.1103/RevModPhys.65.851.
- [51] J. Beaufort. [Ripples in the sand dunes](https://www.publicdomainpictures.net/pictures/170000/velka/ripples-in-the-sand-dunes.jpg). <https://www.publicdomainpictures.net/pictures/170000/velka/ripples-in-the-sand-dunes.jpg>. Viewed on 23.06.2020.
- [52] P. Kratochvil. [Giraffe skin texture](https://www.publicdomainpictures.net/pictures/50000/velka/giraffe-skin-texture-1373555221POB.jpg). <https://www.publicdomainpictures.net/pictures/50000/velka/giraffe-skin-texture-1373555221POB.jpg>. Viewed on 23.06.2020.
- [53] A. V. Getling. *Rayleigh-Bénard Convection*, volume 11 of *Advanced Series in Nonlinear Dynamics*. World Scientific, 1998. doi: 10.1142/3097.
- [54] F. Chillà and J. Schumacher. [New perspectives in turbulent Rayleigh-Bénard convection](#). *Eur. Phys. J. E*, 35(7):58, 2012. doi: 10.1140/epje/i2012-12058-1.
- [55] E. S. C. Ching. *Statistics and Scaling in Turbulent Rayleigh-Bénard Convection*. Springer Singapore, 2014. doi: 10.1007/978-981-4560-23-8.
- [56] M. K. Verma. *Physics of Buoyant Flows*. World Scientific, 2018. doi: 10.1142/10928.
- [57] E. D. Siggia. [High Rayleigh Number Convection](#). *Annu. Rev. Fluid Mech.*, 26(1):137–168, 1994. doi: 10.1146/annurev.fl.26.010194.001033.
- [58] E. Bodenschatz, W. Pesch, and G. Ahlers. [Recent developments in Rayleigh-Bénard convection](#). *Annu. Rev. Fluid Mech.*, 32(1):709–778, 2000. doi: 10.1146/annurev.fluid.32.1.709.
- [59] G. Ahlers, S. Grossmann, and D. Lohse. [Heat transfer and large scale dynamics in turbulent Rayleigh-Bénard convection](#). *Rev. Mod. Phys.*, 81:503–537, 2009. doi: 10.1103/RevModPhys.81.503.

- [60] D. Lohse and K.-Q. Xia. [Small-Scale Properties of Turbulent Rayleigh-Bénard Convection](#). *Annu. Rev. Fluid Mech.*, 42(1):335–364, 2010. doi: 10.1146/annurev.fluid.010908.165152.
- [61] T. Hartlep, A. Tilgner, and F. H. Busse. [Transition to turbulent convection in a fluid layer heated from below at moderate aspect ratio](#). *J. Fluid Mech.*, 544:309–322, 2005. doi: 10.1017/S0022112005006671.
- [62] A. Parodi, J. von Hardenberg, G. Passoni, A. Provenzale, and E. A. Spiegel. [Clustering of Plumes in Turbulent Convection](#). *Phys. Rev. Lett.*, 92(19):194503, 2004. doi: 10.1103/physrevlett.92.194503.
- [63] J. von Hardenberg, A. Parodi, G. Passoni, A. Provenzale, and E. A. Spiegel. [Large-scale patterns in Rayleigh-Bénard convection](#). *Phys. Lett. A*, 372(13):2223–2229, 2008. doi: 10.1016/j.physleta.2007.10.099.
- [64] O. Shishkina and C. Wagner. [Analysis of thermal dissipation rates in turbulent Rayleigh-Bénard convection](#). *J. Fluid Mech.*, 546:51–60, 2006. doi: 10.1017/S0022112005007408.
- [65] C. Schneide, A. Pandey, K. Padberg-Gehle, and J. Schumacher. [Probing turbulent superstructures in Rayleigh-Bénard convection by Lagrangian trajectory clusters](#). *Phys. Rev. Fluids*, 3(11):113501, 2018. doi: 10.1103/PhysRevFluids.3.113501.
- [66] J. Swift and P. C. Hohenberg. [Hydrodynamic fluctuations at the convective instability](#). *Phys. Rev. A*, 15:319–328, 1977. doi: 10.1103/PhysRevA.15.319.
- [67] G. Green, D. G. Vlaykov, J. P. Mellado, and M. Wilczek. [Resolved energy budget of superstructures in Rayleigh-Bénard convection](#). *J. Fluid Mech.*, 887:A21, 2020. doi: 10.1017/jfm.2019.1008.
- [68] G. Ibbeken, G. Green, and M. Wilczek. [Large-Scale Pattern Formation in the Presence of Small-Scale Random Advection](#). *Phys. Rev. Lett.*, 123:114501, 2019. doi: 10.1103/PhysRevLett.123.114501.
- [69] J. C. Wyngaard. *Turbulence in the Atmosphere*. Cambridge University Press, Cambridge, 2010. doi: 10.1017/CBO9780511840524.
- [70] B. Stevens. [Atmospheric Moist Convection](#). *Annu. Rev. Earth Planet. Sci.*, 33(1):605–643, 2005. doi: 10.1146/annurev.earth.33.092203.122658.
- [71] L. R. Glicksman. [Energy efficiency in the built environment](#). *Phys. Today*, 61(7):35–40, 2008. doi: 10.1063/1.2963035.
- [72] G. R. Hunt and P. P. Linden. [The fluid mechanics of natural ventilation—displacement ventilation by buoyancy-driven flows assisted by wind](#). *Build. Environ.*, 34(6):707–720, 1999. doi: 10.1016/S0360-1323(98)00053-5.
- [73] P. F. Linden. [The fluid mechanics of natural ventilation](#). *Annu. Rev. Fluid Mech.*, 31(1):201–238, 1999. doi: 10.1146/annurev.fluid.31.1.201.
- [74] C. Gladstone and A. W. Woods. [On buoyancy-driven natural ventilation of a room with a heated floor](#). *J. Fluid Mech.*, 441:293–314, 2001. doi: 10.1017/S0022112001004876.

- [75] M. Kühn, J. Bosbach, and C. Wagner. [Experimental parametric study of forced and mixed convection in a passenger aircraft cabin mock-up](#). *Build. Environ.*, 44(5):961–970, 2009. doi: 10.1016/j.buildenv.2008.06.020.
- [76] P. Manneville. *Dissipative Structures and Weak Turbulence*. Elsevier, 1990. doi: 10.1016/C2009-0-22357-9.
- [77] M. K. Verma, A. Kumar, and A. Pandey. [Phenomenology of buoyancy-driven turbulence: recent results](#). *New J. Phys.*, 19(2):025012, 2017. doi: 10.1088/1367-2630/aa5d63.
- [78] P. Sagaut and C. Cambon. *Homogeneous Turbulence Dynamics*. Springer International Publishing, Cham, 2 edition, 2018. doi: 10.1007/978-3-319-73162-9.
- [79] E. Guyon, J.-P. Hulin, L. Petit, and C. D. Mitescu. *Physical Hydrodynamics*. Oxford University Press, 2 edition, 2015. doi: 10.1093/acprof:oso/9780198702443.001.0001.
- [80] D. J. Tritton. *Physical Fluid Dynamics*. Springer Netherlands, Dordrecht, 1977. doi: 10.1007/978-94-009-9992-3.
- [81] S. Chandrasekhar. *Hydrodynamic and Hydromagnetic Stability*. Dover Books on Physics. Dover Publications, 2013.
- [82] P. Manneville. [A two-dimensional model for three-dimensional convective patterns in wide containers](#). *J. Phys.*, 44(7):759–765, 1983. doi: 10.1051/jphys:01983004407075900.
- [83] G. E. Willis, J. W. Deardorff, and R. C. J. Somerville. [Roll-diameter dependence in Rayleigh convection and its effect upon the heat flux](#). *J. Fluid Mech.*, 54(2):351–367, 1972. doi: 10.1017/S0022112072000722.
- [84] D. E. Fitzjarrald. [An experimental study of turbulent convection in air](#). *J. Fluid Mech.*, 73(4):693–719, 1976. doi: 10.1017/S0022112076001572.
- [85] F. H. Busse. [Non-linear properties of thermal convection](#). *Rep. Prog. Phys.*, 41(12):1929, 1978. doi: 10.1088/0034-4885/41/12/003.
- [86] F. H. Busse and J. A. Whitehead. [Instabilities of convection rolls in a high Prandtl number fluid](#). *J. Fluid Mech.*, 47(2):305–320, 1971. doi: 10.1017/S0022112071001071.
- [87] R. Krishnamurti and L. N. Howard. [Large-scale flow generation in turbulent convection](#). *Proc. Natl. Acad. Sci.*, 78(4):1981–1985, 1981. doi: 10.1073/pnas.78.4.1981.
- [88] R. V. Cakmur, D. A. Egolf, B. B. Plapp, and E. Bodenschatz. [Bistability and Competition of Spatiotemporal Chaotic and Fixed Point Attractors in Rayleigh-Bénard Convection](#). *Phys. Rev. Lett.*, 79(10):1853–1856, 1997. doi: 10.1103/PhysRevLett.79.1853.
- [89] W. Decker, W. Pesch, and A. Weber. [Spiral defect chaos in Rayleigh-Bénard convection](#). *Phys. Rev. Lett.*, 73(5):648–651, 1994. doi: 10.1103/PhysRevLett.73.648.
- [90] K.-H. Chiam, M. R. Paul, M. C. Cross, and H. S. Greenside. [Mean flow and spiral defect chaos in Rayleigh-Bénard convection](#). *Phys. Rev. E*, 67(5):56206, 2003. doi: 10.1103/PhysRevE.67.056206.

- [91] E. D. Siggia and A. Zippelius. [Pattern Selection in Rayleigh-Bénard Convection near Threshold](#). *Phys. Rev. Lett.*, 47(12):835–838, 1981. doi: 10.1103/PhysRevLett.47.835.
- [92] A. Zippelius and E. D. Siggia. [Stability of finite-amplitude convection](#). *Phys. Fluids*, 26(10):2905, 1983. doi: 10.1063/1.864055.
- [93] M. C. Cross and A. C. Newell. [Convection patterns in large aspect ratio systems](#). *Physica*, 10D(3):299 – 328, 1984. doi: 10.1016/0167-2789(84)90181-7.
- [94] M. C. Cross. [Phase dynamics of convective rolls](#). *Phys. Rev. A*, 27(1):490–498, 1983. doi: 10.1103/PhysRevA.27.490.
- [95] A. C. Newell, T. Passot, and M. Souli. [The phase diffusion and mean drift equations for convection at finite Rayleigh numbers in large containers](#). *J. Fluid Mech.*, 220:187–252, 1990. doi: 10.1017/S0022112090003238.
- [96] H. S. Greenside and W. M. Coughran. [Nonlinear pattern formation near the onset of Rayleigh-Bénard convection](#). *Phys. Rev. A*, 30(1):398–428, 1984. doi: 10.1103/PhysRevA.30.398.
- [97] H. S. Greenside and M. C. Cross. [Stability analysis of two-dimensional models of three-dimensional convection](#). *Phys. Rev. A*, 31(4):2492–2501, 1985. doi: 10.1103/PhysRevA.31.2492.
- [98] P. Manneville. *Instabilities, Chaos and Turbulence*, volume 1 of *ICP Fluid Mechanics*. Imperial College Press, 2 edition, 2010. doi: 10.1142/p642.
- [99] S. H. Strogatz. *Nonlinear Dynamics and Chaos With Applications to Physics, Biology, Chemistry, and Engineering*. CRC Press, 2 edition, 2015. doi: 10.1201/9780429492563.
- [100] K.-H. Goldhorn, H.-P. Heinz, and M. Kraus. *Moderne mathematische Methoden der Physik*. Springer-Lehrbuch. Springer Berlin Heidelberg, Berlin, Heidelberg, 2009. doi: 10.1007/978-3-540-88544-3.
- [101] M. C. Cross. [Derivation of the amplitude equation at the Rayleigh-Bénard instability](#). *Phys. Fluids*, 23(9):1727–1731, 1980. doi: 10.1063/1.863198.
- [102] G. Ahlers, M. C. Cross, P. C. Hohenberg, and S. Safran. [The amplitude equation near the convective threshold: application to time-dependent heating experiments](#). *J. Fluid Mech.*, 110:297–334, 1981. doi: 10.1017/S0022112081000761.
- [103] F. H. Busse. [Transition to turbulence in Rayleigh-Bénard convection](#). In H. L. Swinney and J. P. Gollub, editors, *Hydrodyn. Instab. Transit. to Turbul.*, pages 97–137. Springer Berlin Heidelberg, Berlin, Heidelberg, 1985. doi: 10.1007/3-540-13319-4_15.
- [104] M. Cross. [Theoretical modelling of spiral chaos in Rayleigh-Benard convection](#). *Phys. D Nonlinear Phenom.*, 97(1):65–80, 1996. doi: 10.1016/0167-2789(96)00144-3.
- [105] H. Xi, J. D. Gunton, and J. Viñals. [Spiral defect chaos in a model of Rayleigh-Bénard convection](#). *Phys. Rev. Lett.*, 71(13):2030–2033, 1993. doi: 10.1103/PhysRevLett.71.2030.

- [106] H. S. Greenside, M. C. Cross, and W. M. Coughran. [Mean Flows and the Onset of Chaos in Large-Cell Convection](#). *Phys. Rev. Lett.*, 60(22):2269–2272, 1988. doi: 10.1103/PhysRevLett.60.2269.
- [107] R. Schmitz, W. Pesch, and W. Zimmermann. [Spiral-defect chaos: Swift-Hohenberg model versus Boussinesq equations](#). *Phys. Rev. E*, 65(3):37302, 2002. doi: 10.1103/PhysRevE.65.037302.
- [108] T. Elperin, N. Kleorin, I. Rogachevskii, and S. Zilitinkevich. [Formation of large-scale semiorganized structures in turbulent convection](#). *Phys. Rev. E*, 66(6):066305, 2002. doi: 10.1103/PhysRevE.66.066305.
- [109] T. Elperin, N. Kleorin, I. Rogachevskii, and S. S. Zilitinkevich. [Tangling Turbulence and Semi-Organized Structures in Convective Boundary Layers](#). *Bound.-Layer Meteorol.*, 119(3):449–472, 2006. doi: 10.1007/s10546-005-9041-5.
- [110] T. Elperin, I. Golubev, N. Kleorin, and I. Rogachevskii. [Large-scale instabilities in a nonrotating turbulent convection](#). *Phys. Fluids*, 18(12):126601, 2006. doi: 10.1063/1.2401223.
- [111] E. Fonda, A. Pandey, J. Schumacher, and K. R. Sreenivasan. [Deep learning in turbulent convection networks](#). *Proc. Natl. Acad. Sci.*, 116(18):8667–8672, 2019. doi: 10.1073/pnas.1900358116.
- [112] P. Berghout, W. J. Baars, and D. Krug. [The large-scale footprint in small-scale Rayleigh-Bénard turbulence](#). 2020. arXiv: 2007.09994.
- [113] J. P. Mellado and C. Ansorge. [Factorization of the Fourier transform of the pressure-Poisson equation using finite differences in colocated grids](#). *Z. Angew. Math. Mech.*, 92(5):380–392, 2012. doi: 10.1002/zamm.201100078.
- [114] J. P. Mellado. [Direct numerical simulation of free convection over a heated plate](#). *J. Fluid Mech.*, 712:418–450, 2012. doi: 10.1017/jfm.2012.428.
- [115] S. W. Morris, E. Bodenschatz, D. S. Cannell, and G. Ahlers. [Spiral defect chaos in large aspect ratio Rayleigh-Bénard convection](#). *Phys. Rev. Lett.*, 71:2026–2029, 1993. doi: 10.1103/PhysRevLett.71.2026.
- [116] S. Grossmann and D. Lohse. [Fluctuations in turbulent Rayleigh-Bénard convection: The role of plumes](#). *Phys. Fluids*, 16(12):4462–4472, 2004. doi: 10.1063/1.1807751.
- [117] J. Schumacher, A. Pandey, V. Yakhot, and K. R. Sreenivasan. [Transition to turbulence scaling in Rayleigh-Bénard convection](#). *Phys. Rev. E*, 98(3):033120, 2018. doi: 10.1103/PhysRevE.98.033120.
- [118] D. Krug, D. Lohse, and R. J. A. M. Stevens. [Coherence of temperature and velocity superstructures in turbulent Rayleigh-Bénard flow](#). *J. Fluid Mech.* (in press), 2019. arXiv: 1908.10073.
- [119] J. Lülff, M. Wilczek, and R. Friedrich. [Temperature statistics in turbulent Rayleigh-Bénard convection](#). *New J. Phys.*, 13(1):015002, 2011. doi: 10.1088/1367-2630/13/1/015002.

- [120] J. Lülff, M. Wilczek, R. J. A. M. Stevens, R. Friedrich, and D. Lohse. [Turbulent Rayleigh-Bénard convection described by projected dynamics in phase space](#). *J. Fluid Mech.*, 781:276–297, 2015. doi: 10.1017/jfm.2015.495.
- [121] R. Togni, A. Cimarelli, and E. De Angelis. [Physical and scale-by-scale analysis of Rayleigh-Bénard convection](#). *J. Fluid Mech.*, 782:380–404, 2015. doi: 10.1017/jfm.2015.547.
- [122] S. J. Kimmel and J. A. Domaradzki. [Large eddy simulations of Rayleigh-Bénard convection using subgrid scale estimation model](#). *Phys. Fluids*, 12(1):169–184, 2000. doi: 10.1063/1.870292.
- [123] R. Togni, A. Cimarelli, and E. De Angelis. [Towards an Improved Subgrid-Scale Model for Thermally Driven Flows](#). In R. Örlü, A. Talamelli, M. Oberlack, and J. Peinke, editors, *Progress in Turbulence VII*, pages 141–145, Cham, 2017. Springer International Publishing. doi: 10.1007/978-3-319-57934-4_20.
- [124] R. Togni, A. Cimarelli, and E. De Angelis. [Resolved and subgrid dynamics of Rayleigh-Bénard convection](#). *J. Fluid Mech.*, 867:906–933, 2019. doi: 10.1017/jfm.2019.119.
- [125] V. Valori, A. Innocenti, B. Dubrulle, and S. Chibbaro. [Weak formulation and scaling properties of energy fluxes in three-dimensional numerical turbulent Rayleigh-Bénard convection](#). *J. Fluid Mech.*, 885:A14, 2020. doi: 10.1017/jfm.2019.1000.
- [126] D. Faranda, V. Lembo, M. Iyer, D. Kuzzay, S. Chibbaro, F. Daviaud, and B. Dubrulle. [Computation and Characterization of Local Subfilter-Scale Energy Transfers in Atmospheric Flows](#). *J. Atmos. Sci.*, 75(7):2175–2186, 2018. doi: 10.1175/JAS-D-17-0114.1.
- [127] M. Germano. [Turbulence: the filtering approach](#). *J. Fluid Mech.*, 238:325–336, 1992. doi: 10.1017/S0022112092001733.
- [128] B. I. Shraiman and E. D. Siggia. [Heat transport in high-Rayleigh-number convection](#). *Phys. Rev. A*, 42(6):3650–3653, 1990. doi: 10.1103/PhysRevA.42.3650.
- [129] P. Sagaut. *Large Eddy Simulation for Incompressible Flows*. Springer, 3 edition, 2006. doi: 10.1007/b137536.
- [130] A. Cimarelli and E. De Angelis. [Analysis of the Kolmogorov equation for filtered wall-turbulent flows](#). *J. Fluid Mech.*, 676:376–395, 2011. doi: 10.1017/S0022112011000565.
- [131] G. L. Eyink. [Local energy flux and the refined similarity hypothesis](#). *J. Stat. Phys.*, 78(1):335–351, 1995. doi: 10.1007/BF02183352.
- [132] G. L. Eyink. [Turbulence Theory, course notes, The Johns Hopkins University, 2007-2008, 2007](#). Available at <http://www.ams.jhu.edu/~eyink/Turbulence/notes.html>.
- [133] G. L. Eyink and H. Aluie. [Localness of energy cascade in hydrodynamic turbulence. I. Smooth coarse graining](#). *Phys. Fluids*, 21(11):115107, 2009. doi: 10.1063/1.3266883.
- [134] H. Aluie and G. L. Eyink. [Localness of energy cascade in hydrodynamic turbulence. II. Sharp spectral filter](#). *Phys. Fluids*, 21(11):115108, 2009. doi: 10.1063/1.3266948.

- [135] K. Petschel, S. Stellmach, M. Wilczek, J. Lülff, and U. Hansen. [Kinetic energy transport in Rayleigh-Bénard convection](#). *J. Fluid Mech.*, 773:395–417, 2015. doi: 10.1017/jfm.2015.216.
- [136] J. A. Domaradzki, W. Liu, C. Härtel, and L. Kleiser. [Energy transfer in numerically simulated wall-bounded turbulent flows](#). *Phys. Fluids*, 6(4):1583–1599, 1994. doi: 10.1063/1.868272.
- [137] H. Lomax, T. H. Pulliam, and D. W. Zingg. *Fundamentals of Computational Fluid Dynamics*. Scientific Computation. Springer Berlin Heidelberg, 2001. doi: 10.1007/978-3-662-04654-8.
- [138] R. Verzicco and R. Camussi. [Numerical experiments on strongly turbulent thermal convection in a slender cylindrical cell](#). *J. Fluid Mech.*, 477:19–49, 2003. doi: 10.1017/S0022112002003063.
- [139] O. Shishkina, R. J. A. M. Stevens, S. Grossmann, and D. Lohse. [Boundary layer structure in turbulent thermal convection and its consequences for the required numerical resolution](#). *New J. Phys.*, 12(7):075022, 2010. doi: 10.1088/1367-2630/12/7/075022.
- [140] J. C. Kaimal, J. C. Wyngaard, D. A. Haugen, O. R. Coté, Y. Izumi, S. J. Caughey, and C. J. Readings. [Turbulence Structure in the Convective Boundary Layer](#). *J. Atmos. Sci.*, 33(11):2152–2169, 1976. doi: 10.1175/1520-0469(1976)033<2152:TSITCB>2.0.CO;2.
- [141] J. P. Mellado, C. C. van Heerwaarden, and J. R. Garcia. [Near-Surface Effects of Free Atmosphere Stratification in Free Convection](#). *Boundary-Layer Meteorol.*, 159(1):69–95, 2016. doi: 10.1007/s10546-015-0105-x.
- [142] J. G. Ballouz and N. T. Ouellette. [Tensor geometry in the turbulent cascade](#). *J. Fluid Mech.*, 835:1048–1064, 2018. doi: 10.1017/jfm.2017.802.
- [143] M. Buzzicotti, M. Linkmann, H. Aluie, L. Biferale, J. Brasseur, and C. Meneveau. [Effect of filter type on the statistics of energy transfer between resolved and subfilter scales from a-priori analysis of direct numerical simulations of isotropic turbulence](#). *J. Turbul.*, 19(2):167–197, 2018. doi: 10.1080/14685248.2017.1417597.
- [144] N. Marati, C. M. Casciola, and R. Piva. [Energy cascade and spatial fluxes in wall turbulence](#). *J. Fluid Mech.*, 521:191–215, 2004. doi: 10.1017/S0022112004001818.
- [145] A. Cimarelli and E. De Angelis. [Anisotropic dynamics and sub-grid energy transfer in wall-turbulence](#). *Phys. Fluids*, 24(1):015102, 2012. doi: 10.1063/1.3675626.
- [146] A. Cimarelli, E. De Angelis, P. Schlatter, G. Brethouwer, A. Talamelli, and C. M. Casciola. [Sources and fluxes of scale energy in the overlap layer of wall turbulence](#). *J. Fluid Mech.*, 771:407–423, 2015. doi: 10.1017/jfm.2015.182.
- [147] K. Petschel, S. Stellmach, M. Wilczek, J. Lülff, and U. Hansen. [Dissipation Layers in Rayleigh-Bénard Convection: A Unifying View](#). *Phys. Rev. Lett.*, 110(11):114502, 2013. doi: 10.1103/PhysRevLett.110.114502.
- [148] J. D. Scheel and J. Schumacher. [Local boundary layer scales in turbulent Rayleigh-Bénard convection](#). *J. Fluid Mech.*, 758:344–373, 2014. doi: 10.1017/jfm.2014.536.

- [149] G. Ibbeken. *Pattern Formation in the Swift-Hohenberg Equation with Fluctuating Advection*. Bachelor's thesis, University of Göttingen, 2017. Bachelor thesis at the Max Planck Institute for Dynamics and Self-Organization.
- [150] A. C. Newell and J. A. Whitehead. [Finite bandwidth, finite amplitude convection](#). *J. Fluid Mech.*, 38(2):279–303, 1969. doi: 10.1017/S0022112069000176.
- [151] Lee A. Segel. [Distant side-walls cause slow amplitude modulation of cellular convection](#). *J. Fluid Mech.*, 38(1):203–224, 1969. doi: 10.1017/S0022112069000127.
- [152] Y. Pomeau and P. Manneville. [Wavelength selection in cellular flows](#). *Phys. Lett.*, 75A(4):296–298, 1980. doi: 10.1016/0375-9601(80)90568-X.
- [153] A. C. Newell, T. Passot, and J. Lega. [Order parameter equations for patterns](#). *Annu. Rev. Fluid Mech.*, 25(1):399–453, 1993. doi: 10.1146/annurev.fl.25.010193.002151.
- [154] M. S. Heutmaker and J. P. Gollub. [Wave-vector field of convective flow patterns](#). *Phys. Rev. A*, 35:242–260, 1987. doi: 10.1103/PhysRevA.35.242.
- [155] Y. Hu, R. Ecke, and G. Ahlers. [Convection for Prandtl numbers near 1: Dynamics of textured patterns](#). *Phys. Rev. E*, 51:3263–3279, 1995. doi: 10.1103/PhysRevE.51.3263.
- [156] R. H. Kraichnan. [Small-Scale Structure of a Scalar Field Convected by Turbulence](#). *Phys. Fluids*, 11(5):945–953, 1968. doi: 10.1063/1.1692063.
- [157] A. P. Kazantsev. Enhancement of a magnetic field by a conducting fluid. *Sov. Phys. JETP*, 26(5):1031, 1968.
- [158] G. Falkovich, K. Gawędzki, and M. Vergassola. [Particles and fields in fluid turbulence](#). *Rev. Mod. Phys.*, 73(4):913, 2001. doi: 10.1103/RevModPhys.73.913.
- [159] C. Gardiner. *Stochastic Methods: A Handbook for the Natural and Social Sciences*. Springer Series in Synergetics. Springer, New York, 4 edition, 2010.
- [160] K. Furutsu. [On the statistical theory of electromagnetic waves in a fluctuating medium \(I\)](#). *J. Res. Nat. Bur. Stand.*, 67D(3):303–323, 1963. doi: 10.6028/jres.067D.034.
- [161] M. D. Donsker, On Function Space Integrals, in. *Proc. of the Conf. on Theory and Applications of Analysis in Function Space*. The MIT Press, Cambridge, 1964.
- [162] E. A. Novikov. Functionals and the random-force method in turbulence theory. *Sov. Phys. JETP*, 20(5):1290–1294, 1965.
- [163] See Supplemental Material for a description of the generalization of our approach to time averaging, as well as a detailed discussion of its limitations.
- [164] G. Eyink and J. Xin. [Statistical analysis of a semilinear hyperbolic system advected by a white in time random velocity field](#). *Nonlinearity*, 15(3):551, 2002. doi: 10.1088/0951-7715/15/3/302.
- [165] P. C. Hohenberg and J. B. Swift. [Effects of additive noise at the onset of Rayleigh-Bénard convection](#). *Phys. Rev. A*, 46:4773–4785, 1992. doi: 10.1103/PhysRevA.46.4773.

- [166] K. R. Elder, J. Viñals, and M. Grant. [Ordering Dynamics in the Two-Dimensional Stochastic Swift-Hohenberg Equation](#). *Phys. Rev. Lett.*, 68:3024–3027, 1992. doi: 10.1103/PhysRevLett.68.3024.
- [167] J. Garcia-Ojalvo and J. Sancho. *Noise in Spatially Extended Systems*. Institute for Nonlinear Science. Springer New York, 2012. doi: 10.1007/978-1-4612-1536-3.
- [168] J. García-Ojalvo, A. Hernández-Machado, and J. M. Sancho. [Effects of External Noise on the Swift-Hohenberg Equation](#). *Phys. Rev. Lett.*, 71:1542–1545, 1993. doi: 10.1103/PhysRevLett.71.1542.
- [169] N. Platt, E. A. Spiegel, and C. Tresser. [On-off intermittency: A mechanism for bursting](#). *Phys. Rev. Lett.*, 70:279–282, 1993. doi: 10.1103/PhysRevLett.70.279.
- [170] S. Aumaître, F. Pétrélis, and K. Mallick. [Low-Frequency Noise Controls On-Off Intermittency of Bifurcating Systems](#). *Phys. Rev. Lett.*, 95(6):064101, 2005. doi: 10.1103/PhysRevLett.95.064101.
- [171] H. Fujisaka, K. Ouchi, and H. Ohara. [On-off convection: Noise-induced intermittency near the convection threshold](#). *Phys. Rev. E*, 64(3):036201, 2001. doi: 10.1103/PhysRevE.64.036201.
- [172] C. Bailly and G. Comte-Bellot. *Turbulence*. Experimental Fluid Mechanics. Springer International Publishing, Cham, 2015. doi: 10.1007/978-3-319-16160-0.
- [173] W. Paul and J. Baschnagel. *Stochastic Processes*. Springer International Publishing, Heidelberg, 2 edition, 2013. doi: 10.1007/978-3-319-00327-6.
- [174] B. Øksendal. *Stochastic Differential Equations*. Universitext. Springer Berlin Heidelberg, Berlin, Heidelberg, 6 edition, 2003. doi: 10.1007/978-3-642-14394-6.
- [175] S. A. Orszag. [On the Elimination of Aliasing in Finite-Difference Schemes by Filtering High-Wavenumber Components](#). *J. Atmos. Sci.*, 28(6):1074–1074, 1971. doi: 10.1175/1520-0469(1971)028<1074:OTEOAI>2.0.CO;2.
- [176] B. Stevens. [Bulk boundary-layer concepts for simplified models of tropical dynamics](#). 20(5-6):279–304, 2006. doi: 10.1007/s00162-006-0032-z.
- [177] J. A. Trangenstein. *Scientific Computing*, volume 20 of *Texts in Computational Science and Engineering*. Springer International Publishing, Cham, 2017. doi: 10.1007/978-3-319-69110-7.
- [178] P. Virtanen, R. Gommers, T. E. Oliphant, M. Haberland, T. Reddy, D. Cournapeau, E. Burovski, P. Peterson, W. Weckesser, J. Bright, S. J. van der Walt, M. Brett, J. Wilson, K. J. Millman, N. Mayorov, A. R. J. Nelson, E. Jones, R. Kern, E. Larson, C. J. Carey, Í. Polat, Y. Feng, E. W. Moore, J. VanderPlas, D. Laxalde, J. Perktold, R. Cimrman, I. Henriksen, E. A. Quintero, C. R. Harris, A. M. Archibald, A. H. Ribeiro, F. Pedregosa, and P. van Mulbregt. [SciPy 1.0: fundamental algorithms for scientific computing in Python](#). *Nat. Methods*, 17(3):261–272, 2020. doi: 10.1038/s41592-019-0686-2.
- [179] P. A. Durbin. [Some Recent Developments in Turbulence Closure Modeling](#). *Annu. Rev. Fluid Mech.*, 50(1):77–103, 2018. doi: 10.1146/annurev-fluid-122316-045020.

- [180] K. Hanjalić. [One-point closure models for buoyancy-driven turbulent flows](#). *Annu. Rev. Fluid Mech.*, 34(1):321–347, 2002. doi: 10.1146/annurev.fluid.34.082801.161035.
- [181] L. Berselli, T. Ilescu, and W. J. Layton. *Mathematics of Large Eddy Simulation of Turbulent Flows*. Scientific Computation. Springer-Verlag, Berlin/Heidelberg, 2006. doi: 10.1007/b137408.
- [182] C. Meneveau and J. Katz. [Scale-Invariance and Turbulence Models for Large-Eddy Simulation](#). *Annu. Rev. Fluid Mech.*, 32(1):1–32, 2000. doi: 10.1146/annurev.fluid.32.1.1.
- [183] B.-C. Wang, E. Yee, J. Yin, and D. J. Bergstrom. [A General Dynamic Linear Tensor-Diffusivity Subgrid-Scale Heat Flux Model for Large-Eddy Simulation of Turbulent Thermal Flows](#). *Numer. Heat Transf. Part B Fundam.*, 51(3):205–227, 2007. doi: 10.1080/10407790601102274.
- [184] B.-C. Wang, E. Yee, D. J. Bergstrom, and O. Iida. [New dynamic subgrid-scale heat flux models for large-eddy simulation of thermal convection based on the general gradient diffusion hypothesis](#). *J. Fluid Mech.*, 604:125–163, 2008. doi:10.1017/S0022112008001079.
- [185] B. A. Younis, C. G. Speziale, and T. T. Clark. [A rational model for the turbulent scalar fluxes](#). *Proc. R. Soc. A Math. Phys. Eng. Sci.*, 461(2054):575–594, 2005. doi: 10.1098/rspa.2004.1380.
- [186] S. B. Pope. [A more general effective-viscosity hypothesis](#). *J. Fluid Mech.*, 72(02):331, 1975. doi: 10.1017/S0022112075003382.
- [187] F. X. Trias, F. Dabbagh, A. Gorobets, and C. Olier. [On a Proper Tensor-Diffusivity Model for Large-Eddy Simulation of Buoyancy-Driven Turbulence](#). *Flow, Turbul. Combust.*, 2020. doi: 10.1007/s10494-020-00123-3.
- [188] F. Dabbagh, F. X. Trias, A. Gorobets, and A. Oliva. [A priori study of subgrid-scale features in turbulent Rayleigh-Bénard convection](#). *Phys. Fluids*, 29(10):105103, 2017. doi: 10.1063/1.5005842.
- [189] S.-H. Peng and L. Davidson. [On a subgrid-scale heat flux model for large eddy simulation of turbulent thermal flow](#). *Int. J. Heat Mass Transf.*, 45(7):1393–1405, 2002. doi: 10.1016/S0017-9310(01)00254-X.
- [190] C. W. Higgins, M. B. Parlange, and C. Meneveau. [The heat flux and the temperature gradient in the lower atmosphere](#). *Geophys. Res. Lett.*, 31(22), 2004. doi: 10.1029/2004GL020053.
- [191] M. Schmelzer, Richard P. Dwight, and P. Cinnella. [Discovery of Algebraic Reynolds-Stress Models Using Sparse Symbolic Regression](#). *Flow, Turbul. Combust.*, 104(2-3): 579–603, mar 2020. doi: 10.1007/s10494-019-00089-x.
- [192] W. Pesch. [Complex spatiotemporal convection patterns](#). *Chaos An Interdiscip. J. Non-linear Sci.*, 6(3):348–357, 1996. doi: 10.1063/1.166194.
- [193] J. Korsgaard. [On the representation of two-dimensional isotropic functions](#). *Int. J. Eng. Sci.*, 28(7):653–662, 1990. doi: 10.1016/0020-7225(90)90093-X.

- [194] Q.-S. Zheng. [On the representations for isotropic vector-valued, symmetric tensor-valued and skew-symmetric tensor-valued functions.](#) *Int. J. Eng. Sci.*, 31(7):1013–1024, 1993. doi: 10.1016/0020-7225(93)90109-8.
- [195] Q.-S. Zheng. [Theory of Representations for Tensor Functions—A Unified Invariant Approach to Constitutive Equations.](#) *Appl. Mech. Rev.*, 47(11):545–587, 1994. doi: 10.1115/1.3111066.
- [196] T. B. Gatski and C. G. Speziale. [On explicit algebraic stress models for complex turbulent flows.](#) *J. Fluid Mech.*, 254:59–78, 1993. doi: 10.1017/S0022112093002034.
- [197] J. A. Weliwita, A. M. Rucklidge, and S. M. Tobias. [Skew-varicose instability in two-dimensional generalized Swift-Hohenberg equations.](#) *Phys. Rev. E*, 84(3):036201, 2011. doi: 10.1103/PhysRevE.84.036201.
- [198] S. L. Brunton and J. N. Kutz. *Data-Driven Science and Engineering.* Cambridge University Press, 2019. doi: 10.1017/9781108380690.
- [199] D. Forsyth. *Applied Machine Learning.* Springer International Publishing, Cham, 2019. doi: 10.1007/978-3-030-18114-7.
- [200] A. Sen and M. Srivastava. *Regression Analysis.* Springer Texts in Statistics. Springer New York, New York, NY, 1990. doi: 10.1007/978-1-4612-4470-7.
- [201] J. F. Cornwell. *Group Theory in Physics.* Elsevier, 1997. doi: 10.1016/B978-0-12-189800-7.X5000-6.
- [202] T. Inui, Y. Tanabe, and Y. Onodera. *Group Theory and Its Applications in Physics*, volume 78 of *Springer Series in Solid-State Sciences.* Springer Berlin Heidelberg, Berlin, Heidelberg, 1990. doi: 10.1007/978-3-642-80021-4.
- [203] N. Jeevanjee. *An Introduction to Tensors and Group Theory for Physicists.* Springer International Publishing, Cham, 2 edition, 2015. doi: 10.1007/978-3-319-14794-9.
- [204] K. Duraisamy, G. Iaccarino, and H. Xiao. [Turbulence Modeling in the Age of Data.](#) *Annu. Rev. Fluid Mech.*, 51(1):357–377, 2019. doi: 10.1146/annurev-fluid-010518-040547.
- [205] S. H. Rudy, S. L. Brunton, J. L. Proctor, and J. N. Kutz. [Data-driven discovery of partial differential equations.](#) *Sci. Adv.*, 3(4):e1602614, 2017. doi: 10.1126/sciadv.1602614.
- [206] S. L. Brunton, J. L. Proctor, and J. N. Kutz. [Discovering governing equations from data by sparse identification of nonlinear dynamical systems.](#) *Proc. Natl. Acad. Sci.*, 113(15):3932–3937, 2016. doi: 10.1073/pnas.1517384113.
- [207] X. Zhu, V. Mathai, R. J A M Stevens, R. Verzicco, and D. Lohse. [Transition to the Ultimate Regime in Two-Dimensional Rayleigh-Bénard Convection.](#) *Phys. Rev. Lett.*, 120(14):144502, 2018. doi: 10.1103/PhysRevLett.120.144502.
- [208] J. Schmalzl, M. Breuer, and U. Hansen. [On the validity of two-dimensional numerical approaches to time-dependent thermal convection.](#) *Europhys. Lett.*, 67(3):390–396, 2004. doi: 10.1209/epl/i2003-10298-4.

- [209] E. P. van der Poel, R. J. A. M. Stevens, and D. Lohse. [Comparison between two- and three-dimensional Rayleigh-Bénard convection](#). *J. Fluid Mech.*, 736:177–194, 2013. doi: 10.1017/jfm.2013.488.
- [210] J. H. Curry, J. R. Herring, J. Loncaric, and S. A. Orszag. [Order and disorder in two- and three-dimensional Bénard convection](#). *J. Fluid Mech.*, 147(-1):1, 1984. doi: 10.1017/S0022112084001968.
- [211] E. P. van der Poel, R. J. A. M. Stevens, K. Sugiyama, and D. Lohse. [Flow states in two-dimensional Rayleigh-Bénard convection as a function of aspect-ratio and Rayleigh number](#). *Phys. Fluids*, 24(8):085104, 2012. doi: 10.1063/1.4744988.
- [212] F. B. Lipps. [Dynamics of Variable Wavelength in Finite-Amplitude Bénard Convection](#). *Phys. Fluids*, 14(4):759, 1971. doi: 10.1063/1.1693502.
- [213] Q. Wang, R. Verzicco, D. Lohse, and O. Shishkina. [Multiple States in Turbulent Large-Aspect-Ratio Thermal Convection: What Determines the Number of Convection Rolls?](#) *Phys. Rev. Lett.*, 125(7):074501, 2020. doi: 10.1103/PhysRevLett.125.074501.
- [214] Y. Ogura. [A Numerical Study of Wavenumber Selection in Finite-Amplitude Rayleigh Convection](#). *J. Atmos. Sci.*, 28(5):709–717, 1971. doi: 10.1175/1520-0469(1971)028<0709:ANSOWS>2.0.CO;2.